JACOBS UNIVERSITY

Robust and Reliable Multiscale Modeling of Molecular Photoinduced Processes

by

Sayan Maity

A thesis submitted in partial fulfillment
of the requirements for the degree of

Doctor of Philosophy

in Chemistry

Approved Dissertation Committee

Prof. Dr. Ulrich Kleinekathöfer
(Jacobs University Bremen, Germany)

Prof. Dr. Arnulf Materny
(Jacobs University Bremen, Germany)

Prof. Dr. Thomas Frauenheim
(University of Bremen, Germany)

Date of Defense: **2nd June 2021**

Department of Physics & Earth Sciences

Family Name, Given/First Name	Maity, Sayan
Matriculation number	20331986
What kind of thesis are you submitting: Bachelor-, Master- or PhD-Thesis	PhD-Thesis

English: Declaration of Authorship

I hereby declare that the thesis submitted was created and written solely by myself without any external support. Any sources, direct or indirect, are marked as such. I am aware of the fact that the contents of the thesis in digital form may be revised with regard to usage of unauthorized aid as well as whether the whole or parts of it may be identified as plagiarism. I do agree my work to be entered into a database for it to be compared with existing sources, where it will remain in order to enable further comparisons with future theses. This does not grant any rights of reproduction and usage, however.
The Thesis has been written independently and has not been submitted at any other university for the conferral of a PhD degree; neither has the thesis been previously published in full.

German: Erklärung der Autorenschaft (Urheberschaft)

Ich erkläre hiermit, dass die vorliegende Arbeit ohne fremde Hilfe ausschließlich von mir erstellt und Christensen worden ist. Jedwede verwendeten Quellen, direkter oder indirekter Art, sind als solche kenntlich gemacht worden. Mir ist die Tatsache bewusst, dass der Inhalt der Thesis in digitaler Form geprüft werden kann im Hinblick darauf, ob es sich ganz oder in Teilen um ein Plagiat handelt. Ich bin damit einverstanden, dass meine Arbeit in einer Datenbank eingegeben werden kann, um mit bereits bestehenden Quellen verglichen zu werden und dort auch verbleibt, um mit zukünftigen Arbeiten verglichen werden zu können. Dies berechtigt jedoch nicht zur Verwendung oder Vervielfältigung.
Diese Arbeit wurde in der vorliegenden Form weder einer anderen Prüfungsbehörde vorgelegt noch wurde das Gesamtdokument bisher veröffentlicht.

Date, Signature

Acknowledgments

The complete journey of my Ph.D. was memorable. It is my pleasure to remember those names whose support made this journey possible. Here, I take this opportunity to acknowledge all of them.

First and foremost, I would like to sincerely thank my supervisor Prof. Dr. Ulrich Kleinekathöfer for giving me opportunity to work in his group at the Jacobs University Bremen and environment of the DFG Research Training Group "Quantum Mechanical Materials Modelling" mainly based at the University of Bremen. I am extremely grateful for his continuous support and encouragement towards some interesting and exciting research projects during my Ph.D. tenure. Moreover, I am also thankful for all his kind discussions and corrections in writing manuscripts as well as this thesis. I would also like to express my deepest gratitude to Prof. Dr. Arnulf Materny and Prof. Dr. Thomas Frauenheim for being my dissertation committee members and their valuable time to evaluate the present thesis.

I would also like to thank my collaborator Prof. Dr. Marcus Elstner and his group members especially Dr. Tomáš Kubař, Dr. Beatrix M. Bold and Monja Sokolov from the Karlsruhe Institute of Technology for their continuous support and discussions for development of present multiscale methods within the DFTB framework. Moreover, I would also like to thank my another collaborator Prof. Vangelis Daskalakis from the Cyprus University of Technology for all interesting discussions regarding the plant light-harvesting complexes. Especially, I would also like to thank him for listening and answering all my questions patiently and giving quick feedback in email. Moreover, I would also like to thank Research Training Groups especially the group of Dr. Susan Köppen from the University of Bremen and her group members Filippo Balzaretti and Maria von Einem for the collaboration and providing files for surface simulations in an ongoing project. I am also grateful to Dr. Bálint Aradi from the Research Training Group for the supports regarding the DFTB calculations for my projects.

I am also thankful to the Jacobs University Bremen for providing the computa-

tional resources of the CLAMV cluster. Moreover, I would also like to thank to Dr. Achim Gelessus and Florian Neu for their continuous technical supports and the CLAMV facilities. Additionally, my special thanks to Dr. Achim Gelessus for his discussion regarding the DFT/MRCI calculations in a collaborative project. Moreover, I would also like to thank our team assistants Britta Berninghausen and Ronja Avdo for helping me in all administrative works.

I thank all my current and former group members – Dr. Carlos, Dr. Karunakar, Dr. Shreyas, Dr. Hasan, Dr. Anusha, Dr. Vinay, Dr. Jignesh, Abhishek, Dr. Kaylan, Pooja, Yannick for interesting discussions, group parties and continuous support. My special thanks to Jigensh for his guidance during my beginning time in Bremen and motivating me in research. Moreover, I would also like to all the members of the Research Training Group and friends for wonderful times in Bremen. I am very grateful to my parents and sisters for their constant support and good wishes throughout my research.

Finally, I would like to praise and thank God, the almighty for granting the blessings that I am ultimately able to finish the thesis.

Abstract

The light-harvesting protein-pigment complexes of plants, bacteria and algae play a major role in the conversion of solar energy into sustainable forms of chemical energy during photosynthesis. Chlorophyll, bacterio-chlorophyll and bilin molecules are the key pigments present in those complexes which mainly control the excitation energy transfer processes. However, due to the large size and the electronic complexity of these pigment molecules, multiscale quantum-classical methods are often required to study the dynamical processes within protein environments. In this direction, the present thesis aims to formulate an efficient strategy in order to describe the underlying foundation of energy transfer process in these complexes and provides an outlook for the modeling of artificial LH complexes. To this end, the density functional based tight-binding (DFTB) method has been applied to perform ground state molecular dynamics simulations coupled to an electrostatic classical environment within a quantum mechanics/molecular mechanics (QM/MM) fashion. In a subsequent step, the time-dependent extension of the long-range-corrected DFTB formalism has been applied to calculate the excitation energies of each pigment molecules also in a QM/MM setting. This provides the basis of the multiscale scheme which is then applied to various bacterial and plant LH complexes to extract the major excitonic parameters like site energies, couplings and spectral densities. Moreover, based on these input parameters, exciton dynamics and transfer rate calculations have been performed for some of these systems. Furthermore, the calculated results were compared with the experimental counterparts resulting remarkable agreement for these large bio-molecular systems. These findings motivated further investigations on an artificially designed light-harvesting system by employing porphyrin molecules attached to a clay surface which is experimentally found to exhibit excellent energy transfer properties.

Funding

The funding for present thesis has been supported by the Deutsche Forschungsgemeinschaft (DFG) through Research Training Group “Quantum Mechanical Materials Modelling” (RTG-QM3) **GRK 2247** and **KL-1299/18-1**.

Dedicated to my friends and family

List of Publications

1. S. Maity, P. Sarngadharan, V. Daskalakis and U. Kleinekathöfer, Time-Dependent Atomistic Simulations of the CP29 Light-Harvesting Complex, **J. Chem. Phys.** 155, 055103 (2021).

2. S. Maity, V. Daskalakis, M. Elstner and U. Kleinekathöfer, Multiscale QM/MM Molecular Dynamics Simulations of the Trimeric Major Light-Harvesting Complex II, **Phys. Chem. Chem. Phys.** 23, 7407 (2021).

3. S. Maity, B. M. Bold, J. D. Prajapati, M. Sokolov, T. Kubař, M. Elstner and U. Kleinekathöfer, DFTB/MM Molecular Dynamics Simulations of the FMO Light-Harvesting Complex, **J. Phys. Chem. Lett.** 11, 8660 (2020).

4. B. M. Bold, M. Sokolov, **S. Maity**, M. Wanko, P. M. Dohmen, J. J. Kranz, U. Kleinekathöfer, S. Höfener and M. Elstner, Benchmark and Performance of Long-Range Corrected Time-Dependent Density Functional Tight Binding (LC-TD-DFTB) on Rhodopsins and Light-Harvesting Complexes, **Phys. Chem. Chem. Phys.** 22, 10500 (2020).

5. S. Maity, A. Gelessus, V. Daskalakis and U. Kleinekathöfer, On a Chlorophyll-Caroteinoid Coupling in LHCII, **Chem. Phys.** 526, 110439 (2019).

6. V. Daskalakis, **S. Maity**, C. L. Hart, T. Stergiannakos, C. D. P. Duffy and U. Kleinekathöfer, Structural Basis for Allosteric Regulation in the Major Antenna Trimer of Photosystem II, **J. Phys. Chem. B** 123, 9609 (2019).

Poster and Oral Presentations

1. P. Sarngadharan, S. Maity and U. Kleinekathoefer, 57th Symposium on Theoretical Chemistry, Würzburg, Germany (poster, September 2021).

2. S. Maity and U. Kleinekathöfer, RTG-QM3 Virtual Retreat, Bremen, Germany (oral, October 2020).

3. S. Maity and U. Kleinekathöfer, CECAM Workshop OUTBOX, Bremen, Germany (poster, October 2019).

4. S. Maity and U. Kleinekathöfer, RTG-QM3 Midterm-Workshop, Bremen, Germany (oral, October 2019).

5. S. Maity, B. Bold, J. D. Prajapati, M. Elstner and U. Kleinekathöfer, 55th Symposium on Theoretical Chemistry, Rostock, Germany (poster, September 2019).

6. S. Maity, B. Bold, J. D. Prajapati, M. Elstner and U. Kleinekathöfer, 12th North German Biophysics Meeting, Borstel, Germany, (poster, January 2019).

7. S. Maity and U. Kleinekathöfer, RTG-QM3 Midterm-Workshop, Bremen, Germany (oral, September 2018).

8. S. Maity, B. Bold, J. D. Prajapati, M. Elstner and U. Kleinekathöfer, 54th Symposium on Theoretical Chemistry, Halle, Germany (poster, September 2018).

Contents

1 Introduction **1**

1.1 Natural LH Complexes 2

1.1.1 Bacterial LH Complexes 4

1.1.2 Plant LH Complexes 6

1.2 Artificial LH Complexes 8

1.3 Theoretical Background 9

1.3.1 Ground State Simulations 12

1.3.2 Excited State Calculation 14

1.3.3 Excitonic Coupling and System Hamiltonian 15

1.3.4 Autocorrelation Function and Spectral Density 17

1.3.5 Wave Packet Dynamics 18

1.4 Outline of Results and Discussion 21

2 Benchmark and Performance of Long-range Corrected Time-dependent Density Functional Tight Binding (LC-TD-DFTB) on Rhodopsins and Light-Harvesting Complexes **23**

2.1 Introduction 24

2.2 Computational Details 30

2.2.1 Models and geometry optimization 30

2.2.2 Classical and QM/MM MD simulations 31

2.2.3 Excitation energies 32

2.2.4 Exciton couplings 34

2.3 Benchmark 36

2.3.1 Retinal 36

2.3.2 Bacteriochlorophyll a (BChl a) 40

2.4 Performance of LC-DFTB in biological model systems 47

2.4.1 Rhodopsin models 47

2.4.2 Light-harvesting complexes 52

2.5 Summary 61

3 DFTB/MM Molecular Dynamics Simulations of the FMO Light-Harvesting Complex 65

3.1 Introduction 66

3.2 Results and Discussion 70

3.2.1 Site energy distributions 70

3.2.2 Spectral Density 72

3.2.3 Wave Packet Dynamics 75

3.3 Conclusions 77

4 Multiscale QM/MM Molecular Dynamics Simulations of the Trimeric Major Light-Harvesting Complex II 80

4.1 Introduction 81

4.2 Computational Method 86

4.3 Results and Discussion 88

4.3.1 Site Energy Calculations 88

4.3.2 Spectral Density 91

4.4 Excitation Energy Transfer Rate between Chl-a 612 and Lut-1 . . . 96

4.5 Conclusions 100

5 Time-Dependent Atomistic Simulations of the CP29 Light-Harvesting Complex 103

5.1 Introduction 104

5.2 Computational Method 107

5.2.1 Theoretical Background 111

5.3 Results and Discussion 113

5.3.1 Site Energy Calculations 113

5.3.2 Autocorrelation Functions and Spectral Densities 115

5.3.3 Comparison to Experimental Spectral Densities 116

5.3.4 Impact of the Classical Force Fields on Spectral Density in the QM/MM MD Simulation 118

5.3.5 Comparison of Spectral Density for other LH Complexes . . 120

5.3.6 Excitonic Coupling and Wave Packet Dynamics 121

5.4 Absorption Spectra 125

5.5 Conclusions 127

6 On a Chlorophyll-Caroteinoid Coupling in LHCII 131
6.1 Introduction . . . 131
6.2 Computational Methods . . . 136
6.2.1 MD Simulation . . . 136
6.2.2 Basics of the TrESP Coupling Formalism . . . 136
6.2.3 Calculation of the Transition Charges . . . 138
6.3 Results and Discussions . . . 140
6.3.1 Distribution of Transition Charges for the Chl-a and Lut Molecules 140
6.3.2 Distribution of the Excitonic Couplings of the Chl-a 612/Lut1 Pairs . . . 143
6.4 Conclusions . . . 148

7 Outlook on the Modeling of Porphyrin/Clay-surface Artificial LH Complex 151

8 Summary 153

A Chapter 2: Supporting Information 155
A.1 Computational Details . . . 155
A.1.1 Equilibration and classical MD simulation of the LH complexes 155
A.1.2 Excitonic Coupling . . . 156
A.2 Benchmark . . . 157
A.2.1 Retinal . . . 157
A.2.2 Bacteriochlorophyll a . . . 158
A.3 Performance of LC-DFTB on biological model systems . . . 164
A.3.1 Rhodopsins . . . 164
A.4 Light-harvesting complexes . . . 165
A.4.1 LH2 complex of *Rs. molischianum*, QM/MM optimized model 165

B Chapter 3: Supporting Information 176
B.1 Computational Details . . . 176
B.2 Bond Length Alternation . . . 180
B.3 Excitation Energy Distributions . . . 182
B.4 Autocorrelation Function and Spectral Density . . . 183
B.5 Sampling Issues for the Spectral Density . . . 186
B.6 Experimental Spectral Density . . . 188
B.7 Comparison to Other Computed Spectral Densities . . . 189

B.8 Wave Packet Dynamics 191

C Chapter 4: Supporting Information 193

C.1 Site Energy Distributions for the Individual Chl-a Pigments 193

C.2 Autocorrelation Functions and Spectral Densities for the Individual Chl-a Pigments 194

C.3 Comparison of Experimental Spectral Density with Different Broadening Parameter 195

C.4 Excitonic Coupling between Chl-a 612/Lut-1 Pair 196

D Chapter 5: Supporting Information 197

D.1 Structural Comparison of Chl and BChl Molecules 197

D.2 Density of States 197

D.3 Shifted Site Energies 198

D.4 Spectral Densities for Two Different Sets of QM/MM MD Simulations 200

D.5 Comparison of Experimental Spectral Density between Plant and Bacterial LH Complexes 202

D.6 Absorption Spectrum at Low Temperature 202

D.7 TrESP Charges for Chl-a and Chl-b Pigments 203

References 206

Chapter 1

Introduction

In the future, solar power will become an evermore important source of energy over fossil fuels as it is clean, renewable and affluent in nature. To employ solar energy as a "chemical fuel", photo-chemical reactions are of prime importance. The photo-biological process which is commonly known as photosynthesis is the primary source of energy conversion for the living organisms on Earth. It is an unique mechanism where solar energy is directly transformed into a stable form of chemical energy and produces O_2 by absorbing CO_2 in many cases [1–3]. Recently,

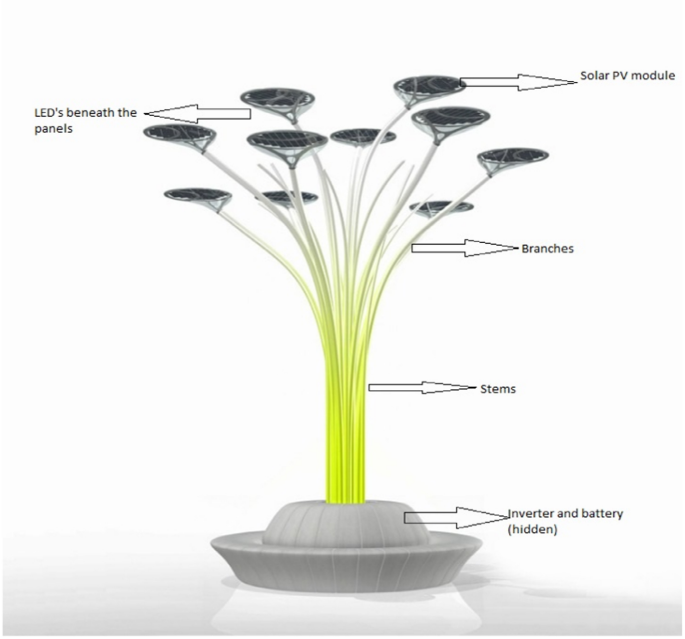

Figure 1.1: A sketch of a man-made solar tree producing clean energy. Reprinted from [4], Copyright (2018) with permission from Elsevier.

because of the extensive demand of renewable energy and in order to control the environmental pollution caused by fossil fuels, the man-made mimicking of photosynthesis has attracted huge attention. In this direction photovoltaic batteries are being utilized as fuel cells to produce electric energy. In the industrial production

of low cost and efficient solar energy devices, various emerging photovoltaic compounds like perovskite, organic photovoltaic materials and dye-sensitized solar cells (DSSC) are considered as good choices [5–8]. An array of several photovoltaic systems is generally combined together to build solar panels or solar trees which can supply electricity in day to day life. A sketch of an artificial solar tree which can produce clean, sustainable and renewable energy is depicted in Fig. 1.1. To be able to construct a solar energy tree first one needs to understand the mechanism of natural photosynthesis which mainly occurs in green plants, bacteria and algae. The chlorophyll (Chl), bacterio-chlorophyll (BChl) and bilin molecules are the key pigments which harvest the solar energy during photosynthesis [9–12]. These pigments are surrounded by protein environments in the respective photosystem which are commonly known as light-harvesting (LH) complexes. The primary role of these LH complexes are to transport the solar energy to the reaction center for further processes in photosynthesis.

In the following section, a brief overview of several natural LH complexes of bacteria and plants are shown and their role during photosynthesis is explained. Moreover, some examples of artificial LH complexes are also presented.

1.1 Natural LH Complexes

Photosynthesis can be categorized into two types depending upon the release of oxygen as oxygenic and anoxygenic. Plants are known to participate in oxygenic photosynthesis and split water molecule (H_2O) into molecular oxygen. Moreover, some algae and cyanobacteria can also perform oxygenic photosynthesis via a similar kind of process as green plants. However, green sulfur bacteria and purple bacteria are known to conduct anoxygenic photosynthesis with the help of a terminal reductant like hydrogen sulfide (H_2S) and produce other byproducts such as sulfur instead of molecular oxygen [1, 13, 14]. The general equation of natural photosynthesis can be expressed as

$$nCO_2 + 2nH_2X + h\nu \rightarrow (CH_2O)_n + 2nX + nH_2O \tag{1.1}$$

where H_2X is the reducing agent, either H_2O or H_2S and CH_2O is carbohydrate.

In both these variants of photosynthesis, solar energy is stored in the stable form chemical energy as adenosine triphosphate (ATP). During the energy conver-

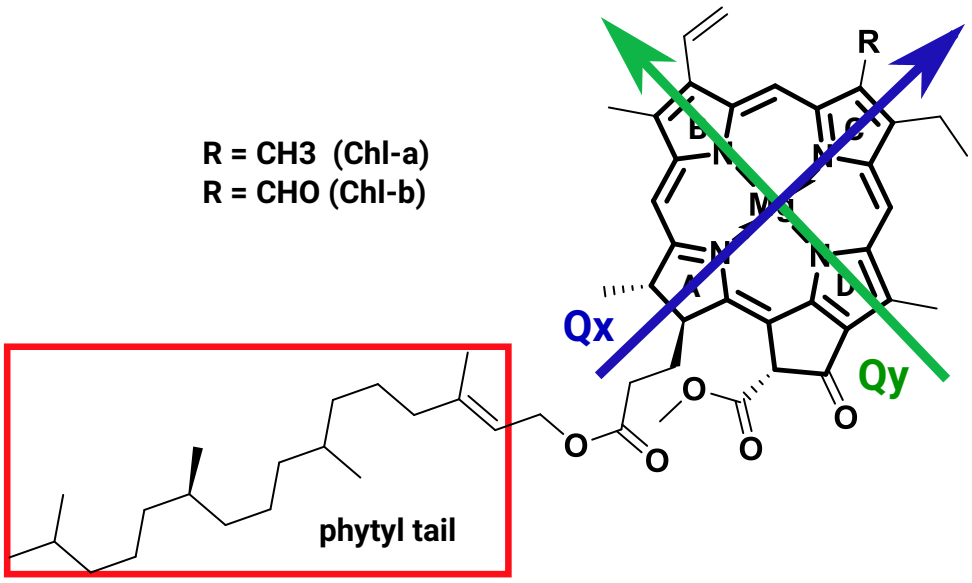

Figure 1.2: Structural overview of Chl-a/b pigment molecules from plant LH complexes. The Q_x and Q_y axes represent the directions of transition dipole moment.

sion process, the protein-pigment antenna complexes which are commonly known as LH complexes are playing a major role. Aim of these complexes is to transport the absorbed solar energy in form of excitons i.e. as a combined form of electron-hole pair to the reaction center so that the subsequent steps of photosynthesis can occur. During the energy transfer process, the lowest excited state of the BChl or Chl pigment molecules whose transition moment is directed along the Q_y axis transfer the excitation energy to the closely coupled neighboring pigment. Upon the absorption of sunlight, the Q_x, Q_y and other states are mainly excited because of the conjugated Mg-porphyrin ring of the Chl/BChl molecule. However, the phytyl tails together with the protein and solvent act as an environment and influence the excitation energy fluctuations during the transfer process. An example of the structural features together with the different transition dipole moment axes are shown in Fig. 1.2 for Chl pigment molecules. In the first part of the present thesis, several QM methods have been employed to benchmark the Q_y excitation energies and the excitonic couplings of the pigment molecules in gas phase as well as inside a protein environment for several LH complexes. Afterwards, calculations of the exciton dynamics on some of the model LH systems were performed.

Aim of the present thesis is to develop a robust and efficient methodology to investigate the excitation energy transfer processes in LH complexes of plants and bacteria. In all studies which are described in the following chapters, the focus is mainly on the ground and excited state electronic structure of the pigment molecules within the protein environment. However, because of the large size and

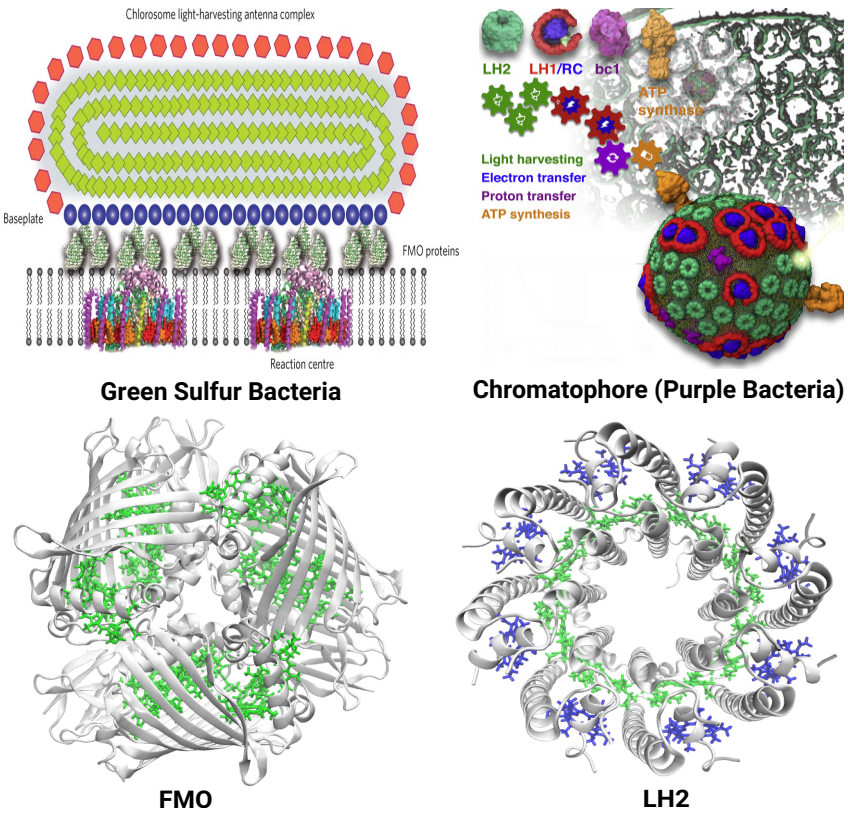

Figure 1.3: Upper panel shows the photosynthetic machinery of green sulfur and purple bacteria. The lower panel depicts the FMO complex from green sulfur bacteria and the LH2 complex from purple bacteria. The figure of green sulfur bacteria is reprinted by permission from Ref. 22, Copyright (1969) with permission from Springer Nature and the figure of purple bacteria is reprinted by permission from Ref. 23, Copyright (2019) with permission from Elsevier.

complex electronic structure of pigments like Chl and BChl, the methods were developed within a mixed quantum-classical approach as explained in the following theoretical section.

1.1.1 Bacterial LH Complexes

BChl-a are the major pigment molecules responsible for the energy transfer processes in bacterial LH complexes. In the last two decades, the FMO (Fenna-Mathews-Olson) and LH2 complexes of bacteria have become extensively studies systems because of the experimental claim of long-lived quantum coherence phenomena [15–21]. During the photosynthesis process, these antenna complexes work as a mediator to transport the absorbed solar energy to the respective reaction centers. The FMO complex is a water-soluble LH system which is found in green sulfur bacteria. It acts as the bridge between the chlorosome, a large antenna complex and the reaction center for the transportation of solar energy. The structural orientation of the FMO complex inside the green sulfur bacteria and its

geometrical architecture is shown in the Fig. 1.3. The first X-ray crystallographic measurements of the FMO complex were done in 1975 by Fenna, Mathews and Olson. The spatial distribution was characterized as a trimeric C3-symmetry containing seven BChl pigments in each monomer [24]. Later in 2009, the eighth pigment was identified in the respective monomers. The eighth BChl is weakly bound to a monomeric unit and only obtained stability in a trimeric architecture [25]. In the year 2007, Engel et al. found a wave-like energy transfer in the FMO complex and the coherence time was captured up to the pico-second timescale at 77 K temperature in their two-dimensional spectroscopic measurements [15]. This opened a new research field known as "quantum biology". Extensive studies were performed in experiment followed by theoretical calculations on several LH complexes at both low and room temperature to figure out the reason behind the long-lived coherence phenomena [20, 21, 26, 27]. At some point it was assumed that correlated site energy fluctuations of the pigments could be the origin of such long-lived coherence. This assumption, however, ruled out by simulations [26, 28] and also some recent studies raised serious doubts on the electronic nature of the coherence [19, 29, 30]. In these studies, another model system was considered comprehensively which is the LH2 complex of the purple bacteria [31]. Different types of LH2 complexes are identified from different organisms e.g. *Rhodopseudomonas acidophila* [9] and *Rhodospirillum molischianum* [32] containing 27 and 24 BChl pigment molecules. The carotenoids act as accessory pigments but most of the investigations were focused on the BChl molecules of the LH2 complex. Moreover, two types of pigment rings named as B800 and B850 are present in these complexes based on their absorption wavelength. The B800 ring contains 9 and 8 BChl molecules whereas the B850 ring holds 18 and 16 BChl pigments for the *Rhodopseudomonas acidophila* and *Rhodospirillum molischianum* bacteria, respectively. The BChl molecules inside the B800 ring are weakly coupled and the excitation energy transfer generally takes place within 400 fs whereas the pigment molecules of the B850 are strongly coupled and their transfer rates are around 100 fs [33]. Moreover, within the B850 ring, two types of couplings are present depending the inter and intra-molecular coupling distribution. For this reason, different transfer rates are also observed for this ring [34, 35]. For some organisms, the LH2 complex is part of the large photosynthetic machinery which is known as the chromatophore. The chromatophore contains several LH2 complexes and reaction centers which are surrounded by LH1 ring complexes. A recently modeled

architecture of the chromatophore containing around 136 millions atoms [23] is shown in Fig. 1.3.

1.1.2 Plant LH Complexes

In spite of conducting significant amount of photosynthesis on Earth, the LH complexes of higher plants only recently obtained a large attention because of the unique event of photoprotection. In the presence of excess sunlight, a pH gradient is triggered across the thylakoid membrane which induces conformational changes in the protein environments of the LH complexes in order to release excess solar energy as heat. This regulation of the plant photosynthetic equipment is commonly known as non-photochemical quenching (NPQ) of higher plants [36–38]. Besides the pH gradient, the presence of the photosystem II subunit S (PsbS) protein can also impact the conformational changes in the antenna complexes in order to activate the quenching mechanism [39–41]. In the NPQ process, the major antenna LHCII and the minor antenna CP29 complexes are key LH systems of the photosystem II (PSII) in higher plants. The PSII protein-pigment super-complex of oxygenic photosynthesis found in the thylakoid membrane of plants, algae and cyanobacteria. It consists of several major antennas of the LHCII complexes, minor antennas like CP29, CP26, CP24 complexes, a dimeric PSII-core having CP43, CP47 complexes and reaction centers. Moreover, the oxygen evolving complex Mn_4CaO_5 is also present inside the PSII-core complex which is responsible for the water oxidation and production of molecular oxygen. During the water splitting process, a proton gradient is generated across the thylakoid membrane which helps the ATP-synthase motor to produce the chemical fuel ATP. The free electron that is formed in the PSII complex travels via an electron acceptor chain and reaches the PSI complex for further charge separation processes at the PSI reaction center [42]. The structural overview of the PSII and PSI super-complexes and their location in higher plants is shown in the upper panel of the Fig. 1.4. During the photosynthesis process, it is believed that the PSII complex is mostly responsible for controlling the regulation since in some cases, the biological conditions are not relevant for the PSI complex to participate in the NPQ mechanism [43]. Moreover, LHCII complexes are present in the periphery of the PSII system whereas the CP29 complex acts as a bridge between the LHCII complex and the PSII core complex of the reaction center. Hence under intense light conditions, these two

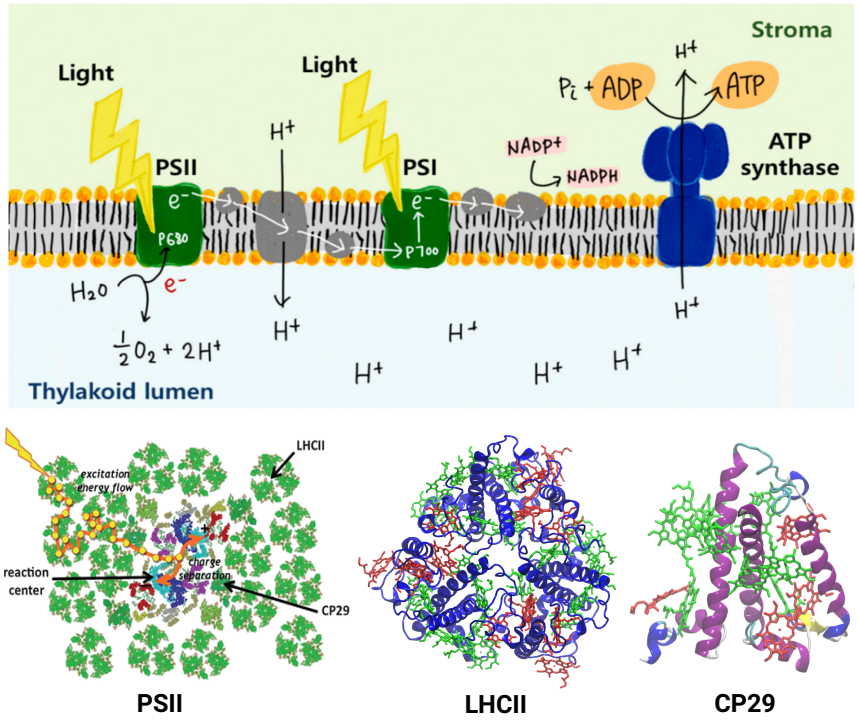

Figure 1.4: Upper panel shows the complete photosynthetic machinery of the higher plants. The picture of the plant photosystem is reprinted by permission from Ref. 44. Lower panel depicts the architecture of PSII super-complex, the major antenna LHCII and the minor antenna CP29 complex. The figure of the PSII super-complex is reprinted by permission from the Ref. 45, Copyright (2012) with permission from Royal Society of Chemistry.

antenna complexes can easily dissipate excess energy load before it can reach the reaction center. The crystal structure of the LHCII complex shows a trimer and each monomer accommodates 14 Chl (eight Chl-a and six Chl-b) molecules. Moreover four carotenoids including two luteins (Lut), one neoxanthin (Neo) and one violaxanthin (Vio) are also present in a monomeric unit [46]. The CP29 minor antenna complex contains total 13 Chl (nine Chl-a and four Chl-b) and three carotenoids such as Lut, Neo and Vio [47]. The pool of Chl-b is present in the surrounding of the Chl-a pool in both these antenna complexes and its role is supplementary in the EET process by transferring the excitation energy towards the Chl-a pool. In plants, Chl-a and Chl-b are the major pigment molecules responsible for the energy transfer process whereas the carotenoids are known for controlling the quenching regulation together with light harvesting. The structural features of the Chl molecules are similar to BChl molecules of the bacterial LH complexes and both pigment types have similar Q_x and Q_y excited states. However, the Mg-porphyrin ring in Chl molecule contains one C=C less compared to the BChl pigments, which makes Chl pigments more flexible during the energy transfer process.

In the present thesis, the multiscale method was employed mainly on the LHCII and CP29 complexes to compute several excitonic parameters such as site energies, excitonic couplings and spectral densities in order to study the energy transfer rates and dynamics. Moreover, based on the results the non-photochemical regulation has partially been explained at different pH states. The photosynthetic machinery of the higher plants including the PSII architecture and its most important LH complexes like LHCII, CP29 are shown in the lower panel of the Fig. 1.4.

1.2 Artificial LH Complexes

Motivated by the natural LH complexes, people have synthesized aggregated porphyrin or tetrapyrolles molecules which also can perform light-harvesting and charge transfer processes. Some molecularly engineered porphyrin dyes utilized in dye-sensitized solar cell (DSSC) have recently been found to show excellent light harvesting properties in experiments [48]. In these DSSC, dye molecules are attached mainly on TiO_2 surfaces and commonly known as Grätzel solar cells since they were first reported by Grätzel and co-workers in 1991 [5]. An exam-

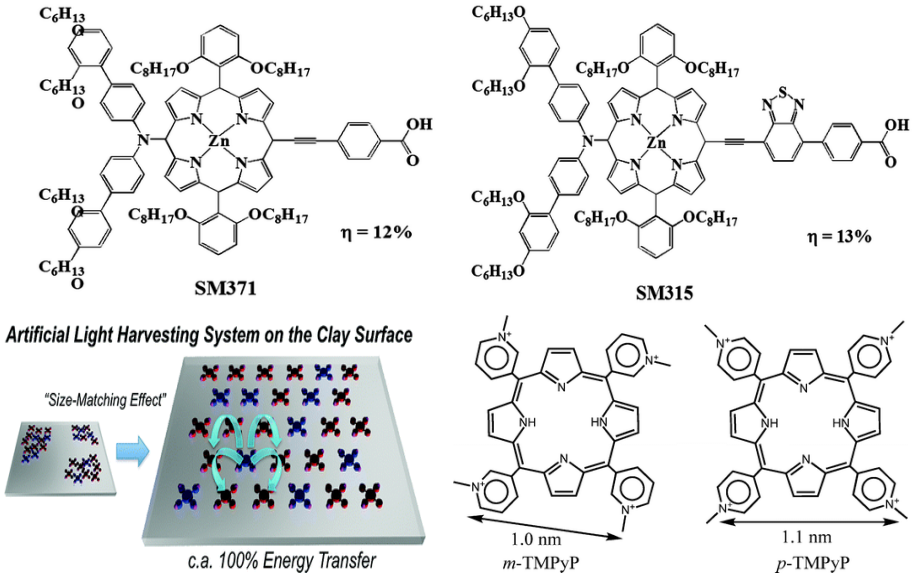

Figure 1.5: Upper panel shows some example dye molecules employed in Grätzel solar cell (figure reprinted by permission from the Ref. [49], Copyright (2014) with permission from Royal Society of Chemistry), whereas the lower panel depicts an artificial light harvesting complex and the porphyrin pigment molecules (figure reprinted by permission from the Ref. [50], Copyright (2011) with permission from American Chemical Society).

ple of such dyes are SM371 and SM315 which feature a prototypical structure of a donor-π-bridge-acceptor (D-π-A) and both maximize the electrolyte compatibility and improve the light-harvesting properties up to 12-13 %. These solar cells

are easy to fabricate, cheap in production and have a relatively high power conversion efficiency η. Moreover, porphyrin molecules attached to some inorganic surfaces were also synthesized and found to exhibit remarkable light harvesting efficiencies. These porphyrin/surface systems are often described as artificial LH complexes where the surface acts as the protein environment and traps the porphyrin pigments like Chl/BChl molecules similar to the biological antenna complexes [50–52]. In some cases, the surfaces are made of clays minerals and act as ideal hosts to assemble the porphyrin dyes for efficient energy transfer. The regular aggregation of the porphyrin molecules are controlled by "size-matching rule" where each dye keeps a separate distance between them. In 2011, experimentalists found that positively charged porphyrin dyes aggregating on an anionic clay surface using the "size machine rule" can show excitation energy transfer up to 100% efficiency [50]. An example of dyes used in a Grätzel solar cell and an artificially synthesized light-harvesting system is presented in Fig. 1.5.

As an outlook of the present thesis, an artificial LH system is modeled by attaching free-base porphyrin molecules on a montmorillonite clay surface and performed some of the steps as described in the present multiscale scheme.

1.3 Theoretical Background

Considering two pigments in LH complexes, sunlight is absorbed by a donor pigment (D) and an excitonic state (D*) is formed from which the excitation energy is transferred to a closely coupled acceptor pigment molecule (A). This kind of transfer process is generally characterized via two possible mechanisms i.e. the Förster transfer [53] and the Dexter transfer [54] mechanisms. In the former case, the energy is transferred in a resonance manner where the donor molecule is de-excited and at the same time the acceptor molecule gets excited without any overlap between the electronic wave functions. In case of the Dexter transfer process, an electron exchange happens between the ground and excited states of donor and acceptor molecules and thus an overlap of the wave functions is necessary. Generally, the Dexter coupling is distance dependent and presents when the intermolecular distance is rather short ($\sim$ 5 Å) in the reaction center of biological LH complexes. However, the Förster transfer process majorly contributes in various LH systems of bacteria and plants where the distance between the pigments is quite large ($\sim$ 10 Å). A graphical representation these two types of transfer

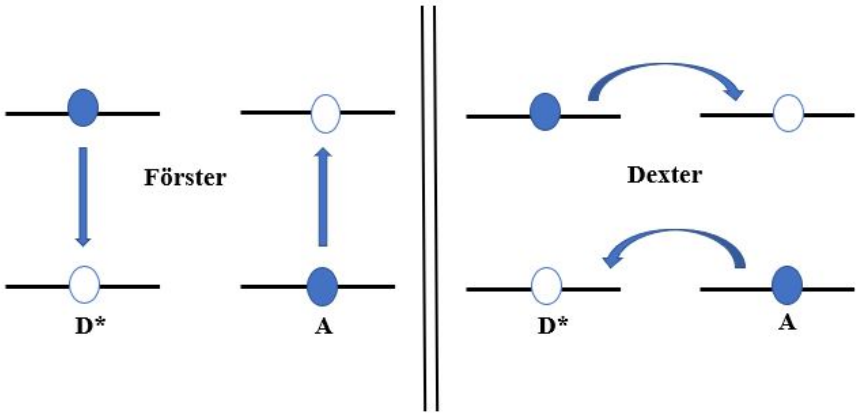

Figure 1.6: A schematic diagram of the Förster and Dexter exciton transfer mechanisms.

processes is shown in Fig. 1.6.

Over the past decades, the LH complexes of bacteria, marine algae and conjugated polymers have been of great interest because of the experimental claim of long-lived quantum coherence events during the energy transfer process at low as well as at room temperature as discussed above [15, 16, 18, 55, 56]. It was speculated that the protein environment mainly controls the correlations between the site energies of pigment molecules which could be the primary reason behind such long coherences. Earlier theoretical calculations based on classical molecular dynamics (MD) simulations, however, did not reveal any spatial correlation between the site-energy fluctuations of closely coupled pigment molecules [26, 28]. Moreover, in recent experiments based on two-dimensional electronic spectroscopy measurements, the coherences were detected only at short time scales for some model LH complexes. These studies also have raised some significant doubts on the electronic nature of the previous proposal of long-lived coherences and the long-lived oscillations are believed to be due to the vibrational dynamics [19, 30, 57]. Apart from the bacterial LH complexes, parallel attention has also been paid to light harvesting for the plant LH systems where a photoprotective process has attracted quite some interest in recent times. This mechanism is known as the NPQ regulation of higher plants [36–38].

To study the energy transfer dynamics in the LH complexes of bacteria, algae or plants, various theoretical models have been established within the context of open quantum systems [58]. In several of these approaches, mixed quantum-classical simulations are performed together with excited state calculations to figure out the evolution of exciton population among the pigment molecules [26, 59–63]. Over the few years, our group has mainly followed two strategies to

study the LH complexes of bacteria and algae. On the one hand, the so-called spectral density of each pigment can be extracted and density matrix calculations are performed. On the other hand, a time-dependent Hamiltonian is di-

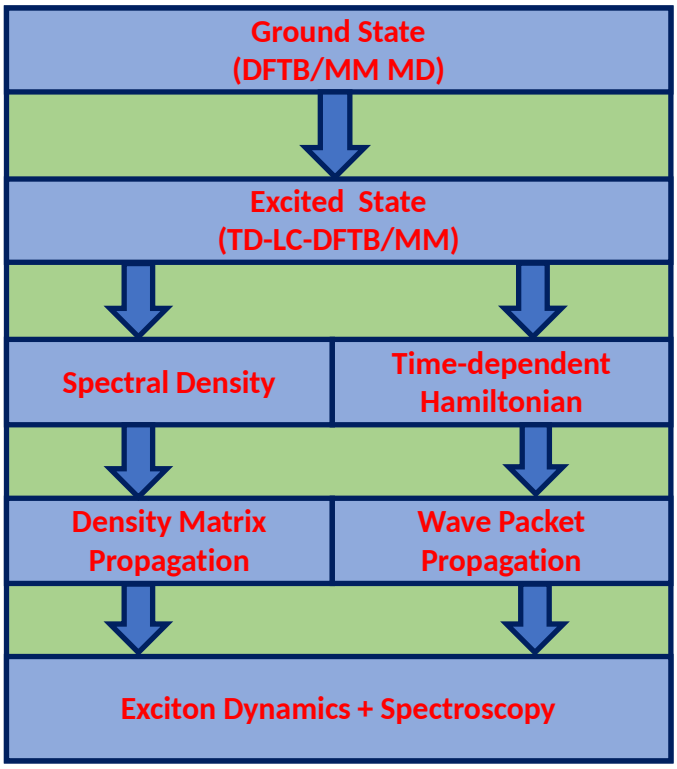

Figure 1.7: A schematic representation of the present mixed quantum-classical approach.

rectly employed to perform ensemble-averaged wave-packet based exciton dynamics [27,28,59,64–66]. The basis for most of these investigations were classical MD simulations followed by excited state calculations based on either ZINDO/S-CIS (Zerner's Intermediate Neglect of Differential Orbital method with spectroscopic parameters together with the configuration interaction using single excitation) or TDDFT (time-dependent density functional theory) methods within a quantum mechanics/molecular mechanics (QM/MM) framework. In spite of being a robust strategy, these approaches often produce artefacts in the spectral density calculation because of the poor quality of the geometries extracted from the classical ground state MD simulations which are subsequently employed in excited state QM calculations [62,63,67]. In order to resolve this problem of the so-called "geometry mismatch" and a poor description of the intramolecular vibrational dynamics, we have replaced the classical ground state MD by a Born-Oppenheimer MD in order to improve the quality of the geometries as well as the associated vibrational dynamics. The numerical costs of the calculation has been reduced by employing the density functional based tight-binding (DFTB) [68] method coupled with a

classical force field in a QM/MM fashion. Subsequently, the time-dependent extension of the long-range corrected DFTB (TD-LC-DFTB) [69] is utilized to perform the excited state calculations along those trajectories also in a QM/MM setting. Based on this improved multiscale approach, the resulting spectral densities show a remarkable agreement with experimental measurements for the bacterial and plant LH complexes as shown in the following chapters. A schematically diagram of the scheme is given in Fig. 1.7. Once the system is prepared, the multiscale method is employed to extract the input parameters and perform an exciton dynamics. In the following, most of the steps in the present multiscale procedure are detailed.

1.3.1 Ground State Simulations

The first step of the present multiscale strategy is the ground state simulations. The 3rd order version of the DFTB method [70] is applied in connection with a classical force field to perform Born-Oppenheimer MD simulations (BOMD) in a QM/MM framework. An example of a QM/MM partitioning is represented in

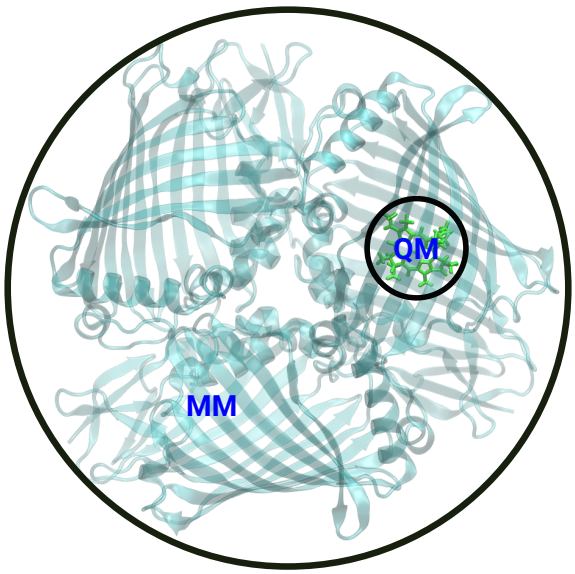

Figure 1.8: An example of QM/MM setting is represented to treat the LH complexes. The pigment molecule is considered as the QM region of interest while the rest (protein, solvent etc.) is included in the MM region.

Fig. 1.8 where the pigment molecule defines the QM region and the rest including protein, solvent etc. are considered as MM region. In BOMD, Newton's equation of motion is applied to propagate the nuclei based on the following expression where the potential energy (V) and its corresponding force (F) are calculated by

solving the electronic wave functions at each time step

$$\vec{F_i}(t) = m_i \frac{d^2\vec{x}_i(t)}{dt^2} = -\nabla_i V[\vec{x_1}, \vec{x_2}, ..., \vec{x_i}] \qquad i = 1, 2, \ldots, N. \tag{1.2}$$

In case of the BOMD simulation in a QM/MM setting, a QM method is applied in the QM region whereas the classical force fields are employed in the MM region in order to obtain a QM/MM MD trajectory of the system. The total energy of the system in QM/MM description is obtained by the following equation

$$E = E^{QM} + E^{MM} + E^{QM/MM} \tag{1.3}$$

where E^{QM} denotes the total energy of the QM region, E^{MM} the total energy of the classical region and $E^{QM/MM}$ the interaction energy between the QM and MM subsystems. There are three types of embedding approaches that are generally used to describe the QM/MM interaction energy: mechanical, electronic also known as electrostatic and polarizable. In our calculation, the electronic embedding procedure is used which takes the electrostatic interaction of the MM point charge over the QM region by the following expression

$$E_{el}^{QM/MM} \approx \sum_{A}^{N_{MM}} \sum_{B}^{N_{QM}} \frac{Q_A . q_B}{|\vec{R_A} - \vec{r_B}|} \tag{1.4}$$

where Q_A is the partial charges of the atoms in the MM region which is described in the classical force field and q_B is the charges of the atoms in the QM region which are updated during the QM/MM MD simulations.

In most QM/MM MD simulations, DFT and semi-empirical methods are used as QM method of choice since wave function-based QM methods are computationally expensive for a dynamical simulation. However, DFT calculations is still numerically expensive to perform a subsequent long dynamics for the large pigment molecules like Chl/BChl. Hence, the numerically efficient DFTB method is utilized for the ground state simulations. The DFTB theory is an approximation of DFT approach achieving a similar accuracy but with a three orders of magnitude faster speed for the double-zeta polarized (DZP) basis set [68]. In the DFTB3 method [70, 71], the total Kohn-Sham (KS) DFT energy is expanded in a Taylor series around a reference density ρ_0 by the following equation

$$E^{DFTB3}[\rho^0 + \delta\rho] = E^0[\rho_0] + E^1[\rho_0, \delta\rho] + E^2[\rho_0, (\delta\rho)^2] + E^3[\rho_0, (\delta\rho)^3] \tag{1.5}$$

where $E^0[\rho_0]$ includes double counting contributions of the KS-DFT and the nuclear-nuclear repulsion. The combination of the first two terms is known as DFTB1, up to three terms as DFTB2. The DFTB2 method is also known as SCC-DFTB, since it includes a self-consistence redistribution of the Mulliken charges. The 3rd-order correction, i.e., DFTB3 also described as SCC-DFTB3 contains all of the terms in the above expression. The negative gradient of the DFTB3 energy is the quantum force acting on the QM region in the ground state simulation of the LH complexes in our studies. The Hamiltonian of the DFTB method is not constructed "on-the-fly" during the simulations rather the parameters are pre-calculated and stored in a separate Slater-Koster file. This fact is the main reason behind the faster calculation of DFTB compared to DFT method. In the present thesis, mainly 3OB and 3OB-f parameter sets were utilized in combination with CHARMM, AMBER and OPLS classical force fields to perform ground state QM/MM MD simulations.

1.3.2 Excited State Calculation

Subsequently, the ground state trajectories have been subjected to the excited state calculations also in a QM/MM style. Here, the QM region is treated by the TD-LC-DFTB method whereas the MM region is represented by the point charges from the classical force field. The LC-DFTB theory is analogous to the LC-DFT method which was developed to treat charge transfer and overpolarization problems in conjugated systems. So far, the LC-DFTB has been developed within the 2nd-order DFTB variant based on the OB2 parameter set and the typical range-separation ansatz for the Coulomb interaction ($1/r_{12}$) is used in terms of short-range and long-range parts [72]

$$\frac{1}{r_{12}} = \frac{\exp(-\omega r_{12})}{r_{12}} + \frac{1-\exp(-\omega r_{12})}{r_{12}} \tag{1.6}$$

where the first part of the Coulomb interaction represents the short-range contribution of the local functional and the second part is the long-range contribution which accounts for the non-local Hartee-Fock exchange. Moreover, ω is the range-separation parameter which controls the contributions of both short-range and long-range part. In the time-dependent extension, the Hamiltonian is perturbed within the linear-response regime from which the vertical excitation energy of the

system can be directly obtained by the Casida equation [69]

$$\begin{pmatrix} A & B \\ B & A \end{pmatrix} \begin{pmatrix} X \\ Y \end{pmatrix} = \Omega \begin{pmatrix} 1 & 0 \\ 0 & -1 \end{pmatrix} \begin{pmatrix} X \\ Y \end{pmatrix} \tag{1.7}$$

where the eigenvectors X, Y are the respective transition density and oscillator strength and the Ω represents the associate vertical excitation energy. The A matrix describes the single particle excitations between the occupied and unoccupied molecular orbitals and the B matrix measures the linear response of the Hamiltonian perturbed by an external electric field. In case of Tamm-Dancoff approximation (TDA) the B matrix is set to zero which can significantly reduce the computational cost. However, here the TDA is not applied in the TD-LC-DFTB calculations.

In the present thesis, an extensive benchmark of the TD-LC-DFTB method is presented with some higher level computationally expensive QM methods like DFT/MRCI, ADC2, CAM-B3LYP, ωB97X etc., by calculating the excitation energies and excitonic couplings of the biological LH complexes. Once the benchmark of the TD-LC-DFTB method is performed, then it is utilized for the trajectory analysis and exciton dynamics calculations.

1.3.3 Excitonic Coupling and System Hamiltonian

To model the LH complexes, one needs to apply the concept of open quantum system by constructing the exciton Hamiltonian within a tight-binding approach as [58]

$$H_S = \sum_m E_m \left|m\right\rangle \left\langle m\right| + \sum_{n \neq m} V_{mn} \left|n\right\rangle \left\langle m\right| \tag{1.8}$$

where E_m denotes excitation energies which are also known as site energies in the present context and V_{nm} denotes the excitonic couplings between pigments m and n. So far, various methods are available to compute this quantity, however, we consider only the electrostatic Coulomb coupling based on the transition charges from the electrostatic potential (TrESP) as formulated by Renger and co-workers [73]. The TrESP coupling is accurate compared to the full excitonic coupling based on supermolecular approach. In the TrESP approach, the excitonic coupling is expressed as

$$V_{mn}^{TrESP} = \frac{f}{4\pi\epsilon_0} \sum_{I,J}^{m,n} \frac{q_I^T \cdot q_J^T}{\mid r_m^I - r_n^J \mid} \tag{1.9}$$

where the atomistic transition charges q_I^T and q_J^T are located at the atoms I and J of the pigments m and n. The transition charges are obtained by the electrostatic CHELPG fitting of the transition density so that the latter can be expressed as $\sum q^T \delta(r - R)$. Moreover, in order to account the environmental influence on the excitonic couplings, a screening function is generally introduced. For example, here a distance-dependent screening constant f which controls the environmental impact on the couplings has an exponential expression as follows [74]

$$f(R_{mn}) = A \exp(-BR_{mn} + f_0) \tag{1.10}$$

where A, B and f_0 denote experimentally determined parameters for biosystems having the values 2.68, 0.27 and 0.54 respectively. The value of this factor becomes 0.54 when the inter-pigment distance becomes larger than 20 Å. Alternatively, a constant screening factor as derived by the Poisson-TrESP approach [75] can also be applied to describe the environmental influence on the coupling fluctuation. A schematic representation of the TrESP approach is depicted in Fig. 1.9A.

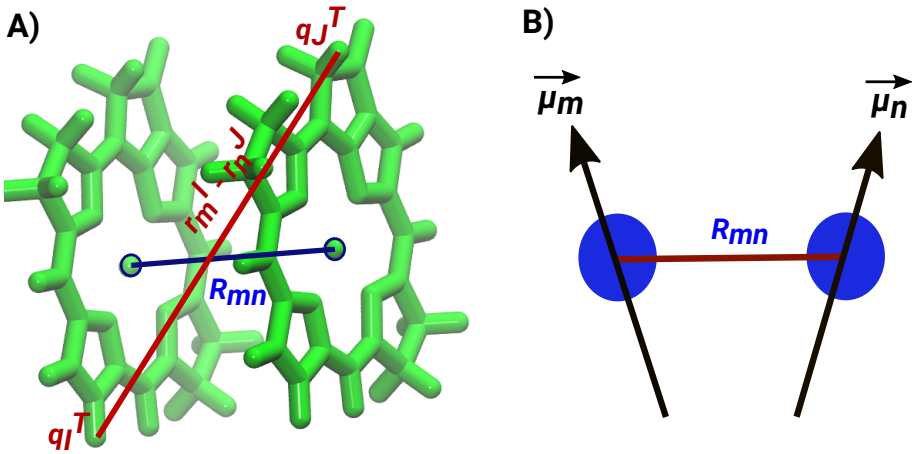

Figure 1.9: A schematic representation of A) TrESP and B) point-dipole excitonic couplings between pigment dimer.

In case of a larger inter-pigment distance the TrESP excitonic coupling can be calculated within the point-dipole approximation (PDA) as

$$V_{mn}^{PDA} = \frac{1}{4\pi\epsilon_0}\left[\frac{\vec{\mu_m}\cdot\vec{\mu_n}}{R_{mn}^3} - \frac{3(\vec{\mu_m}\cdot\vec{R_{mn}})(\vec{\mu_n}\cdot\vec{R_{mn}})}{R_{mn}^5}\right] \tag{1.11}$$

where $\vec{\mu_m}$ and $\vec{\mu_n}$ are the respective transition dipole moment of the donor and acceptor pigments. The PDA is applicable as long as the inter-pigment distance is large enough compared to the size of the pigment molecules. A graphical repre-

sentation of PDA is shown in the Fig. 1.9B.

1.3.4 Autocorrelation Function and Spectral Density

In open quantum systems, the environmental influence on the exciton dynamics is described by the so-called spectral density. This quantity serves as the key input together with the time-average system Hamiltonian as expressed in the Eq. 1.8 to perform a density matrix calculation. The spectral density is a frequency-dependent function and mainly contains the informations of the system-bath Hamiltonian in a open quantum system [58]. It can be expressed as

$$J_m(\omega) = \frac{\pi}{\hbar} \sum_k c_{m,k}^2 \delta(\omega - \omega_k) \tag{1.12}$$

where $c_{m,k}$ are dimensionless coupling parameters for each vibrational mode ω_k.

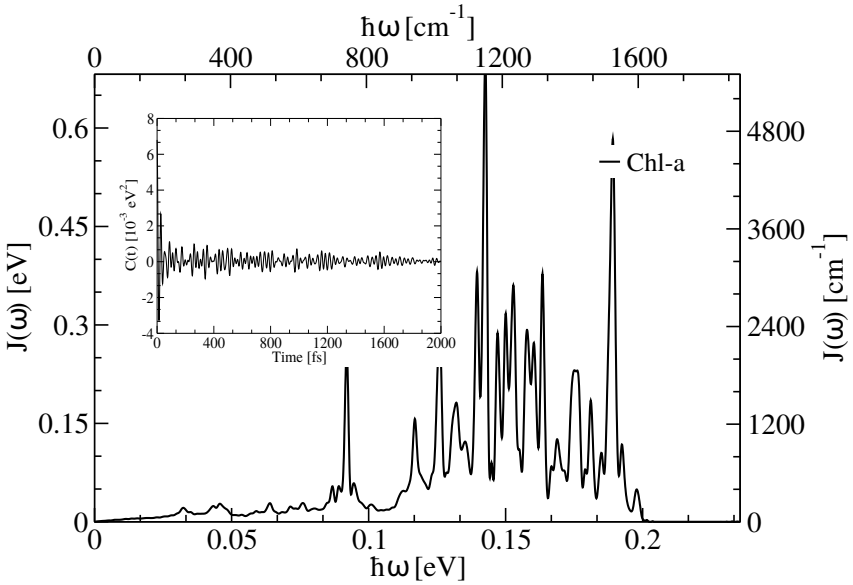

Figure 1.10: Spectral density averaged over Chl-a molecules in the CP29 light-harvesting complex and the associate autocorrelation function (inset) of the site energy fluctuations.

In experiment, spectral densities are obtained by fitting the fluorescence line narrowing and hole burning spectra whereas in the present multiscale method, it can be directly obtained by performing a cosine transformation of the autocorrelation function of the site energy fluctuations [59, 76–78]. Moreover, a thermal prefactor is employed (within the high temperature limit) to obtain the spectral density as [79]

$$J_m(\omega) = \frac{\beta\omega}{\pi} \int_0^\infty dt\; C_m(t) \cos(\omega t) \tag{1.13}$$

where $C_m(t)$ is the autocorrelation function corresponding to each pigment molecules m which is expressed as follows

$$C_m(t_l) = \frac{1}{N-l} \sum_{k=1}^{N-l} \Delta E_m(t_l + t_k) \Delta E_m(t_k) \ . \tag{1.14}$$

ΔE_m represents the difference between the site energy E_m and its average value ($E_m = E_m - \langle E_m \rangle$) and N is the number of frames present in the respective part along the trajectory. Moreover, a windowing technique is generally applied to obtain a proper sampling of the correlation functions and the associate spectral density. The negative peaks which appears during the cosine transformation can be removed by a convolution with some damping functions. However, such an approach can significantly reduce the intensity of some peaks in the spectral density [79]. Here in the present approach, the negative peaks are simply set to zero during the calculations since they are not important in the exciton dynamics. Moreover, the concept of zero padding is applied to extend the correlation function in order to increase the resolution of the spectral density. A structural overview of spectral density with its corresponding autocorrelation function averaged over Chl-a pigments of the CP29 antenna complex is shown in Fig. 1.10.

1.3.5 Wave Packet Dynamics

Once the system Hamiltonian as expressed in Eq. 1.8 is constructed, it can be employed to perform the exciton dynamics of the system. The Hamiltonian can be time-averaged and needs to be employed as an input parameter together with the spectral density in density matrix calculations. A density matrix approach like the hierarchical equation of motion (HEOM) approach is more accurate but computationally expensive for the complex spectral density of the LH systems as shown in Fig. 1.10 [80–82]. Alternatively, the system Hamiltonian can be employed in its time-dependent form and the time-dependent Schrödinger equation needs to be solved within ensemble-averaged wave-packet based calculations. This wave packet based approach which is also known as NISE (numerical integration of the Schrödinger equation) [83] is numerically efficient but often failed to account the temperature dependent dynamics compared to the density matrix calculations. However, within certain approximations both wave packet and density matrix calculations provide same results [65]. In the wave-packet approach, the time-

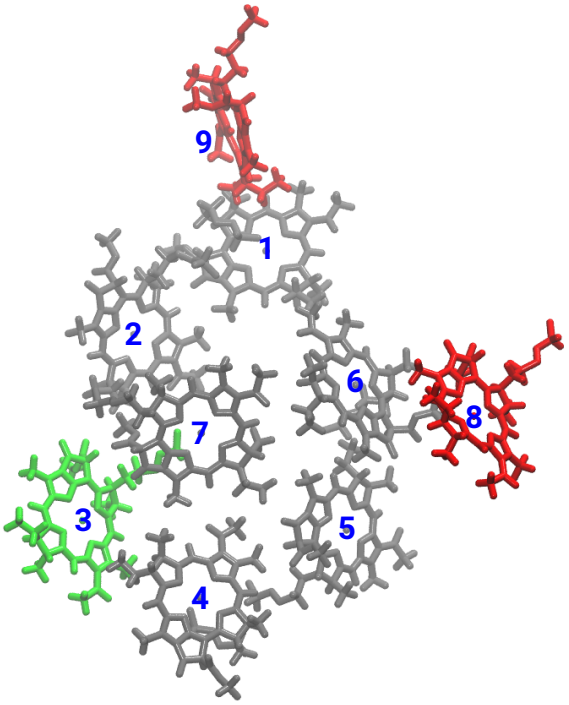

Figure 1.11: Spatial orientation of nine site model system. This is an monomeric unit of the FMO light-harvesting complex of green sulfur bacteria.

dependent Schrödinger equation is expressed as

$$i\hbar\frac{\partial|\Psi_S(t)\rangle}{\partial t} = H_S(t)|\Psi_S(t)\rangle \tag{1.15}$$

where the state of the system $\Psi_S(t)$ is expanded in the excitonic basis $|\alpha\rangle$ as

$$|\Psi_S(t)\rangle = \sum_\alpha c_\alpha(t)\,|\alpha\rangle \tag{1.16}$$

where $c_\alpha(t)$ are the time-dependent coefficients. Furthermore, the excitonic state can be also expressed in a site local basis $|m\rangle$ as

$$|\alpha\rangle = \sum_m c_m^\alpha\,|m\rangle \tag{1.17}$$

These equations lead to the probability of finding an exciton at the local pigment site (m) as

$$P_m(t) = |\langle m|\Psi_S(t)\rangle|^2 = |\sum_\alpha c_m^\alpha c_\alpha(t)|^2. \tag{1.18}$$

Moreover, to obtain sensible exciton dynamics, the propagation of the time-dependent Schrödinger equation needs to be repeated from different starting points along the trajectory. Finally, the resulting dynamics need to be averaged in order to obtain the ensemble-averaged dynamics of the system. The major drawback

of wave-packet dynamics is the implicit high-temperature limit which leads to an equal population of each site in a long time dynamics.

However, this does not agree with the Boltzmann distribution with a finite temperature limit. To solve this problem, a temperature correction is required within the wave-packet formalism [83]. However, in case of the density-based approach this is not problem since the temperature of the system is explicitly used during the calculations. An example of a nine site model system from the monomeric unit of the FMO complex is shown in Fig. 1.11 from which a 40 ps trajectory of the time-dependent system Hamiltonian is employed to obtained the exciton dynamics of 2 ps length. The population dynamics is monitored by exciting the first pigment site and shown in the Fig. 1.12A. An exponential decay of exciton population is observed for the first site and transferred to the other site according to coupling distributions. Moreover, total three sets of dynamics calculations have been performed by exciting the first site and shown in Fig. 1.12B. In the first case, a 5 ps stride has been considered between two initial starting points whereas in the second and third cases it has been taken as 1 ps and 100 fs respectively. The distribution for the first set fluctuates more compared to the second and third case for the small stride between two starting conformations. In order to obtain a sensible exciton dynamics a sufficiently long trajectory of the Hamiltonian is required for a longer stride by doing ensemble averages over many windows. That is why the length of the stride between two windows is very important and normally determined from the correlation functions.

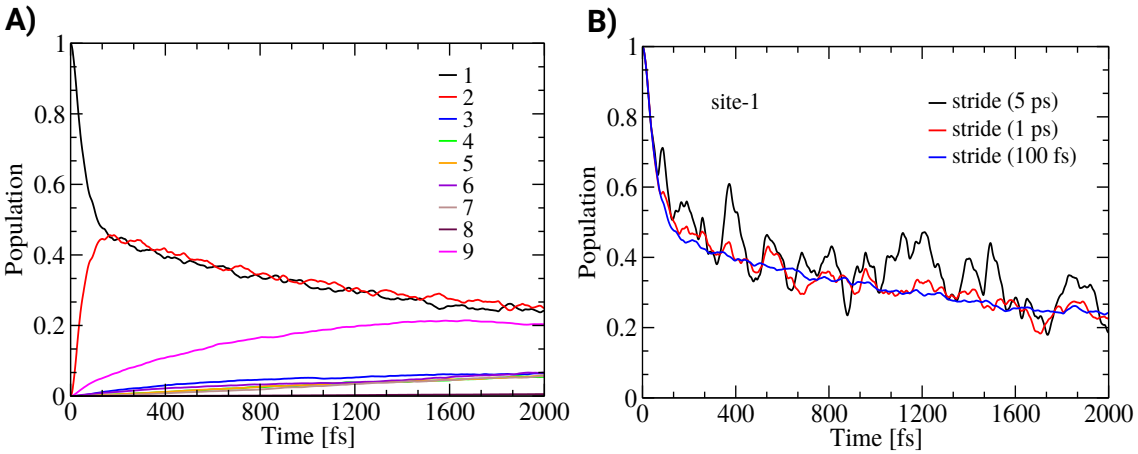

Figure 1.12: A) An example of ensemble averaged exciton dynamics for a nine site model system based on a 40 ps trajectory. B) Exciton decay is shown for the site-1 where two starting conformations are separated by 5 ps, 1 ps and 100 fs respectively.

1.4 Outline of Results and Discussion

Most of the results in the present thesis are already published in collaboration studies with other research groups and they are presented here in the following chapters. The LH complexes which are considered in the present thesis are the FMO and LH2 complexes of bacteria and the LHCII and CP29 complexes of higher plants.

Chapter 2: ***Benchmark and Performance of Long-range Corrected Time-dependent Density Functional Tight Binding (LC-TD-DFTB) on Rhodopsins and Light-Harvesting Complexes***

Benchmark studies of the TD-LC-DFTB method have been performed on the BChl pigments of the LH2 and FMO complexes. Mainly the excitation energies and excitonic couplings have been considered during the investigation. The study has been performed within a collaboration with the group of Prof. Marcus Elstner at the Karlsruhe Institute of Technology, Germany. Our contribution focused on the calculation of DFT/MRCI for the excitation energies and the excitonic couplings using the TrESP and Tr-Mulliken approaches for the BChl pigments based on several DFT functionals. Moreover, we have also contributed to the system preparation and other TD-DFT calculations and couplings based on the super-molecule approach.

Chapter 3: ***DFTB/MM Molecular Dynamics Simulations of the FMO Light-Harvesting Complex***

The so-called geometry mismatch problem has been solved by employing Born-Oppenheimer MD simulations for the ground state in a QM/MM fashion followed by excitation energy calculations based on the TD-LC-DFTB method also in a QM/MM setting. The spectral densities obtained for the FMO complex show a remarkable agreement with the experimental results. Moreover, the calculations of the exciton dynamics have been also performed based on ensemble averaged wave-packet scheme for the same complex.

Chapter 4: ***Multiscale QM/MM Molecular Dynamics Simulations of the Trimeric Major Light-Harvesting Complex II***

A similar method has been applied here for the major antenna LHCII complex of the plant PSII system. The spectral densities calculated for the LHCII complex exhibit better agreement with the experiment compared to the FMO complex. Moreover, the excitation energy transfer rate has also been computed between the

special pair of Chl-a 612 and Lut-1 which is assumed to control the photoprotective mechanism at low and neutral pH states.

Chapter 5: ***Time-Dependent Atomistic Simulations of the CP29 Light-Harvesting Complex***

The site energies, excitonic couplings and spectral densities have been calculated and compared with experiments based on the present multiscale approach for the minor antenna CP29 complex of the higher plants. The spectral densities have been compared for two different of force fields AMBER and OPLS in a QM/MM MD framework. Moreover, the average spectral density between the bacterial and plant LH complexes have also been compared. These comparisons establishes the robustness and reliability of the present multiscale method to study the LH complexes plant and bacteria. In addition, the exciton dynamics has also been computed to understand the energy transfer process in the CP29 complex.

Chapter 6: ***On a Chlorophyll-caroteinoid coupling in LHCII***

The NPQ process of higher plants has been investigated for a monomeric unit of the LHCII complex at different pH states and ion concentrations. Two high-level QM methods, i.e., DFT/MRCI and RASSCF have been utilized to describe the excitonic couplings within the Chl-a 612/Lut-1 pair. The TrESP charges have been extracted based on DFT/MRCI level of theory for the Chl-a and Lut-1 molecules whereas RASSCF charges are taken from literature. A small change in the coupling is observed at the two different pH states, however, further theoretical improvements are required to justify the experimentally observed NPQ phenomena.

Chapter 7: ***Outlook on the Modeling of Porphyrin/Clay-surface Artificial LH Complex***

An artificial LH complex has been modeled by attaching free-base porphyrin molecules on a montmorillonite clay surface. A few steps of the present multiscale scheme has been applied to extract the site energies and excitonic couplings along classical MD trajectories.

The ***Supplementary Information*** of the **Chapters 2, 3, 4 and 5** are presented in the **Appendices A, B, C and D** respectively.

Chapter 2

Benchmark and Performance of Long-range Corrected Time-dependent Density Functional Tight Binding (LC-TD-DFTB) on Rhodopsins and Light-Harvesting Complexes

The chromophores of rhodopsins (Rh) and light-harvesting (LH) complexes still represent a major challenge for a quantum chemical description due to their size and complex electronic structure. Since gradient corrected and hybrid density functional approaches have been shown to fail for these systems, only range-separated functionals seem to be a promising alternative to the more time consuming post-Hartree-Fock approaches. For extended sampling of optical properties, however, even more approximate approaches are required. Recently, a long-range corrected (LC) functional has been implemented into the efficient density functional tight binding (DFTB) method, allowing to sample the excited states properties of chromophores embedded into proteins using quantum mechanical/molecular

Reprinted with permission from the article by B. M. Bold, M. Sokolov, **S. Maity**, M. Wanko, P. M. Dohmen, J. J. Kranz, U. Kleinekathöfer, S. Höfener and M. Elstner, *Benchmark and Performance of Long-range Corrected Time-dependent Density Functional Tight Binding (LC-TD-DFTB) on Rhodopsins and Light-Harvesting Complexes*, Phys. Chem. Chem. Phys. **22**, 10500 (2020). (DOI: 10.1039/C9CP05753F). **My contributions are described in the thesis outline.**

mechanical (QM/MM) with the time-dependent (TD) DFTB approach. In the present study, we assess the accuracy of LC-TD-DFT and LC-TD-DFTB for rhodopsins (bacteriorhodopsin (bR) and pharaonis phoborhodopsin (ppR)) and LH complexes (Light-harvesting complex II (LH2) and Fenna-Matthews-Olson (FMO) complex). This benchmark study shows the improved description of the color tuning parameters compared to standard DFT functionals. In general, LC-TD-DFTB can exhibits a similar performance as the corresponding LC functionals, allowing a reliable description of excited states properties at significantly reduced cost. The two chromophores investigated here pose complementary challenges: while huge sensitivity to external field perturbation (color tuning) and charge transfer excitations are characteristic for the retinal chromophore, the multi-chromophoric character of the LH complexes emphasizes a correct description of inter-chromophore couplings, giving less importance to color tuning. None of the investigated functionals masters both systems simultaneously with satisfactory accuracy. LC-TD-DFTB, at the current stage, although showing a systematic improvement compared to TD-DFTB cannot be recommended for studying color tuning in retinal proteins, similar to some of the LC-DFT functionals, because the response to external fields is still too weak. For sampling of LH-spectra, however, LC-TD-DFTB is a viable tool, allowing to efficiently sample absorption energies, as shown for three different LH complexes. As the calculations indicate, geometry optimization may overestimate the importance of local minima, which may be averaged over when using trajectories. Fast quantum chemical approaches therefore may allow for a direct sampling of spectra in the near future.

2.1 Introduction

Many biological processes are triggered by the absorption of photons. Two prominent and well studied protein classes involving these processes are rhodopsins and light-harvesting (LH) complexes. Microbial rhodopsins consist of seven transmembrane helices (Fig. 2.2) embedded in a membrane, forming an internal binding pocket, where the chromophore all-*trans* retinal (Fig. 2.1) is bonded via a Schiff base (SB) to an ϵ-amino group of a lysine side chain. They are mainly classified through their retinal conformation and binding pocket. In organic solvents the absorption maximum of the chromophore retinal is about 450 nm [84], while in proteins it varies from 360 to 635 nm [85]. As rhodopsin models in this work,

bacteriorhodopsin (bR) and pharaonis phoborhodopsin (ppR), are chosen. The binding pockets of bR and ppR differ in only 10 amino acids within 5 Å of the retinal and features the same arrangement of counter ions. Despite the similarity, the absorption maximum of ppR (497 nm) [86] is blue shifted by about 70 nm relative to bR (568 nm) [87], which has been attributed to a number of small contributions that all add up in a constructive manner. The overall shift between these two proteins hence poses a critical test as the experimental value is less likely achieved due to error cancellation as, e.g., the shift from vacuum to the protein (opsin shift) [88, 89].

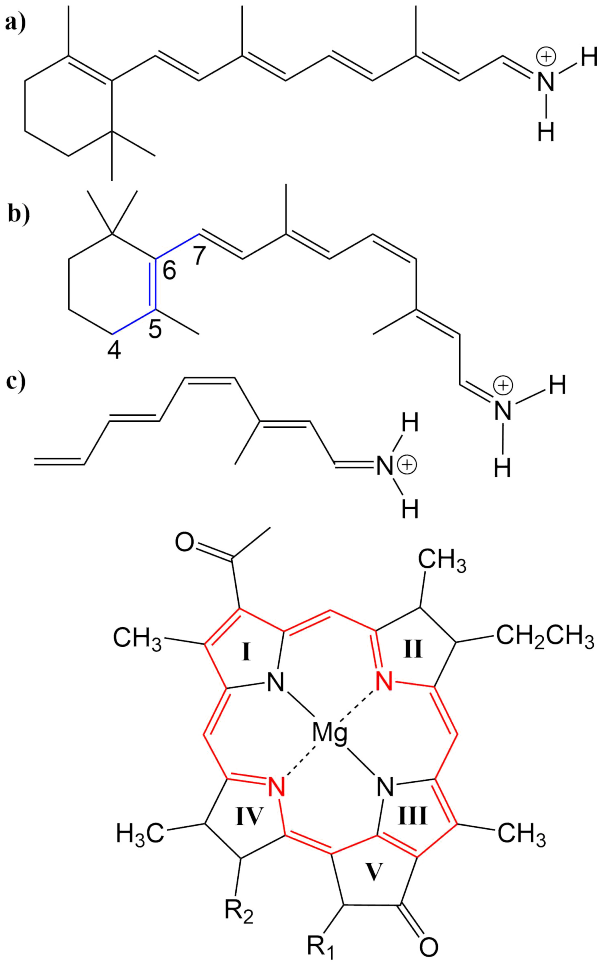

Figure 2.1: Left: a) all-*trans* retinal, b) 6-s-cis-11-cis retinal, in blue: twisted dihedral angle (C4-C5-C6-C7), c) PSB5 model; Right: BChl a; in red diaza[18]-annulene substructure visible; full model: R_1 = COOMe, R_2 = phytyl-tail; model with truncated phytyl-tail: R_1 = COOMe, R_2 = COOMe; truncated model: R_1 = H, R_2 = CH_3.

LH complexes are aggregates of proteins and chromophores, i.e., often bacteriochlorophyll (BChl) or chlorophyll (Chl) chromophores, which are mainly responsible for photosynthesis in bacteria and plants. They absorb light and collect the energy to transfer it to the photosynthethic reaction center (RC) using an ex-

citation energy transfer (EET) mechanism [1]. The absorption spectra of (bacterio)chlorophylls exhibit two key features, which are the Soret-band in the near UV region and the Q-bands in the visible region. The labeling of the absorption peaks is based on the four-orbital model for porphyrin derivatives proposed by Gouterman *et al.* [90, 91] While in free-base porphyrins the two highest occupied molecular orbitals (HOMOs) and lowest unoccupied molecular orbitals (LUMOs) are energetically degenerated, in (bacterio)chlorophylls this degeneracy is lifted due to the reduced symmetry leading to a splitting of the Q-bands into the so-called Q_x and Q_y bands. In this work, only the Q_y state, i.e., the lowest excited state, is considered. In organic solvents the absorption maximum of BChl a (Fig. 2.1) is at around 770 nm [92].

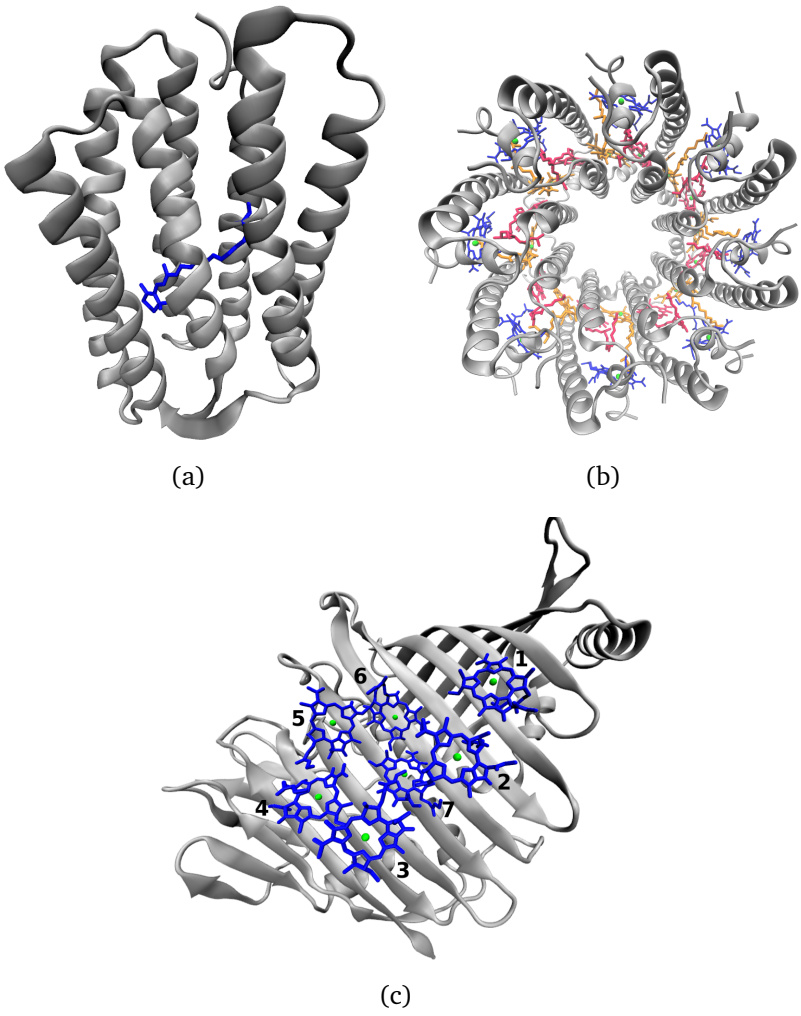

Figure 2.2: (a) Side view of a rhodopsin model, here bR, with retinal in blue. (b) Top view of the LH2 complex from *Rs. molischianum* with the BChl a chromophores of the B800 ring colored in blue and those belonging to the B850 ring in red and orange. (c) FMO monomer with seven BChl a chromophores.

In the present work, two LH2 complexes of *Rs. molischianum* and *Rps. acidophila* and the FMO complex of *C. tepidum* are chosen (Fig. 2.2). The LH2 com-

plex of *Rs. molischianum* (in brackets are given the values for *Rps. acidophila*) contains 24 (27) BChls, arranged in two rings, called B800 (1.55 eV) and B850 (1.46 eV) corresponding to their respective absorption maxima. The B800 ring consists of eight (nine) BChl a chromophores with an inter-chromophore distance of about 20 Å, while the B850 ring consists of 16 (18) BChl a chromophores with a distance of about 9 Å. The FMO complex used here consists of a monomer including seven BChls, which are separated by about 10-20 Å and arranged asymmetrically in contrast to the LH2 complex. The absorption maxima of the FMO complex are found experimentally in a range of 790 nm to 825 nm (1.50-1.57 eV) [93]. The reason for the red-shift compared to the one in organic solvents (770 nm (1.61 eV) [92]) is found to be originating from the protein environment and the excitonic inter-chromophore coupling. In the case of LH2, the absorption shift of the B850 ring mainly originates from the exciton couplings, while the absorption shift of the B800 ring and the ones occurring in the FMO complex are to a large extent caused by the protein environment [62, 94, 95].

The individual chromophores in these biological systems exhibit very specific absorption spectra. In principle, there are several factors determining the absorption maximum, which are (i) the chromophore structure, influenced by the protein environment, (ii) the interaction with the electrostatic environment due to ionic, polar or polarizable groups of amino acids, and (iii) direct hydrogen-bonding or Van der Waals (VdW) interactions and (iv) exciton couplings. All these factors are responsible for "color-tuning" of the respective chromophores within their protein environment. The detailed mechanism of "color-tuning" is experimentally not fully available and computational studies are thus of interest for a deeper understanding. Computational methods can disentangle those factors, however the choice of the method is important in order to confirm that the form of the spectrum results from correct physical description and not due to error cancellation. The computational methods should therefore be sufficiently efficient to allow for sampling of the conformational space. Single structures, e.g., computed by QM/MM geometry optimization may not be representative for ensemble averages, and information about the peak widths can only be gained from standard deviations.

Both chromophores, retinal and BChl a have been shown to be particularly cumbersome for an accurate quantum chemical description. Often even obtaining ground state geometries is a non-trivial task as various methods yield very different values for the bond-length alternation (BLA), which is defined as the difference

between the average single- and double bond lengths along a conjugation chain or ring, and has a sizable impact on excitation energies. Excited states can exhibit multi-reference character, while charge transfer is important, in particular for retinal. In principle, this would require multi-reference configuration interaction methods (MRCI). Complete-active space self-consistent field (CASSCF) together with second-order perturbation theory (CASPT2) yields excited state properties in agreement with experimental results for retinal, however, at high computational costs [96–98]. An alternative method to study retinal is the *ab-initio* spectroscopy oriented configuration interaction (SORCI) method, which yields the same accuracy as CASPT2 but at reduced computational effort [99]. In contrast to retinal, BChl has a large active space, which makes it difficult for MRCI methods to investigate its properties in the excited state. MRCI methods used in previous studies are e.g. RASSCF/RASPT2 [100], [101] or DFT/MRCI [102]. Similarly, optimized geometries have to be computed at a computationally less expensive level of theory.

Single-reference methods with in many cases sufficient accuracy such as the second-order approximate coupled cluster singles and doubles (CC2) can describe retinal excited states for a mostly planar retinal configuration or without the inclusion of the β-ionone ring [103–105]. The optimization of the retinal geometry in the ground and excited state is only accurate if far away from the conical intersection region [104, 106]. Hence, the popular CC2 method is not applicable to all intermediate steps required when studying, e.g., the isomerization of retinal. In the case of BChl, CC2 can successfully describe the excitation energies of truncated BChl structures [107], while it shows weaknesses in the application to the complete BChl structure, as it occurs in proteins due to the sensitivity on the multi-configurational character of BChl [102].

Density functional theory (DFT) methods, although computationally efficient, can only be applied with care: DFT in the generalized gradient approximation (GGA) significantly underestimates the BLA, while hybrid functionals result in improved predictions of the BLA when an increasing amount of exact exchange is included [89, 108]. Excitation energies obtained with the response formalism (TD-DFT) are only reasonable for mostly planar retinal structures [105]. The response of the excitation energies on the electrostatic interaction, is grossly underestimated with standard TD-DFT functionals [99], making these methods effectively useless for color tuning studies. For BChl, however, hybrid functionals seem

to perform reasonably well, when taking DFT/MRCI as reference [102]. Problems with hybrid functionals occur especially when investigating the carotenoids, which are also present in LH complexes [94].

The failure of TD-DFT methods, when using standard GGA or hybrid functionals,is rooted with their inability to capture charge transfer excitations which play a role in rhodopsins and to some extend also in LH complexes [62, 99]. For charge transfer excitations in organic molecules, an improvement is provided by long-range corrected (LC) functionals [109, 110], and even for the isomerization of retinal [111]. A study investigating the excited state relaxation of retinal shows that LC-BLYP [112] provides results in accordance with CASPT2 [113]. In a benchmark study on BChl a in FMO, CAM-B3LYP [114] was reported to yield results in accordance with DFT/MRCI [102]. Furthermore, CAM-B3LYP can reproduce experimental results for excitation energies of BChl a in different solvents [115].

Using *ab-initio* and TD-DFT approaches, excitation energies are often computed for single structures, e.g. for QM/MM optimized geometries of chromophore and protein environment. The computation of excitation energies of sampled structures obtained by molecular dynamics (MD) simulations is required not only to determine correct averages and widths of the absorption spectra, but also to investigate, e.g., temperature effects as reported in previous studies [116, 117]. Therefore, methods with low computing costs based on semi-empirical Hamiltonians are frequently applied. In LH complexes, ZINDO/S-CIS [118, 119] is often used to sample excitation energies [27, 59, 108, 120]. In previous studies on retinal proteins, some of us have used OM2/MRCI for sampling of excitation energies, since its performance for relative excitation energies is comparable to SORCI [99, 121], while absolute excitation energies are blue shifted. The semi-empirical TD-DFTB method faces the same problems as TD-DFT methods using GGA functionals, since TD-DFTB is based on the PBE exchange-correlation expression [122].

Recently, a LC functional has been implemented into the density functional tight binding (LC-DFTB) method and has been extended to the time-dependent scheme (LC-TD-DFTB), which is about three orders of magnitude faster than the LC-TD-DFT method [69, 123]. The newly implemented LC-TD-DFTB allows for extensive sampling of absorption spectra and also for direct propagation of excitons, as recently shown for an anthracene crystal [124]. It is therefore a promising method to study rhodopsins and LH complexes. LC-TD-DFTB has already

been successfully benchmarked for a test set of small organic molecules involving charge-transfer excitations [69] and found its application in the computation of gas-phase relaxation dynamics of cycloparaphenylen molecules [125]. Since TD-DFTB is based on GGA and does not work for retinal proteins, ZINDO/S-CIS likely overestimates electrostatic effects on BChl absorption spectra [102], a thorough test of LC-TD-DFTB seems desirable. Even though previous studies on both retinal and BChl proteins showed that LC functionals lead to an improved description over standard functionals [102, 111, 113, 117, 126, 127], there is still no systematic benchmark regarding the factors of color tuning.

In the present work, we perform a benchmark study on both the isolated chromophores retinal and BChl a as well as on the biological systems, to determine the accuracy of LC-TD-DFT and LC-TD-DFTB for describing color-tuning effects. The article is structured as follows: First, the benchmark study of LC-TD-DFT and LC-TD-DFTB on retinal and BChl a is presented on computing excitation energies with respect to geometry effects and electrostatic effects. Second, a benchmark of LC-TD-DFTB for the computation of excitonic couplings is performed. Finally, the performance of LC-TD-DFT and LC-TD-DFTB is demonstrated on two rhodopsins, bR and ppR, and two LH complexes, the LH2 and FMO complex.

2.2 Computational Details

2.2.1 Models and geometry optimization

The three retinal model systems used in Sec. 2.3, displayed in Fig. 2.1, were taken from Ref. 99. The rhodopsin model systems used in Sec. 2.4, bR (PDB code 1C3W) and ppR (PDB code 1H68), were taken from Ref. 88. Concerning the chromophore BChl a, geometry optimizations were carried out using the Turbomole program package [128] using HF and DFT, employing the functionals BH-LYP, B3LYP and BLYP together with the Karlsruhe basis sets def2-SV(P), def2-SVP, and def2-TZVP [129, 130]. Additionally, geometry optimizations were carried out at the SCC-DFTB level of theory [68], denoted DFTB in the following, and at the DFT level of theory using the range-separated CAM-B3LYP functional together with the def2-SVP and def2-TZVP basis sets, as implemented in the ORCA program package [131]. For these different geometries, the diaza[18]-annulene substructure of BChl a [132], see Fig. 2.1 in red, was used to calculate the BLA. To account for

protein environment effects on the excitation energies of BChl a, the QM/MM optimized structures of the FMO complex (PDB code 3EOJ) of *P. aesturii* were taken from Ref. 102.

For the benchmark study (Sec. 2.3.2) of the exciton couplings of the BChl a chromophores, a model system was constructed. The model system contains a BChl a structure (see Fig. 2.1), where all substituents are replaced by hydrogen atoms except of the carbonyl group of ring V. This structure was firstly optimized using SCC-DFTB. Subsequently, dimers were build differing in the inter-dimer distance.

The LH complexes used in Sec. 2.4 were QM/MM optimized, which are the FMO complex from *C. tepidum* (PDB code 3ENI) and the LH2 complexes from *Rs. molischianum* (PDB code 1LGH) and *Rps. acidophila* (PDB code 1NKZ). All QM/MM optimizations were performed using the DFTB3/3OB method for the QM region as implemented in the GROMACS package (version 2017.1) [133, 134]. The QM regions of the FMO complex and the LH2 complex contain a single BChl a chromophore, while the respective phythyl tail is not part of the QM region. Neglecting the phythyl tail in the QM region saves computational cost and does not significantly effect the excitation energies, cf. Refs. [108, 120]. Both systems have been QM/MM minimized using the steepest descent (SD) algorithm (100000 steps with a tolerance of 1000 $\mathrm{kJ\,mol^{-1}\,nm^{-1}}$).

2.2.2 Classical and QM/MM MD simulations

For rhodopsins, QM/MM MD simulations of both models were performed, since failures of force-field-only descriptions of the active site of retinal proteins were previously reported [116, 135, 136]. Moreover, a well-chosen QM region is important for retinal proteins to be able to investigate effects like charge transfer, protein polarization and dispersion interaction [89]. In the present study, the QM region includes retinal, the counter ions near the retinal Schiff base (RSBH+) (D85 and D212 for bR, D75 and D201 for ppR), the three water molecules near the RSBH+ and a third amino acid close to the active site (R82 for bR and R72 for ppR), see Fig. 2.8(b). The remaining parts of the system were treated with MM using the CHARMM36 force field [137]. The QM/MM MD simulations were carried out with the DFTB3/3OB method (extended self-consistent-charge Density-Functional Tight-Binding) [70, 71, 138] for the QM region, implemented in the

GROMACS package [134]. DFTB3/3OB is known to produce a reliable model of hydrogen bonded structures, which are present in rhodopsins, since it is able to describe hydrogen-bonded networks with similar accuracy as full DFT calculations performed with medium sized basis sets [70]. The QM/MM MD trajectories had a time length of 1 ns. A QM/MM sampling of the LH complexes would require a multichromophoric QM region, which is not easily possible within the current approach. Therefore, classical MD simulations were performed with a time length of 1 ns. Computational details concerning the equilibration of the systems can be found in the ESI, see Sec. S-1.1. The classical MD simulations were carried out using the GROMACS package (version 2016.3) [139] and the CHARMM27 force-field [140].

2.2.3 Excitation energies

Vertical excitation energies were performed at the HF/CIS, ZINDO/S-CIS [118, 119], TD-DFT (BP86, B3LYP) and LC-TD-DFT (CAM-B3LYP, ωB97X, LC-BLYP) level of theory as implemented in the ORCA program package [131]. ZINDO/S is a short hand notation for ZINDO/S-CIS and LC-TD-DFT is abbreviated as LC-DFT in the following. For the HF/CIS computations, the def2-SVP basis set [129] was chosen. For the ZINDO/S calculations an active space of (10,10), i.e., including the 10 highest occupied and the 10 lowest unoccupied states, was employed, which yields a sufficient agreement with experimental results for both BChl a and retinal [59, 141].

The Tamm-Dancoff approximation (TDA) [142] has been invoked for all TD-DFT calculations together with the resolution of identity (RI) [143] to speed up the computations. We used the def2-TZVP basis set [130] and have considered RIJCOSX [144] for the Coulomb integral and HF exchange terms as well as def2/J as an auxiliary basis set [145] in the RI approximation. In order to avoid large errors due to possible charge-transfer contributions in vertical excitations, long-range corrected functionals such as CAM-B3LYP, ωB97X and LC-BLYP were employed. These functionals are compared in the present work as they differ in the amount of exact exchange. For example, LC-BLYP contains 0% exact exchange at short range and 100% at long-range [112], ωB97X contains 16% exact exchange at short range and 100% at long-range [146] and CAM-B3LYP consists of 19% exact exchange at short range and 65% at long-range [114]. Vertical excitation

energies were furthermore performed using the time-dependent generalization of DFTB (TD-DFTB) [147] without and with long-range corrected functionals (LC-TD-DFTB) [69, 72, 123]. LC-TD-DFTB is abbreviated as LC-DFTB in the following. In LC-DFTB, the local BNL functional [148, 149] for the short-range part and a conventional non-local Hartree-Fock exchange for $\omega \to \infty$ for the long-range part was implemented [124]. The range-separation parameter ω is set to $\omega = 0.3/a_0$ for the computation of the electronic parameters, which was already used in previous work [124]. DFTB uses a minimal atomic orbital basis set, which is computed from atomic Kohn-Sham equations, and an additional harmonic potential is introduced to confine the basis function.

The DFT/MRCI calculations were performed with a parallel version of the DFT/MRCI code using an interface to the ORCA program package [150]. For the BChl a chromophores we use a protocol similar to that recently reported for a Chl a chromophore [151]. The first SCF step for vacuum and in the QM/MM framework were performed in ORCA 4.0 using the BH-LYP functional together with a def2-SV(P) split valence basis set [129]. The latest Hamiltonian (R2018) and the "short" parameter sets were employed with a 0.8 E_h threshold for the initial and production DFT/MRCI run with 12 roots required for all structures in the present study. The reference space has been considered as eight HOMOs and six LUMOs including single and double excitations.

In order to provide reference values for vertical excitation energies, wavefunction methods are often applied. Since in the present study large systems are investigated, only low-scaling wavefunction methods could be applied to guarantee applicability for the entire set of models used. Therefore, the reference method for small molecules is a second-order approximate coupled-cluster singles and doubles (CC2) method and the algebraic diagrammatic construction scheme of second order, denoted ADC(2) [152, 153]. Both methods employ RI. Since with increasing system size even these efficient excited-state methods can become unfeasible, these schemes are employed in the scaled-opposite-spin approximation in combination with the Laplace transformation (LT) to reduce the computational scaling, i.e. LT-SOS-RICC2 and LT-SOS-RIADC(2), [154, 155]. In the following, these methods are denoted SOS-CC2 and SOS-ADC(2) since the RI and LT introduce only deviations significantly below the method error. All these wavefunction based methods are performed using the Turbomole program package [128]. The vertical excitation energies are based on geometries obtained with the def2-SVP

basis set. No significant difference were found when performing, as an exemplary comparison, the same calculations using the def2-TZVP basis set.

For the computation of the vertical excitation energies on the chromophores within their protein environment, the QM region were chosen as described above. The electrostatic environment was considered as the reminder of the protein included as fixed MM point charges for rhodopsins and the FMO complex. In the case of the LH2 complex a charge sphere around the Mg atom with a size of 20 Å was chosen as MM environment. In order to obtain proper thermal averages, structures were extracted from classical (LH complexes) as well as the QM/MM MD trajectories (rhodopsins). Along these 1 ns-long trajectories, 1000 snapshots were used for the computation of the vertical excitation energies.

In the case of rhodopsins, LC-DFTB and OM2/MRCI calculations were employed for the computation of the vertical excitation energies. The OM2/MRCI calculations were carried out using the MNDO2005 program package [156,157] with an active space of (20,20) [158]. Due to missing Mg parameters, the OM2/MRCI approach can presently not be used for the computation of the vertical excitation energies of LH complexes. In this case, the computation were performed using LC-DFTB and ZINDO/S as detailed above.

2.2.4 Exciton couplings

In a next step we focus on the determination of excitonic couplings. Supermolecular calculations were performed on the model system using DFT/MRCI with the same setup as described above, HF/CIS with the basis set def2-SVP, TD-DFT (B3LYP) and LC-DFT (ωB97X, CAM-B3LYP) with the basis set def2-TZVP employing the TDA as implemented in the ORCA program package [131]. Furthermore, the RI has been taken into account to speed up the TD-DFT calculations. As in the case of individual chromophores, we used the RIJCOSX for the Coulomb integral and HF exchange and def2/J as an auxiliary basis set in the RI approximation. Additionally, supermolecular calculations were performed using TD-DFTB and LC-DFTB.

For LC-DFTB, two different parameter sets have been employed for the computation of Coulomb couplings and supermolecular calculations. The original LC-DFTB parameters reported in Ref. 124, yield very good vertical excitation energies and also quite accurate Coulomb couplings, but achieve this by using quite com-

pact atomic orbital basis sets. They were generated by a homogeneous scaling of the original GGA parameter set *mio-0-1* of all radii [124]. It has been shown, however, that using such a confined basis set leads to an underestimation of electron-transfer couplings [159]. For this type of property, more diffuse basis functions are required since it depends on the overlap of molecular fragments in VdW distance. Therefore, a parameter set was generated using fully uncompressed radii. This parameter set was used for the supermolecular calculations.

For larger inter-chromophore distances, the excitonic couplings can be approximated by the respective Coulomb coupling only. For the model systems, Sec. 2.3.2, these Coulomb couplings were computed using LC-DFTB based on Mulliken transition charges and an approximation to second order Coulomb interaction described by a γ-function. [69, 124] We further tested the TrESP approaches (transition charges from electrostatic potentials) [59, 73] as well as a very similar approach based on Mulliken rather than electrostatic charges (Tr-Mulliken). To be able to perform a systematic benchmark, we refrained from rescaling the TrESP or Mulliken charges to match the experimental values of the dipole moment as done in the original TrESP scheme. For a discussion of these rescaling and screening factors, see, e.g., Ref. 160. The computations of TrESP and Tr-Mulliken charges on the transition densities between ground and first excited state using B3LYP and CAM-B3LYP functionals as implemented in the ORCA program package. Subsequently, the atomic transition charges were obtained using a fitting procedure implemented in the Multiwfn program package [161]. Additionally, both the TrESP and the Tr-Mulliken charges have been fitted for the actual conformation of one of the two identical monomers. For the TrESP approach this procedure is slightly unusual since the charges are normally fitted for the equilibrium geometry which would potentially lead to some (model) differences between the TrESP and the supermolecular results. Details concerning the computation of the respective Coulomb couplings can be found in the ESI, see Sec. S-1.2.

In addition, supermolecular calculations were performed directly on a biological system, Sec. 2.3.2, i.e. on the B850 ring system belonging to the LH2 complex, where we considered only pairs of neighboring chromophores. The B850 ring consists of so-called α and β chromophores which have slightly varying properties due to differences in their environments. Thus the BChl a dimer exciton couplings V are subdivided into two groups denoted as, cf. Ref.117: inter-dimer couplings V^1, where BChl a α and β are arranged together with one BChl a of the B800 ring,

and intra-dimer couplings V^2, with only one $\alpha-$ and β BChl a chromophore. For the biological system supermolecular computations are performed with LC-DFT and LC-DFTB with the computational setups as described for the model system. For TrESP, however, the charges have been calculated only for the equilibrium conformations and then mapped onto all other conformations. This procedure is sometimes termed "frozen" TrESP approach [162]. This scheme was chosen here since is usually employed when computing Coulomb couplings along trajectories, as described above.

2.3 Benchmark

The aim of this section is to investigate the accuracy of LC-DFTB for different model systems. In particular, it is studied whether LC-DFTB can yield qualitatively correct excitation energies for different geometries and point charges used to model a protein environment. In Sec. 2.3.1 these influences are investigated for a retinal model, followed by an analysis using BChl a in Sec. 2.3.2 for which also excitonic couplings are compared.

2.3.1 Retinal

Bond length alternation

The excitation energies of the chromophore retinal are sensitive to its configuration and correlate with the BLA. An increased BLA leads to a blue shift of the excitation energies [89, 99]. The BLA varies significantly as the geometry is optimized with different QM methods. While BLYP has the smallest BLA, it increases in hybrid approaches with the amount of exact exchange added. HF and CASSCF lead to the highest BLA, see Tab. S1 in the ESI. The use of different methods for geometry optimization allows to assess the impact of the BLA on the excitation energies in a systematic manner. This finding is shown in Fig. 2.3 for all-*trans* retinal.

SORCI as the reference method displays an expected blue shift that increases with the BLA [99]. HF-based single-reference methods show the same trend. While CIS overestimates the excitation energies by a factor of about 1.5, SOS-ADC(2) agrees more quantitatively with SORCI, which also applies to OM2/MRCI. Without spin-component scaling ADC(2) agrees very well with SORCI for small

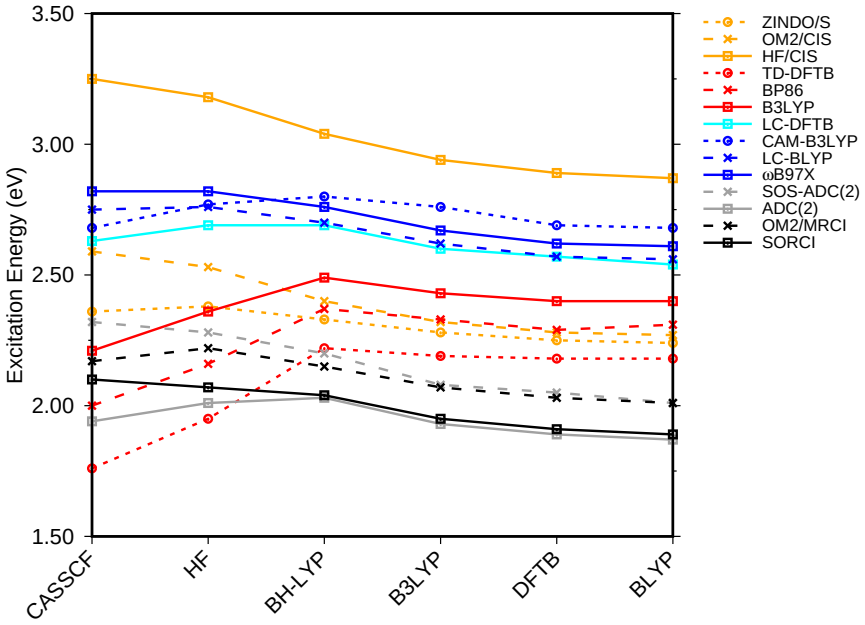

Figure 2.3: Influence of the optimization method on the excitation energies: The results for the BP86, DFTB, B3LYP, OM2/CIS, HF/CIS, OM2/MRCI, and SORCI calculations have been taken from Ref. 99.

BLA, however, yields a red shift for CASSCF and HF optimized structures (-0.16 eV). GGA, hybrid DFT functionals and TD-DFTB excitation energies are red-shifted by up to 0.4 eV with CASSCF geometries.

The *ab-initio* LC functionals, LC-BLYP and ωB97X, which use 100% HF exchange in the long-range limit, obtain the same trend as SORCI, while CAM-B3LYP with only about 60% HF exchange still has a qualitative problem. The same trend as described by CAM-B3LYP is obtained by LC-DFTB, however, showing a significant improvement for the HF and CASSCF optimized retinal structures compared to the DFT-GGA and TD-DFTB based on GGA functional. As expected, absolute excitation energies are overestimated by LC functionals.

An important property is the change in excitation energy due to variation in BLA, which shows up, e.g., in the width of the absorption band due to fluctuations. SORCI has a range of $\Delta = 0.21$ eV. SOS-ADC(2) overestimates this range, while ZINDO/S as well as CAM-B3LYP and LC-DFTB underestimate it. A similar range compared to SORCI is obtained by LC-BLYP as well as ωB97X.

Twist of the β-ionone ring

Another important geometrical parameter of retinal is the dihedral twist angle of the β-ionone ring, see Fig. 2.1. A planar retinal conformation describes a π-system that is delocalized over the whole conjugated chain, whereas a highly twisted C_6-C_7 decouples the ring-internal double bond from the rest of the π-system, which causes a blue shift, according to the particle-in-a-box model.

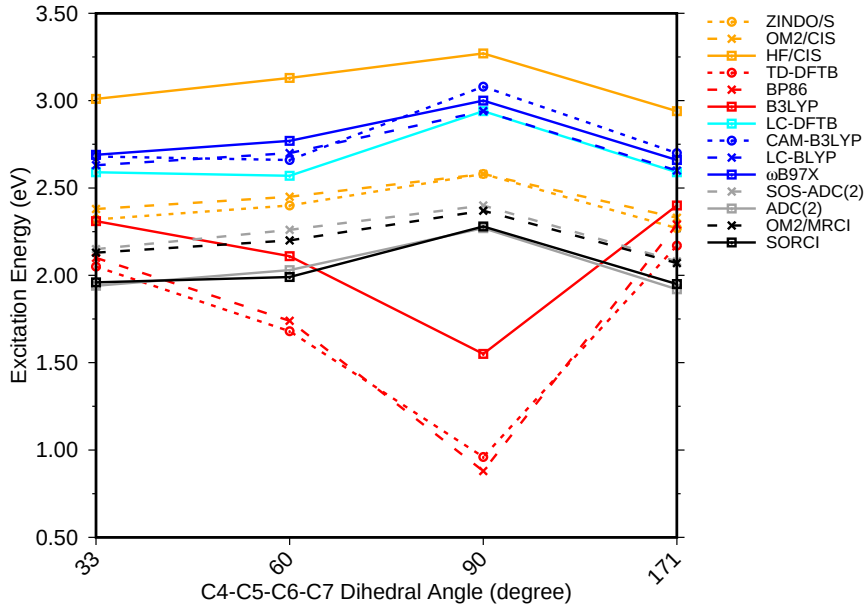

Figure 2.4: Excitation energies of a 6-s-cis-11-cis PSB in vacuum for different twist angles. The results for the BP86, DFTB, B3LYP, OM2/CIS, HF/CIS, OM2/MRCI, and SORCI calculations have been taken from Ref. 99.

To investigate the effect of delocalization on the excitation energies, a 6-s-cis-11-cis PSB model with different dihedral twist angles has been taken from Ref. 99. The results of the methods tested, are shown in Fig. 2.4. The corresponding numerical values can be found in the ESI (Tab. S2). ADC(2) shows a very good agreement with SORCI, as well as SOS-ADC(2), which is only slightly blue-shifted. Moreover, CIS-based methods follow also the same trend as SORCI with higher absolute excitation energies as obtained in the case of the optimized all-*trans* retinal structures in Fig. 2.3. The failure of standard DFT functionals is visible in a red shift of the excitation energies by the retinal twist. As for the BLA, LC-DFT functionals as well as LC-DFTB show an improvement obtaining a blue shift for the twisted retinal configuration.

This failure of hybrid and GGA TD-DFT approaches is even more dramatic as

in the case of BLA. In many retinal proteins, i.e., in bovine rhodopsins a blue shift of absorption energy is found due to a twist in the retinal conformation around the C_6-C_7 single bond [163]. The latter is induced by steric interaction of the environment with the retinal chromophore and represents one effective way of color tuning. It is therefore encouraging to see, that the LC-DFT methods and LC-DFTB are able to reproduce this feature.

Effect of the electrostatic environment

Retinal proteins absorb light over a wide spectral range of nearly 300 nm, and a major contribution results from electrostatic interactions with the protein environment. The most prominent contribution to the electrostatic interactions with the environment comes from negatively charged groups, i.e., counterions in the binding pocket of the retinal chromophore causing a significant hypsochromic shift of the S_1 excitation energy [97]. Depending on the location of the counterions, e.g., near the protonated SB or near the β-ionone ring, the energy gap varies. For example, the location of the counterion near the protonated SB energetically stabilizes the electronic ground state and thus leads to a larger energy gap (blue shift) [164].

Table 2.1: Vertical excitation energy (eV) of the bare PSB5 model (VEE), shifts due to the presence of a point charge (-1.1).

	VEE	Shifts		
Charge[b]		0.0[c]	-0.5[c]	-1.1
ZINDO/S	2.78	+0.02	+0.13	+0.31
TD-DFTB[a]	2.77	-0.09	+0.00	+0.11
LC-DFTB	3.24	+0.03	+0.15	+0.28
CAM-B3LYP	3.34	-0.01	+0.10	+0.27
LC-BLYP	3.30	+0.03	+0.18	+0.37
ωB97X	3.36	+0.04	+0.18	+0.37
SOS-ADC(2)	2.74	+0.09	+0.35	+0.71
ADC(2)	2.61	+0.04	+0.28	+0.60
OM2/MRCI[a]	2.61	+0.07	+0.39	+0.73
SORCI[a]	2.67	+0.03	+0.28	+0.58

[a] Taken from Ref. 99. [b] Charges in atomic units. [c] Vertical excitation energy with downscaled charge but geometry optimized in presence of the full charge of -1.1 e.

For meaningful benchmarks, a simple counterion model has been proposed, which consists of a PSB5 analog and a single point charge, see Fig. 2.1 interacting with a point charge in its immediate environment.The PSB5 geometry was

reoptimized with DFTB using a charge of -1.1 au at a distance of 2.22Å to the SB proton [99], which results in a shift when computing the excitation energy of the reoptimized model compared to the model in vacuum. When adiabatically calculating the shift in excitation energy caused by an external field, two effects contribute, (i) the change in geometry and (ii) the interaction of the excitation-induced charge transfer with the external field. When using HF-based methods, these two contributions add up constructively whereas with GGA functionals they can partially cancel out. To show this, we first only include the point charge in the ground-state geometry optimization (column with shift "0.0" in Tab. 2.1), then also in the excited-state calculation (columns with shifts “-0.5” and “-1.1”).

SORCI, considered to be the reference method, shows a blue shift of $+0.58$ eV with a charge of -1.1 au. ADC(2) and SOS-ADC(2) nicely reproduce this shift, whereas TD-DFT using GGA and hybrid functionals grossly underestimate the shift with values of less than 0.2 eV, see Ref. 99. TD-DFTB reproduces this failure, and ZINDO/S shifts which are only half of the ones of the SORCI approach. An improvement is observed with LC-DFT functionals as well as LC-DFTB. LC-BLYP and ωB97X with $+0.4$ eV show a larger shift than CAM-B3LYP and LC-DFTB ($+0.3$ eV). However, the shifts are still substantially smaller, which implies a weakness of the LC functionals. In short, this finding can be termed “color-weakness”. In conclusion, TD-DFT with GGA and hybrid functionals are not able to predict color-tuning effects. Furthermore, LC-DFT cannot be considered a quantitative method in this respect neither.

2.3.2 Bacteriochlorophyll a (BChl a)

Geometric and conformational impact on the absorption maximum

Similarly to the first benchmark system, we first investigate the influence of the geometry on excitation energies, in particular on the BLA, see Fig. 2.5. Different methods for ground state optimization lead to different values of BLA. The computed BLA values are provided in the ESI (Tab. S3). In the case of BChl a, the use of a multi-reference method like SORCI is impossible due to the large active space required for this chromophore. Thus, we consider DFT/MRCI as a reference, as previously suggested in a benchmark study on BChl a, cf. Ref. 102. The performance of DFT/MRCI, however, is dependent on the particular Hamiltonian used and the choice of method specific parameters. To consolidate the reference calcu-

lations, we therefore also consider the wavefunction-based methods SOS-CC2 and SOS-ADC(2). These are single-reference methods and their reliability is therefore sensitive to the multi-reference character of the ground-state wavefunction, indicated by the D_1 diagnostic. [165] However, this D_1 value is not a strict measure. To avoid distorted structures which lead to a multi-reference ground state, we have, following Ref. 107, truncated some substituents, see Fig. 2.1, which break the symmetry of the BChl a chromophore. When comparing the excitation energies of the truncated and the full geometries using LC-DFTB, we find that the truncation does not lead to significant changes, see ESI (Tab. S3).

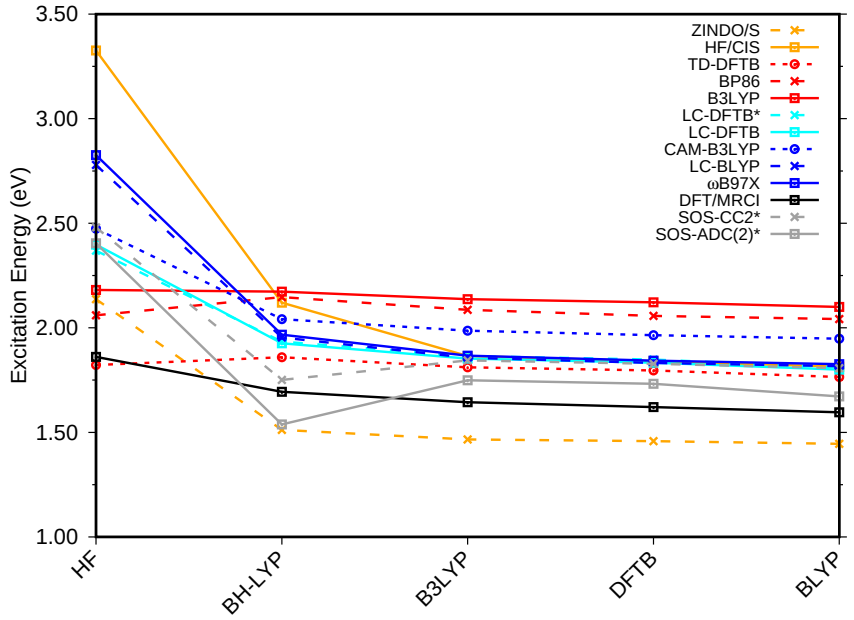

Figure 2.5: BChl a gas phase excitation energies vs. BLA. The geometries differing in BLA were obtained by using different methods to optimize the ground state structure. The structures are ordered by descending BLA ranging from large (0.102 for HF) to small (0.004 for BLYP). The asterisk * indicates that a truncated structure was used.

Most methods show a blue shift of excitation energies with increasing BLA, with the exception of the GGA and hybrid DFT methods and the ADC and CC variants. For small to intermediate BLA values, all methods perform similarly. This behavior may be relevant when sampling excitation energies along MD simulations, since the BLA changes along the C-C stretch modes, which is one of the relevant modes in the molecular dynamics. The blue shift is largest for CIS and ZINDO/S, and seems to depend on the HF-amount in the LC functionals, which becomes apparent when comparing e.g. ωB97X and CAM-B3LYP. LC-DFTB shows

a behavior quite close to that of CAM-B3LYP, which resembles the change of excitation energy with BLA closely to DFT-MRCI. DFT in general has be considered to been robust with respect to the multi-configurational character, in particular for BChl chromophores [102,108,166], it can be concluded that LC-DFT and LC-DFTB are sufficiently accurate for these systems.

Effect of an electrostatic environment

To assess the accuracy of excitation energies with respect to the influence of the protein electrostatic field, QM/MM optimized structures of the FMO complex consisting of seven chromophores, as reported in Ref. 102 have been used. For consistency, we recalculated the excitation energies for some methods already reported in Ref. 102 (B3LYP, CAM-B3LYP, ZINDO/S) due to the different computational setup. The results show only small changes in the absolute excitation energies while the trends and conclusions form Ref. 102 are completely reproduced.

Fig. 2.6(a) shows the excitation energies of the isolated BChl a chromophores (solid lines) in comparison with the excitation energies calculated including the protein electrostatic field represented by point charges (dashed lines). The corresponding numerical values can be found in the ESI (Tab. S4). The axial ligand or the amino acids hydrogen bonded to the BChl a chromophore seem to have a small impact on the excitation energy, as reported before [101, 102, 166]. This behavior can partially be explained by the transition dipole moment of 6 D of BChl a [34, 167], which is only about 50% of the transition dipole moment of retinal (12 D) [168]. B3LYP, CAM-B3LYP as well as LC-DFTB and TD-DFTB lead to accurate vacuum excitation energies, being in agreement with the DFT/MRCI method, which predicts only a small variation in the excitation energies of less than 0.1 eV. Slightly larger variations are obtained for LC-DFT methods with larger fractions of HF exchange, e.g., in the case of ωB97X for the BChl a chromophores 5 and 6. A significantly different behavior is obtained using SOS-ADC(2), being similar to CC2, *cf.* Ref. 102.

To better visualize the behavior, we show the shifts in excitation energies due to the protein environment w.r.t. the DFT/MRCI reference method in Fig. 2.6(b), values see ESI Tab. S5. Due to the interaction with the environment, chromophore 6 is the most blue shifted one, and this shift is clearly dependent on the method used. ZINDO/S shows the strongest response to the electrostatic field, as previously reported, *cf.* Ref. 102. B3LYP slightly underestimates the shift with respect

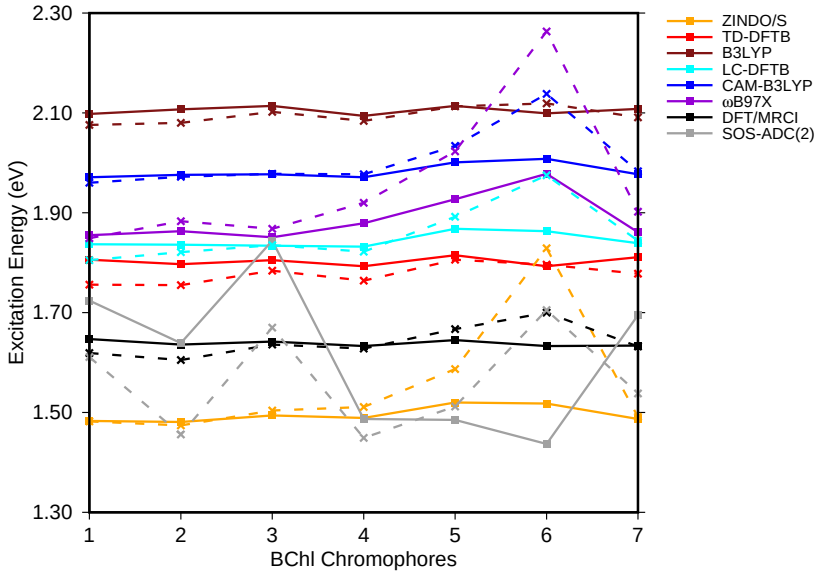

(a)

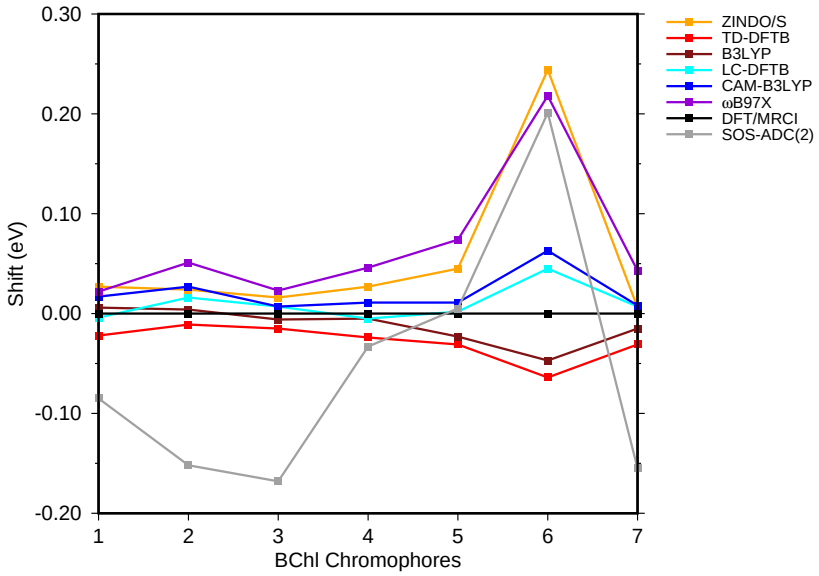

(b)

Figure 2.6: (a) Excitation energies of the chromophores from the FMO complex including (solid lines) and not including (vacuum, dashed lines) the surrounding point charges. (b) Shifts of excitation energies due to the protein electrostatic field, displayed with respect to the respective DFT/MRCI values. Structures taken from Ref. 102.

.

to DFT/MRCI. For the LC functionals, the amount of exact exchange plays a significant role. For example, ωB97X leads to a larger shift than CAM-B3LYP, and LC-DFTB reproduces the CAM-B3LYP behavior quite well, deviating only up to

0.05 eV from DFT/MRCI.

Excitonic coupling I: Model dimers

In LH complexes the shifting and broadening of the absorption spectra is significantly influenced by the interaction of the excited states of the different BChl a chromophores, also denoted as excitonic coupling. Due to the large separation of the BChl a monomers, both, supermolecular or Coulomb couplings can be used to compute the exciton splittings. In the supermolecular approach, the exchange contribution to the coupling is formally included but in practice is negligible for the systems studied here [169].

To benchmark LC-DFT as well as LC-DFTB, we first consider a model system consisting of parallel displaced dimers of truncated BChl a chromophores, as described in Sec. 2.2.1, to avoid any intra-molecular influences on the exciton coupling. The ADC(2) method is excluded from the assessment of the excitonic couplings due to the large deviations of excitation energies in the protein electrostatic environment compared to all other methods, see Sec. 2.3.2.

In Tab. 2.2 results are collected, which have been obtained from supermolecular calculations for which excitonic coupling are determined as half of the energy splitting of the lowest two states, at least for a homogeneous dimer. The exciton couplings become smaller with increasing distance between the dimers. Compared to DFT/MRCI, CIS slightly overestimates the couplings, while all other DFT methods (hybrid and LC functionals) reproduce the reference quite well. TD-DFTB significantly underestimates the coupling, most likely due to the GGA functional applied, since the absence of exact exchange leads to an underestimation of the energy splittings, a further problem is the state mixing [170]. LC-DFTB is in good agreement with CAM-B3LYP and improves significantly over TD-DFTB.

Table 2.2: Excitonic couplings (eV) of the model system obtained as half of the energy splitting from supermolecular calculations.

Distance (Å)	7	8	9	10
CIS	0.069	0.051	0.040	0.031
DFT/MRCI	0.046	0.035	0.028	0.022
ωB97X	0.059	0.044	0.034	0.027
CAM-B3LYP	0.058	0.044	0.034	0.026
B3LYP	0.051	0.039	0.030	0.023
LC-DFTB	0.063	0.048	0.037	0.030
TD-DFTB	0.031	0.024	0.019	0.015

Having assessed the accuracy of the supermolecular energy splittings, the same model system is used to investigate the accuracy of LC-DFTB, TrESP and Tr-Mulliken for Coulomb couplings describing the energy splittings. The Coulomb couplings are collected in Tab. 2.3. The TrESP method without any scaling factor can reproduce the corresponding supermolecular results since for the large inter-chromophore distances the exchange contributions can be neglected. This was already reported in a previous study employing the B3LYP functional [160]. For CAM-B3LYP and B3LYP using TrESP, the Coulomb couplings are, as expected, slightly smaller than those computed with the supermolecular approach. The difference is not big, indicating that the point charge representation of transition densities is a good approximation for these distances. Further, there is no significant difference between ESP and Mulliken charges, indicating that the transition dipole is a quite robust quantity. However, in the case of LC-DFTB it is vice versa. LC-DFTB also uses transition charges computed from a Mulliken charge analysis. In TrESP, these charges are fitted to transition densities using larger basis sets, which seems to be a good approximation. The LC-DFTB Coulomb couplings, however, differ from the Tr-Mulliken calculations in two aspects: first, a minimal basis set is used to compute the Mulliken charges and second, the TD-DFT amplitudes enter the calculation of the Coulomb couplings [124] as well. LC-DFTB Coulomb couplings possibly can be improved by investigating the applied charge model in more detail.

Table 2.3: Coulomb couplings (eV) of the model system using the TrESP, Tr-Mulliken and LC-DFTB schemes. The partial charges of the TrESP and Tr-Mulliken values are based on either the B3LYP and or the CAM-B3LYP functionals.

	Distance (Å)	7	8	9	10
TrESP	B3LYP	0.050	0.038	0.029	0.023
	CAM-B3LYP	0.056	0.043	0.033	0.026
Tr-Mulliken	B3LYP	0.047	0.036	0.028	0.022
	CAM-B3LYP	0.054	0.041	0.032	0.025
-	LC-DFTB	0.082	0.063	0.049	0.039

Exciton coupling II: Light Harvesting Complex II (LH2) B850 ring

The LH2 complex serves as a case study to investigate the role of excitonic interactions in the tuning of an absorption spectrum in real systems [62, 171]. We start with supermolecular calculations on the 16 BChl a dimers (B850 ring), for which results are shown in Fig. 2.7, the values are collected in the ESI (Tab. S6). The results for the biological system show significant differences compared to the

model system in Sec. 2.3.2. Depending on the relative orientation of the BChl a monomers, the values of the couplings range from about 0.04 eV to about 0.08 eV. These values are mostly larger than those in the model system. LC-DFTB values compare quite well with ωB97X and CAM-B3LYP results. LC-DFTB slightly overestimates the couplings in the model system, which is not the case for the dimers in the B850 ring, and LC-DFTB also reproduces the correct trend of the couplings in the ring system.

Fig. 2.7 also includes Coulomb couplings. TrESP and Tr-Mulliken methods reproduce the coupling fluctuations along the ring quite well, however, now systematically underestimating the coupling strengths. This may be related to the 'frozen' TrESP approach, where transition charges are only computed for the equilibrium geometry and then mapped to the actual conformer. There is, however, a second factor which may be responsible for the deviation: since exchange effects depend on the mutual overlap of electron densities, which may be dominated by the densities of the highest occupied orbitals, we expect a sensitive geometry dependence of this property. This is less pronounced for the Coulomb couplings, because those are only dependent on the relative orientations of the transition dipole moments. A more detailed study on dimers of organic molecules [172] seem to support this argument.

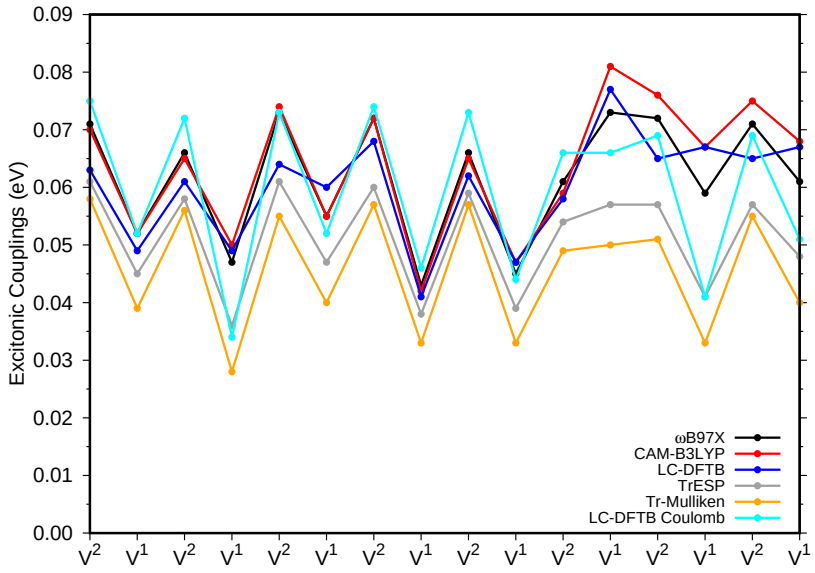

Figure 2.7: Excitonic couplings V (eV) for the respective BChl a dimers V^1 and V^2 of the LH2 B850 ring. The excitonic couplings have been obtained by the supermolecular approach determined as half of the energy splitting. The partial charges of the TrESP and Tr-Mulliken schemes are based on CAM-B3LYP.

Both approaches, TrESP and LC-DFTB, have certain shortcomings, namely the use of transition charges determined for an equilibrium conformation ('frozen' TrESP approach) and the application of a minimal basis set as discussed in Sec. 2.3.2. However, the mean absolute error (MAE) (see, ESI Tab. S6) computed for all methods with respect to the supermolecular ωB97X and CAM-B3LYP calculations are small, while LC-DFTB supermolecular as well as LC-DFTB Coulomb couplings show only half of the MAE value compared to TrESP and Tr-Mulliken.

The LC-DFTB Coulomb couplings are in agreement with those obtained from a transition density cube (TDC) approach without an additional scaling factor in Ref. 127. A detailed comparison with couplings computed in previous studies, as summarized in Tabs. S7, S8 in the ESI, is difficult due to the frequent use of screening factors.

2.4 Performance of LC-DFTB in biological model systems

In this section, the performance of LC-DFTB on biological model systems, i.e., on rhodopsins and LH complexes is discussed. Due to the efficiency of the LC-DFTB method, not only single-point excitation energies can be computed for minimized geometries but also a statistical average of several thousands structures as obtained by classical or QM/MM MD simulations.

2.4.1 Rhodopsin models

QM/MM optimized models of bR and ppR

In Tab. 2.4, we compare the excitation energies of retinal in different electrostatic environments. For each protein, we used the QM/MM optimized structures of bR and ppR from Refs. [88, 99, 173] and show the calculated excitation energies in vacuum (omitting the MM point charges) and within the protein environment, as obtained by different QM methods. All methods agree that without point charges, the excitation energies in bR and ppR are very similar and differ by only 0.03 eV on average. This is due to the similar geometry of retinal in the two proteins. When including the protein environment in the calculations, ppR gives a larger blue shift than bR. All methods reproduce this trend, but the magnitude of the shifts varies

and reflects the accuracy of the methods in describing the electrostatic influence of the environment. When comparing with the experimental shifts of 0.18 and 0.50 eV for bR and ppR, respectively, all wavefunction based methods overestimate the shift w.r.t. vacuum, whereas DFT based methods underestimate the difference in shift between the two proteins.

The latter observation is consistent with the underestimated response of the model chromophore to external charges, as described in Sec. 2.3.1, whereas the first one requires a different explanation. Based on our earlier results, the opsin shift should be underestimated by DFT methods rather than overestimated by all other methods. Here, we refer to previous works, which have shown that point charges obtained by electronic embedding over-polarize the chromophore region. This can be improved by a polarizable embedding. When replacing the point charges in the binding pocket by the electron density of a separate QM region [175], or by a polarizable force field [176], significantly lower excitation energies are obtained. When the chromophore is described with SORCI and the rest of the protein with the polarization model, excitation energies of 2.16 and 2.42 eV have been reported for bR and ppR, respectively [175, 176]. Compared to vacuum (2.00 eV) [174], this corresponds to shifts of 0.16 and 0.42 eV, which are in good agreement with the experiment.

The comparison of calculated and measured properties for the purpose of validating theoretical methods is often hampered by experimental measurements in solution. In the present case, the MM modeling of the protein environment introduces errors that can be of the same order of magnitude as those associated with the applied QM methods. Rather than validating, the following discussion therefore attempts to rationalize the results of the different methods and we will employ SORCI shifts as a reference point.

The shifts obtained with OM2/MRCI, CC2, and ADC(2) are in the range of the SORCI ones, with an average deviation of 0.02–0.04 eV. The SOS variants of CC2 and ADC(2) yield shifts larger by 0.06 eV on average. Moreover, the LC functionals ωB97X and CAM-B3LYP underestimate the shifts by 0.20 and 0.30 eV on average, respectively. TD-DFTB underestimates the shift by even up to 0.35 eV with respect to SORCI. Surprisingly, LC-DFTB does not improve the shifts.

Otherwise, these trends are similar to the ones shown in the previous section for the model chromophore in presence of a single point charge and consistent with previous works (see Ref. 99 and references therein), which show that also CIS

Table 2.4: Lowest excitation energies and shifts of QM/MM optimized structures of bR and ppR, in eV. Δ denotes the difference of the two systems including the protein environment. The excitation energies are computed only with static external charges without polarization effects leading to higher excitation energies.

	Exp.	Wavefunction						DFT		DFTB	
		SORCI	OM2/MRCI	CC2	SOS-CC2	ADC(2)	SOS-ADC(2)	ωB97X	CAM-B3LYP	LC-DFTB	TD-DFTB
bR											
vacuum	2.00[a]	1.86[d]	2.22[d]	2.08	2.25	1.89	2.13	2.65	2.64	2.58	2.04
protein	2.18[b]	2.34[d]	2.66[d]	2.48	2.76	2.35	2.64	2.94	2.85	2.77	2.22
shift	+0.18	+0.48	+0.44	+0.40	+0.51	+0.46	+0.51	+0.29	+0.21	+0.19	+0.18
ppR											
vacuum	2.00[a]	1.91[d]	2.24[d]	2.08	2.30	1.92	2.20	2.67	2.65	2.60	2.00
protein	2.50 [c]	2.63[d]	2.96[d]	2.80	3.11	2.70	3.01	3.18	3.06	2.95	2.37
shift	+0.50	+0.72	+0.72	+0.72	+0.81	+0.78	+0.81	+0.51	+0.39	+0.35	+0.37
Δ(ppR - bR)	+0.32	+0.29	+0.30	+0.32	+0.35	+0.35	+0.37	+0.24	+0.21	+0.18	+0.16

[a] Ref. 174 [b] Ref. 87 [c] Ref. 86 [d] Ref. 88

(based on HF or an OM2 Hamiltonian) underestimates the shift in bR. Therefore, it is not surprising that the shift obtained with LC functionals is larger than that of pure or fixed-hybrid DFT functionals but still significantly lower than that of higher-level methods, like SORCI or CASPT2. Regarding the shifts, the ωB97X functional performs better than CAM-B3LYP due to its larger amount of HF-X in the long-range limit, but this improvement is paid with a larger error in absolute excitation energies.

QM/MM MD simulation of bR and ppR

A static structure of retinal with its surrounded protein environment obtained by QM/MM optimization misses the fluctuation of the protein environment and the retinal conformations. A QM/MM MD simulation is carried out to sample several structures to assess other influences such as temperature, which are subsequently used for the computation of excitation energies. Hence, the excitation energies are computed on 1000 snapshots using LC-DFTB and OM2/MRCI for bR and ppR, respectively. All excitation energies are weighted by the oscillator strength and plotted as histograms, see Fig. 2.8(a). The absorption maxima are obtained with a fit using a Gaussian function and displayed in Tab. 2.5.

Table 2.5: Absorption maxima (eV) of bR and ppR, obtained by sampled excitation energies over the QM/MM trajectories with subsequent Gaussian fit of the histograms.(ppR - bR) denotes the difference of the two systems in the protein environment.

	Exp.	OM2/MRCI	LC-DFTB
bR			
vacuum	-	2.24	2.52
protein	2.18[a]	2.65	2.73
shift	-	+0.41	+0.21
ppR			
vacuum	-	2.26	2.53
protein	2.50[b]	2.98	2.93
shift	-	+0.72	+0.40
Δ(ppR - bR)	+0.32	+0.33	+0.20

[a] Ref. 87 [b] Ref. 86

The absorption maxima of the retinal chromophore in bR and ppR in vacuum differ by about ± 0.02 eV for each method. This result is expected, since the retinal conformations are similar in bR and ppR. In comparison with the QM/MM optimized models, OM2/MRCI displays a slight blue shift of +0.02 eV and LC-DFTB a

red shift of about -0.06 eV for the vacuum excitation energies. The same behavior is obtained for the absorption maxima including the protein environment.

In bR and ppR the inclusion of the protein environment results in a blue shift for both methods. In the case of bR, OM2/MRCI leads to a slightly smaller blue shift (0.41 eV) compared to the QM/MM optimized models (0.44 eV). Whereas in the case of ppR, LC-DFTB computes a slightly higher blue shift (0.40 eV) compared to the QM/MM optimized models (0.35 eV). The slight deviations compared to the QM/MM optimized models of both rhodopsins bR and ppR is mainly reflected by the strong hydrogen bond network (see Fig. 2.8(b)) in the active site confining the chromophore retinal in its structural fluctuation. In this case the QM/MM MD simulations describe only an oscillation of the chromophore retinal around the energy minimum [88]. However, it has to be mentioned that rhodopsins exist, e.g. channelrhodopsin-2 wild-type (ChR2-WT), exhibiting a very flexible structure and therefore needs sampling by QM/MM MD simulations [158]. The difference of the absorption maxima between both rhodopsins (ppR-bR) obtained by OM2/MRCI (+0.33 eV) is as expected in agreement to the experimental shift (+0.32 eV). LC-DFTB shows with +0.20 eV a smaller shift of the absorption maxima between bR and ppR. Here, the color-weakness of LC-DFTB is again visible.

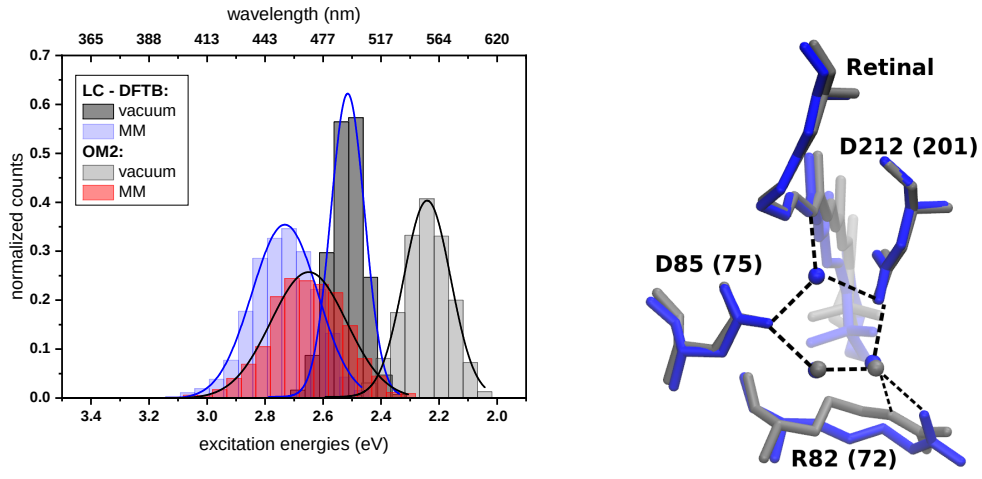

(a) (b)

Figure 2.8: (a) Simulated absorption spectrum of bR. LC-DFTB and OM2/MRCI are used for the computations of the excitation energies. The histograms are based on snapshot geometries of QM/MM MD trajectories of 1 ns length. Plotted are the excitation energies weighted by the oscillator strength for (i) only the retinal chromophore (vacuum) and (ii) with additional fixed MM point charges to account for the protein environment (MM). Gaussian functions are used to determine the corresponding maxima, in blue: LC-DFTB and in black: OM2/MRCI. (b) Active site of bR (in blue) and ppR (in gray) with the typical pentagonal hydrogen bond network. Residue numbers of ppR in brackets.

The computed excitation energies of the sampled structures are plotted as histograms in Fig. 2.8(a) for bR. The histogram for ppR is shown in the ESI (Fig. S3). In the case of OM2/MRCI, a broad simulated absorption spectrum is obtained, while LC-DFTB tends to yield less broad absorption spectra, especially when considering only the retinal chromophore without the protein environment. The width of the absorption spectra reflects in the case of vacuum, the different obtained retinal conformations differing in their BLA. The inclusion of the protein environment includes then also the fluctuation of the protein itself. Hence, weaknesses of LC-DFTB become visible also in this property since it cannot reproduce the same width as OM2/MRCI.

2.4.2 Light-harvesting complexes

To asses the performance of LC-DFTB, we focus on the energy ranges of three LH complexes, LH2 complex of *Rs. molischianum* and *Rps. acidophila* and the FMO complex of *C. tepidum*. To this end, we analyze the energy range spanned by all individual uncoupled BChl a chromophores with and without the protein environment as well as the energy range of the excitons.

Light-harvesting complex II (LH2)

QM/MM optimized model

In a first step, we considered a DFTB-QM/MM optimized structure for the complex and computed excitation energies for the B800 and B850 ring systems using LC-DFTB as summarized in Tab. 2.6. More detailed information can be found in the ESI (Tabs. S9 and S10). The BChl a structures are not significantly influenced by the protein environment and thus the excitation energies show only a minute standard deviation of 0.01 eV due to structural effects. The electrostatic interaction based on the QM/MM point charge model leads to a larger variation of the excitation energies, which is also illustrated in Fig. 2.9. It leads to a larger range for the B800 ring (0.092 eV) than for the B850 ring (0.034 eV). This finding can be explained by a more pronounced influence of the protein environment in B800, since the chromophores are less densely packed than in B850 and thereby exposed to a more polar protein environment [76, 177]. As expected from the benchmark results (Sec. 2.3), ZINDO/S overestimates the effect of the electrostatic tuning and results in a larger variation as shown in Tab. S11, ESI.

Table 2.6: Average excitation energies and standard deviations (in eV) based on DFTB-QM/MM optimized BChl a structures of the B800 and B850 ring systems. Shown are the excitation energies for the individual BChl a chromophores with and without the influence of the protein environment. In addition, excitonic energies (in eV), i.e., the lowest eigenvalues are shown for the ring system. The excitation energies have been computed using LC-DFTB, Coulomb couplings with LC-DFTB and TrESP.

	B800	B850	B850 shift
vacuum[a]	1.829 ± 0.007	1.829 ± 0.004	± 0.000
protein[a]	1.837 ± 0.028	1.828 ± 0.011	–0.009
ring system			
LC-DFTB	1.795	1.740	–0.055
TrESP	1.794	1.730	–0.064
Experimental [178]			–0.085

[a] BChl a monomer

LC-DFTB Coulomb couplings are about 0.006 eV for neighboring BChl a in a B800 ring, while we find a range of 0.033–0.075 eV for the B850 ring. TrESP gives smaller Coulomb couplings, as expected from the benchmark study (Sec. 2.3), which are around 0.004 eV for the B800 ring and 0.038–0061 eV for the B850 ring. The excitonic energies resulting from the diagonalization of the Hamiltonian for the two individual ring systems show a range of excitonic energies of 0.096 eV for B800, and 0.274 eV for B850. A similar energy range of 0.317 eV for the B850 ring was already reported previously [179]. Although for LH2 of *Rs. molischianum* no experimental data is known regarding the excitonic energy range, experimental data for the bacterium *Rps. acidophila* suggests an energy range of about 0.179 eV for the B850 ring at low temperatures [180]. Therefore, LC-DFTB overestimates this range of energies, and the reason for this overestimation is two-fold: first, the spread of the excitation energies of the individual chromophores may be slightly overestimated due to the QM/MM point charge electrostatics, i.e., inclusion of polarizable embedding may damp this spread slightly [117, 175, 176]. Second, LC-DFTB overestimates the values of the Coulomb couplings, as seen in Sec. 2.3. The Coulomb couplings are larger than the LC-DFTB supermolecular couplings, which in turn are in very good agreement with full LC-DFT couplings. Moreover, effects of polarization on the couplings are neglected. But all these effects are small (0.01–0.02 eV), but they accumulate when determining the eigenvalues of the Hamiltonian of the ring system. Therefore, we expect that our approach overestimates the spread of eigenvalues by about 0.1 eV.

In order to estimate the B800-B850 energy splitting, we use the lowest eigen-

values of the two ring Hamiltonians. As shown in Tab. 2.6, this range is close to the experimental value, i.e., the errors cancel out to some extent. The reason can be understood by inspecting Fig. 2.9.

On the one hand, the Coulomb couplings are overestimated, partially due to neglect of polarization. This significantly affects the B850 excitonic energies, i.e., additionally lowering the lowest energy states. Since the couplings between the B800 chromophores are much smaller, this spectrum is not much affected. The neglect of polarization, on the other hand, also lowers the energies of the individual chromophores, i.e., the site energies of the excitonic Hamiltonian: this, as discussed above, affects mostly B800 energies. Therefore, the energies of both ring systems are artificially lowered due to computational errors, i.e. for the B800 the site energies are mostly affected, for B850 the couplings. Since in both cases, the excitonic energies are lowered, we find a cancellation of errors.

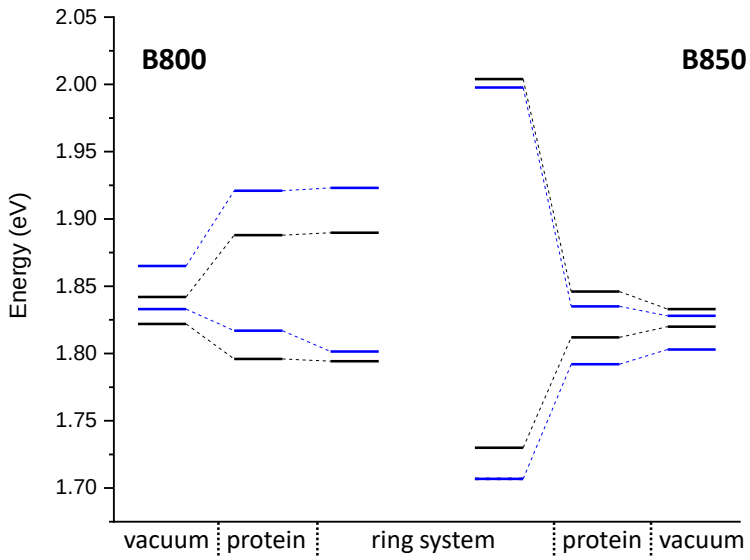

Figure 2.9: Excitation energy range (vacuum and with electrostatic environment) combined with the excitonic energy range for the QM/MM optimized structures, computed using LC-DFTB. LH2 of *Rs. molischianum* in black and LH2 of *Rps. acidophila* in blue.

The computation of such small energy differences, i.e., below 0.1 eV, is very challenging for these large systems, where approximations are inevitable. A recent study [117] on the LH2 complex of *Rps. acidophila* reported an overestimation of the experimental gap, while the computed excitonic couplings are smaller than ours (around 0.05 eV) due to the consideration of polarization effects. Since it is interesting to see how different approaches perform for the same system, we also studied the LH2 complex of *Rps. acidophila*. A detailed discussion and compari-

son of methods can be found in the ESI. The monomer excitation and excitonic energies of this complex are shown in Fig. 2.9. Although the two LH2 complexes studied here differ in conformation and number of chromophores, the spectra are quite similar.

Classical MD simulation

QM/MM MD simulations for multi-chromophoric complexes are not straightforward, since a QM approach with multiple QM regions would be required which is not implemented in the present DFTB scheme. Therefore, we use classical MD trajectories to sample the excitation energies. The corresponding average excitation energies and standard deviations are shown in Tab. 2.7. Moreover, in Fig. 2.10 histograms based on snapshots of the BChl a chromophores belonging to the B800 ring determined using 1 ns-long MD trajectories are displayed. The results for the B850 ring are given in the ESI (Fig. S4). While the vacuum excitation energy distribution is similar for LC-DFTB and ZINDO/S, the different response of both methods to the electrostatic field of the protein, as discussed in Sec. 2.3, is clearly visible. Both methods show a broadening while ZINDO/S shows a strongly asymmetric distribution with a long tail towards higher energies as reported earlier [59, 78].

Table 2.7: Average excitation energies and standard deviations (in eV) based on the classical MD trajectories. Shown are the excitation energies for the individual BChl a chromophores with and without the influence of the protein environment. The average excitation energies are obtained by averaging the maxima of Gaussian fits of the distributions of the respective chromophore. In addition, the excitonic energies (in eV), i.e., the lowest eigenvalues are shown for the Hamiltonians considering Coulomb couplings between the BChl a chromophores within one ring system. The excitonic energies are extracted as the maxima of the Gaussian fits to the exciton energy distributions. The excitation energies have been computed using LC-DFTB, Coulomb couplings with LC-DFTB and TrESP.

	B800	B850	B850 shift
vacuum[a]	1.833 ± 0.003	1.835 ± 0.005	-0.002
protein[a]	1.844 ± 0.007	1.839 ± 0.002	-0.005
ring system			
LC-DFTB	1.815	1.737	–0.078
TrESP	1.817	1.771	–0.046
Experimental [178]			–0.085

[a]BChl a monomer

Compared to the QM/MM optimized structures, the standard deviations (Tab. 2.7) are reduced for the average excitation energies with and without the protein

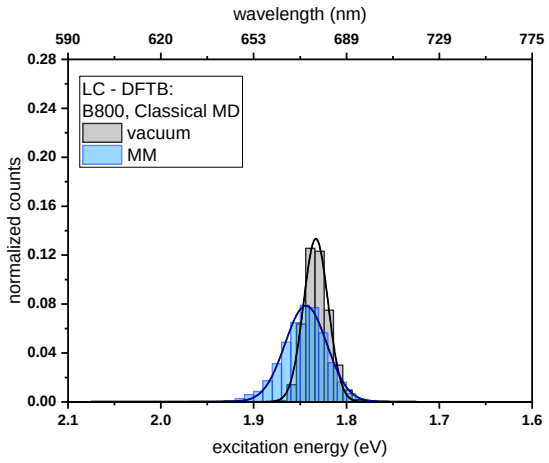

(a)

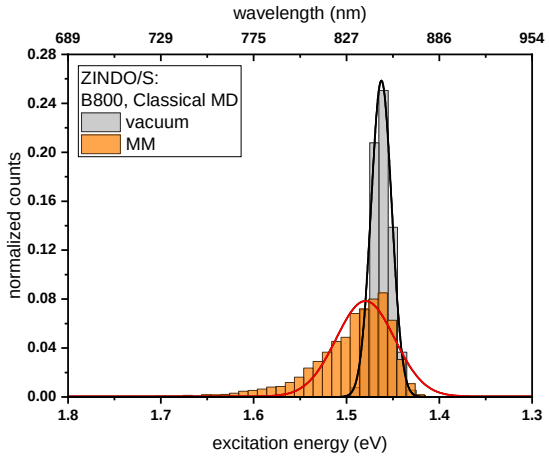

(b)

Figure 2.10: Histogram of the excitation energies for the B800 ring computed with (a) LC-DFTB and (b) ZINDO/S. Plotted are the excitation energies weighted by the oscillator strength for (i) only the BChl a chromophore (vacuum) and (ii) with additional fixed MM point charges to account for the protein environment (MM). Gaussian functions have been used to determine the corresponding maxima.

environment. For LC-DFTB, the diagonal disorder, i.e., the range of excitation energies, is smaller compared to that of the QM/MM optimized structures, as can be seen from Fig. 2.11. It seems, that optimization leads to local minima, where excitation energy differences between the BChl a chromophores are more pronounced. Hence, the differences between both LH2 complexes are reduced, comparing Figs. 2.11 and 2.9 (more details, see Tab. S15).

The sampled Coulomb couplings over the classical MD trajectory clearly show differences when comparing LC-DFTB and TrESP. An example plot is given in the ESI (Fig. S5). The LC-DFTB couplings fluctuate in a range of 0.004–0.008 eV for B800 and 0.060–0.080 eV for B850, while the TrESP couplings show lower fluctu-

ations of 0.0018–0.0025 eV for B800 and 0.035–0.045 eV for B850. The variation arises only from geometric changes, since the LC-DFTB computed couplings undergo changes due to changes in the transition charges, while in the case of TrESP the transition charges are constant. Please note, that we found the TrESP approach to lead to smaller couplings already for the model systems presented above. The B800-B850 energy splitting estimated from the sampled structures is higher in the case of LC-DFTB compared to the QM/MM optimized model and closer to the experimental value. As discussed above, error cancellation might also be responsible for the better agreement with the experimental energy range.

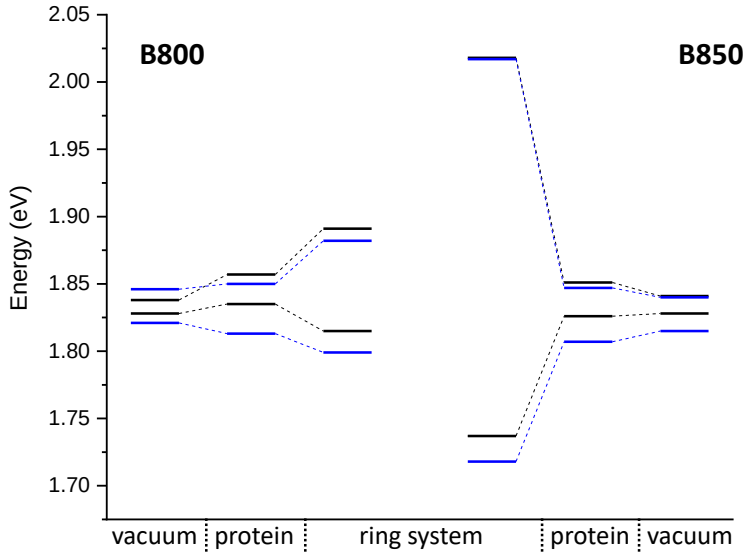

Figure 2.11: Excitation energy range of maxima of Gaussian fits (vacuum and with electrostatic environment) combined with excitonic energy range (in eV) for the sampled structures, computed with LC-DFTB. LH2 of *Rs. molischianum* in black and LH2 of *Rps. acidophila* in blue.

The resulting excitonic energy range computed using LC-DFTB decreases after sampling compared to the QM/MM optimized model in the case of B800, while it slightly increase in the case of B850 (see ESI, Tab. S14). As discussed for the QM/MM optimized model, the diagonal disorder is dominant in the B800 ring, since the couplings do not contribute much. Since the excitation energy splitting of the protein environment decreased after sampling, the excitonic splitting decreased as well. In the case of B850, smaller differences are observed compared to the QM/MM optimized model. For B850, the off-diagonal disorder is smaller through the more tight packing [76, 177] (see also discussion above), the chromophores are less exposed to the fluctuations of the protein electrostatic field. Thus, at the LC-DFTB level, there is no significant change in the exciton splitting

when compared to the QM/MM optimized case, which can be seen by comparing Figs. 2.11 and 2.9. For the TrESP couplings, however, a sizable decrease is found upon sampling, where the exciton splitting of 0.163 eV is closer to the experimental value at room temperature of about 0.158 eV [180]. This however, may be an accidential agreement, since the TrESP couplings are much smaller than those from supermolecular calculations.

One has to note, however, that the averaging process for the excitonic energies is ambiguous in itself: one can average the Hamiltonian and then compute its eigenvalues or one can average the excitonic energies computed for every snapshot. The latter one is used in the present work. Since the diagonalization is a non-linear operation, the two approaches lead to different results (Tab. S14, ESI). Thus, these two averaging procedures do not commute. In the first case, the deviations from the average value will not receive an appropriate weight in the exciton formation, while in the second case an instantaneous response of the electronic structure to the nuclear motion is assumed. This is a time-scale problem occurring typically, when a transport process is coupled to nuclear motions: how to treat fluctuations, e.g., in the context of Marcus theory [181] or Landauer tunneling [182]. When the time scales of the fluctuations in the electronic structure, resulting for the nuclear motion, and transport of the charge or energy are on the same time scale, non-adiabatic methods seem to be more appropriate.

Fenna-Matthews-Olson (FMO) complex

QM/MM optimized model

Next we analyze the excitation energies of the individual BChl a chromophores from the FMO of *C. tepidum*. In Fig. 2.12, the results for the DFTB QM/MM optimized FMO complex are depicted, computed in vacuum and within the protein environment using LC-DFTB. As observed for the LH2 complex, the BChl a geometries are not significantly influenced by the protein environment, since the BLA values are in the same range. Furthermore, the ZINDO/S results show a stronger response to the electrostatics (see ESI, Tab. S18).

The respective minimum and maximum of the energy range obtained in vacuum and with the protein environment are presented in Tab. 2.8. As expected, the resulting energy range in vacuum of 0.017 eV is smaller than the experimental range of 0.060 eV [183]. The consideration of the electrostatic environment

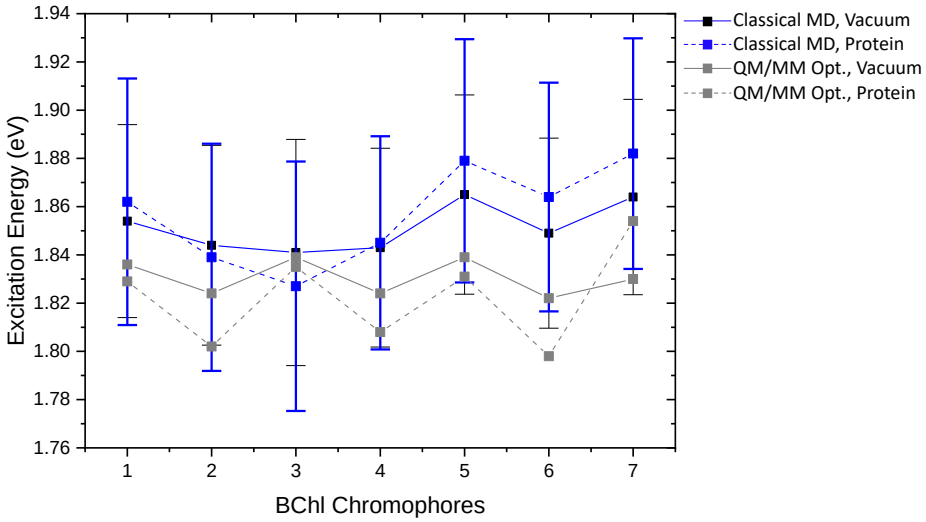

Figure 2.12: Excitation energy range of the FMO complex of the seven BChl a chromophores of the DFTB QM/MM optimized model and maxima with error bars of the Gaussian distributions belonging to the sampled structure over the classical trajectory; calculated in vacuum and with fixed MM point charges using LC-DFTB.

increases this value to 0.056 eV. A previous study using QM/MM optimized structures of the FMO complex of *P. aesturii* reporting an energy range of about 0.025 eV using CAM-B3LYP and including polarization contribution [126]. Therefore, using point charges only, the protein electrostatic effect may be overestimated, since polarization is neglected here.

Table 2.8: Range of excitation and excitonic energies of the DFTB QM/MM optimized BChl a chromophores of the FMO complex. LC-DFTB is used for the computation of excitation energies without (vacuum) and with the protein environment as fixed MM point charges. Coulomb couplings are computed using LC-DFTB and TrESP.

	Max	Min	shift
vacuum[a]	1.839	1.822	–0.017
protein[a]	1.854	1.798	–0.056
coupled chromophores			
LC-DFTB	1.898	1.756	–0.142
TrESP	1.968	1.784	–0.184
Experimental [183]	1.563	1.503	–0.060

[a]BChl a monomer

For LC-DFTB Coulomb couplings, a range of values between 0.019 eV and 0.045 eV is obtained for the strongest couplings, i.e., for the neighboring BChl a chromophores. In the case of TrESP a range of 0.012–0.029 eV is found showing lower values than LC-DFTB as expected from the benchmark study, see Sec. 2.3.

The Hamiltonian and the excitonic energies of the QM/MM optimized model computed with LC-DFTB are given in the ESI (Tab. S17, 21). The resulting energy range between the maximum and the minimum of the excitonic energies overestimates the experimental energy range, see Tab. 2.8, as expected, due to the overestimation of the Coulomb couplings and the neglect of polarization effects, similar to the LH2 case discussed above.

Classical MD simulation

In a next step, we analyze the excitation energies for the single BChl a chromophores sampled along a classical MD trajectory. The maxima of Gaussian fits to the distributions with the respective standard deviations are plotted in Fig. 2.12. LC-DFTB was used for the computation of the excitation energies of the sampled structures with and without protein environment. Again, ZINDO/S shows a stronger response to the electrostatic environment as shown by the broader excitation energy distributions depicted in the ESI (Fig. S9-11). However, the standard deviations of both LC-DFTB and ZINDO/S are similar, showing values of about 0.048 eV. The vacuum excitation energy range of the BChl a chromophores is in the case of LC-DFTB slightly larger (0.027 eV) than for the QM/MM optimized model (0.017 eV), see Tab. 2.9 due to the fluctuations.

Table 2.9: Range of excitation and excitonic energies along a classical MD trajectory of the FMO complex. LC-DFTB is used for the computation of excitation energies without (vacuum) and with the protein environment. The Coulomb couplings have been computed using LC-DFTB and TrESP.

	Max	Min	shift
vacuum[a]	1.865	1.841	–0.024
protein[a]	1.882	1.827	–0.055
coupled chromophores			
LC-DFTB	1.979	1.775	–0.204
TrESP	1.876	1.777	–0.099
Experimental [183]	1.563	1.503	–0.060

[a]BChl a monomer

The energy range computed for the protein environment is similar to that obtained by the QM/MM optimized model (see Tabs. 2.8 and 2.9). The results are consistent with those from a previous study cf. Ref. 184, which also did not include polarization effects. As already mentioned polarization effects reduce this range to 0.025 eV [185].

The average Coulomb couplings sampled along the trajectories are slightly

smaller than for the QM/MM optimized model, see ESI (Tab. S19). These are plotted together with Coulomb couplings obtained by previous studies using TD-DFT/MMPol [185] and PDA [186], see ESI (Fig. S8). LC-DFTB obtains qualitatively the same trend, however overestimates the Coulomb couplings by about a factor of 2. In the case of FMO, the Coulomb couplings seems to be slightly more overestimated than for the LH2 complex, when comparing to previous studies [117, 127]. Protein polarization leads to a screening of electrostatic interactions, which can be represented by a screening factor specific for the chromophores in different protein environments. Jurinovich et *al.* [185], reported a screening factor of about 1.7 for the FMO complex, which is larger than the screening factor obtained for the LH2 complex of 1.47 [117]. This indicates a higher influence of polarization, which explains the different deviations of our results.

The energy range resulting from the average excitonic energies (see ESI, Tab. S21), i.e., the exciton energy range from the coupled FMO chromophores shown in Tab. 2.9, is larger than the experimental energy range. It is even larger compared to the energy range obtained by the QM/MM optimized model. In the case of FMO, the off-diagonal disorder is dominant, leading to an increase of the exciton energy range compared to the QM/MM optimized model. Furthermore, the Coulomb couplings might have been overestimated more severely in the FMO complex compared to the LH2 aggregate due to the above discussed polarization influence.

2.5 Summary

In this study, we have investigated the performance of LC-DFT and LC-DFTB for two major light-activated protein classes, rhodopsins and light-harvesting complexes. Both present significant challenges for a theoretical description: rhodopsins show a large variance in absorption energies, i.e., have a sophisticated mechanisms of color tuning depending on chromophore geometry and interaction with the environment, while light-harvesting complexes are less responsive to the interaction with the environment, but are large in size and to a large extent change color by inter-chromophore coupling. For both systems, standard DFT functionals give non-satisfactory results while range-separated functionals seem to be a promising alternative.

For retinal, GGA and hybrid DFT functionals both fail to describe color tuning

w.r.t. changes in geometry and protein electrostatic interactions, while LC-DFT and LC-DFTB, in contrast, give a quite good account for geometrical changes. However, the correct response to the protein electric field is sensitively dependent on the amount of exact exchange. Therefore, the ωB97X and LC-BLYP functionals come close to the reference methods and might be useful in applications, while for CAM-B3LYP and LC-DFTB the response to the protein electrostatic field is too weak, therefore, these methods are not suitable for studies of retinal protein color tuning.

For BChl a, the changes of absorption energies w.r.t. geometries are well reproduced by LC-DFT and LC-DFTB. Electrostatic effects are much smaller than in retinal proteins but still relevant, since small energy differences lead to sizable effects in the red part of the spectrum. Taking DFT/MRCI as reference, it seems that less exact exchange in the LC-DFT functionals leads to a better agreement, so that CAM-B3LYP and LC-DFTB yield comparably the best results. Therefore, CAM-B3LYP might be the LC reference method of choice. For the calculation of excitonic couplings in BChl a, the choice of the LC-DFT functional is not critical, and they are also quite well described by LC-DFTB. Coulomb couplings computed from LC-DFTB, however, are slightly overestimated.

Therefore, the LC functionals have to be chosen carefully according to the target systems, since the correct description of absorption energies of retinal and BChl a depends on the amount of exact exchange. And this is inherited by LC-DFTB due to the particular choice of the LC functional.

The low computational cost of semi-empirical methods allows for extensive sampling of absorption spectra along MD trajectories, but also for a direct propagation of the exciton wavefunction on relevant time-scales [124]. We have performed QM/MM MD simulations to sample rhodopsin absorption energies using LC-DFTB and OM2/MRCI as fast quantum methods. While OM2/MRCI performs quite well, LC-DFTB computed spectra have to be considered carefully, due to the too small response to the protein electrostatic fields.

Considering the LH complexes, in a first step we have QM/MM optimized their structures iteratively, by successively selecting one chromophore in the QM region. The calculated excitation energies for these QM/MM optimized structures indicate, that of the diagonal disorder in the excitonic Hamiltonian is overestimated. This leads to an overestimation of the width of the computed spectrum. It seems, that geometry optimization drives the geometries into local minima, which show

a large variation of excitation energies among the chromophores. These may be shallow minima, which seem to contribute less when averaging over trajectories at 300 K. A problem, which can be solved by either imposing symmetry [117] or by averaging. We tested this for both LH complexes studied here, showing a clear reduction of energy range differences after sampling. We sampled the excitation spectra using trajectories from classical MD, since QM/MM MD simulations for the entire LH complexes are not possible at the moment. A multi-chromophore QM region would be required, work is in progress to make this property available in DFTB.

The comparison of exciton splittings for both LH2 and FMO computed with LC-DFTB and ZINDO/S show clear differences: since ZINDO/S shows a stronger response to the electrostatic environment, the width of the exciton spectrum is overestimated. LC-DFTB seems to be a good alternative method to ZINDO/S representing the electrostatic interaction in a more balance way. Up to now, effects of protein polarization, which we included in our previous studies on retinal proteins [173, 175, 176] have not been taken into account. However, chromophore excitation energies and exciton couplings are affected by polarization. Both, diagonal disorder and the coupling strength are slightly reduced when considering protein polarization effects, therefore, not taking polarization into account leads to an overestimation of the exciton band width.

Interestingly, the experimental B800-B850 energy splitting is reproduced quite well, since polarization effects tend to cancel. This is not the case for the FMO complex, where the width of the exciton band is overestimated. Therefore, LC-DFTB will most likely give quite accurate results for LH complexes excited states properties, if polarization is included in future work.

In summary, LC-DFTB is an accurate and efficient method for studying exciton spectra and dynamics in LH complexes, since it is about three orders of magnitude faster than the full TD-DFT scheme with a minimum loss in accuracy.

Acknowledgments

The authors acknowledge support by the DFG through the joint grant EL 206/18-1 and KL-1299/18-1, the DFG-Research Training groups 2247 "Quantum Mechanical Materials Modelling", 2039 "Molecular architecture for fluorescent cell imaging", 2450 "Tailored Scale-Bridging Approaches to Computational Nanoscience" and the

DFG-SFB 1249 "N-Heteropolyzyklen als Funktionsmaterialien" (Projects B02 and B07). Moreover, support by the state of Baden-Württenberg through bwHPC and the German Research Foundation (DFG) through grant no INST 40/467-1 FUGG (JUSTUS cluster) is gratefully appreciated. The project has been supported in part by the bwHPC initiative and the bwHPC-C5 project. We thank N. H. List for providing us with the structures and benchmark data of the FMO complex from Ref. 102.

Supporting Information

Supporting information for this chapter are given in **Appendix A**.

Chapter 3

DFTB/MM Molecular Dynamics Simulations of the FMO Light-Harvesting Complex

Because of the size of light-harvesting complexes and the involvement of electronic degrees of freedom, computationally these systems need to be treated with a combined quantum–classical description. To this end, Born-Oppenheimer molecular dynamics simulations have been employed in a quantum mechanics/molecular mechanics (QM/MM) fashion for the ground state followed by excitation energy calculations again in a QM/MM scheme for the Fenna-Matthews-Olson (FMO) complex. The self-consistent-charge density functional tight-binding (DFTB) method electrostatically coupled to a classical description of the environment was applied to perform the ground-state dynamics. Subsequently, long-range-corrected time-dependent DFTB calculations were performed to determine the excitation energy fluctuations of the individual bacteriochlorophyll a molecules. The spectral densities obtained using this approach show an excellent agreement with experimental findings. In addition, the fluctuating site energies and couplings were used to estimate the exciton transfer dynamics.

Reprinted with permission from the article by **S. Maity**, B. M. Bold, J. D. Prajapati, M. Sokolov, T. Kubař, M. Elstner and U. Kleinekathöfer, *DFTB/MM Molecular Dynamics Simulations of the FMO Light-Harvesting Complex*, J. Phys. Chem. Lett. **11**, 20, 8660 (2020). (DOI: 10.1021/acs.jpclett.0c02526). **As first author I did most of the calculations.**

3.1 Introduction

Light-harvesting (LH) protein-pigment complexes of plants, bacteria and marine algae are key players in the conversion of sunlight into stable forms of chemical energy during the process of photosynthesis. Chlorophyll (Chl), bacteriochlorophyll (BChl) and bilin molecules are the main chromophoric pigments present in those complexes which absorb solar light and subsequently pass it on to other pigments via excitation energy transfer processes. Aim is to transport the excitation energy to reaction centers where charge separation takes place for further processing [1, 10]. As example, in green sulfur bacteria pigment molecules present in large vesicles commonly known as chlorosomes absorb the sunlight. Subsequently, the absorbed energy is transported to reaction centers through small protein-pigment complexes known as Fenna-Matthews-Olson (FMO) complexes [187]. Since decades, the FMO complex is one of the most extensively studied light-harvesting systems in both theory and experiment. In earlier studies, it was assumed to be monomeric with seven BChl a pigments embedded in a protein scaffold. Later on, it was revealed that the complex is trimeric with eight pigments per monomer and C_3 symmetry [24, 25, 188] (see Fig. 3.1).

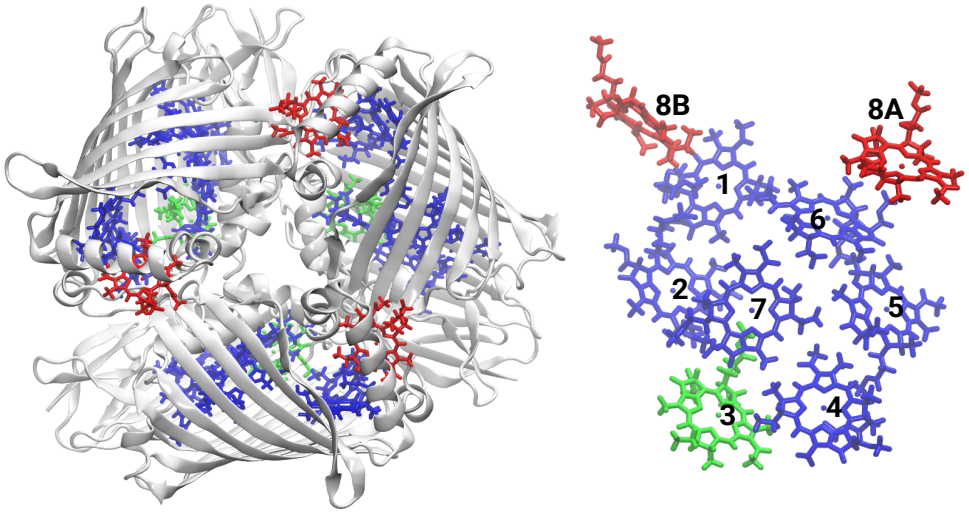

Figure 3.1: Trimeric architecture of the FMO complex from the green sulfur bacterium *Chlorobaculum tepidum*. The protein matrix is depicted in grey cartoon representation while the BChl pigments are shown in blue, green and red. In addition, the BChl arrangements for a monomer are displayed on the right. For BChl 8 two copies are shown in red, one from the same monomer as the other seven pigments and one from a neighboring monomer with a strong excitonic coupling. BChl 3 (green) is supposed to be the terminal emitter leading the excitation energy towards the reaction center.

The claim of long-lived electronic quantum coherences in the FMO and similar complexes at low and room temperatures has triggered an enormous interest in

these systems [15, 19, 20]. Similar observations were also reported for marine algae [55] and conjugated polymers [56] at room temperature. It was proposed that the long-lived coherences are due to correlated protein-induced site energy fluctuations [15, 189]. In earlier classical molecular dynamics (MD) simulations, however, no indications for such correlated fluctuations were observed [26, 28]. Moreover, recent two-dimensional electronic spectroscopic measurements were not able to find long-lived electronic coherences in LH or model systems [19, 29, 30, 190].

To understand the excitation energy transfer dynamics in LH complexes in general, numerous experimental and theoretical studies specially on the LH2 and FMO complexes have been performed (see, e.g., Refs. 26, 59, 62, 76, 191–195). In experiments, often two-dimensional electronic spectroscopy has been employed whereas in most theoretical investigations classical MD simulations followed by quantum chemistry calculations were utilized. In some studies, these calculations have then be followed by either density matrix or ensemble-averaged wave packet dynamics. For the first approach, time-averaged Hamiltonians and spectral densities need to be determined while the latter one employs the time-dependent site energies and couplings directly. Spectral densities represent the system-bath coupling and can be calculated from the autocorrelation function of the excitation energy fluctuations of the individual pigment molecules. So far, mainly ZINDO/S-CIS (Zerner's Intermediate Neglect of Differential Orbital method with spectroscopic parameters together with the configuration interaction using single excitation) and TDDFT (time-dependent density functional theory) calculations have been utilized in order to calculate the site energy fluctuations along classical MD-based ground state simulations in a quantum mechanics/molecular mechanics (QM/MM) fashion [26, 27, 59, 60, 77, 79, 193, 196]. Although the TDDFT approach is numerically less expensive than wavefunction-based schemes, it is still more CPU time demanding than semi-empirical ZINDO/S-CIS calculations [59]. TDDFT calculations based on long-range corrected (LC) or hybrid functional are known to overestimate the energy gap between ground and excited states while the ZINDO/S-CIS scheme has been parameterized for BChl type pigment molecules. At the same time, there are indications that the energy fluctuations in TDDFT calculations are more reasonable than those from the ZINDO/S-CIS scheme which seems to overestimate the amplitude of fluctuations [78, 197]. However, all these approaches based on classical MD simulations followed by quantum chemical calculations suf-

fer from the so-called "geometry mismatch" problem, i.e., conformations obtained by the force-field approach are not consistent with the subsequent quantum chemical calculations [198–200]. One attempt to overcome this problem is to parameterize classical force fields to capture some quantum effects in the ground state dynamics though it is unclear how much of the geometry mismatch problem is removed in this manner [201, 202]. It is, however, not clear if with such an approach one is able to sample the phase space properly and at the same time to obtain a correct frequency spectrum for the vibrational modes. An alternative is to perform QM/MM dynamical simulations for the ground state dynamics. This kind of formalism has been employed using semi-empirical QM schemes [203] as well as DFT calculations [204] and will also be the foundation of the present study. Another strategy introduced by Coker and co-workers is to determine the intra- and intermolecular contributions to the spectral density separately with the intramolecular part being computed by a normal mode analysis [67, 205, 206]. This technique has yielded results in quite good agreement with experiment [206]. In this scheme, the intermolecular component is calculated by the electrostatic coupling [205]. Although this approach results in a good agreement with experiment, the distortions of the ground state geometry along each individual normal mode followed by TDDFT calculations for all modes makes this strategy numerically challenging [200]. In a further approach by Rhee and co-workers, an interpolated potential energy surface (PES) has been determined in a QM/MM framework for the ground and excited states from a set of energies and their derivatives in the required coordinate subspace [184, 207, 208]. On these ground and excited-state surfaces one can subsequently perform long-time nuclear dynamics. The construction of such PESs is, however, by no means trivial and computationally expensive for a large molecule like a BChl molecule since one needs to perform many DFT as well as TDDFT calculations [207]. At the same time, this approach provides spectral densities in good agreement with experiment while some peaks in the high-frequency region are shifted with respect to the latter [195].

In this work, we want to introduce an efficient and accurate approach for the computation of spectral densities. As we will show, extensive sampling of the ground state conformations is required to achieve a converged spectrum of monomer excitation energies. Therefore, we apply approximate DFT methods for ground and excited states calculations. Previous work used different semi-empirical QM [203] and DFT [204] which, however, is computationally demand-

ing when applied for MD simulations.

Here, we apply the density functional based tight binding (DFTB) method [68, 70, 71] within an QM/MM framework using CHARMM36m in the classical region to perform the ground state dynamics of the individual BChl molecules in the FMO complex. It is roughly three orders of magnitude faster than DFT-GGA methods using a medium sized basis set, e.g., DZP. In quantum chemistry, compound methods are routinely used, mixing DFT and wave-function based methods for the determination of molecular properties. The above mentioned "geometry mismatch" problem has two components, which may be easily overlooked: first, the proper phase-space region has to be sampled, for which excitation energies are computed. This is required to reproduce, e.g., absorption spectra with reasonable quality. For chromophores like retinal this is a challenging task, since quantum chemical methods show a large variation in the ground state geometries, which is much less severe for BChl molecules [197]. Second, since the power spectra sensitively depend on the vibrational characteristics of the chromophores, methods are needed which accurately reproduce vibrational spectra. Furthermore, this fact can be also explained by the bond length alteration (BLA) values of conjugated systems. As shown in the section S2 in the SI, classical MD simulations can also provide a geometrical phase-space of BChl molecules close to the one based on the DFTB method. It fails, however, to describe the vibrational frequencies accurately. Hybrid DFT methods, like B3LYP are known to overestimate vibrational frequencies, therefore, local functionals like BLYP have been applied more successfully for such problems. A small benchmark in Ref. 71, Table 6, relevant for this work, illustrates this point (see also Ref. 70). The important C=C, C=N and C=O double bond stretch modes are overestimated by about 70 cm^{-1} when using B3LYP. The results for BLYP are, however, closer to experiment as shown in several other studies before. Since there is such a variation among DFT methods for this property, we have derived a DFTB parametrization which is very accurate for the description of vibrational properties. The so called DFTB3/3OB-f method uses the 3rd-order DFTB method in conjunction with the 3OB-f parameter set specifically derived for vibrational properties [71].

Concerning excited states, local and hybrid DFT methods meet severe challenges for excited states of many biomolecules. The range-separation concept as introduced in the DFT formalism, also called long-range correction (LC-DFT), has been shown to ameliorate some of these problem, especially concerning charge

transfer excited states and the overpolarization problem of conjugated molecules [114,209,210], which is relevant for the description of excited states of large conjugated molecules like BChl [197,211]. The LC-approach has been implemented for DFTB in ground and excited states [69, 122, 147, 212], and has been tested for retinal proteins and BChl chromophores in detail, reporting also QM/MM applications for LH2 and FMO [197]. LC-DFTB can reproduce excitation energies and electronic couplings with an accuracy very close to that of LC-DFT approaches with functionals like CAM-B3LYP, ωB97X, however, at a fraction of their computational cost. This allows to compute QM/MM MD trajectories in the nanoseconds regime, for which absorption and spectral density can be evaluated.

As detailed below, the present approach leads to a quite good agreement with experimental spectral density. Apart from the TD-LC-DFTB method for the excited state calculations, we have also considered the semi-empirical ZINDO/S-CIS scheme to calculate the excitation energy along the DFTB-QM/MM trajectories. A comparison with the results based on classical MD trajectories shows clear differences especially in the high-frequency region of the spectral density to the findings based on the QM/MM MD trajectories. Furthermore, we have calculated the excitonic couplings based on the so-called TrESP (transition charge from electrostatic potential) procedure [73,75] and performed ensemble-averaged wave packet dynamics. Details of the setup and the computational methods are given in section S1 of the SI.

3.2 Results and Discussion

3.2.1 Site energy distributions

The excitation energy gaps between the ground and the Q_y state are also termed site energies in the following since they serve as site energies in tight-binding models of exciton transfer. In Fig. S3A, a piece of a trajectory of these site energies is shown based on the QM/MM dynamics. To get a better view on the energy ladder in the FMO complex, we first want to focus on the average site energies of the different approaches shown in Fig. 3.2. As can be seen, the four different schemes do differ considerably (results for ZINDO/S are shown in Fig. S3D). In one version, a 40 ps QM/MM MD trajectory was employed which we also need for the calculation of spectral densities. In a second step, this trajectory has been extended to

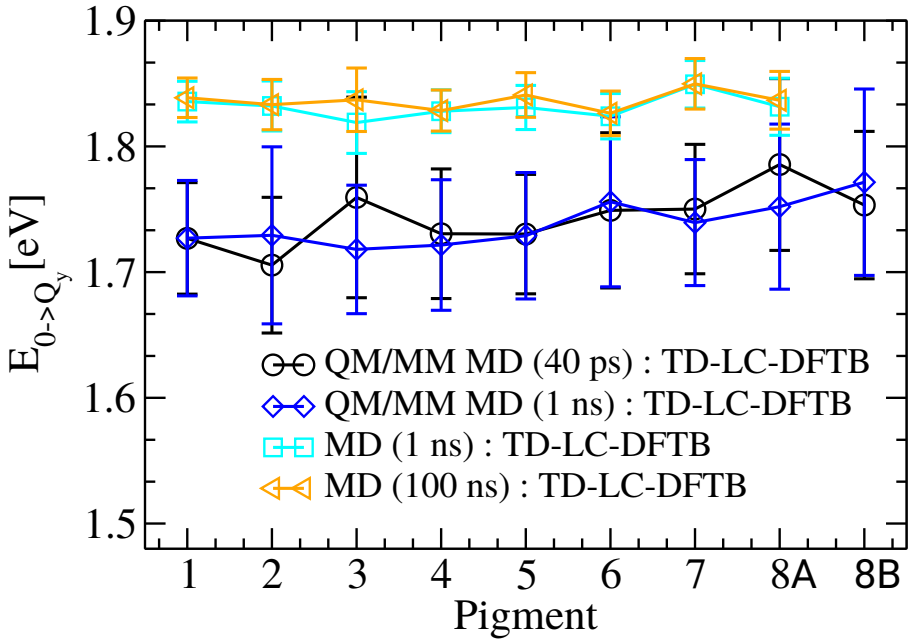

Figure 3.2: Average site energies associated with the respective error bars for the individual pigment in the FMO complex based on different types of ground state trajectories and TD-LC-DFTB for the excited state calculations.

1 ns with a larger stride between the individual frames leading to an improved sampling. A clear impact on the site energies can be seen showing the necessity for a proper sampling. Even longer QM/MM MD trajectories become numerically expensive using DFTB as well. To further test the sampling, we compared the site energies based on 1 ns and 100 ns classical MD trajectories with 1,000 and 10,000 equally spaced snapshots. In the case of the MD-based trajectories, the site energies have also been averaged over the three monomers of the FMO trimer. It can be seen that still small changes are visible but these are much smaller than those when increasing the trajectory length from 40 ps to 1 ns and thus we conclude that the site energies based on the 1 ns QM/MM dynamics is close to convergence with respect to sampling. Note, however, the energies computed for the classical MD-trajectory are blue shifted by about 0.1 eV due to the different geometries.

Structurally, BChl 3 is the terminal emitter to the reaction center and is believed to participate in the lowest exciton state having the lowest site energy [187, 191, 192] although this is not undisputed [102, 196, 213]. It is reassuring that the QM/MM dynamics with the best sampling, i.e., the 1 ns trajectory, yields that BChl 3 actually has the lowest site energy in this calculation. At the same time, we want to emphasize that the differences in the site energies of the different pigments is very low and likely below the accuracy of the employed ground and excited state methods. Moreover, the differences at room temperature are below 2 k_BT at

maximum and might not have a strong “driving” effect for the excitons since the effect of the coupling to the respective exciton source, i.e., the chlorosome, and drain, i.e., the reaction center, will likely be much larger.

3.2.2 Spectral Density

To calculate the exciton dynamics in LH complexes, one usually uses the concept of open quantum systems. For density matrix-based approaches, a key property therein is the environmental spectral density J(ω) [58]. Several approaches exist to obtain this quantity while here we determine it as the cosine transformation of the energy autocorrelation function using [77, 79]

$$J_m(\omega) = \frac{\beta\omega}{\pi} \int_0^\infty dt C_m(t) \cos(\omega t) \tag{3.1}$$

where $\beta = 1/k_B T$ denotes the inverse temperature. The energy autocorrelation function $C_m(t)$ for each individual pigment m can de obtained from a discrete time series as [76]

$$C_m(t_l) = \frac{1}{N-l} \sum_{k=1}^{N-l} \Delta E_m(t_l + t_k) \Delta E_m(t_k) \tag{3.2}$$

where E_m denotes the site energy of pigment m, i.e., the excitation energy of the Q_y state, and ΔE_m the difference from its average $\Delta E_m = E_m - \langle E_m \rangle$ [59]. In the present calculations, 40,000 frames from the 40 ps trajectories for both, the QM/MM and the classical MD simulation, were taken into account. For the determination of the spectral density, windows of 4 ps length were employed fixing the number of snapshots N in Eq. 3.2 to 4,000. From such a window one can construct a trustworthy autocorrelation function of 2 ps length. To enhance sampling and assuming that the fluctuations of the site energies are basically independent after 1 ps already, we used starting points for the calculation of the autocorrelation functions which were 1 ps apart [77, 214]. Finally, the 37 obtained correlation functions were averaged. In order to enhance the frequency resolution of the spectral densities, we used the concept of zero padding and prolonged the average autocorrelation in time by adding zeros for additional 2 ps. Moreover, a cubic spline fit has been employed using 4,000 points to smoothen the final spectral density.

Shown in Fig. 3.3 is the spectral density averaged of a monomeric unit from

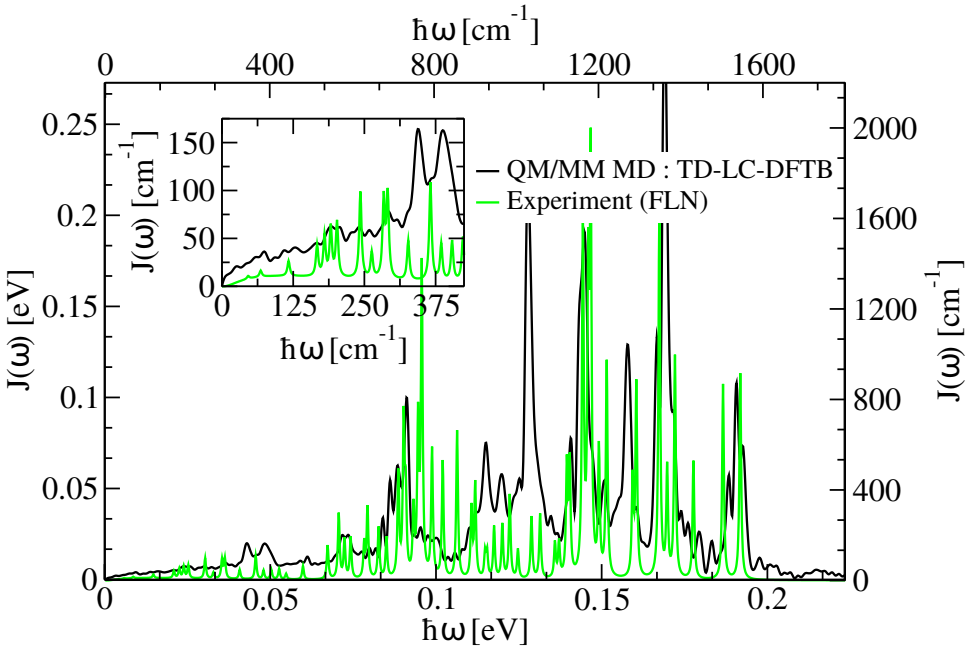

Figure 3.3: Comparison between the QM/MM MD-based spectral density averaged over the different pigments and initial conditions determined using the TD-LC-DFTB approach and the experimental fluorescence line narrowing (FLN) results [215, 216]. The inset focuses on the low frequency region.

TD-LC-DFTB calculations along the QM/MM MD trajectory of 40 ps length. The counterpart using the ZINDO/S scheme and the spectral densities of the individual pigments are shown in the SI. As can be seen in Fig. 3.3 and Fig. S5, the major peak positions are in the range of 1030 to 1550 cm^{-1} for each BChl pigment. This observation signifies that the shortest oscillation periods in the auto correlation functions are around 22-32 fs (see S4 in the SI). The major peaks originate mainly from intra-molecular vibrational modes involving C=C, C=N and C=O bond stretching [217] while the low-frequency regions of the spectral densities are mainly due to electrostatic interactions with the environment of the individual pigment molecules [66]. As a very important point, we have compared our spectral density averaged over all calculated pigments from different starting structures with the available experimental results by Kell et al. [216] and Rätsep et al. [215] measured using ΔFLN spectroscopy as shown in Fig. 3.3. In the experiment reports, only Huang-Rhys (HR) factors and their corresponding frequency are listed from which a combination of log-normal and Lorentzian expressions are fitted to model the complete spectral density. The fitting equations are described in the SI. Looking at the general behavior, the agreement is very good. The positions and in many cases also the amplitudes of several peaks are almost identical. The most obvious difference in the QM/MM MD results is the additional high peak at around 1010-1060 cm^{-1}. Surprisingly this peak also appears in another theo-

retical calculation as shown in the Fig. S10. Maybe the experimental resolution in this frequency region should be revisited also because experimental findings for similar molecules like Chl in the LHCII complex of higher plants do include peaks in that region [218, 219]. Moreover, the calculated spectral density is somewhat higher than the experimental findings in the low frequency regime while the origin of this difference can be manifold. Potentially it might be an issue of the CHARMM force field in a QM/MM framework with DFTB. Further work in this direction is needed.

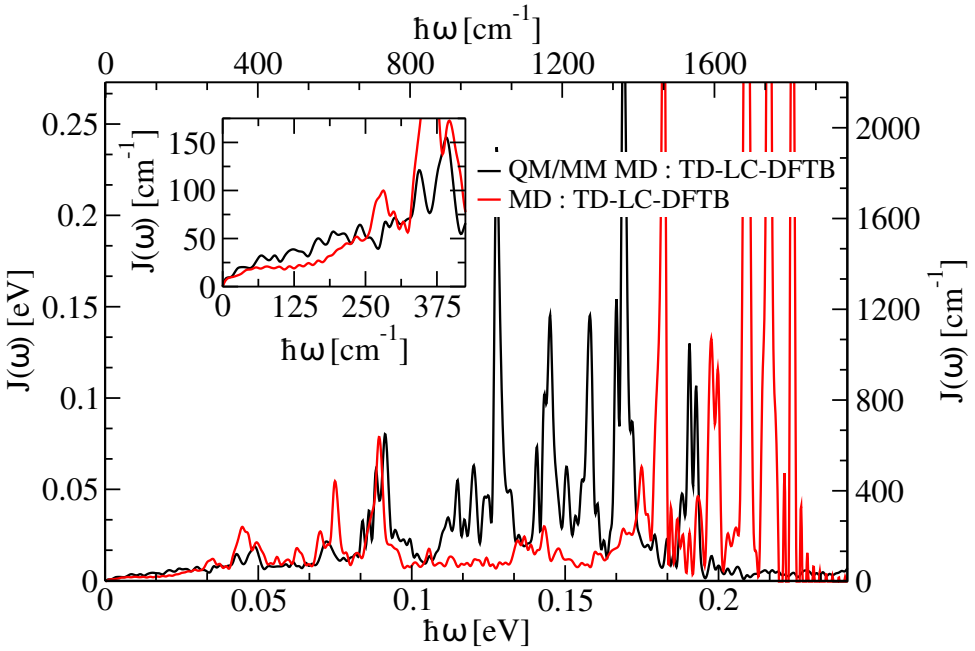

Figure 3.4: Average spectral densities of the FMO complex along the QM/MM MD and the classical MD trajectories both based on the TD-LC-DFTB method. For the QM/MM MD trajectory, the average was calculated for a monomer while for the classical MD trajectory the average was employed for the trimer. The inset highlights the low frequency region.

For comparison, we have also calculated the spectral densities for the trimeric unit along the first set of the classical MD trajectories based on the TD-LC-DFTB theory for the excited state energies. Moreover, we have compared the classical MD-based average spectral density with the QM/MM MD-based one with the excitation energies determined using TD-LC-DFTB in both cases. The comparison is shown in Fig. 3.4. As in earlier studies [60, 78, 79], the major peaks of the classical MD-based spectral densities are in the range from 1450 to 1800 cm^{-1} as also found here. It can be seen that the major peaks for the QM/MM MD-based spectral densities are shifted towards lower frequencies compared to the classical MD-based ones and have reduced amplitudes. Since the high-frequency contribution are internal modes of the BChl molecules, these are parameterized in the force field in

the classical MD-based method which one cannot expect a force field to reproduce properly. Furthermore, in the QM/MM MD-based trajectory the BChl geometries are already based on a DFTB basis which should lead to a proper sampling of the corresponding phase space. Moreover, the usage of the 3OB-f parameter set ensures an accurate description of the vibrational dynamics. A comparison to the computed spectral densities by Kim et al. [184] as well as Lee and Coker [67] is shown in Fig. S10 and discussed in section S7.

3.2.3 Wave Packet Dynamics

To be able to perform calculations of the exciton transfer dynamics one has to determine the excitonic couplings between the BChl molecules in the FMO system. In the present study, we have employed the TrESP approach [73, 75] with a distance-dependent screening factor to calculate the excitonic couplings between the pigments (see S1 in the SI). To this end, the coordinates of pairs of BChl molecules are necessary to determine the couplings. Above we have used the QM/MM ground state dynamics where the QM region consists of a single pigment molecule at a time. Performing DFTB-QM/MM dynamics with two or even more pigments in the QM region for all possible pairs of (neighboring) pigments is numerically challenging and thus we determined the couplings based on classical MD trajectories.

Concerning the calculation of the exciton dynamics numerous approaches exist from the area of open quantum systems often using the above determined spectral density as key input parameter. Accurate approaches using density matrices can, however, be computationally quite challenging especially with numerically determined spectral densities and thus we restrict ourselves here to an ensemble-averaged wave packet scheme. This kind of approaches and density matrix-based ones have been shown to yield the same results in certain parameter regimes [65]. The Hamiltonian with the site energies E_m and coupling V_{nm} can be written as

$$H_S(t) = \sum_m E_m(t) \left|m\right\rangle \left\langle m\right| + \sum_{n \neq m} V_{mn}(t) \left|n\right\rangle \left\langle m\right| \ . \tag{3.3}$$

This time-dependent Hamiltonian is utilized to propagate the system by solving the time-dependent Schrödinger equation

$$i\hbar \frac{\partial |\Psi_S(t)\rangle}{\partial t} = H_S(t) |\Psi_S(t)\rangle \tag{3.4}$$

with $\Psi_S(t)$ denoting the total wave function of the system. This wave function can be expanded in terms of exciton basis function $|\alpha\rangle$ resulting in $|\Psi_S(t)\rangle = \sum_\alpha c_\alpha(t)\,|\alpha\rangle$ with the time-dependent coefficients $c_\alpha(t)$. The excitonic state $|\alpha\rangle$ can be represented in terms of site-local basis $|m\rangle$ as

$$|\alpha\rangle = \sum_m c_m^\alpha\,|m\rangle \ . \tag{3.5}$$

Together this leads to the probability of finding an exciton on a particular pigment (m) given by

$$P_m(t) = |\langle m|\Psi_S(t)\rangle|^2 = |\sum_\alpha c_m^\alpha c_\alpha(t)|^2 \ . \tag{3.6}$$

Solving the time-dependent Schrödinger equation needs to be repeated many times with different starting points along the trajectory to obtain a sensible exciton transfer dynamics. The time-dependent probabilities of the excitonic populations $P_m(t)$ reveal how the excitons move from one pigment to another inside the FMO complex.

For the wave packet dynamics based on a fully time-dependent Hamiltonian, one needs site energies and couplings for the same snapshots along a trajectory. Due to the above mentioned arguments for the coupling calculations, we first determined such a Hamiltonian along a classical MD trajectory using TD-LC-DFTB for the excited state calculations. Furthermore, we have found that the time-dependent Hamiltonian based on couplings and site energies from each snapshot revealed almost the same dynamics when compared to the same simulations but with time-averaged coupling values (see S8 in the SI). This result is due to the small magnitude of coupling fluctuations and, different from the site energies, there are no resonance effects. A similar finding has already been reported in an earlier study for bilin molecules [220]. For this reason, here we have taken the average coupling values obtained from the classical MD trajectory and propagated it together with the TD-LC-DFTB site energies obtained from QM/MM MD trajectories to reveal an improved exciton dynamics as shown in Fig. 3.5.

As an example, we show the exciton dynamics for the case of an initial excitation of BChl 1. The population dynamics is depicted in Fig. 3.5 for site energies based on the TD-LC-DFTB site energies from QM/MM MD trajectories and time-averaged couplings from a MD trajectory. The figure shows that the population leaves the initially excited pigment in a roughly exponential manner and is first

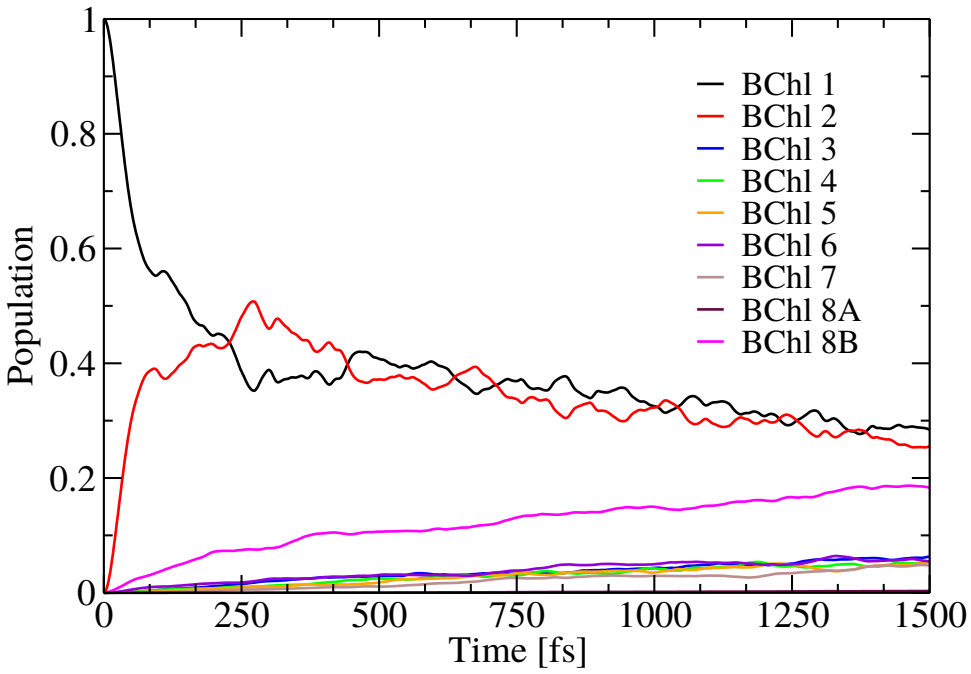

Figure 3.5: Exciton dynamics in a FMO monomer based on TD-LC-DFTB site energies from QM/MM MD trajectories and time-averaged couplings based on classical MD. As an example, BChl 1 was initially excited.

transferred to BChl 2 and moves on from there. Interestingly, also the population transfer to BChl 8B, i.e., the BChl 8 pigment from the neighboring monomer is quite fast. Analyzing the coupling distributions, this finding is, however, not so surprising anymore. With this technique, the transfer dynamics between all pigments can be determined if necessary.

3.3 Conclusions

In this present study, we have employed an improved strategy based on a QM/MM ground state dynamics using DFTB together with the parameter set 3OB-f, which has been developed with a special emphasis on vibrational frequencies, followed by TD-LC-DFTB calculations to obtain the excitation energies of the BChl pigments in an FMO complex. This approach has cured problems arising in some earlier procedures due to quantum chemical excited state calculations along classical MD trajectories. The new approach has been applied to determine the time-averaged site excitation energies and spectral densities which describe the environmental influence on the exciton dynamics. The average excitation energies are very similar with BChl 3 having the lowest site energy in agreement with earlier finding reported in literature. Here it has to be noted that a reasonably good sampling seems to be necessary to obtain trustworthy results. Thus, a fast but reliable ap-

proach such as the DFTB/3OB-f scheme is the method of choice. For the spectral density, the major peak positions of the spectral density in this scheme are in the range from 1030 to 1550 cm^{-1} which corresponds to oscillation periods of 22 to 32 fs in the energy gap autocorrelation functions. A comparison to previous calculations as well as experimental findings has shown that the spectral densities based on the QM/MM dynamics yield results significantly superior to those based on classical MD trajectories. Moreover, we noticed that for QM/MM dynamics, there is a sampling issue to obtain spectral density which was less prominent in the case of the classical MD trajectory. Finally, we performed an ensemble-averaged wave packet based dynamics together with the TD-LC-DFTB site energies from QM/MM MD trajectories and time-averaged coupling values from a classical MD-only trajectory. This "mixed" procedure was performed due to the high computational costs of coupling calculations along a QM/MM MD trajectory as detailed above but might not significantly influence the results. The exciton dynamics can the yield estimates how the excited energy is transferred between the pigments. In the present study we showed, for example, how the energy from the initially excited BChl 1 pigment moves to the closely coupled BChl 2 and BChl 8B pigments within a couple of 100 fs and then is further distributed to the other chromophores.

In summary, the present study can be seen as a new approach towards the investigation of exciton dynamics for LH and similar complexes of biological interest. It is well known that force field-based ground state dynamics is not accurate enough to describe the spectral density due to an incomplete sampling of the respective phase space and more importantly due to a poor description of the vibrational dynamics. So far, several approximations were carried out to tune the ground state coordinates and dynamics in order to cure these problems. More sophisticated DFT-based QM/MM MD is a good candidate to solve these problems. However, due to the size and complexity of LH complexes, DFT-based ground state dynamics and subsequently excited state calculations are still computationally very demanding [204]. Hence, the present DFTB-based approach is a very efficient but accurate scheme to perform dynamical QM/MM calculations.

Acknowledgments

The authors acknowledge support by the DFG through the joint grant EL 206/18-1 and KL-1299/18-1 as well as the DFG-Research Training groups 2247 "Quantum

Mechanical Materials Modelling" and 2450 "Tailored Scale-Bridging Approaches to Computational Nanoscience". We thank Prof. Young Min Rhee for providing the spectral densities for BChl 3 from Ref. 195.

Supporting Information

Supporting information for this chapter are given in **Appendix B**.

Chapter 4

Multiscale QM/MM Molecular Dynamics Simulations of the Trimeric Major Light-Harvesting Complex II

Photosynthetic processes are driven by sunlight. Too little of it and the photosynthetic machinery cannot produce the reductive power to drive the anabolic pathways. Too much sunlight and the machinery can get damaged. In higher plants, the major Light-Harvesting Complex (LHCII) efficiently absorbs the light energy, but can also dissipate it when in excess (quenching). In order to study the dynamics related to the quenching process but also the exciton dynamics in general, one needs to accurately determine the so-called spectral density which describes the coupling between the relevant pigment modes and the environmental degrees of freedom. To this end, Born–Oppenheimer molecular dynamics simulations in a quantum mechanics/molecular mechanics (QM/MM) fashion utilizing the density functional based tight binding (DFTB) method have been performed for the ground state dynamics. Subsequently, the time-dependent extension of the long-range-corrected DFTB scheme has been employed for the excited state calculations of the individual chlorophyll-a molecules in the LHCII complex. The analysis of this data resulted in spectral densities showing an astonishing agreement with the

Reprinted with permission from the article by **S. Maity**, V. Daskalakis, M. Elstner and U. Kleinekathöfer, *Multiscale QM/MM Molecular Dynamics Simulations of the Trimeric Major Light-Harvesting Complex II*, Phys. Chem. Chem. Phys. **23**, 7407 (2021). (DOI: 10.1039/D1CP01011E). **As first author I did most of the calculations.**

experimental counterpart in this rather large system. This consistency with an experimental observable also supports the accuracy, robustness, and reliability of the present multi-scale scheme. To the best of our knowledge, this is the first theoretical attempt on this large complex system is ever made to accurately simulate the spectral density. In addition, the resulting spectral densities and site energies were used to determine the exciton transfer rate within a special pigment pair consisting of a chlorophyll-a and a carotenoid molecule which is assumed to play a role in the balance between the light harvesting and quenching modes.

4.1 Introduction

Photosynthesis is one of the key processes for life on earth. Phototrophic organisms capture the sunlight and convert it into chemical energy. Subsequently, this energy is also accessible to heterotrophic organisms such as animals, fungi and many bacteria. In green plants and algae, thylakoid membranes host supramolecular pigment-protein aggregates including the photosystem I (PSI) and II (PSII) complexes together with antenna systems. These antennas in the thylakoid membrane are responsible for the first steps of photosynthesis enabling light harvesting and excitation energy transfer (EET) processes among the pigments at an ultrafast timescale. In plants, chlorophyll-a (Chl-a), b (Chl-b) and carotenoid molecules are the main players primary contributing to light harvesting. Well-orchestrated networks of pigments have the ultimate goal of directing energy in the form of excitons from the antennas to the PSI/PSII reaction centers (RCs) where charge separation takes place [1]. During these energy transfer processes, a pH gradient is built up across the thylakoid membrane, which is also utilized to fine tune the photosynthetic load under fluctuating light intensities in order to reduce potential photochemical damage. Under conditions of excess light, the fastest regulation is triggered by this enhanced trans-thylakoid pH gradient. The latter is part of a process termed non-photochemical quenching (NPQ) of higher plants [11, 36, 37, 221]. The self-regulation of light harvesting within the thylakoid membranes is very important for the organism since the PSII complex is highly susceptible to photodamage under excess light conditions [222, 223]. This self-regulation occurs on the molecular level by aggregation and allosteric regulation of the major light-harvesting complex (LHCII) attached to the PSII

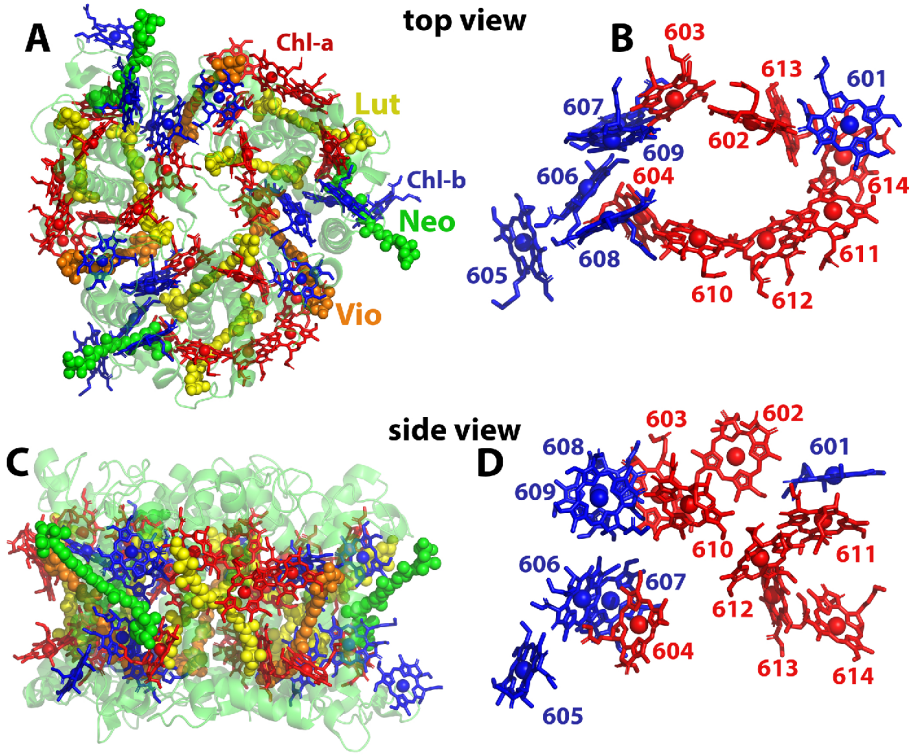

Figure 4.1: Structure of the major LHCII trimer. A) top view of the LHCII trimer in green cartoon representation. The protein is shown transparently for visualization purposes while the Chl-a molecules are shown in red, the Chl-b molecules in blue and the three different types of carotenoids in yellow, green, and orange. B) The chlorophylls of one monomeric unit are shown separately. C, D) Side views corresponding to panels A and B.

system [11, 224, 225]. The antenna complexes of PSII mainly consist of LHCII trimers (see Fig. 4.1) with each monomer binding fourteen chlorophyll molecules (eight Chl-a, six Chl-b) and four carotenoid molecules namely two luteins (Lut), one neoxanthin (Neo), and one violaxanthin Vio) [46]. The Chl-b molecules are present in the periphery of the antenna complexes. Their auxiliary role is to harvest blue-shifted sunlight and transfer it to the Chl-a pool [226,227]. The sunlight excites the Chl-a molecules mainly into their lowest singlet excited state (termed S1 or Q_y), prior to being transferred/spread among the pigments, mainly of the same kind, with a quantum efficiency close to one [228]. In this study, the focus is on the light harvesting mode of the LHCII trimer, in which the Chl-a molecules play a key role and the carotenoids are mainly responsible for its regulation [11]. Experiments carried out by Novoderezhkin et al. [229, 229] identified fast relaxation rates between the strongly coupled 606-607 and 608-609 Chl-b dimers, as well as the Chl-a 602-603, 613-614 pairs and the 610-611-612 triples. Further investigations by Schlau-Cohen et al. [230] have indicated that Chl-a 612 and Chl-a 610 are the most red-shifted pigments in LHCII which act as terminal emitter sites

towards the RC. Geometrically, Chl-a 612 is closest to the reaction center but in the measurements Chl-a 610 is found to have the lowest site energy [229, 230] while exciton and not site energies do matter at the end. Müh et al. [231, 232] suggested that within LHCII, the three Chl-a molecules 610-611-612 constitute a potential energy sink and that the Chl-a 610 pigment has the lowest site energy at cryogenic temperatures. Finally, from this emitter domain, the excitonic energy is mainly directed to the minor antenna, i.e., the CP29 complex, the core of the PSII, and to the RCs [233]. Furthermore, Müh et al. [231, 232] found that the pigments Chl-a 602, 603, 604, and 613 may contribute to the red edge of the absorption spectrum of the LHCII complex and that especially Chl-a 604 can act as a bottleneck for the energy transfer with its site energy being strongly influenced by the protein environment. These partially conflicting findings suggest that in order to understand the energy transfer process in the LHCII complex properly, the Chl-a pool needs to be analyzed in more detail and an accurate description of the ground and excited state electronic structures of the Chl-a molecules becomes a necessity.

In experiment, often two-dimensional electronic spectroscopy is used to study LH complexes [19]. To calculate the excitation energy transfer dynamics among the pigments, one needs to use the concept of open quantum systems either fully quantum mechanically or within a mixed quantum-classical description [58]. Two different types of approaches are often employed, i.e., either a density matrix or an ensemble-averaged wave-packet formalism [59, 80, 234]. For the former, the spectral density is a key ingredient and combined with the time-averaged Hamiltonian this quantity is employed to propagate the density matrix of the system. For the latter case, a time-dependent Hamiltonian is constructed consisting of the excitation energies and excitonic coupling values based on which an ensemble-averaged wave packet dynamics can be performed. The latter approach usually involves more approximations leading to problems in reaching the proper thermal equilibrium in case of Ehrenfest dynamics or by including dephasing in case of surface hopping. A wealth of different density matrix approaches exists with the hierarchy equation of motion (HEOM) approach being one of the more popular ones in the field of exciton transfer in LH complexes [80, 81, 204, 235, 236]. This scheme has the advantage that it can be converged with respect to the system-bath coupling strength. It assumes that the spectral density can be written as a form of Lorentzian functions while numerically it can be quite expensive [81, 82].

One way to obtain some of the necessary ingredients for these quantum dynamics schemes are classical molecular dynamics (MD) simulations followed by excitation energy calculations along the trajectories [26, 27, 59, 62, 63, 237]. In such a scheme, often the ZINDO/S-CIS (Zerner's Intermediate Neglect of Differential Orbital method with spectroscopic parameters together with the configuration interaction using single excitation) approach or variants of the time-dependent density functional theory (TDDFT) were applied to obtain the excitation energies along a trajectory in a quantum mechanics/molecular mechanics (QM/MM) fashion. In recent benchmark studies it became clear that the description of the excitation energy fluctuations along trajectories are more accurate using (long range-corrected) TDDFT theories than the semi-empirical ZINDO/S-CIS approach [59, 197]. One should keep in mind that the TDDFT approaches suffer from an overestimation of the absolute excitation energies but for the excitation energy transfer dynamics only relative energies are of importance.

Apart from the exciton dynamics on a femtosecond to picosecond time scale, also the excitonic lifetimes on the nanosecond time scale are of interest. This need is especially high for LH complexes of plants since within that time regime the pH value on the lumenal side of the thylakoid membrane can be shifted to trigger the photoprotection in the antenna systems. In order to calculate the lifetimes of the excited states, the Förster rate constant of the excitation transfer can be determined based on Fermi's golden rule where the site energy, spectral density and excitonic coupling values are necessary input parameters [225, 238]. Hence, a similar multi-scale strategy based on an MD simulation followed by an excited state analysis within a mixed approach can be utilized to describe the excitonic lifetimes.

Although mixed quantum-classical approaches on top of a classical MD trajectory can provide a reasonable description of the system, these scheme encounter the so-called "geometry mismatch" problem arising due to the inconsistency of the force-field based coordinates and the electronic structure calculations [62, 239, 240]. This mismatch in geometry generates artifacts in the spectral density and thus can subsequently affect the exciton dynamics as well as the transfer rates to some extent. Another manifestation of the same problem is that the representation of the internal vibrational modes of the pigments in classical MD schemes is limited by the accuracy of the employed force fields. To overcome these problems, Rhee and co-workers have proposed to propagate the sys-

tem on a pre-determined quantum mechanical potential energy surface (PES) for the ground state and calculated the excitation energies based on the respective pre-determined interpolated excited state PES [184]. Furthermore, Coker and co-workers suggested an alternative formalism to accurately describe the intra-molecular part of spectral densities [67]. Although, both approaches provide an impressive agreement between the theoretical and experimental spectral densities taking into account the size of the studied system, they suffer from high numerical costs required to construct the PES [207] or to determine the normal mode analysis while calculating the intra-molecular contribution at a high level of accuracy [200]. A reliable ground state QM/MM MD dynamics followed by excitation calculations using a high level QM method would be an ideal choice to accurately describe the dynamics of the energy gap for pigment molecules. However, because of the size of the pigments in LH systems, it is numerically challenging to perform state of the art QM/MM MD simulations based on DFT [204] or even semi-empirical methods [203]. In this direction, our recent protocol based on the density functional tight-binding (DFTB) level of theory [68] is a numerically affordable alternative to perform an accurate ground state dynamics followed by excited state calculations for the relatively large pigment molecules [197, 241]. Based on this strategy, in the present contribution we report on a DFTB-QM/MM MD ground state dynamics for the Chl-a molecules in connection with a classical description of the environment based on the OPLS force field. Subsequently, the time-dependent long-range-corrected extension of DFTB (TD-LC-DFTB) [69] has been applied again in a QM/MM setting along those QM/MM MD trajectories to determine the energy gap fluctuation of each pigment. We found that the average spectral densities calculated using this scheme show a remarkable agreement compared with the results of fluorescence line narrowing (FLN) experiments of the LHCII complex. The accurate description of the major peaks clearly demonstrates the power of the DFTB-based QM/MM MD for the biologically relevant LH complexes. Finally, the spectral densities and the site energies averaged on a nanosecond timescale have been utilized to determine the excitation transfer rate within the Chl-a 612/Lut-1 pair based on our previously reported excitonic couplings for the low and neutral lumenal pH states of the LHCII complex [225].

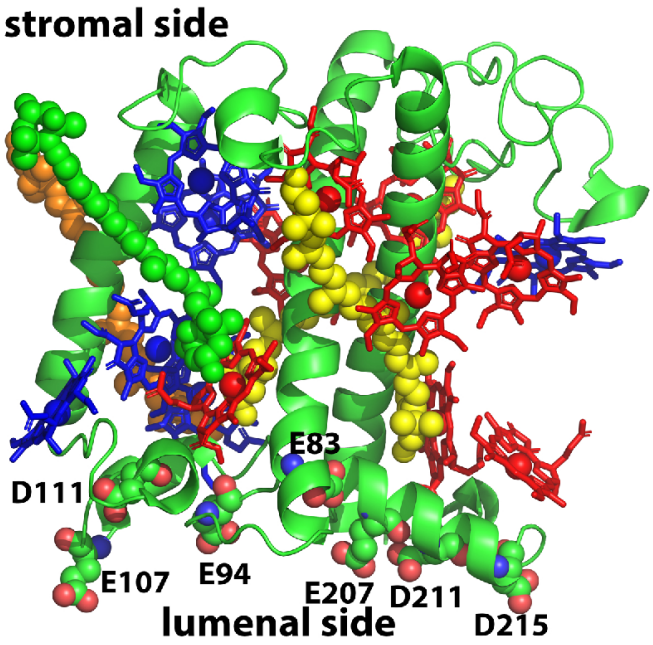

Figure 4.2: Lumen exposed residues in one monomer unit of the LHCII complex which have been protonated or deprotonated to mimic the two different lumenal pH states.

4.2 Computational Method

As starting structure, the solvated trimeric LHCII complex (pdb code 1RWT, chains C, E, H) was modeled with roughly 221k atoms and equilibrated under low (pH $\sim$ 5.5) and neutral lumenal pH (pH $\sim$ 7) as described in Ref. 225. The carboxylic groups belonging to side chains of lumen exposed residues in each monomeric unit (GLU E-83, 94, 107, 207 and ASP D-111, 211, 215) have been treated as protonated (-COOH) or deprotonated (-COO^-) to mimic the low and neutral lumenal pH state of the system, respectively. These titratable polypeptide residues have been predicted in experiment [39, 242, 243], modeled using the PDB2PQR server with the PROPKA approach [225, 244] and are highlighted in Fig. 4.2 in van der Waals representation. For each pH state, three simulations were performed to obtain a reasonable sampling of the available phase space for converged spectral densities based on the QM/MM ground state dynamics. The initial structures for these sets have been extracted in an equally spaced manner from 1.5 μs long classical MD simulations for both pH states as reported in Ref. 225. As the crystal structure conformation of the LHCII complex refers to the quenched state [36, 245, 246], the system built at low lumenal pH is assumed to be trapped in conformations close to the crystal geometry during the unbiased simulations. In case of the QM/MM ground state dynamics as well as the excitation energy calculations, the phytyl tail of the Chl-a molecule under investigation was truncated at the C1-C2 bond and

capped by an H atom. Subsequently, the truncated Chl-a molecule has been considered as the QM region in the QM/MM calculations. The third-order version of DFTB with the 3OB-f parameter set (DFTB3/3OB-f) has been employed to perform the ground state dynamics combined with the OPLS force field for the classical description of the environment. The 3OB-f is a variant of the standard 3OB set with an optimized description of the vibrational frequencies which especially improves the C=C, C=O and C=N stretching modes within the DFTB framework [70, 71]. This enhancement has already shown to yield very reasonable results for the spectral densities in the bacterial Fenna-Matthews-Olson (FMO) complex [241]. For each pigment, a 60 ps NPT simulation with a 0.5 fs time step was carried out at 300 K using the GROMACS/DFTB+ interface [134, 197, 247]. Snapshots were stored for the last 40 ps of the dynamics with a stride of 1 fs. This scheme produces 40,000 frames per pigment which then served as input coordinates for the excitation energy calculations in the subsequent step. Thus, for both low and neutral pH, a total of $2\times24\times40{,}000$ frames were generated for the 24 Chl-a pigments in the LHCII trimer since the current DFTB/MM implementation can only handle one QM region at a time. The same number of frames were also produced for the other two sets of initial coordinates out of the 1.5 μs trajectories. Moreover, we have extended the first set of simulations up to 1.1 ns with a 1 fs time step. For the last 1 ns the snapshots were stored every 1 ps. This scheme produced another 1,000 frames for each of the 2×24 QM/MM MD simulations which were then utilized to determine the average excitation energies on a nanosecond timescale.

The excitation energies along the ground state trajectories were calculated with the help of the DFTB+ code in which the time-dependent extension of long-range corrected DFTB method is implemented with the OB2 parameter set (TD-LC-DFTB/OB2) [69, 247, 248]. Furthermore, during the excitation energy calculations, the QM region has been shifted towards the center of the simulation box with the MM region being moved accordingly which is possible due to the periodic boundary condition. This kind of treatment is necessary to avoid artificial boundary effects in the non-periodic QM/MM excited state calculations [77, 78]. The computational costs for the ground state QM/MM MD and the excited QM/MM calculations were similar to those of our previous study for a bacterial system [241] while numerically being cheaper than DFT-based approaches with similar accuracy [197]. After performing the TD-LC-DFTB calculations, the energies of the first excited state have been extracted along the QM/MM MD trajectories.

This first excited state, i.e., the Q_y state, plays a major role in the light absorption as well as in the energy transfer among the Chl molecules. In a last step, the autocorrelation functions of the excitation energies are determined followed by a calculation of the spectral densities as described in the following section.

4.3 Results and Discussion

4.3.1 Site Energy Calculations

To be able to perform the exciton dynamics within LH systems, usually a tight-binding Hamiltonian H_S of the system is constructed [58, 249]. Generally, the Hamiltonian has the following generic form

$$H_S = \sum_m E_m \left|m\right\rangle \left\langle m\right| + \sum_{n \neq m} V_{mn} \left|n\right\rangle \left\langle m\right| \tag{4.1}$$

where E_m denotes the excitation energy gap of pigment m which is also called the site energy and V_{mn} is the excitonic coupling between pigment molecules m and n. Depending on the theory used for the exciton dynamics, the Hamiltonian is either used directly in its time-dependent variant or averaged over time to get a time-averaged Hamiltonian. Moreover, diagonalizing the Hamiltonian yields the excitonic energies and states in a time-dependent or time-averaged fashion. In this study, the site energy for each Chl-a molecule in the LHCII trimer is determined at the TD-LC-DFTB level along the respective QM/MM MD trajectory. The average site energies for the first set of the 40 ps and the 1 ns QM/MM MD trajectories are shown in Fig. 4.3 for the low and neutral lumenal pH states. No significant differences in the site energies of the individual pigments can be observed for the two different pH states which is not completely surprising due to the quite similar electrostatic environment at the two different pH values. Moreover, the average excitation energies of the Chl-a molecules based on TD-LC-DFTB are in the same range as those from TDDFT calculations determined using the CAM-B3LYP functional [250, 251]. This finding is consistent with our recent benchmark study where we have shown that the TD-LC-DFTB approach is an accurate alternative for the calculation of excitation energies in natural LH systems. Long-range corrected (LC) and hybrid functionals (CAM-B3LYP, ωB97X, LC-BLYP, B3LYP etc.) within TDDFT theory can obtain reasonable results for the excited state calculations nec-

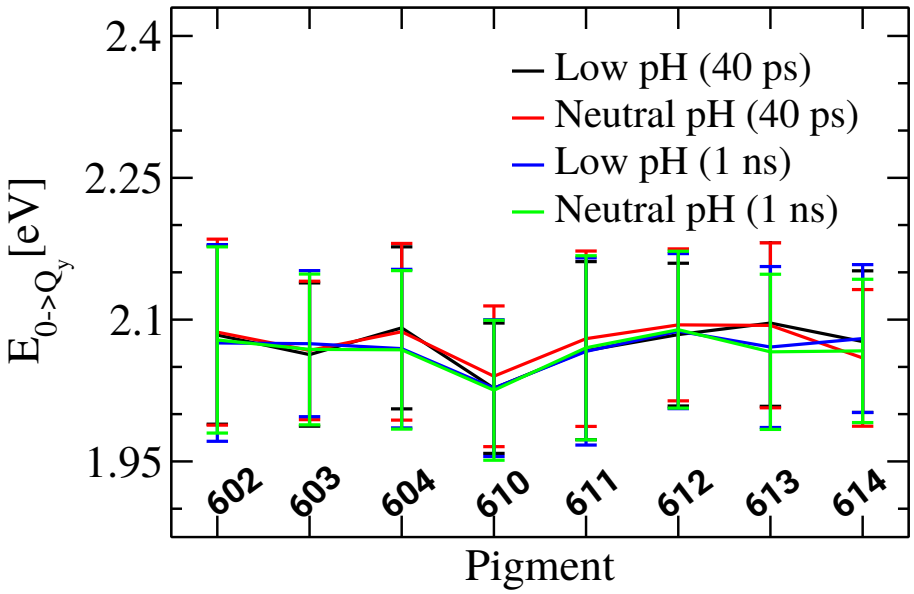

Figure 4.3: Average site energies and associated standard deviations for the Chl-a pigments in the LHCII complex based on QM/MM MD trajectories and subsequent TD-LC-DFTB excited state calculations. The results for the first set of the 40 ps and the 1 ns QM/MM MD trajectories at both pH values are depicted. For each pigment the site energy is averaged over the equivalent molecules in the three monomer units.

essary in the present study. However, they are numerically quite expensive when performed along trajectories [197]. In other investigations, the semi-empirical ZINDO/S-CIS method has been employed along classical MD trajectories for the LHCII complex leading to site energy values close to the experimental ones [252]. Although, the ZINDO/S-CIS approach is numerically very efficient and results in average site energies of Chl and BChl molecules that are rather accurate due to its parametrization for this molecule class, the fluctuations and the influence of environmental charges are less well represented [197, 241]. This inadequacy of the ZINDO/S-CIS scheme is likely due to its parametrization for equilibrium conformations but not out-of-equilibrium ones [253, 254]. The corresponding site energy distributions of the eight pigments are of Gaussian shape as shown in Figs. S1 and S2. The shapes of the distributions look quite similar for the individual monomers though not identical which shows that the sampling of the individual monomers is not yet perfect. Looking again at the average site energies in Fig. 4.3 and comparing the results of averaging over the 40 ps and the 1 ns dynamics, a small but clearly visible difference can be observed for some Chl-a molecules. The 1 ns QM/MM MD simulation is assumed to be sufficiently long for a proper sampling of the relevant conformations and gives some insight into the energy ladder of the LHCII complex. Despite the small differences, for all trajectories the pigment

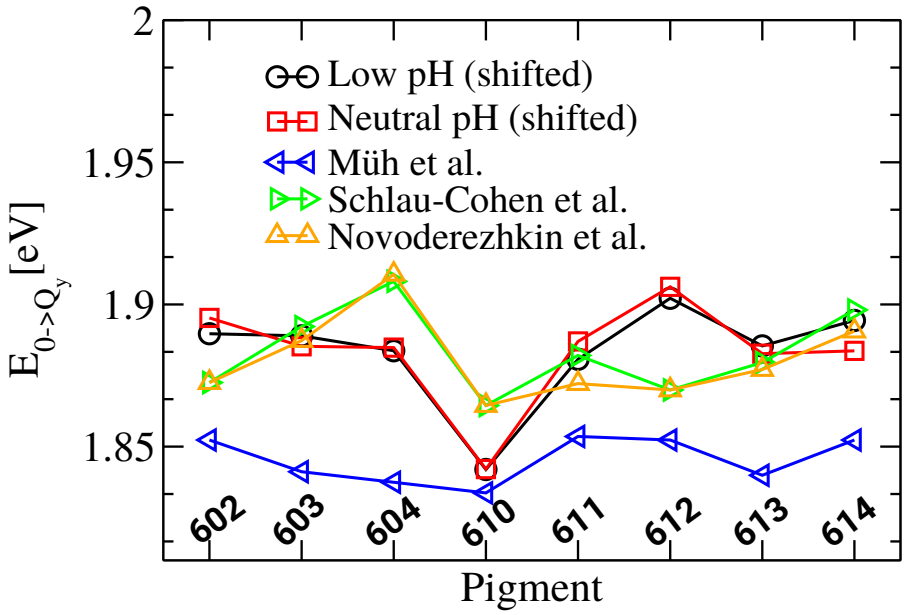

Figure 4.4: Average site energies based on the 1 ns QM/MM MD simulations at both pH states compared to the results by Müh et al. [232], by Schlau-Cohen et al. [230] and Novoderezhkin et al. [229]. The present results have been shifted towards the experimental measurements by Schlau-Cohen et al. [230].

Chl-a 610 has the lowest average site energy in the Chl-a pool while one has to clearly state that the differences in the site energies are smaller than the respective standard deviations. Moreover, one needs to take into account the good but limited accuracy of DFTB but also other electronic structure theories, a fact which should not be forgotten when interpreting the small energy differences found in the present study. At any rate, the fact that the differences between the average energies are smaller than the standard deviations clearly shows that there is only a very weak energy funnel which drives the excitation energy in a certain direction.

The present outcome shows that Chl-a 610 has the lowest average site energy in agreement with experimental [229,230] and theoretical findings [232,251]. In Fig. 4.4 a comparison between the present average site energies based on the 1 ns QM/MM MD trajectories and site energies from some earlier studies are shown. Since DFT-based approaches are well-known to overestimate excitation energies, we have shifted our energies in such a way that the average over the eight site energies agrees with the respective average of the experimental measurements by Schlau-Cohen et al. [230]. This shift does not affect the dynamics among the Chl molecules but is important when looking at the transfer to a lutein molecule below for which the site energy is taken from experiment. All experiment-based site energies have been determined indirectly since they cannot be measured but

exciton energies can be estimated from spectroscopic signals. For the determination of site energies the excitonic couplings were either assuming dipole-dipole coupling [229,230] or the Poisson-TrESP scheme (transition charges from electrostatic potentials) [232]. Though pigment 610 has the lowest energies in all shown results, the variations among the various site energies are significantly smaller in the results by Müh et al. [232]. At the same time, Müh et al. [231, 232] suggested based on their calculations that Chl-a 610 has the lowest site energy at low temperatures and that the triplet Chl-a 610-611-612 should be considered as the terminal emitter of LHCII. Structurally, Chl-a 610 is a special pigment coordinated to a native (structurally resolved) thylakoid lipid and not to a protein residue. Therefore, one can expect that its site energy is able to fluctuate substantially during the dynamics.

4.3.2 Spectral Density

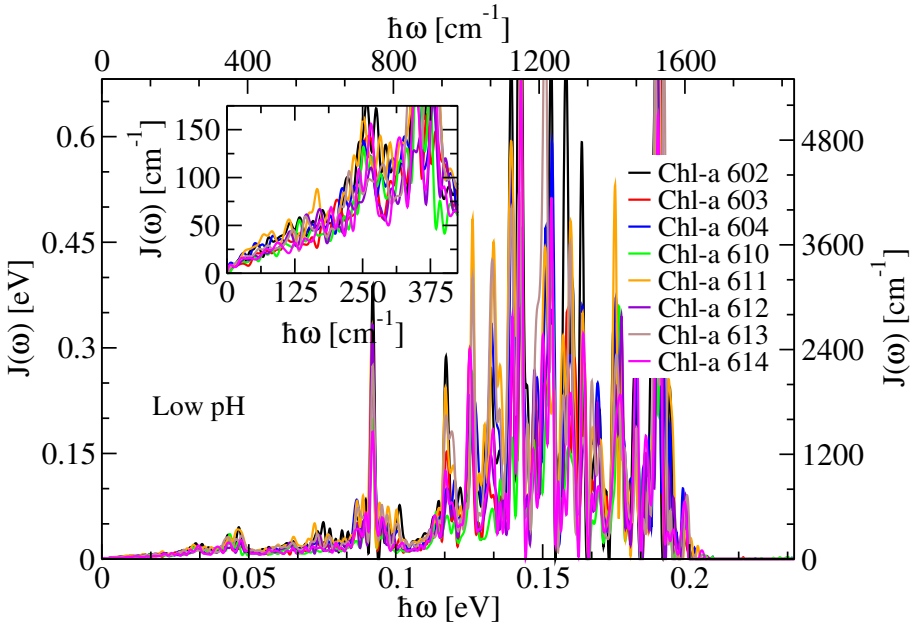

Figure 4.5: Spectral densities for the individual Chl-a pigments in the LHCII trimer in the low lumenal pH state based on first set of 40 ps QM/MM MD trajectory. The inset shows the low-frequency region. The spectral densities have been averaged over the equivalent chromophores in the three monomers.

In the context of theory of open quantum systems, the bath-induced spectral density is one of the key features for studying the exciton dynamics in LH complexes [58]. The spectral density describes the frequency-dependent coupling of selected modes of the pigment with environmental modes which also include modes of the system which do not belong to the primary system. There are various methods to obtain this quantity using different theoretical or experimental

techniques. In this study we have employed a well-established technique which has been applied earlier to bacterial and algae LH complexes. In this formalism, a cosine transformation of the site-energy autocorrelation function decorated with a thermal factor is performed to determine the spectral density of each pigment molecule [59, 60, 127, 214, 240, 241]. To this end, the spectral density of pigment m can be written as

$$J_m(\omega) = \frac{\beta\omega}{\pi} \int_0^\infty dt C_m(t) \cos(\omega t) \tag{4.2}$$

where $\beta = 1/k_B T$ denotes the inverse temperature. For consistency we use the prefactor $\beta\omega/\pi$ which corresponds to the high-temperature limit of the quantum prefactor $2\tanh(\beta\hbar\omega/2)/(\pi\hbar)$ since we employ a classical correlation function. Using the latter factor might lead to a spurious temperature-dependence of the spectral density [77, 79]. The site-energy autocorrelation function $C_m(t)$ can be determined from a time series of the energy gaps as

$$C_m(t_l) = \frac{1}{N-l} \sum_{k=1}^{N-l} \Delta E_m(t_l + t_k) \Delta E_m(t_k) \ . \tag{4.3}$$

In this expression E_m denotes the site energy, i.e., the energy difference between the Q_y and the ground state while $\Delta E_m = E_m - \langle E_m \rangle$ refers to the difference from its average. Moreover, we have employed the same windowing technique as well as zero padding as described in our recent study to compute the final autocorrelation functions and from them the corresponding spectral densities [241]. Here, the autocorrelation functions and the associated spectral densities have been extracted for a total of 24 Chl-a molecules for the LHCII trimer complex based on TD-LC-DFTB calculations along three sets of QM/MM MD trajectories (see Fig. S3). The spectral densities averaged over the equivalent pigments in the three monomers based on first set of 40 ps QM/MM MD trajectory are shown in Fig. 4.5 for the low lumenal pH state. The spectral densities computed at neutral lumenal pH have similar shapes like the ones at low lumenal pH (see Fig. S4 for a comparison). Moreover, in order to see if the different pH states have an effect on the reorganization energies for the individual pigments

$$\lambda_m = \int_0^\infty \frac{J_m(\omega)}{\omega} d\omega \tag{4.4}$$

we have listed them in Table. S1. Some differences can be observed but their

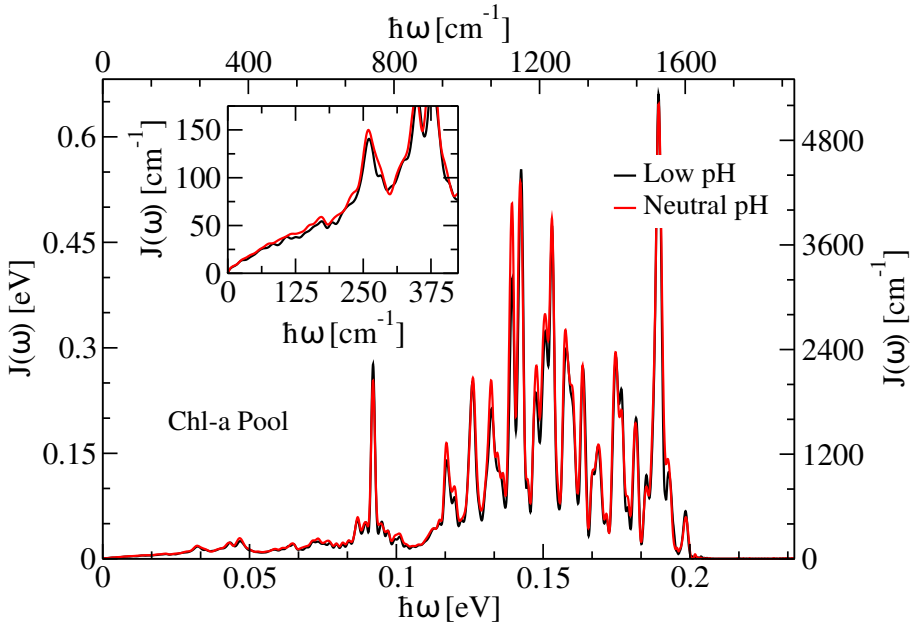

Figure 4.6: Spectral densities averaged over all 24 Chl-a molecules in the LHCII trimer at low and neutral lumenal pH states based on three sets of QM/MM MD trajectories. The inset shows the low-frequency region.

significance and origins need a more detailed analysis.

As can be seen in Fig. 4.5, the major peaks of the spectral densities are in the range between 1030 and 1550 cm^{-1} which mainly represent collective intramolecular vibrational modes which include C=C, C=O and C=N bond stretching [241]. The fastest oscillation periods in the corresponding autocorrelation function are in the range of about 22 to 32 fs as shown in the Fig. S3. This is in line with our previous findings for the BChl pigments in the FMO complex [241]. However, the intensities of the spectral densities for the Chl molecules is somewhat higher than those of the BChl pigments. This is likely due to the structural difference in the two Mg-porphyrin-based molecules. Additional studies are necessary to compare the spectral densities of plant and bacterial LH complexes in more detail. Although all computed LHCII spectral densities have their major peaks in the same frequency range, their peak heights differ substantially among the various Chl-a molecules. Since sampling issues were observed already in the spectral density calculations based on QM/MM MD trajectories for the FMO complex [241], three sets of QM/MM MD simulations were performed from where the autocorrelation functions and the associated spectral densities were determined. The comparison of the spectral densities based on these three sets of QM/MM MD trajectories is given in the Fig. S3 for both pH values. From this figure, one can see that the intensities and positions of some major peaks are different in the three sets of QM/MM MD trajectories. Although, the calculated spectral densities for in-

dividual Chl-a have been averaged over the three monomers, a moderate sampling issue still can be observed. The average spectral density over all pigments in the Chl-a pool is assumed to be converged when comparing the results for the three sets of QM/MM dynamics. This finding suggests that the sampling issue can be eliminated by averaging over longer time series and/or more simulations. One has to keep in mind that at the beginning of a dynamical simulation usually not all modes are excited to the same extent and thus these modes appear with different intensity in the cosine transform until the sampling is good enough. Here, we would like to point out that this issue was not observed, at least not to the present degree, for the spectral densities based on classical MD trajectories. In the latter case, the amount of sampling needed for a proper reproducibility was smaller which might indicate a faster energy redistribution among the modes in classical MD simulations [77, 241]. In the final steps, we have averaged the spectral densities from the three sets of QM/MM MD trajectories over all pigments within the Chl-a pool. This procedure has been performed for both pH values and the results are displayed in Fig. 4.6. Only small differences between the average spectral densities can be seen. This outcome is not very surprising since the residues in the local neighborhoods of the pigment molecules exert subtle changes between the different pH states shown in our previous work [225]. Anyhow, the environment would only influence the low-frequency part of the spectral densities while the medium to high-frequency portion of the spectral density is governed by internal modes. At the same time, the reproducibility of the spectral density from different initial coordinates for the two pH states is reassuring highlighting the robustness of the employed scheme for the determination of the spectral densities.

Considering the robustness of our results, it is of course interesting to see how accurate they are. To this end, we turn to the experimentally determined spectral density for the LHCII complex [218]. This spectral density $J^{exp}(\omega)$ was modeled using a combination of Drude and Lorentzian functions using the following expression [218, 255]

$$J^{exp}(\omega) = \frac{2\hbar}{\pi}\lambda\gamma\frac{\omega}{(\omega^2+\gamma^2)} + \frac{2\hbar}{\pi}\sum_k s_k\omega_k^3\frac{\omega\gamma_k}{(\omega_k^2-\omega^2)^2+\omega^2\gamma_k^2}\,. \tag{4.5}$$

The first part of this expression has been designed to mainly describe the low frequency modes due to the electrostatic coupling to the environment. It has been modeled as an over-damped Brownian oscillator. The second part of the expres-

sion for $J^{exp}(\omega)$ is given by a sum over Lorentzian functions based on a modeling of the high-frequency modes as under-damped Brownian oscillators [255]. The exciton-phonon and exciton-vibrational coupling parameters , i.e., λ, γ , s_k, and ω_k, have been determined based on fluorescence line narrowing (FLN) measurements and are listed in Tables 1 and 2 of Ref. 218. The same frequencies of vibrational modes have also been reported in Ref. 255 for the complete PSII supercomplex (not only LHCII) with slightly different peak intensities and/or widths. In the expression for the experimental spectral density, the width parameter γ_k has a more or less arbitrary value controlling the broadening of the respective peaks in the high frequency region. Here, we have set its value to $\hbar\gamma_k = 7$ cm^{-1} in order to obtain peak intensities comparable to those of our computed average spectral density. In Ref. 218, this parameter was assumed to be 3 cm^{-1} whereas based on the parameters in Ref. 255, it is usually considered in theoretical modeling studies to be 10 cm^{-1} [82, 256]. See Fig. S5 for a comparison of the computed spectral density with these two experimental ones. The fluorescence line narrowing experiments were performed for the LHCII complexes including both Chl-a and Chl-b pigments. Thus, the results could be influenced by the presence of the Chl-b molecules to some extent but because of the large structural similarity of the two pigment types one can assume that the spectral densities for both slightly different chromophores are very similar [255]. The comparison between the experimental and calculated spectral densities is given in Fig. 4.7. Since the crystal structure of the LHCII complex refers to a quenched state [36, 245, 246], we use the spectral density calculated at the low lumenal pH state for this comparison. Fig. 4.7 reveals an outstanding agreement between the simulated spectral density and the respective experimental one in low and especially in the high-frequency region. The positions and intensities of most peaks display a remarkable similarity between the two variants. In the low frequency region the experimental spectral density shows more individual peaks while the theoretical counterpart shows less well separated peaks. More work on this part is needed likely from both the computational and the experimental part. For theoretical studies of the exciton transfer dynamics and spectroscopic properties, so far the experimental spectral density of the LHCII complex was utilized as input parameter [82,218,251,255–258]. Thus, to the best of our knowledge, the present study is the first attempt in which accurate spectral densities for the LHCII complex have been determined based on fully atomistic modeling. Moreover, the overall accuracy, reliability and robustness of the method

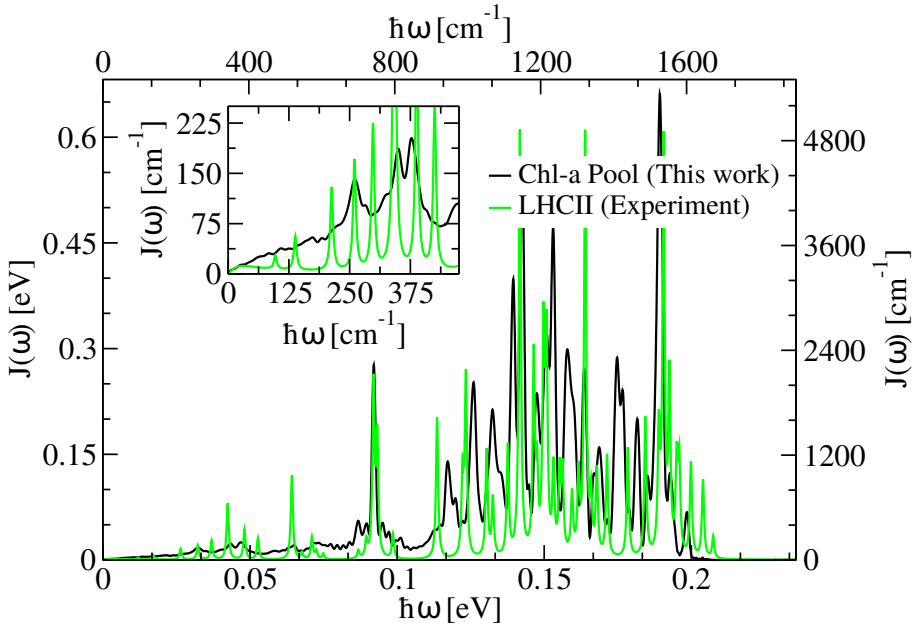

Figure 4.7: Comparison between the computed spectral density averaged over the Chl-a pool with the experimentally determined one based on fluorescence line narrowing (FLN) experiments of the LHCII complex [218]. The inset allows for a closer look at the low-frequency region.

applied here can be seen as a motivation for future investigations of this and similar biologically relevant LH complexes. To this end, we have employed the present results to calculate the exciton transfer rate between the pigment pair Chl-a 612 and Lut-1 (620) in order to give some insight into the experimentally observed pH-dependent regulation of the LHCII complex.

4.4 Excitation Energy Transfer Rate between Chl-a 612 and Lut-1

The LHCII complex is the major player in the NPQ mechanism in higher plants [11,36,37,221]. It has been found that the excitonic lifetime of the LHCII complex shifts from the nanosecond to the picosecond time scale when an enhanced pH gradient is built up across the thylakoid membrane. In this process, it is speculated that the pigment pair Chl-a 612 and Lut-1 (see Fig. 4.8) is a key player in the NPQ mechanism by releasing excess solar energy as heat [245]. NPQ is assumed to rely on the excitation energy transfer between these two pigments, while in a recent study a model involving a charge-transfer state was proposed as well [260]. In the excitonic model, the rate of the energy being transferred between the two pigments can be calculated using the Förster transfer rate $k_{m\to n}$ within the weak

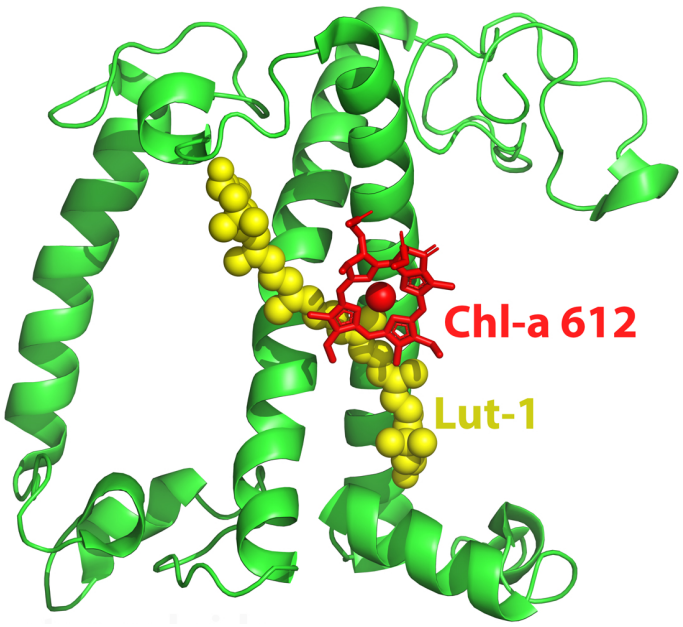

Figure 4.8: Structural arrangement of the pigments Chl-a 612 and Lut-1 in one monomeric subunit of the LHCII complex.

inter-pigment coupling limit as [238, 255, 259, 261]

$$k_{m\to n} = \frac{2}{\hbar^2}|V_{mn}|^2 \,\mathrm{Re}\int_0^\infty F_m^*(t)A_n(t)dt \tag{4.6}$$

where V_{mn} denotes the excitonic coupling between pigments m and n. The donor fluorescence F_m and the acceptor absorption A_n response functions in the time domain can be written as [238, 255, 259, 261]

$$F_m(t) = \exp\left[-i\Big(\frac{E_m - 2\lambda_m}{\hbar}\Big)t - g_m^*(t)\right] \tag{4.7}$$

and

$$A_n(t) = \exp\left[-i\Big(\frac{E_n}{\hbar}\Big)t - g_n(t)\right] \tag{4.8}$$

where E_m and E_n denote the site energies of the respective donor m and the acceptor n pigments. The reorganization energy λ_m and the line-shape function $g_{m/n}$ can be directly calculated from the spectral density $J(\omega)$ as given in the Eq. 4.4 and in the following expression

$$g_{m/n}(t) = \int_0^\infty \frac{d\omega}{\hbar\omega^2} J_{m/n}(\omega)\left[(1-\cos(\omega t))\coth\left(\frac{\hbar\omega}{2k_BT}\right) + i(\sin(\omega t) - \omega t)\right] \tag{4.9}$$

From the above expressions, it is clear that the site energies, excitonic coupling and the spectral densities are the main inputs to calculate the transfer rate and

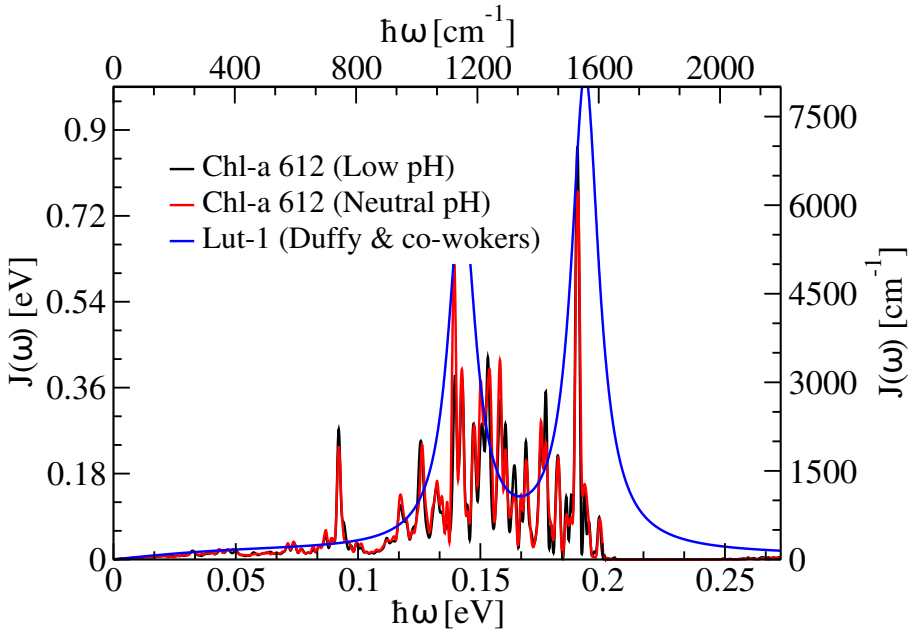

Figure 4.9: Spectral density of Chl-a 612 as computed in this study together with its counterpart for Lut-1 modeled from the parameters of Duffy and co-workers [259].

its inverse, i.e., the transfer time. However, the spectral density of the Lut-1 carotenoid cannot easily be determined within the DFT framework because of the failure of the DFT functionals to correctly describe the order of the exited states which include double excitation [151, 262]. Although in some recent studies, DFT-based calculations were employed to explain the color tuning phenomena of carotenoids [260, 263, 264], we refrain here from using a DFT scheme for the calculation of carotenoid energies before having performed a proper benchmarking study. Since multi-configurational methods are numerically too expensive to be performed along trajectories for carotenoids, here we use a model of the spectral density of Lut-1 based on experimental findings. The functional form is the same as in Eq. 4.5 but now the parameters were taken from a study by Duffy and co-workers. In that work, the two-photon absorption spectrum of the carotenoid's S_1 state [265] was fitted in order to obtain the reported values [225, 238, 259]. Fig. 4.9 depicts the spectral density of Lut-1 together with that of the pigment Chl-a 612 pigment from the present study. The spectral density of Lut-1 looks quite reasonable when compared to the computed Chl-a one although by far not as detailed. The main peaks are, however, at very similar frequencies even with comparable amplitudes. This finding is probably due to the fact that both molecules contain C=C bonds in their chromophoric parts. Moreover, the site energy of the dark S_1 state of Lut-1 is also taken from a fitting result of the two-photon absorption spectrum to be 14000 cm^{-1} [225, 265] by Duffy and co-workers [225, 238, 259].

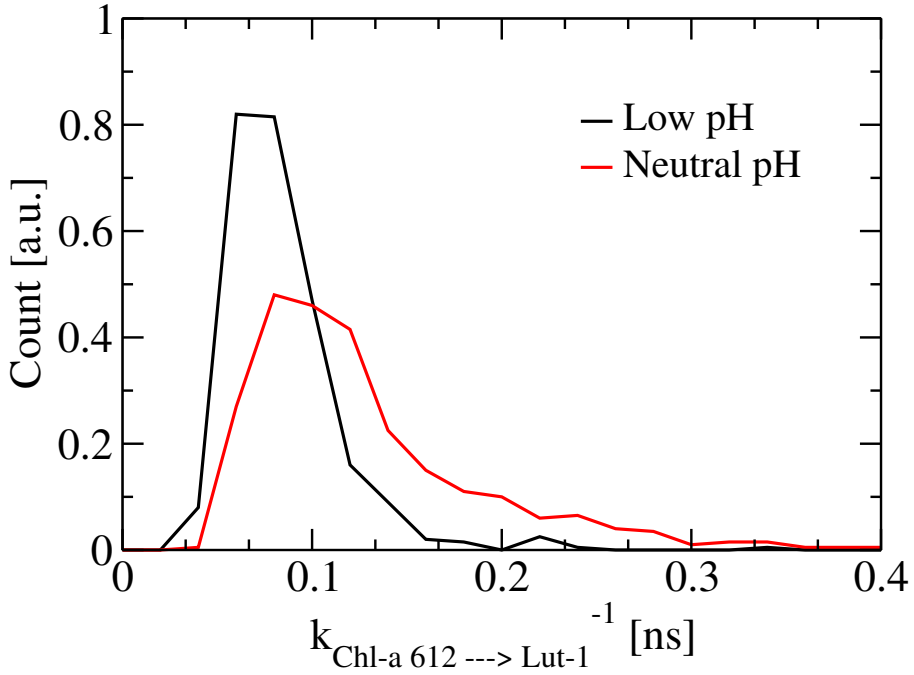

Figure 4.10: Inverse excitation energy transfer rate between the pigments Chl-a 612 and Lut-1 based on the scaled TrESP couplings extracted from Ref. 225 as well as the spectral densities and site energies for Chl-a 612 determined in this study.

For the Chl-a 612 pigment, we have utilized the shifted average site energies as 15342 cm^{-1} and 15374 cm^{-1} at low and neutral pH values based on the TD-LC-DFTB calculations along the 1 ns-long QM/MM MD trajectory as shown in the Fig. 4.4.

Concerning the excitonic coupling values between the components of this special pigment pair, we have extracted the data from our previous work where the TrESP (transition charge from electrostatic potential) [73, 151] method based on RASSCF transition charges [266] was applied to 500 ns-long unbiased trajectories at both pH states [225]. Moreover, a constant screening factor of 0.69 has been employed in the present study to capture the environmental effects on the excitonic couplings [75]. Since the crystal structure of the LHCII complex is quenched, the equilibrium dynamics for the neutral pH was performed starting from a selected free energy minimum as described in Ref. 225. Subsequently, based on those couplings, the spectral densities and site energies as detailed above, the excitation energy transfer rates and the corresponding transfer times between the Chl-a and Lut-1 molecules have been calculated together with the respective distribution shown in Fig. 4.10. The differences in the transfer times are consistent with the pH-dependent change in the coupling since the NPQ regulation mainly depends on the conformational changes of the protein which can directly affect the long-chain carotenoid Lut-1 and subsequently the coupling values but not the

rest of the parameters. Differences in the transfer rates for the two pH states are clearly visible. At the same time, these changes are most likely not large enough to explain the NPQ phenomenon in total. In order to explain this phenomenon in more detail, longer simulations might be necessary to be able to find a significant change in the coupling values between both pH states (see Fig. S6 for the coupling distribution). Moreover, a combination of EET and charge transfer mechanisms within the Chl-a/Lut-1 pair might explain the onset of the NPQ mechanism as shown by Mennucci and co-workers [260]. Nevertheless, the present study helps to reduce the uncertainty in one of the input parameters, i.e., the spectral density of the involved Chl-a molecule.

4.5 Conclusions

The LHCII complex balances between the light-harvesting and the photoprotective mode. In this complex, the Chl-a molecules are the major players in the energy transfer process while the carotenoids are regulators of photoprotection besides some additional light-harvesting roles. To be able to numerically determine the exciton dynamics in these processes, the bath-induced spectral density serves as a key input within the theory of open quantum systems [58]. In order to calculate this quantity, one approach is to perform classical MD simulations followed by semi-empirical ZINDO/S-CIS or TDDFT excited state calculations. This procedure, however, is known to produce artifacts because of the poor quality ground state coordinates and dynamics. DFT-based QM/MM MD for the ground state are numerically quite expensive [204] while our recent protocol using the DFTB framework is an efficient alternative to deal with systems of the size of pigments or even larger [241]. Thus, we have performed DFTB-based QM/MM MD simulations in combination with the OPLS force field for the ground state of all Chl-a molecules in the LHCII trimer. Subsequently, TD-LC-DFTB calculations along those trajectories also in a QM/MM setting have been carried out to obtain the excitation energy fluctuations which are then utilized to determined the respective spectral densities. The results obtained with this procedure have revealed a remarkable agreement with experimental findings. Almost all major peak positions and amplitudes agree astonishingly well between theory and experiment, which clearly shows the power of the DFTB method towards the modeling of biologically LH complexes. Moreover, the present approach also has been found to be robust by

reproducing the spectral densities from different starting geometries and at low and neutral lumenal pH values. Furthermore, we determined the energy ladder of the Chl-a pool which is important for studying the exciton transfer process from a sufficiently long QM/MM MD trajectory. The pigment Chl-a 610 has been found to possess the lowest site energy agreeing with previous experimental [229,230] and theoretical measurements [231,232,251] for the same LH complex. At first sight, this outcome seems to be contrast with the structural orientation of the LHCII complex from which one would assume the Chl-612 to be the terminal emitter contributing lowest site energy during the energy transfer process for the Chl-a pool. At the same time, previous theoretical studies by Müh et al. [231, 232] suggest that Chl-a 610 can also be seen as the terminal emitter at cryogenic temperature. Moreover, at ambient temperatures the triplet Chl-a 610-611-612 is assumed to act as terminal emitter for the energy transfer process. In addition, the spectral densities and site energies have been utilized to calculate the excitation transfer rate within a pair consisting of a Chl-a 612 and a Lut-1 which is one of the key components for the allosteric regulation of the NPQ mechanism [225,245]. The trend in the rates at different pH states is consistent with our previous work [225]. The present work, however, improves the previous estimate by employing the newly determined Chl-a spectral density.

In summary, we have applied a state-of-the-art QM/MM MD technique to the LHCII complex which produces accurate results in terms of the obtained spectral density which is a key component in modeling all kind of quantum dynamical processes. So far, the experimental spectral density was mainly used to explain excitonic processes including the allosteric regulation of the LHCII complex. This is due to the numerical challenges in obtaining accurate descriptions of the spectral density, which make the numerical determination of spectral densities for large biological LH complexes still computational demanding . In this direction, the present study is the first theoretical approach where an accurate description of the spectral density is obtained for the LHCII complex. Moreover, the resulting site energies and spectral densities have also been employed to formulate a kinetic model of NPQ that involves the Chl-a 612/Lut-1 pair. This also opens the way for considering other Chl-a/carotenoid pairs in the LHCII complex.

The present study has given a hint which accuracy might be reachable in the future in modeling light-harvesting complexes of higher plants. These simulations are especially complex since one has to deal with large non-periodic complexes at

least partially on a quantum mechanical level. At the same time, these complexes are rather floppy and proper sampling needs to be added as well. In the present study, for example, about 5.8 million TD-LC-DFTB calculations have been performed. In the future the assembly of several protein-pigment aggregates might shed more light on the cooperative effects and how the whole machinery works together [267] as has been shown for a bacterial system recently [23].

Acknowledgments

We thank Dr. Taxiarchis Stergiannakos of Cyprus University of Technology for setting up part of the initial LHCII structures. The latter was funded through the European Regional Development Fund and the Republic of Cyprus through the Research and Innovation Foundation (Project: POST-DOC/0916/0049). The authors acknowledge support by the DFG through the joint grant EL 206/18-1 and KL-1299/18-1 as well as the DFG-Research Training groups 2247 “Quantum Mechanical Materials Modelling” and 2450 “Tailored Scale-Bridging Approaches to Computational Nanoscience”.

Supporting Information

Supporting information for this chapter are given in **Appendix C**.

Chapter 5

Time-Dependent Atomistic Simulations of the CP29 Light-Harvesting Complex

Light harvesting as the first step in photosynthesis is of prime importance for life on earth. For a theoretical description of photochemical processes during light harvesting, spectral densities are key quantities. They serve as input functions for modeling the excitation energy transfer dynamics and spectroscopic properties. Herein, a recently developed procedure is applied to determine the spectral densities of the pigments in the minor antenna complex CP29 of photosystem II which has recently gained attention because of its active role in non-photochemical quenching processes in higher plants. To this end, the density functional based tight binding (DFTB) method has been employed to enable simulation of the ground state dynamics in a quantum-mechanics/molecular mechanics (QM/MM) scheme for each chlorophyll pigment. Subsequently, the time-dependent extension of the long-range corrected DFTB approach has been used to obtain the excitation energy fluctuations along the ground-state trajectories also in a QM/MM setting. From these results the spectral densities have been determined and compared for different force fields and to spectral densities from other light-harvesting complexes. In addition, time- and time-independent excitonic Hamiltonians of the system have been constructed and applied to the determination of absorption spectra as well

Reprinted with permission from the article by **S. Maity**, P. Sarngadharan, V. Daskalakis and U. Kleinekathöfer, *Time-dependent Atomistic Simulations of the CP29 Light-Harvesting Complex*, J. Chem. Phys. **155**, 055103 (2021). (DOI: 10.1063/5.0053259). Copyright (2021) American Institute of Physics. **As first author I did most of the calculations.**

as exciton dynamics.

5.1 Introduction

Chlorophylls (Chl), bacterio-chlorophylls (BChl) and carotenoids (Car) are the key pigment molecules involved in excitation energy transfer (EET) processes in light-harvesting (LH) complexes of plants and bacteria. Actively involved are mainly the low-lying excited states of these pigment molecules. Aim of these processes is to transport the energy absorbed from the sunlight to reaction centers where charge separation takes place as one of the steps of photosynthesis [1]. In the last two decades, the interest in some LH complexes of bacteria and marine algae has been spurred due to the claim of experimentally observed long-lived quantum coherences in EET processes at low as well as at ambient temperatures [15, 18, 19, 55, 56]. Recently, however it became clear that these long-lived oscillations likely originate from impulsively excited vibrations and are too short-lived to have any functional significance in photosynthetic energy transfer [19, 29, 30].

Independent of these developments, the attention towards plant LH systems has significantly increased in recent years. Especially the topic of photoprotection became a field of growing interest. Under the stress of excess solar energy, LH complexes of plants activate a mechanism termed non-photochemical quenching (NPQ) which can be invoked to avoid photo-inhibition [36–38]. Excess sunlight leads to an enlarged pH gradient across the thylakoid membrane containing the LH complexes of the photosystem II (PSII). An increased pH gradient triggers the switching between the photochemical light harvesting and a non-photochemical quenching mode [221, 268–270]. Moreover, not only the pH gradient but also the presence of a protein termed photosystem II subunit S (PsbS) induces conformational changes in the antenna complexes and thus take part in activating the quenching mechanism [41, 271–273]. The detailed changes in the conformations are, however, still not well understood at the molecular level. The excess sunlight absorbed by the Chl molecules gets released as heat via carotenoid pigments in a mechanism that is a topic of active research [11, 36, 221]. Based on experimental findings, it has been claimed that the major antenna LHCII and the minor antennas, in particular the CP29 complex, play a crucial role in protecting the photosynthetic apparatus of PSII from excess excitation energy [38, 221, 268, 273–275]. At the same time, CP29 acts as a bridge between LHCII and the reaction center core

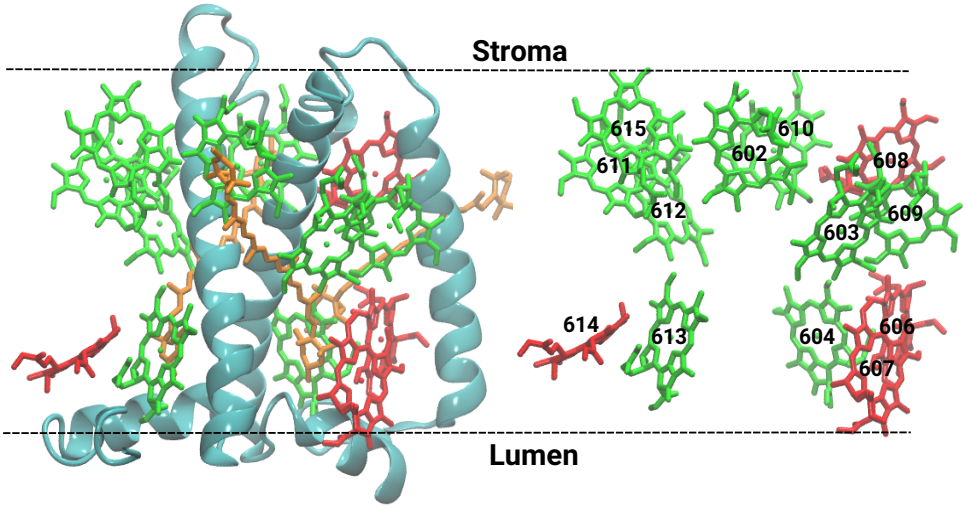

Figure 5.1: The protein part of the CP29 minor antenna complex of spinach represented in an iceblue cartoon representation. The Chl-a and Chl-b molecules are depicted in green and red while the carotenoids Lut, Vio and Neo are shown in orange. In addition, the arrangement of the chlorophylls is displayed in the right panel together with the respective residue numbering according to the crystal structure [47] (pdb code: 3PL9).

of PSII.

In order to study the dynamics of the LH systems of plants, various models were built based on crystal structures of the LHCII [46, 231, 232, 261, 276] and CP29 complexes [47,250,277–280]. Furthermore, additional models were created taking into account the lumenal pH gradient and the presence of PsbS proteins trying to realistically mimic the NPQ process [40, 151, 224, 225, 281]. In these models, either the population transfer of excitons [82,257] or the associated rates were determined [225, 280]. The major input parameters which are required in such calculations are the excitation energies of the individual pigments, also known as site energies, the excitonic couplings between the pigments and the so-called spectral densities. In the present study, the latter quantity is in the focus while also some of the parameters are being determined.

The spectral density is the key ingredient for performing exciton dynamics of LH complexes within the framework of open quantum systems [58]. It accounts for effects of the pigment environment but also internal modes on the energy gap between ground and first excited states. The accurate determination of spectral densities is, however, a challenging task especially for LH systems due to the complexity of these entities and the numerical effort involved. One approach to determine spectral densities which has been employed in several previous investigations [26,59,60,66,76] is to determine the excitation energy gap along a classical MD trajectory using ZINDO/S-CIS (Zerner's Intermediate Neglect of Differential

Orbital method with spectroscopic parameters together with the configuration interaction using single excitation) or TDDFT (time-dependent density functional theory) calculations. This approach, however, has problems especially in the high frequency region of the respective spectral densities [67, 241]. The shortcoming is due the inability of classical force fields to accurately described the vibrational modes of the pigments as well as to provide a proper sampling of the geometrical phase space. Inaccuracies in the ground state conformations and dynamics are subsequently passed on to the determination of the energy gap fluctuations. The inconsistency in geometry between the ground and excited state is commonly known as "geometry mismatch" problem [62]. Some recent methods to determine the intramolecular vibrational modes accurately are based on normal mode analyses [67, 206] or ground state dynamics on pre-calculated quantum mechanical potential energy surfaces [184, 207] and have been employed in calculations of spectral densities. In spite of providing impressive agreements compared to experimental results, these aforementioned schemes are computationally still demanding [200, 207]. A sophisticated quantum-mechanics/molecular mechanics (QM/MM) MD with an accurate description of the vibrational properties of the pigments would be an alternative way, however, semi-empirical schemes have a limited accuracy [203] while DFT-based calculations are numerically expensive for pigments in LH systems [204]. To this end, we recently proposed a scheme using QM/MM MD dynamics employing the numerically efficient density functional based tight binding (DFTB) approach [68] and have shown to be able to obtain a good agreement between the spectral densities obtained in such a manner and their experimental counterparts [241, 282].

In this study, we have applied a recently developed multiscale protocol to determine the spectral densities of the individual pigments within the minor antenna complex CP29 of the PSII system. The CP29 complex contains a total of thirteen chlorophyll molecules including nine Chl-a and four Chl-b. In addition, three different types of carotenoids, i.e., lutein (Lut), violaxanthin (Vio) and neoxanthin (Neo) are present in this antenna complex (see Fig 5.1). The Chl-b chromophores in the periphery of the protein matrix act as accessory pigments transferring the absorbed light energy towards the pool of Chl-a molecules quite rapidly since the excited states of the latter pigments are slightly lower in energy. From the Chl-a molecules, the energy obtained during light harvesting is moved on to the PSII reaction center. While the carotenoids are speculated to participate in the quenching

process, here the aim is to accurately determine the spectral densities for the key pigments, i.e., the chlorophyll molecules in the CP29 complex. To this end, the AMBER force field has been employed in connection with the DFTB approach in a QM/MM framework. Details of the computational scheme can be found in the following method section. The spectral density profiles obtained in the present calculations show a very good agreement with the experimental counterparts in line with our previous work for other LH systems [241, 282]. Furthermore, the impact of the choice of the classical force field in the QM/MM setting has been investigated by redoing the calculations using the OPLS force field in connection with the DFTB method. Only very small differences can be seen in the spectral density profiles when using the two different force fields within the QM/MM framework. This finding indicates that both force fields are suitable for the modeling LH complexes. The present study also incorporates a brief comparison of the spectral densities of the BChl and Chl pigments in different LH systems. Before concluding, we report on time-averaged and time-dependent exciton Hamiltonians and on ensemble-averaged wave-packet dynamics within the Ehrenfest formalism for the exciton transfer in the CP29 complex.

5.2 Computational Method

The X-ray crystal structure of the CP29 antenna complex from spinach (pdb code: 3PL9) [47] has been used as the starting point for the atomistic modeling. The first 87 residues were not resolved in the X-ray structure and neglected in the present study since their influence on the spectral densities is assumed to be small. Furthermore, the glyceraldehyde 3-phosphate (G3P) molecule which was tentatively found in-between Chl-a 611 and 615 was not taken into account during the system preparation. The AMBER03 force field [283] has been employed for the protein using the GROMACS-5.1.4 suite of programs [133] for the simulations. Moreover, the force field parameters for Chl-a/b [217, 284] and carotenoids [285] have been taken from previous studies. First, a POPC lipid membrane was prepared using the CHARMM-GUI server [286], then the topology for the membrane was generated using the LEaP program of AmberTools-20 together with the Lipid-17 force field of AMBER. Thereafter, the topology and coordinates were transformed to the GROMACS format with the help of the ACEPYPE interface [287]. The simulation box size was chosen to be 115 $\times$ 115 $\times$ 90 Å and the system was solvated with

TIP3P water molecules. Furthermore, four potassium ions were added to neutralize the whole system. After preparing the system, an energy minimization was performed using the steepest-descent algorithm to remove close contacts. Subsequently, a 2 ns NVT equilibration was carried out at 300 K with a 1 fs integration time step, keeping position restraints on protein, lipid and cofactor atoms. Subsequently, a 20 ns NPT run was performed using the same time step and position restraints. After that, another 10 ns NPT simulation was run keeping the restraints on protein, pigments and the phosphorous atoms of the lipid molecules. An additional 10 ns NPT run was carried out using a 1 fs time step in which the first 5 ns were performed with restraints on protein and pigments whereas for the last 5 ns the restraints were only on the protein and Chl molecules. Subsequently, in the next 5 ns NPT equilibration, the position restraint was kept only on the protein and the Mg atoms of Chl pigments. Subsequently, yet another 5 ns NPT run was performed using a 2 fs time step in which the position restraints were kept on the protein for the first 2 ns, then for 1 ns on the side chains atoms and 1 ns on the Cα atoms of the protein. Finally, a 50 ns long NPT unbiased simulation was carried out without any position restraints and the coordinates were stored using a 25 ns stride which were subsequently employed as starting structures for the QM/MM MD simulations in the next step. The LINCS algorithm was applied and the constraints were kept on the H-bonds throughout the equilibration process. The equilibrated structure was further equilibrated for another 200 ns where the coordinates were stored at 20 ps. This produces 10,000 frames which were utilized for the excitonic coupling calculations using the TrESP (transition charges from electrostatic potentials) approach [27, 73] in order to construct the system Hamiltonian. A shift in the position of pigment Chl-a 615 was observed after the classical simulations (see Fig. 5.2). Structurally, this pigment is solvent exposed in case of an isolated CP29 crystal structure and thus can more easily move than a pigment embedded in the middle of the protein. A movement by 3.97 Å was found after the 100 ns equilibration whereas after the 200 ns production run the movement was by 7.12 Å. This finding is consistent with the latest cryo-EM structure of the $C_2S_2M_2$ supercomplex [233], in which a different Chl-a 601 was found close to the position where Chl-a 615 was found in the X-ray structure used in the present study [47]. Thus, we assume that the contribution of Chl-a 615 will be similar to that of the Chl-a 601 found in the latter case.

Two sets of QM/MM MD simulations, based on starting geometries extracted

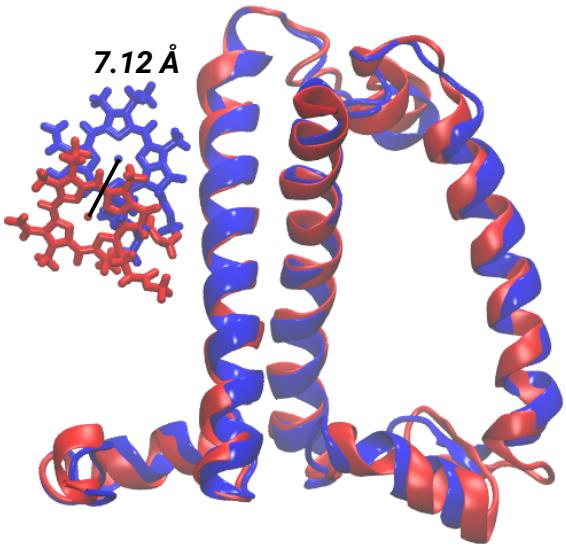

Figure 5.2: Structural shift of the pigment Chl-a 615 after the 300 ns classical unbiased simulation (red) compared to the crystal structure used as starting structure (blue).

at 25 and 50 ns from the unbiased classical simulations, were performed to minimize the sampling problems of spectral densities found earlier for the present kind of simulations [241]. A 80 ps NPT QM/MM dynamics was performed with a 0.5 fs integration time step without any bond constraints for the Chl-a and Chl-b molecules. The phytyl tail was truncated at the so-called "C1-C2" bond and capped by a hydrogen link atom. This truncation is sensible since the tails play no role in the π-conjugated rings but their partial charges potentially influence the Q_y excitation energies of the Chl molecules and thus need to be included in the MM part. Such a treatment significantly reduces the computational costs compared to a full QM treatment of the Chl molecules [197]. The DFTB3 theory [70] with the frequency corrected 3OB parameter set (3OB-f) [71] was employed coupled to an AMBER force field as implemented in the GROMACS-DFTB+ interface for the ground state dynamics [134, 247]. The 3OB-f parameter set was specially designed in connection with the so-called 3OB parameters to describe the vibrational frequencies of C=C, C=N and C=O bond stretching modes more accurately. These modes are very relevant for molecules including porphyrins ring such as Chl pigments. The last 60 ps of each trajectory were stored with a stride of 1 fs. This procedure results in 2 $\times$ 60,000 frames for each Chl molecule using the two different starting structures of the QM/MM MD trajectories. In addition, we extended the first set of the simulations up to 1.1 ns with a 1 fs integration time step and stored the geometries for the last 1 ns dynamics with a stride of 100 fs. Thus, another 10,000 frames were generated which were mainly utilized to calculate the

average site energies of the CP29 complex. Furthermore, the CP29 complex, as modeled using the OPLS force field in a previous study [40], was used as starting structure for QM/MM MD simulations. Again, two different starting structures were considered as the initial geometries for the QM/MM dynamics. This time the starting structure were 10 ns apart in the unbiased trajectories. Again we have stored 2 $\times$ 60,000 frames for each Chl pigment in order to perform the spectral density calculations.

The snapshots collected from the DFTB-QM/MM MD trajectories were utilized to calculate the Q_y excitation energies employing the time-dependent extension of the long-range corrected DFTB (TD-LC-DFTB) in a QM/MM fashion. The LC-DFTB method is the DFTB analogue of the long-range corrected DFT (LC-DFT) approach with functionals like CAM-B3LYP and ωB97X which has lately been developed to overcome problems related to charge transfer and overpolarization in conjugated systems [69]. In recent studies, we have shown that TD-LC-DFTB is a close to ideal alternative to DFT with long-range corrected functionals in order to compute excitation energies and excitonic couplings in a numerically efficient way [197]. To this end, we have employed the DFTB+ package in which the TD-LC-DFTB scheme is implemented based on the OB2 parameter set [69, 247]. Moreover, during the excitation energy calculations the QM region is shifted towards the center of the simulation box to avoid boundary problems during the non-periodic QM/MM calculations. After capturing the excitation energies along the QM/MM trajectories, these were used to determine the autocorrelation functions from which the spectral densities were calculated by performing Fourier transformations as described in below.

The excitonic couplings have been determined based on the 200 ns classical MD simulation. 10,000 snapshots were collected and utilized for the TrESP excitonic coupling calculations as described below. For this purpose, the transition charges for the Chl-a and Chl-b molecules were determined with the help of the Multiwfn [161] and the ORCA [131] packages. Transition charges of these molecules exist [278], but we repeat them here with a long-range corrected functional and a larger basis set. First, a geometry optimization was performed at the B3LYP level of theory together with a def2-TZVP basis set as implemented in the ORCA program. Furthermore, the resolution of identity RIJCOSX was employed together with the auxiliary basis set def2/J in order to speed up the calculations. In a subsequent step, the optimized geometries were utilized to performed ex-

cited state TD-DFT calculation employing the Tamm-Dancoff approximation at the CAM-B3LYP level of theory as implemented in ORCA. The same basis set and the resolution identity were applied again for these calculation. Finally, the transition densities obtained from the TD-DFT calculations were used in the Multiwfn package for the electrostatic fitting. During the fitting procedure, the charges on the hydrogen atoms were set to zero and the transition densities were distributed among the heavier atoms of the Chl-a and Chl-b molecules. The obtained TrESP charges are listed in the SI (see Table S1) and were used in the TrESP calculations for the excitonic couplings. Moreover, we have employed a scaling factor of 0.81 for the Chl-a charges and of 0.83 for the Chl-b charges in order to reproduce the experimental transition dipole moments of 5.7 D and 4.6 D, respectively [167].

5.2.1 Theoretical Background

To be able to determine the exciton dynamics in LH complexes within a tight-binding model, one needs to construct the excitonic system Hamiltonian based on the site energies E_m of the pigments m and the respective couplings V_{nm} [58]

$$H_S = \sum_m E_m \left|m\right\rangle \left\langle m\right| + \sum_{n \neq m} V_{mn} \left|n\right\rangle \left\langle m\right| \ . \tag{5.1}$$

If the site energies and coupling are determined based on (quantum) molecular dynamics trajectories, these quantities are time-dependent. Two main options are available how to determine the exciton dynamics. One option is to perform calculations directly based on these time-dependent Hamiltonians, e. g., some kind of ensemble-averaged Ehrenfest approach (without back-reaction on the bath) [65] sometimes also termed NISE (numerical integration of the Schrödinger equation) [83]. In the present study we refrain from introducing correction factors trying to fix this problem of missing thermalization in these approaches [65, 83]. These problems are not present if one uses proper density matrix approaches. To this end, one averages the elements of the Hamiltonian over time. The site energy fluctuations are then represented by the so-called spectral density. In principle, one can also define spectral densities for the coupling fluctuations but this is very rarely done since the effect of these fluctuations on the dynamics is negligible [220]. On the experimental side, spectral densities corresponding to those based on the excitation energy fluctuations can be obtained using delta fluorescence line narrowing (ΔFLN) spectroscopy. In the present study, we employ a

cosine transformation of the energy autocorrelation functions decorated with a thermal prefactor to determine the spectral density [60, 76, 79]

$$J_m(\omega) = \frac{\beta\omega}{\pi} \int_0^\infty dt\ C_m(t) \cos(\omega t) \tag{5.2}$$

with $\beta = 1/(k_B T)$. The necessary autocorrelation functions for each pigment m can be written as

$$C_m(t_l) = \frac{1}{N-l} \sum_{k=1}^{N-l} \Delta E_m(t_l + t_k) \Delta E_m(t_k)\ . \tag{5.3}$$

Here ΔE_m denotes the difference of site energy E_m from its average value $E_m = E_m - \langle E_m \rangle$ and N the number of snapshots present in the respective part of the trajectory. Moreover, we follow the same procedure as detailed in our previous work [241, 282] to obtain the final correlation functions and spectral densities.

For computing excitonic couplings in LH complexes, the TrESP method has been shown to be accurate for medium and large distances.Once the atomic transition charges of the pigment molecules have been determined, the coupling values can be calculated as

$$V_{mn} = \frac{f}{4\pi\epsilon_0} \sum_{I,J}^{m,n} \frac{q_I^T \cdot q_J^T}{\mid r_m^I - r_n^J \mid}\ , \tag{5.4}$$

where q_I^T and q_J^T denote the transition charges of atoms I and J and f a distance-dependent screen factor which taking environmental influences on the excitonic coupling into account. For this reason, here we have employed a well-established exponential screening factor derived by Scholes et al. [288]

$$f(R_{mn}) = A \exp(-B R_{mn} + f_0)\ . \tag{5.5}$$

In this expression A, B, and f_0 have the values 2.68, 0.27 and 0.54, respectively [288]. We note that this kind of empirical screening factor takes only explicit effects (cavity effect and screening of interaction) into account but not of implicit effects (enhancement of transition dipole moments by environment) [288]. Thus, the chosen screening function is not perfect and one could also consider other empirical screening functions such as distance-independent ones. The effect of choosing other reasonable empirical screening functions should, however, be limited.

5.3 Results and Discussion

5.3.1 Site Energy Calculations

As starting point of the analysis, the average site energies of the thirteen Chl molecules have been determined for the three QM/MM MD trajectories. The structurally very similar Chl-a and Chl-b pigments contain Mg-porphyrin rings which are main responsible for the electronic properties of the respective molecules and especially the excited Q_y state. When the methyl group of a Chl-a porphyrin ring is oxidized to become an aldehyde group, the molecules becomes a Chl-b molecule with a blue shift in the excitation energies (see Fig. S1). Due to the higher Q_y excitation energies of Chl-b molecules, excitation energy from these pigments will, depending on the respective couplings, flow to neighboring Chl-a molecules. The energy is subsequently shared between the Chl-a molecules and transferred further into the direction of lower energies ending up at a reaction center. In the present study, the TD-LC-DFTB approach has been employed as the QM approach to compute the excitation energies for the individual Chl molecules along the QM/MM MD trajectories. As for basically all DFT approaches, the energy gaps are overestimated which in line with our previous observations [197, 241, 282]. In many cases, this does, however, not cause problems since we are mainly interested in the relative site energies. The energy ladder and the corresponding standard deviations due to the thermal fluctuations along the two different 60 ps-long and the one 1 ns-long QM/MM MD trajectories are shown in Fig. 5.3A. The results for the average site energies of the individual pigments are almost identical for the three different trajectories. Although, the 1 ns QM/MM MD trajectory is averaging over a much longer time span than the 60 ps runs, no significant differences are observed. The respective distributions for the site energies which are also known as the densities of states (DOS) are depicted in Figs. S2 and S3. The shape of these distributions is Gaussian, i.e., symmetric, and not skewed as observed in similar calculations using the semi-empirical ZINDO/S-CIS approach [59, 66]. As expected, the average site energies of the Chl-b pigments are higher in energy than the Chl-a molecules although the spectral densities for these two types of molecules are almost identical as shown below. The structural difference between the Chl-a and b molecules has already been mentioned above and, as depicted in Fig. S1, is the only reason behind the blue shifted site energies of Chl-b molecules. Furthermore, the excitation energy fluctuations of the Chl-a molecules are in the

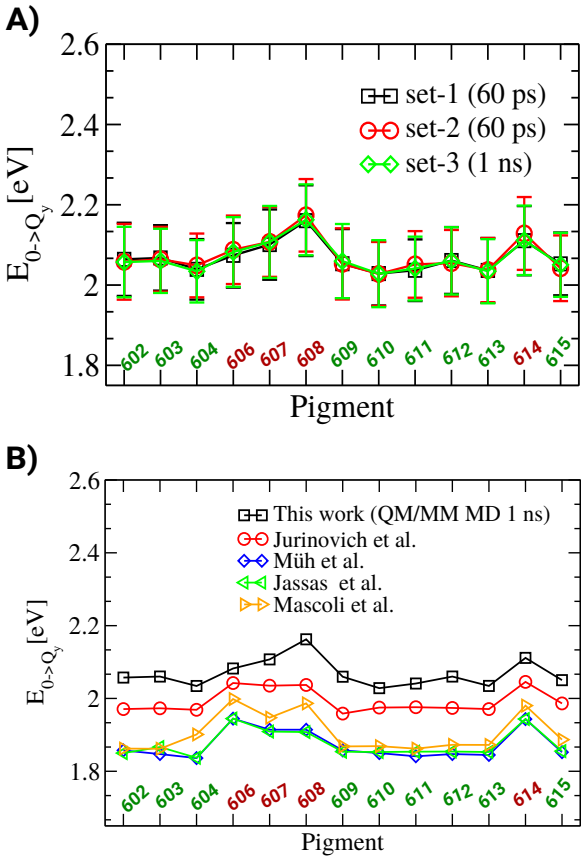

Figure 5.3: A) Average site energies of the Chl molecules in the CP29 complex with the respective error bars indicating the fluctuations along the three different QM/MM MD trajectories. The residues 602, 603, 604, 609, 610, 611,612, 613, and 615 refer to Chl-a molecules (green) while the residues 606, 607, 608, and 614 to are Chl-b molecules (red). B) Comparison with other computed site energies for the CP29 complex by Jurinovich et al. [250], Müh et al. [278], Jassas et al. [289] as well as Mascoli et al. [290].

same range as those found for the same pigment type in the LHCII complex [282]. Moreover, we have compared the calculated site energies with literature results as shown in Fig. 5.3B. In case of the results by the Jurinovich et al. [250], TD-DFT calculations were carried out along classical MD trajectory based on the CAM-B3LYP/6-31G(d) level of theory within a polarizable QM/MM description. Since CAM-B3LYP is a long-range corrected DFT functional, the site energies obtained employing this approach, are quite similar to our TD-LC-DFTB calculations. In case of the calculations by Müh et al. [278], the results are accurately matching the findings by Jassas et al. [289]. This agreement is due to the fact that the TrESP approach was applied in both studies to calculate the excitonic couplings and energies. Subsequently the absorption spectrum was fitted to determine the site energies. However, in case of the results by Mascoli et al. [290], the site energies differ slightly from the former results due to the utilization of the dipole-dipole approximation to determine the excitonic energies and the corresponding

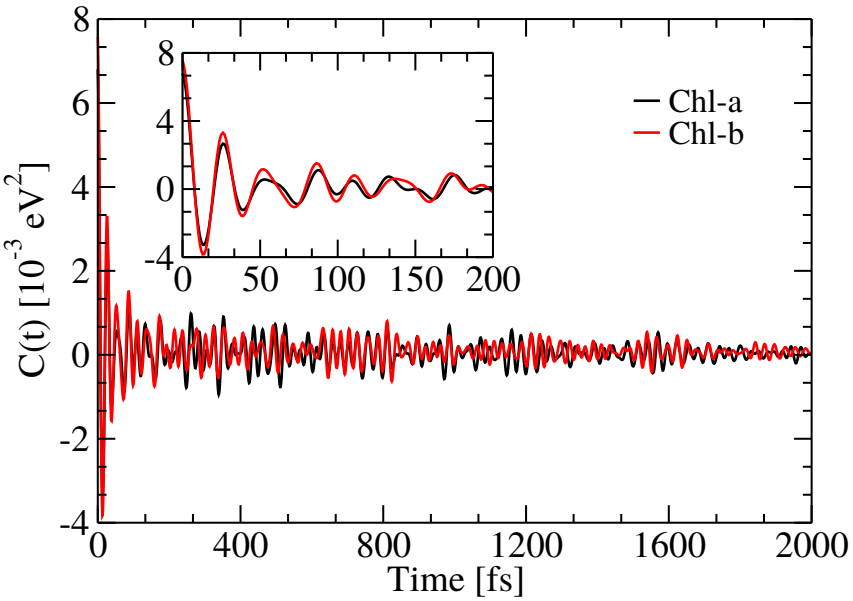

Figure 5.4: Average Chl-a and Chl-b autocorrelation function calculated along the two sets of QM/MM MD trajectories and averaged over the pigments of the same time. The inset highlights the first 200 fs.

spectrum. As mentioned above, the results based on DFT approaches clearly show an overall overestimation of the excitation energy gaps which is also reflected in a shift in site energies compared to the experimental outcomes. For this reason, we introduced a common shift for our site energies towards the experimental values and compared with measurements by Jassas et al. [289] and Mascoli et al. [290]. The shifted energies are depicted in the Fig. S4.

5.3.2 Autocorrelation Functions and Spectral Densities

The primary step of calculating spectral densities from site energy trajectories is to compute the autocorrelation functions of the site energy fluctuations. Here, we have determined the correlation functions for each Chl-a and Chl-b molecule separately. The autocorrelation functions averaged over the two 60 ps-long QM/MM MD trajectories and the nine Chl-a and the four Chl-b molecules, respectively, are depicted in Fig. 5.4. From the figure, it is clear that the Chl-a and Chl-b molecules have very similar correlation functions. This was, however, to be expected because of their very similar structures and fluctuations of site energies. The resulting correlation functions show that the shortest oscillation period is around 22-32 fs which can be attributed to intramolecular collective modes including C=C, C=O and C=N vibrational stretching in the porphyrin rings. This observation is in line with our previous work on different LH systems based on DFTB-QM/MM MD simulations [241, 282]. The associated spectral densities are shown in Fig. 5.5

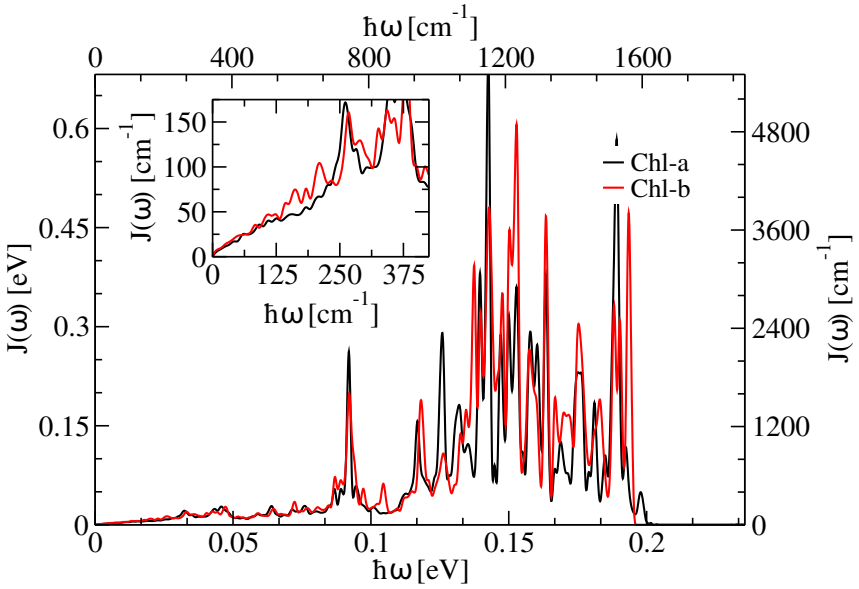

Figure 5.5: Spectral densities based on the autocorrelation functions shown in Fig. 5.4.

for the Chl-a and Chl-b molecules and, as to be expected, also show very similar lineshapes. The spectral densities of the individual Chl molecules are shown in Figs. S5 and S6.

5.3.3 Comparison to Experimental Spectral Densities

In experiment, ΔFLN spectroscopy is used to determine the exciton-phonon and exciton-vibrational coupling of pigment molecules. From the fluorescence profiles, the corresponding frequencies ω are extracted together with the respective Huang-Rhys (HR) factors. In a subsequent step, these HR factors and the frequencies ω are used to construct the spectral densities. Often these spectral densities are given in the form

$$J^{exp}(\omega) = J_0^{exp}(\omega) + J_{vib}^{exp}(\omega) \ , \tag{5.6}$$

where $J_0^{exp}(\omega)$ represents the continuous low frequency component of the spectral density representing the exciton-phonon coupling, i.e., the coupling to the protein and solvent environment. This part is estimated as one over-damped Brownian oscillator. The second part, $J_{vib}^{exp}(\omega)$, describes the high frequency component consisting of more or less separate parts describing intramolecular vibrations of the pigment molecules. Experimentally, in total 48 vibrational frequencies were extracted for the Chl molecules in the entire PSII system [255] or separately for the LHCII complex [218] which are generally described by under-damped Brownian oscillators. The first part of the spectral density can be modeled by a log-normal

expression [216]

$$J_0^{exp}(\omega) = \frac{\hbar\omega S}{\sigma\sqrt{2\pi}} \exp^{-[\ln(\omega/\omega_c)]^2/2\sigma^2} \tag{5.7}$$

where the HR factor S, the cut-off frequency ω_c and the standard deviation σ are given in Fig. 3 of Ref. 216. The second part of the spectral density is specified by a sum of Lorentzian functions given by

$$J_{vib}^{exp}(\omega) = \frac{2\hbar}{\pi} \sum_k s_k \omega_k^3 \frac{\gamma_k \omega}{(\omega_k^2 - \omega^2)^2 + \gamma_k^2 \omega^2} \tag{5.8}$$

where the HR factors s_k and their corresponding frequencies ω_k have been extracted from Table S4 in Ref. 290 for the CP29 complex. Moreover, the broadening factor γ_k has been chosen to be $\hbar\gamma_k = 7$ cm^{-1} (for all k) to obtain intensities of the experimental spectral density peaks similar to those calculated here. This broadening factor γ_k can be chosen freely within certain limits to control the width and intensity of the respective peaks. Moreover, the HR factors utilized for the CP29 complex are the same as for the LHCII complex [218] but scaled by a factor in order to reproduce the fluorescence spectrum [290]. The present procedure of computing spectral densities does not include any broadening factors while the widths of these peaks is determined through the Fourier transformation of the respective autocorrelation functions.

The comparison of the theoretically calculated average spectral density of the CP29 complex with the experimentally determined one are depicted in Fig. 5.6A. Since the average over all pigments washes out some peaks, here we have also compared the experimental results of the entire CP29 complex with the computed one for the individual pigment Chl-a 604 (shown in Fig. 5.6B) which has the lowest site energy in our calculations. In both plots, the simulated spectral density for the CP29 complex shows a remarkable agreement with the experimental results. The major peaks and their amplitudes are matching well as shown in Fig. 5.6. This finding agrees well with our previous studies for the FMO [241] and the LHCII complexes [282]. In the low frequency region, however, the amplitude is moderately overestimated. The reason is not entirely clear but may be due to inaccuracies in the classical point charges in the QM/MM simulations and the finite length of the correlation functions since low frequencies correspond to modes with long periods. Further research in this direction is ongoing.

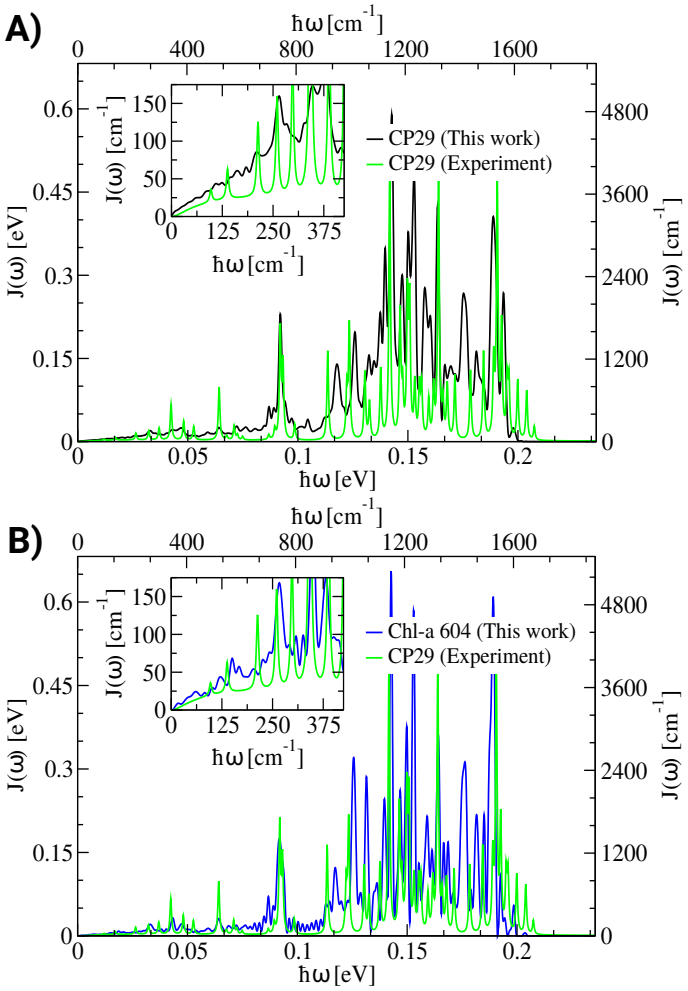

Figure 5.6: A) Average theoretically determined spectral density of the CP29 complex in comparison to the experimental spectral densities of the CP29 [290]. The inset enhances the low frequency region. B) Same as panel A but for the single pigment Chl-a 604.

5.3.4 Impact of the Classical Force Fields on Spectral Density in the QM/MM MD Simulation

The major peaks in the spectral densities lie in the range from 1030 to 1550 cm^{-1} caused by the fastest oscillations in the correlation functions. Here, we would like to point out that in case of spectral densities based on pure classical force fields, the major peaks were located in the region from 1450 to 1800 cm^{-1} as found in previous work on bacterial LH complexes [59, 60, 66, 241]. Furthermore, the spectral densities for Chl molecules based on the semi-empirical PM6 method in a QM/MM MD dynamics showed a shift in the dominant frequencies by about 100 to 130 cm^{-1} compared to the experimental results [203]. The inaccurate positions of the high-amplitude peaks in the spectral densities arise due to poor descriptions of the vibrational features using classical force fields or low-level semi-empirical theories. Using DFTB ground state dynamics together with the 3OB-f parameter

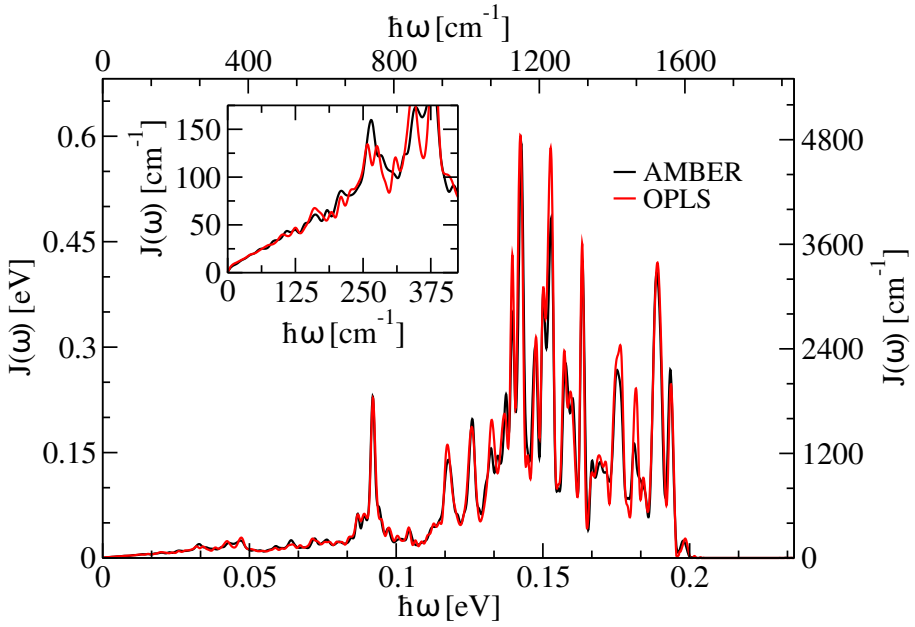

Figure 5.7: Average spectral density of the CP29 complex based on the DFTB approach in combination either with the AMBER or the OPLS force field. The inset highlights the low frequency region.

set, however, leads to a proper description of the most important vibrational frequencies. The choice of the DFTB method rather than DFT approaches becomes necessary due to the high numerical cost of the latter for larger molecules especially when calculating along trajectories. The low frequency part in the spectral densities is due to electrostatic interactions with the environment, i.e., protein as well as water and ions. However, different force field sets follow (partially) unlike parametrization schemes for the partial charges. Since the partial charges are key ingredients in electrostatic QM/MM schemes as employed in the present study, we have analyzed the effect of different force field sets. For the ground state dynamics based only on classical MD simulations a comparison between CHARMM and AMBER-compatible force fields has been performed earlier [78]. Although, quite some differences between the spectral densities were seen in that case one has to keep in mind that the parametrization of the pigment molecules was of large importance. For this reason, in the present case, we have utilized a setup of the CP29 complex pre-equilibrated using the OPLS force field [40] and determined the spectral densities in the same way as for the AMBER force field in a QM/MM fashion. As can be seen in Fig. 5.7, the average spectral density based on the OPLS force field shows an almost identical profile to that one based on the AMBER force field in the QM/MM simulations. The positions of the peaks are at the same for both variants since these basically rely on the QM part, i.e., the DFTB approach only which was the same in both variants. More surprisingly, the contributions in the

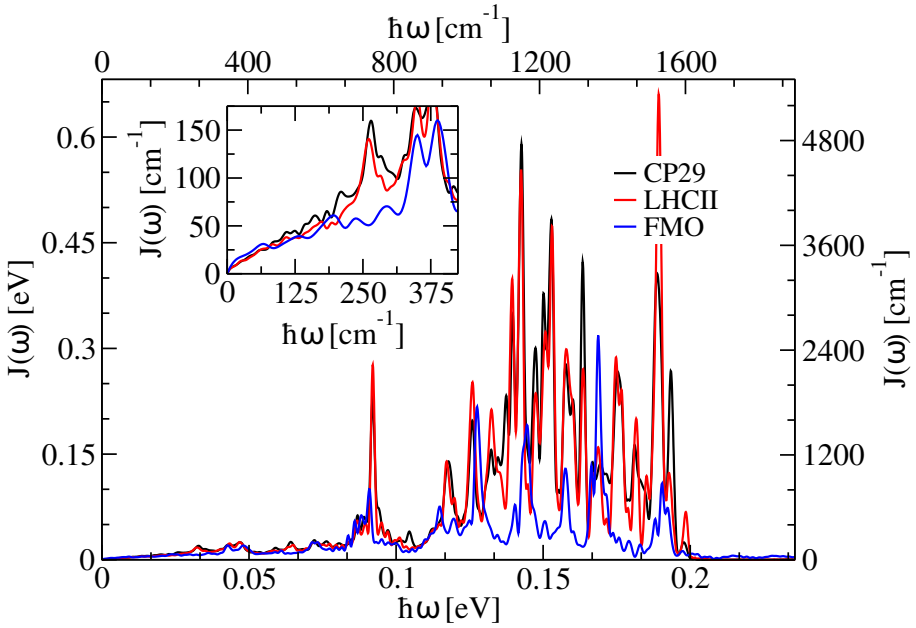

Figure 5.8: Average spectral density of the CP29 complex compared to those from the FMO [241] and the LHCII [282] system.

low frequency part of the spectral density are almost identical although the environment is described by different force fields, i.e., different sets of partial charges. This finding is probably due to the fact that the partial charges in both both force fields are determined by fitting of the electrostatic potentials [291]. The observed similarity between the QM/MM simulations in combination with different force fields suggests that both force fields are equally well suited for the present kind of calculations on LH systems.

5.3.5 Comparison of Spectral Density for other LH Complexes

Furthermore, in order to analyze the accuracy and robustness of our method for LH systems, in Fig. 5.8 we have compared the average spectral density of the CP29 complex with those of the Fenna-Matthews-Olson (FMO) [241] and LHCII [282] complexes obtained using the same QM/MM procedure. In case of the LHCII complex, the Chl-a pool was considered for the whole trimeric complex [282] whereas for FMO, all BChl-a pigments have been taken into account from one monomeric unit of the trimer [241]. As can be seen, the CP29 and LHCII complexes have almost identical average spectral density profiles. This is, however, not too surprising since in both complexes Ch-a and Chl-b are considered which show almost identical spectral densities as described earlier. In case of the bacterial FMO complex, however, the amplitudes of the major peaks are lower compared to those of the plant complexes [241]. This finding is consistent with the fact that the range of

site energy fluctuations is higher for the Chl molecules in the respective complexes than those of the BChl pigments in the FMO protein. Likely, the larger values of the Q_y excitation energies in Chl molecules is one of the fact behind this larger site energy fluctuations in plant LH complexes, however, further investigation is required to understand this observation in more detail. Moreover, the number of major peaks in the FMO complex is less than for the two plant ones which seems to be surprising since the porphyrin ring of the BChl molecules is more flexible having one C=C double bond less than the Chl molecules (see Fig. S1). This computational observation is also underlined by experimental measurements since in case of the FMO complex 62 vibrational peaks were resolved [215] whereas for the plant systems 48 peaks were found [218, 255]. A comparison between the experimental spectral densities of the FMO and CP29 complexes are shown in the Fig. S7. The higher number of vibrational peaks in the experiments suggests that in our calculations, some peaks have probably been washed out during the averaging procedure over all pigments or that some peaks might have merged to form a single peaks with larger width.

5.3.6 Excitonic Coupling and Wave Packet Dynamics

DFTB-QM/MM MD simulations are still computationally expensive when one wants to treat several pigments at a time. Therefore, we have constructed the time-averaged Hamiltonian based on the coupling values calculated from the 200 ns classical MD simulation and the site energies based on the 1 ns QM/MM MD trajectory (see Table. 5.1). As described in the methods section, the excitonic couplings between all Chl pigments of the CP29 complex were calculated using the TrESP approach. A total of 10,000 frames from the 200 ns long classical MD trajectory were employed to calculate the coupling values. The distribution of larger coupling values are represented in Fig. 5.9. Most of the larger coupling values originate from the Chl-a pairs as a consequence of their spatial proximity. In case of the Chl-b chromophores, pigments 606 and 608 are participating in stronger couplings with Chl-b 606 shows the highest coupling value to neighboring pigments. Once the excitonic couplings have been determined, the system Hamiltonian can be established based on Eq. 5.1. This time-independent Hamiltonian together with the spectral densities obtained in the present study can serve as a starting point for future calculations using density matrix approaches.

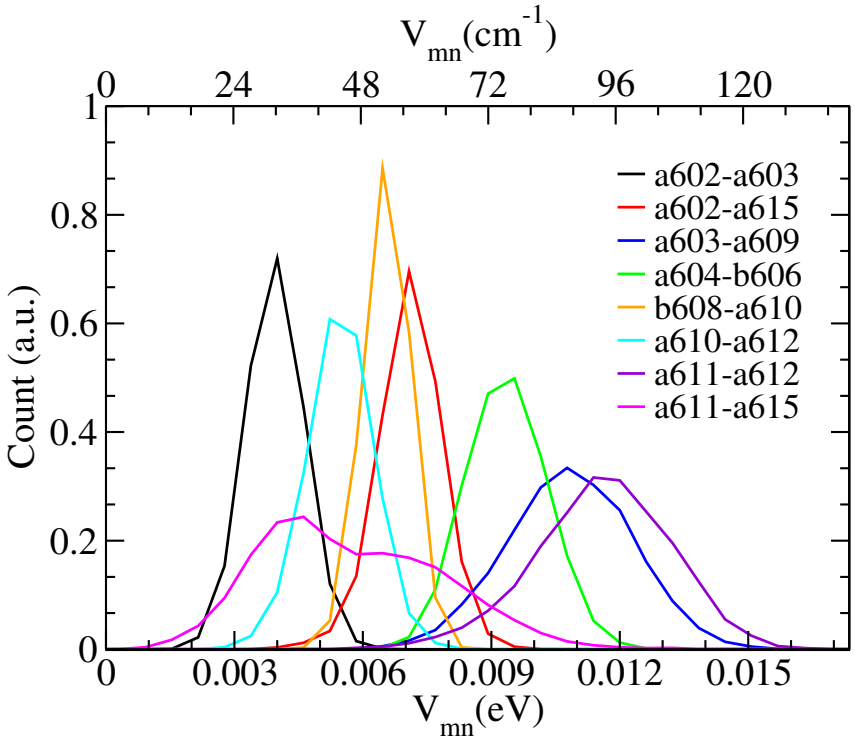

Figure 5.9: Distribution of excitonic coupling values for the pigment pairs whose average absolute values are above 30 cm^{-1}.

Table 5.1: Time-averaged system Hamiltonian of the CP29 complex based on the exciton coupling values along the 200 ns classical MD trajectory and the site energies from the 1 ns QM/MM MD simulation. The site energies and couplings (in cm^{-1}) with absolute values above 30 cm^{-1} are shown in bold.

	a602	a603	a604	b606	b607	b608	a609	a610	a611	a612	a613	b614	a615
a602	**16594**	**29.39**	4.13	3.33	1.68	-3.85	-23.10	-5.62	-1.23	7.15	-1.94	0.58	**54.74**
a603	**29.39**	**16617**	-1.03	-2.97	9.64	2.96	**84.79**	6.35	-0.65	-2.02	0.65	-2.92	-3.57
a604	4.13	-1.03	**16408**	**72.97**	2.37	-2.05	-0.66	-1.54	-1.93	0.75	0.51	-1.95	-2.13
b606	3.33	-2.97	**72.97**	**16796**	1.77	-1.93	5.14	-1.18	-1.50	1.11	0.73	-0.84	-1.33
b607	1.68	9.64	2.37	1.77	**16997**	-2.17	-8.71	1.87	-1.08	0.13	-1.26	-1.75	-0.23
b608	-3.85	2.96	-2.05	-1.93	-2.17	**17442**	22.17	**50.39**	3.48	-1.51	-1.42	0.63	3.00
a609	-23.10	**84.79**	-0.66	5.14	-8.71	22.17	**16612**	-0.92	3.06	-0.25	-2.10	1.28	4.51
a610	-5.62	6.35	-1.54	-1.18	1.87	**50.39**	-0.92	**16360**	-26.80	**41.58**	5.11	-0.12	-2.78
a611	-1.23	-0.65	-1.93	-1.50	-1.08	3.48	3.06	-26.80	**16462**	**90.94**	-4.02	-1.18	**43.95**
a612	7.15	-2.02	0.75	1.11	0.13	-1.51	-0.25	**41.58**	**90.94**	**16617**	-5.94	1.50	-3.73
a613	-1.94	0.65	0.51	0.73	-1.26	-1.42	-2.10	5.11	-4.02	-5.94	**16409**	-7.38	6.33
b614	0.58	-2.92	-1.95	-0.84	-1.75	0.63	1.28	-0.12	-1.18	1.50	-7.38	**17030**	-10.65
a615	**54.74**	-3.57	-2.13	-1.33	-0.23	3.00	4.51	-2.78	**43.95**	-3.73	6.33	-10.65	**16537**

As accurate density matrix calculations are numerically not feasible at present for larger systems with spectral densities as the ones derived here, we have performed ensemble-averaged wave-packet dynamics within the Ehrenfest approach (without back reaction of the thermal bath). We note in passing that work is in progress trying, e.g., by our group, to derive density matrix approaches which can handle numerically obtained spectral densities [292]. For certain parameter regimes, however, the Ehrenfest (NISE) wave packet approach has been shown to yield the same results as accurate density matrix calculations properly representing the dephasing but not the relaxation [65]. In the wave packet-based

scheme, the time-dependent Schrödinger equation needs to be solved for the time-dependent system Hamiltonian

$$i\hbar\frac{\partial|\Psi_S(t)\rangle}{\partial t} = H_S(t)|\Psi_S(t)\rangle \tag{5.9}$$

where $|\Psi_S(t)\rangle$ denotes an excitonic state in the single-exciton manifold. This state can be expanded in terms of time-independent states $|\alpha\rangle$

$$|\Psi_S(t)\rangle = \sum_\alpha c_\alpha(t)\,|\alpha\rangle \tag{5.10}$$

with time-dependent coefficients $c_\alpha(t)$. Moreover, the excitonic states $|\alpha\rangle$ can be written in terms of the site-local states $|m\rangle$ as

$$|\alpha\rangle = \sum_m c_m^\alpha\,|m\rangle\ . \tag{5.11}$$

Combining these equations, the probability density of finding an exciton on an individual pigment site m is given by

$$P_m(t) = |\langle m|\Psi_S(t)\rangle|^2 = |\sum_\alpha c_m^\alpha\ .c_\alpha(t)|^2 \tag{5.12}$$

The dynamics of the probability density $P_m(t)$ shows how an exciton can propagate from pigment to pigment and spread at the same time. To obtain a meaningful exciton transfer dynamics, the solution of the time-dependent Schrödinger equation needs to be repeated many times form different starting point along the trajectory to obtain ensemble-averaged results.

In case of the CP29 complex, we have taken the average coupling values calculated from the 200 ns classical MD simulation together with the site energies obtained from the first set of the 60 ps QM/MM MD trajectories to propagate the wave packet dynamics. This leads to a realistic time-dependent Hamiltonian for the 60 ps trajectory since the coupling fluctuations hardly impact the exciton propagation as shown in earlier studies [220, 241]. Furthermore, for the averaging procedure we have assumed that the temporal site energy fluctuations are basically uncorrelated after 500 fs (see also Fig. 5.3). Thus, every 500 fs a new starting point in the trajectory is used for the averaging procedure using a sliding window technique. Since CP29 mainly acts as a bridge between LHCII and the core complex and since we do not include any source or drain terms, the dynamics

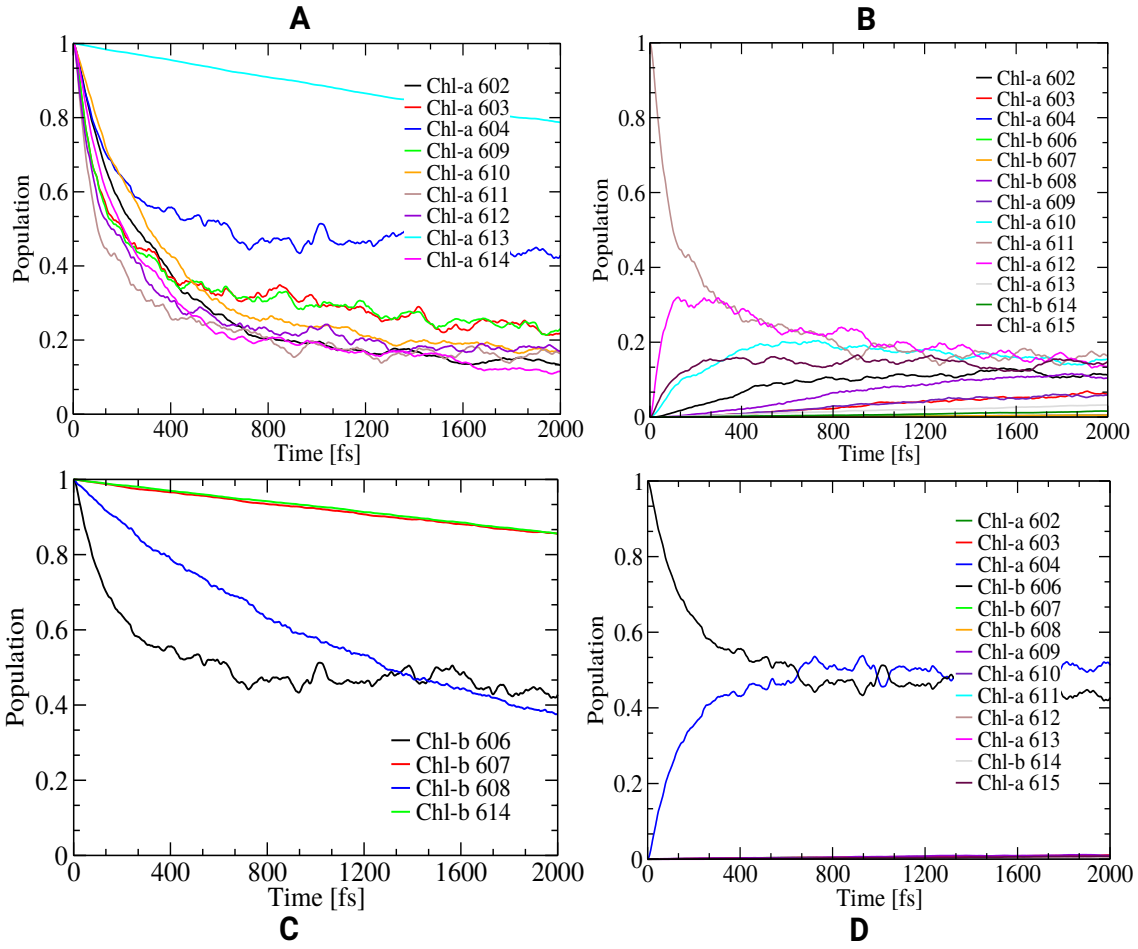

Figure 5.10: A) Decay of the exciton population from different initially excited Chl-a pigments. B) Population transfer from an initially excited Chl-a 611 pigment to the other pigment molecules inside the CP29 complex. C) Same as panel A but for the Chl-b pigments. D) Same as panel B but for the initially excited Chl-b 606 pigment.

here is limited to the exciton propagation within the complex. In our calculations, we initially excite a single pigment and then monitor the propagation of the exciton wave function towards the other pigments inside the CP29 complex. Each of the 13 Chl pigments was excited individually and the exciton distributions were captured for each case. To this end, Fig. 5.10A shows the decay of an excitation from individually excited Chl-a pigments. The pigment Chl-a 611 shows the fastest decay since it has the largest excitonic coupling values to its neighbors whereas for Chl-a 613 the decay is very slow because of its weak interpigment couplings. In Fig. 5.10B we show the case of Chl-a 611 separately including the populations of the other chlorophylls to which the excitation energy is transferred. The population leaves pigment Chl-a 611 exponentially fast and moves to neighboring pigments within a few 100 fs. Since Chl-a 612 is strongly coupled to Chl-a 611, its population gain is very fast within the first 400 fs before the excitation energy is transferred further. At this point one has to keep in mind that due to the implicit

high-temperature approximation in the Ehrenfest approach, the scheme will not lead to a proper thermodynamic equilibrium state but rather to an equal population of all sites. Moreover, it should be mentioned that the population curves become smoother within increasing the number of samples in the averaging procedure which is limited here due to the finite length of the QM/MM trajectory.

Similar to the Chl-a pigments, the transfer dynamics for the Chl-b molecules is shown in Figs. 5.10C and D. Since the pigments Chl-b 607 and 614 have only weak coupling values to the other chlorophylls, the exciton transfer is expected to be slow from these sites. As one can see in Fig. 5.10C, more than 80% of the population is still present on these pigments if they were initially excited. The coupling values of pigment Chl-b 608 are slightly higher which is also visible in the respective exciton transfer time. However, Chl-b 606 is strongly coupled to its neighboring pigment Chl-a 604 and within about 500 fs, almost the full population is equally shared between these pigments. Moreover, the dynamics continues for a longer time more than 1.5 ps where the population gain of the other pigments is close to zero.

5.4 Absorption Spectra

The time-average system Hamiltonian as shown in the Eq. 5.1 together with the site-dependent spectral densities can be employed to model the linear absorption. While various approximations to calculate the linear absorption $I(\omega)$ are known [293–295], here we employ one based on Redfield theory [198, 219]

$$I(\omega) \propto \omega \sum_{\alpha} \mid \mu_{\alpha} \mid^2 D_{\alpha}(\omega) \ , \tag{5.13}$$

where the $\mu_{\alpha} = \sum_m c_m^{\alpha} \mu_m$ denote the excitonic transition dipole moments and μ_m the transition dipole moments in site basis. Within a cummulant expansion the homogeneous line-shape $D_{\alpha}(\omega)$ can be written as

$$D_{\alpha}(\omega) = \int_{-\infty}^{\infty} e^{-i(\omega_{\alpha}-\omega)t - g_{\alpha}(t) - |t|/\tau_{\alpha}} dt \ , \tag{5.14}$$

where τ_{α} and g_{α} denote the excitonic lifetimes and lineshape function for the excitonic state α, respectively. Within Redfield theory the the inverse of the excitonic

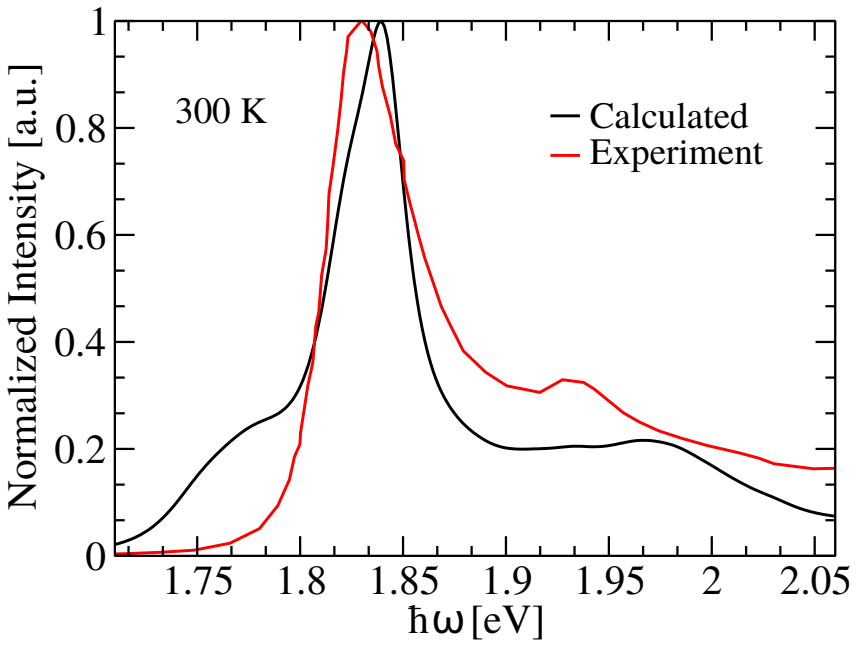

Figure 5.11: Absorption spectrum modeled at 300 K compared to an experimental finding at room temperature [296].

lifetimes τ_α are given by

$$\tau_\alpha^{-1}(\omega) = \frac{1}{2}\sum_{\beta}^{\beta\neq\alpha} k_{\alpha\to\beta} \; . \tag{5.15}$$

The rate constants can be estimated using the site-dependent spectral densities for $\omega_{\alpha\beta} > 0$ as

$$k_{\alpha\to\beta} = \sum_m \mid c_m^\alpha \mid^2 \mid c_m^\beta \mid^2 J_m(\omega_{\alpha\beta}) \tag{5.16}$$

and for $\omega_{\alpha\beta} < 0$ as

$$k_{\beta\to\alpha} = k_{\alpha\to\beta}\, e^{-\hbar\omega_{\alpha\beta}/k_BT} \; . \tag{5.17}$$

Moreover, one needs to work out the excitonic line-shape functions g_α. When neglecting site energy correlations and fluctuations of the couplings between the site, the g_α are connected to their site-dependent counterparts g_m via

$$g_\alpha(t) = \sum_m \mid c_m^\alpha \mid^4 \; g_m(t) \tag{5.18}$$

where the site-dependent line-shape functions g_m. The latter functions are connected to the site-dependent spectral density J_m through

$$g_m(t) = \int_0^\infty \frac{d\omega}{\hbar\omega^2} J_m(\omega) \left[(1-\cos(\omega t)) \coth\left(\frac{\hbar\omega}{2k_BT}\right) + i(\sin(\omega t) - \omega t) \right] . \tag{5.19}$$

In the present study, we have calculated the absorption spectra of the CP29

complex at temperatures of 300 K and 77 K using the time-averaged Hamiltonian listed in Table. 5.1 together with the spectral densities for the individual pigments. The transition dipole moments were extracted from the TD-LC-DFTB calculations and averaged over the 1 ns-long trajectory. Shown in Fig. 5.11 is the comparison of the calculated and measured absorption spectra [296] at room temperature. The absorption spectrum calculated at low temperature (77 K) is shown in Fig. S8. Because of the overestimation of excitation energy gaps in DFT-based approaches, we have shifted the peak positions of the calculated spectra to match that of the measured ones. The width of the main peak shows a good agreement experiment although we have not considered any broadening due to static disorder. Moreover, the vibrational sideband towards higher energies shows a nice agreement between theory and experiment. In the calculations, this sideband is due to the high-frequency peaks in the spectral densities. The good agreement of the linear absorption between theory and experiments further validates the present formalism for modeling LH complexes, though the shoulder towards lower frequencies at 300 K and the extra peak at 77 K indicate some possible problems with the DFTB calculations of site energies and/or transition dipole moments. Furthermore, it can be noted that distributions of the excitation energies shown in Figs. S2 and S3 are significantly wider than the main peaks of the absorption spectra. This confirms the earlier finding that the distributions of (excitonic) energy are in general not very good approximations for absorption spectra [295].

5.5 Conclusions

The molecular details and the mechanism of the pH-induced photoprotective mechanism in higher plants has raised significant interest in recent years [36–38, 225]. It has been proposed that under excess sunlight an enhanced pH gradient is established across the thylakoid membrane embedding the PSII complex which induces conformational changes in the associated proteins in order to release the extra energy as heat. In this process, the major antenna complex LHCII has been identified as one of the key players. Furthermore, recent studies show that the minor antenna complex CP29 which acts as a bridge between LHCII and the reaction center is also involved in this quenching mechanism [221, 268, 273]. In order to study the energy transfer dynamics involved in this system, the bath-induced spectral density is one of the key ingredients in tight-binding descriptions of the

underlying processes.

Earlier theoretical approaches for calculating spectral densities were based on classical MD simulations for the ground state dynamics followed by excited state calculations. In these calculations, the high frequency regions of these spectral densities were rather inaccurately described since standard classical force fields cannot properly describe the intramolecular vibrational dynamics of the respective pigments. To avoid this issue, a QM/MM MD ground state dynamics has to be performed. Using DFT approaches with a reasonable functional and basis set is numerically quite expensive. To this end, we performed the ground state QM/MM MD dynamics followed by excited state calculations within the numerically efficient DFTB formalism. This procedure yielded spectral densities with a remarkable accuracy compared to experimental findings. In this study, we have extended this multiscale approach to the CP29 minor antenna complex containing Chl-a and Chl-b molecules as primary pigments.

The trend of the site energy ladder is in good agreement with other computed and measured results while the values of the site energies are overestimated due to the well-known issues of DFT approaches with overestimating excitation energy gaps [241,282]. For this reason, we introduced a common shift for the present site energies towards the experimental energies to match the average experimental results. Moreover, as expected, the average site energies based on TD-LC-DFTB calculations along DFTB-QM/MM MD trajectories for the Chl-b molecules in the CP29 complex are slightly blue shifted compared to those of the Chl-a chromophores. However, in the energy gap autocorrelation functions and spectral densities, such a difference is not visible since both Chl molecules produce very similar correlation functions and spectral densities. Moreover, the accuracy of the present method can also be judged by comparing with spectral densities obtained from experiments. Most of the major peaks are found at the same frequencies and the intensities show a very good agreement with experimental results. In the present findings the lower frequency peaks are, however, moderately overestimated which needs to be further analyzed.

Moreover, in order to check the robustness and reliability of the present scheme, two different variants of classical force fields, i.e., AMBER and OPLS, were employed together with the DFTB approach in a QM/MM fashion. The description of the environment with the two different force fields resulted in almost indistinguishable spectral densities which supports the fact that either of the two force

fields might be used when modeling LH complexes within a QM/MM framework. Moreover, based on our previous study on the FMO complex of green sulfur bacteria, the range of the site energy fluctuations of BChl pigments is noticeable smaller than that of the Chl molecule calculated in the present study and in a previous one for the LHCII complex [282]. This fact is also reflected in the amplitudes of the spectral density peaks which are lower for the FMO complex when compare to those of the two plant systems. In experimental measurements, the spectral density of the FMO complex shows more peaks since it contains one C=C double bond less in the Mg-porphyrin rings compared to the bacterial systems. However, in our theoretical calculations, we found a smaller number of peaks since some of them seem to be merged to form wider peaks.

In addition to determining site energies and spectral densities, we have also calculated the excitonic couplings based on the TrESP approach and constructed a time-averaged system Hamiltonian. Since the QM/MM MD simulation numerically is still expensive when talking several pigments into account simultaneously, the couplings were determined from a 200 ns classical MD trajectory and combined with the site energies from the 1 ns QM/MM MD trajectory. This mixed approach is reasonable as the coupling fluctuations are less significant during the energy transfer dynamics [220, 241]. A time-averaged version of the Hamiltonian together with the obtained spectral densities can possibly be employed in future density matrix-based studies. In the present study, however, the time-averaged coupling values together with the time-dependent site energies from the first set of 60 ps QM/MM MD trajectories have been used in an ensemble-averaged wave packet scheme. Using such an approach, one can analyze how excitons are transferred between the individual pigments and how they spread within the system.

Moreover, we have calculated the absorption spectrum within a standard approach using the time-averaged Hamiltonian and the site-dependent spectral densities as key inputs. The calculated spectrum shows a nice agreement with the experimental counterpart. Interestingly, the high-energy peaks in the spectral density lead to a shoulder in the absorption spectrum which is also found in experiment. This finding further validates the robustness and reliability of our present multiscale method which can be applied to various LH complexes of plants, bacteria and algae.

In summary, we have established a multiscale protocol with the numerically efficient DFTB method which can accurately describe spectral densities which are

key quantities for modeling of photochemical processes [241, 282]. In the present study, the approach has been tested once more for an important plant LH system and it has been shown that the scheme produces reproducible, robust and reliable results based on different simulations and various LH complexes. To this end, the multiscale protocol was utilized for the CP29 complex which recently has gained quite some interest because of its active participation in the non-photochemical quenching [275, 290]. The outcome of the present calculations are the site energy, couplings and most importantly the spectral densities. Moreover, we have also presented a realistic time-averaged Hamiltonian and obtained results for the exciton dynamics based on a time-dependent Hamiltonian. In conclusion, the present study has shed light on the electronic properties of the pigment molecules in the CP29 complex as well as on the exciton-phonon and exciton-vibrational couplings within this pigment-protein aggregate. This molecular-level insight can be used in future investigations of this biologically relevant complex or of the whole PSII machinery. Simulations of entire bacterial photosynthetic organelles became possible recently [23] while similar simulations of larger aggregates of plant pigment-protein complexes are yet to come.

Acknowledgments

The authors acknowledge support by the DFG through grant KL-1299/18-1 as well as through the Research Training Group 2247 “Quantum Mechanical Materials Modelling”.

Supporting Information

Supporting information for this chapter are given in **Appendix D**.

Chapter 6

On a Chlorophyll-Caroteinoid Coupling in LHCII

Higher plants have evolved elaborate mechanisms to fine-tune their photosynthetic activity for the optimal yield under low light and at the same time they cope with its fluctuations. Proposals in the literature have indicated that a specific chlorophyll-a (Chl-a)/carotenoid (Car) pair within the major light harvesting complex (LHCII) of photosystem II can play the role of a quencher in terms of energy transfer between the Q_y state of Chl-a to the short-lived dark S_1 state of the carotenoid. For the respective coupling calculation, we employ the TrESP approach (transition charge from electrostatic potential) which needs atomic transitions charges as input. In this study, we determine these charges using different quantum chemical approaches as well as compare to existing data. Furthermore, the excitonic couplings for the Chl-a/Car pair are determined along molecular dynamics trajectories and the results are discussed in terms of varying pH and ionic strengths.

6.1 Introduction

Photosynthesis contributes to the atmospheric oxygen cycle and fuels the metabolic pathways of numerous organisms in our biosphere by storing the solar energy into chemical bonds. The latter organisms depend on the harvested sun light

Reprinted with permission from the article by **S. Maity**, A. Gelessus, V. Daskalakis and U. Kleinekathöfer, *On a Chlorophyll-Caroteinoid Coupling in LHCII*, Chem. Phys. **526**, 110439 (2021). (DOI: 10.1016/j.chemphys.2019.110439). Copyright (2019) Elsevier. **As first author I did most of the calculations.**

to sustain their homeostasis. However, fluctuations in light intensity and quality, due to the diurnal cycle or environmental conditions [297, 298], can render the photosynthetic source of energy unreliable. Thus, plants have evolved elaborate mechanisms to fine-tune their photosynthetic activity for optimal yield under low light and at the same time can cope with the light variations [11, 12]. Scientists are constantly targeting the latter mechanisms to mimic nature towards modeling of artificial photosynthesis [299] or to get insight into the so far obscure details of the photosynthetic (down)regulation [38]. Over the past decades, computational approaches have been developed to describe the elaborate energy transfer within photosynthetic complexes [198]. As such, photosystem II (PSII) is a highly modular multi-protein super-complex and the most vulnerable part of the photosynthetic apparatus under high intensity illumination. Light-harvesting complexes (LHC) act as peripheral antennas for PSII and embed chlorophylls (Chl) and carotenoids (Car) in a well-orchestrated pigment network that absorbs light. Excess photon absorption, however, saturates the photosynthetic apparatus and thus the lifetime of the singlet excited ^{1}Chl* state is extended to allow relaxation through the triplet excited ^{3}Chl* state via inter-system crossing [300]. The triplet excited ^{3}Chl* state reacts with molecular oxygen and leads to the formation of harmful reactive oxygen species (ROS) that damage the photosynthetic apparatus [301]. Green plants and algae avoid ROS by regulating the LHC-PSII function in mechanisms cumulatively known as non-photochemical quenching (NPQ) of chlorophyll fluorescence that act at various time scales to dissipate the excess energy as heat [302]. The major energy-dependent component (qE) of NPQ is activated rapidly (within seconds to minutes) by the acidification of the lumen space in the thylakoid photosynthetic membranes as a response to bright light [37]. The exact mechanism of NPQ at the molecular scale is still under debate and remains an important and currently active research field with applications in artificial and more efficient solar energy harvesting [303] or the increase of crop yields [303, 304].

The excess proton gradient (ΔpH) that is built-up across the thylakoid membranes, by the lumen acidification, activates the PSII subunit S (PsbS) as a requirement for the NPQ induction [37, 271]. The NPQ response is also enhanced allosterically by the conversion of the carotenoid violaxanthin to zeaxanthin which is proposed to regulate the light-harvesting efficiency of the photosynthetic apparatus [305]. PsbS and the xanthophyll cycle can potentially regulate the response

of the peripheral antenna of PSII (LHCII) to ΔpH and are associated with LHCII structural changes [306,307]. LHCII includes the major trimers (Lhcb1-3) and the minor monomers CP29 (Lhcb4), CP26 (Lhcb5) and CP24 (Lhcb6). Aggregation of the major LHCII trimers has also been associated with structural changes within LHCII and the stabilization of the quenched state of the protein-pigment complexes [308, 309]. These changes are reversibly activated upon the NPQ (qE) induction and can in turn switch on or off the quenching sites. The widely-accepted location of the NPQ site is the major LHCII of PSII, whereas the minor antenna complexes have also been proposed to participate in the process [37, 274, 310]. The structure of the major LHCII is shown in Fig. 6.1A (chain A, monomer) [46]. Each major LHCII monomer binds fourteen chlorophylls (eight Chl-a, six Chl-b) and four carotenoids (two luteins (Lut), one violaxanthin (Vio), and one neoxanthin (Neo)) [46]. The Lut molecules are arranged in an X-shaped pattern and contribute to the overall structural stability of the complex [46].

Proposals for the quenching site within the major LHCII include energy dissipation through strong electronic coupling of adjacent Chls towards the formation of charge transfer (CT) states [311, 312]. However, most proposals on the NPQ mechanism at the molecular level include the direct involvement of a carotenoid [36, 38, 313–315]. Electron transfer from the Car to the photo-excited Chl can generate radical pairs (Car cation, Chl anion) that quench the excess energy via quick charge recombination and decay to the ground state [315–318]. In addition, lutein-620 (Lut1, Fig. 6.1B) can potentially quench the excess excitonic energy within LHCII via slow energy transfer from the adjacent Chl-a 612 to its short lived S_1 state (10-25 ps) [36, 238, 261]. It has been proposed that energy transfer is possible between the lowest Q_y singlet state of Chl-a 612 and the Lut1 S_1 state that can become the energy sink [319] because the chlorin ring of Chl-a 612 is oriented parallelly to the Lut1 middle conjugation plane (Fig. 6.1C) [259]. In this study, we focus on the latter pair that has been associated with photoprotection [238, 259, 315, 320] given also the role of Chl-a 612 as the terminal emitter of the major LHCII that controls the energy transfer to the minor CP29 and the PSII core [46, 229, 231, 321, 322]. The description of the dark state S_1 of Lut by computational methods becomes thus important but at the same time a matter of considerable scientific debate [259, 262, 266]. Herein, we describe the Lut S_1 dark state by different computational methods and discuss the results in the context of recent studies [259, 262, 266]. Going a step further, we calculate

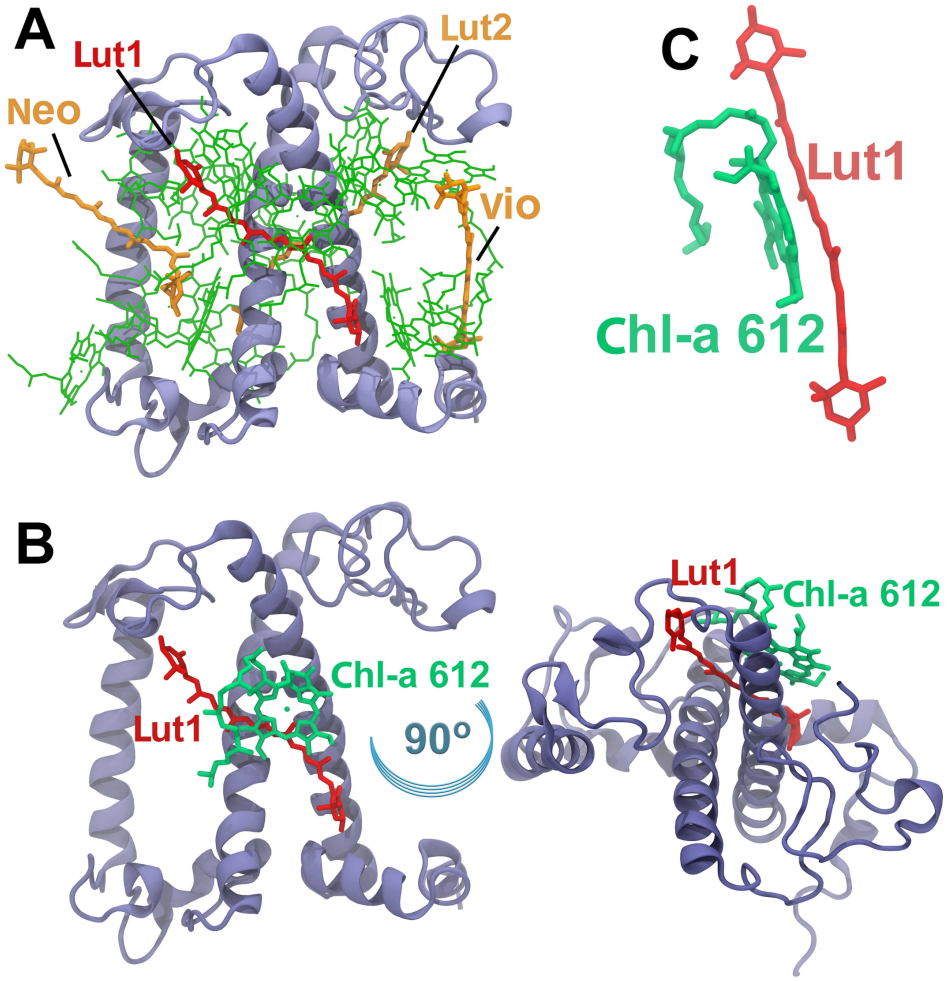

Figure 6.1: A) Structure of LHCII monomer (chain A) from spinach. The protein matrix is depicted in blue cartoon, chlorophylls are shown in green, the carotenoids neoxanthin (Neo), violaxanthin (Vio) and lutein-621 (Lut2) in orange and lutein-620 (Lut1) in red. B) The Chl-a 612/Lut1 pair is shown within the LHCII in two orientations. Please note that Chl-a 612 is the terminal emitter site of LHCII. C. The chlorin ring of this Chl-a is oriented parallel to the Lut1 middle conjugation plane.

the TrESP coupling (transition charge from electrostatic potential) [73, 266, 323] between Chl-a 612 and Lut1 along molecular dynamics (MD) trajectories of the monomeric major LHCII at different lumenal pH states (neutral and low pH) and ionic strengths (120 mM and 240 mM KCl) [324]. Probing the all-atom dynamics of the major LHCII monomer (chain A) is a good starting point to identify inter-pigment interactions at NPQ conditions [245, 324]. In this way, we will identify whether it is possible to reasonably accurately describe inter-pigment dynamics (Chl-a/Lut1) within the LHCII protein scaffold, that can guide the transition from the light harvesting to the NPQ mode under high-light conditions.

The calculation of excitonic couplings, when carotenoids are involved, is tricky because of the multi-reference character of these pigments [325]. For exam-

ple, Mennucci and co-workers have shown that DFT functionals like B3LYP and CAM-B3LYP fail to describe the excited states in carotenoids accurately. Even the state ordering is usually wrong [262, 326, 327]. Multi-configuration and double-excitation effects play a significant role in these systems and hence more sophisticated multi-reference approaches are necessary. The combined density functional theory and multireference configuration interaction (DFT/MRCI) method has shown to perform well for carotenoids [262, 327] and is also applied in the present study. Moreover, it was shown that meta-GGA functionals like TPSS, MN11L, and MN12L together with the Tamm-Dancoff approximation (TDA) can correctly describe the order of the excitonic states and the excitation energies for the carotenoids [262, 327]. However, in comparison to the DFT/MRCI results these functionals overestimate the oscillatory strength and the transition dipole moment leading to an overestimation of the excitonic couplings. To this end, it has been proposed to scale down the dipole moments to values obtained using DFT/MRCI to obtain reasonable excitonic couplings.

It has to be emphasized that the objective of the present study is to determine the coupling between the Chl-a Q_y and the Lut1 S_1 state in the context of NPQ. In other studies, also the coupling between the Chl-a Q_y and the second excited state S_2 of Lut1 has been discussed [328]. A quite recent summary of the available chromophore Coulomb couplings of the LHCII crystal structure is given in Ref. 328. Moreover, we would like to mention a determination of the coupling by a full configuration interaction calculation within a complete active space using the semi-empirical AM1 Hamiltonian (AM1-CAS-CI) [259] in which the Chl-a and Lut transition dipole moments were re-scaled. In addition, Khokhlov and Belove performed multi-configurational self-consistent field calculations using a state-specific restricted active space (RASSCF) [266] without an additional dipole scaling. The latter approach should be well suited for carotenoids in order to capture the multi-reference character of these pigments. Thus, we also test the performance of the respective RASSCF transition charges along MD trajectories.

This article is organized as follows. In the subsequent section, the computational methods, i.e., the MD simulations, the TrESP approach, and TD-DFT as well as DFT/MRCI methods are briefly described. In the results section, we first analyze the transition charges from the various approaches before determining the Chl-a/Lut1 couplings along MD trajectories. Moreover, the couplings are discussed in view of the NPQ mechanism. This investigation closes with some final remarks.

6.2 Computational Methods

6.2.1 MD Simulation

Models of a monomer (pdb:1rwt, chain A) of the major LHCII from spinach [46] have been built based on a published protocol [324]. The monomer was embedded in a fully hydrated lipid bilayer membrane that mimics the native thylakoid membrane [245]. Two different states of the LHCII monomer are considered, i.e., at (i) neutral lumenal pH (light-harvesting state) and (ii) lower lumenal pH (NPQ state) [37]. The NPQ conditions (lumen acidification and cross-membrane ΔpH induction) are simulated by protonating key residues exposed to the lumen of the LHCII protein, i.e., E83, E94, E107, E207 and D111, D211, D215 based on experiments [39, 242, 243, 329] and PROPKA 3.0 predictions as part of the PDB2PQR scheme [244] to simulate in vivo low ($<$6) or neutral ($\sim$7) lumenal as well as neutral stromal ($\sim$7) pH values [40, 324]. At NPQ conditions it has been proposed that the pKa values of lumen exposed LHCII residues are increased, e.g., by interactions with zeaxanthin molecules or the PsbS protein [37, 302, 330]. Thus, all lumen-exposed LHCII titratable residues have been protonated to simulate NPQ conditions (low lumenal pH or excess ΔpH samples). These titratable residues are, however, treated deprotonated for the neutral lumenal pH or low ΔpH samples. In addition, counter ions neutralize the simulation system and, furthermore, a surplus of KCl at ionic strength of 120 mM as well as 240 mM was added to account for physiological ion fluxes [305]. In total, we consider four LHCII system setups (two different lumenal pH values and two ionic strengths). Based on published protocols [40, 331], the samples are relaxed and equilibrated prior to the production runs. MD trajectories have been produced for the four different setups integrating Newton's equations of motion for 200 ns each. Further details concerning the setup of the molecular dynamics simulations can be found in Ref. 324.

6.2.2 Basics of the TrESP Coupling Formalism

The excitonic coupling between pigments can be determined in a variety of approaches [59, 160] with the point-dipole approximation being the simplest among them. For example, the supermolecule approach is straightforward for homo-dimers, i.e., the coupling equals half of the energy splitting between the two lowest electronic states but gets more involved for hetero-dimers [160]. Only for

small inter-pigment densities the exchange part plays a significant role. Otherwise, one can accurately approximate the excitonic coupling by determining only the Coulomb interaction between the pigments as done in the present study. The TrESP approach (transition charges from electrostatic potentials) has the advantage of being accurate and computationally efficient at the same time [160]. In its standard version the transition charges are calculated only for the equilibrium configuration and subsequently projected onto non-equilibrium conformation, e.g., along an MD trajectory. An extension of this scheme with calculating the transition charges on the fly has been tested [162] but is computationally quite expensive and not applied in the present investigation. Moreover, a calculation of transition charges on the fly along classical trajectories is likely to yield inaccurate results because of the geometry mismatch problem and thus might even lead to inferior results compared to the standard TrESP scheme.

In the TrESP approach the Coulomb coupling is given by [73, 323]

$$V_{mn} = \frac{f}{4\pi\epsilon_0} \sum_{I,J}^{D,A} \frac{q_I^T . q_J^T}{\mid r_D^I - r_A^J \mid} \tag{6.1}$$

where $q_{I,J}^T$ denote the transition charges located at each atom I, J of the respective donor (D) and acceptor (A) molecule. The transition density can be obtained as $\sum_I q_I^T \delta(r - R_D^I)$. Moreover, the environmental influence on coupling can be taken into account by a screening factor f [74, 198]. In the original TrESP procedure, Renger and co-workers have suggested that the transition charges should be rescaled in order to reproduce the experimental transition dipole moment [73, 332]. Thus, there are two parameters which are difficult to determine from first principle. The scaling factor to reproduce the experimental dipole moment values is certainly well reasoned for these distances since in this case the coupling is accurately given by the point-dipole approximation. At intermediate and shorter distances, however, the situation is more complex. As has, for example, been shown in Ref. 160, the couplings between pigments at inter-pigment distances common in light-harvesting systems can be determined using the TrESP and the supermolecule approaches. If the same level of theory is employed, the results have shown to be equal [160]. For the supermolecule approach, however, a scaling in order to reproduce the monomeric dipole moments is very artificial and not commonly used. In the present study, we refrain from scaling to reproduce the experimental dipole moment also because some of the approaches below do

give reasonable dipole moment values already and for dark states no experimental dipole moments are available.

The environmental factor is supposed to take the solvent effects on the electronic coupling into account through a possibly distance dependent screening factor f [74]. A comparison of the effect of various approaches can be found in Refs. 75 and 220. In the simplest formalism the environmental screening factor is assumed to be constant and based on the Poisson-TrESP method has found to have values of $f = 0.80$ for the Fenna-Matthews-Olson complex and $f = 0.69$ for photosystem I monomers [75]. In this study, we do not take this additional factor into account since the debate on the proper environmental scaling factor is beyond the scope of this investigation. Using a constant environmental factor, the present results can, of course, easily be adapted.

6.2.3 Calculation of the Transition Charges

To determine the transition charges in case of the chlorophyll-a and lutein molecules, we first optimized the structures using the B3LYP/6-311G(d,p) level of theory. Subsequently, different approaches for determining the excited states have been employed. TD-DFT calculations including the Tamm-Dancoff Approximation (TDA) as implemented in Gaussian09 [333] have been one option. The popular DFT functional CAM-B3LYP has been employed together with a 6-311+G(d,p) basis set to perform the TDA-DFT calculations for the Chl-a molecule. However, for the lutein molecule we have considered the TPSS and MN12 functionals with a 6-311+G(d,p) basis set as CAM-B3LYP fails to predict the proper order of states for this molecule but TPSS and MN12L do [262], i.e., the first excited state (S_1) is dark state and the second excited state (S_2) is bright. After performing these TD-DFT calculations, the respective transition densities have been analyzed using the Multiwfn package [161]. To this end, we have used the electrostatic CHELPG fitting in order to obtain the atomic TrESP charges. In this fitting procedure the hydrogen atoms have been omitted, i.e., atomic transition charges are only placed on the heavy atoms of the respective molecules.

Furthermore, DFT/MRCI single-point calculations have been performed on the same B3LYP equilibrium structures discussed above using a parallel version of the DFT/MRCI code which has an interface to the ORCA package [150]. To this end, a protocol similar to that described in literature for Chl/BChl molecules [102, 334]

and carotenoids [262, 326] was followed. A split valence basis set (def2-SV(P)) containing d-polarization functions on all non-hydrogen atoms was employed for all atom types. The ORCA package in version 4.0 was used to perform SCF calculations using the BH-LYP functional in order to generate optimized Kohn-Sham orbitals. For the construction of the configuration state functions in the MRCI expansion, these orbitals build the basis.

In case of the Chl-a molecule, we have employed the latest DFT/MRCI Hamiltonian (R2018) [335] together with the "standard" parameter set. The range from the eight highest occupied to the six lowest unoccupied molecular orbitals was included in the initial MRCI reference space expansion considering all single and double excitations. Moreover, the orbital selection threshold was set to 0.8 E_h together with requiring 12 roots for the initial DFT/MRCI run. The final reference space for the production run contained all configurations which contribute to one of the 12 roots with a squared coefficient of at least 0.003. In the production DFT/MRCI calculation, we have increased the orbital threshold up to 1.0 E_h in order to calculate the excitation energies for all 12 roots. In case of the lutein molecule, we have considered the original DFT/MRCI Hamiltonian [336] again with the "standard" parameter set. Moreover, we tested the more recent Hamiltonian versions (R2016 [337], R2017 [338], R2018 [335]) together with a 0.6 E_h orbital selection threshold but these combinations failed to describe the correct ordering of the excited states. With an increased threshold of 0.8 E_h, the Hamiltonians R2016 and R2017 predict S_2 as bright state but still the latest Hamiltonian R2018 fails for this parameter. We refrained from further tests but these preliminary calculations indicate that the lutein molecule has to be handled with care also within the DFT/MRCI approach. All results below have been obtained using the original Hamiltonian. Moreover, we followed the same steps as described for the Chl-a molecule above but used an orbital threshold of 1.0 E_h for the initial and 1.2 E_h for the production run requiring 8 roots. Subsequent to the DFT/MRCI calculations, we have extracted the transition densities using an in-house interface and extracted atomic transition charges using the Multiwfn package as described above for the TD-DFT charges.

A third approach to determine TrESP charges especially suited for the lutein molecule which we take into account in this study, is the multi-configurational restricted active space self-consistent field (RASSCF) scheme. Khokhlov and Belov [266] have recently determined and published RASSCF transition charges for the

Chl-a and Lut molecules. In their study, these authors performed a state-specific RASSCF calculation including only states with ^1A_g symmetry assuming the $2A_g^-$ symmetry of the S_1 state based on the C_{2h} polyene symmetry [266]. This technique yields a very low, i.e., basically zero, dipole moment for the dark state of Lut, a property not often found with other approaches. Thus, the couplings are also determined with these sets of transition charges along MD trajectories.

6.3 Results and Discussions

6.3.1 Distribution of Transition Charges for the Chl-a and Lut Molecules

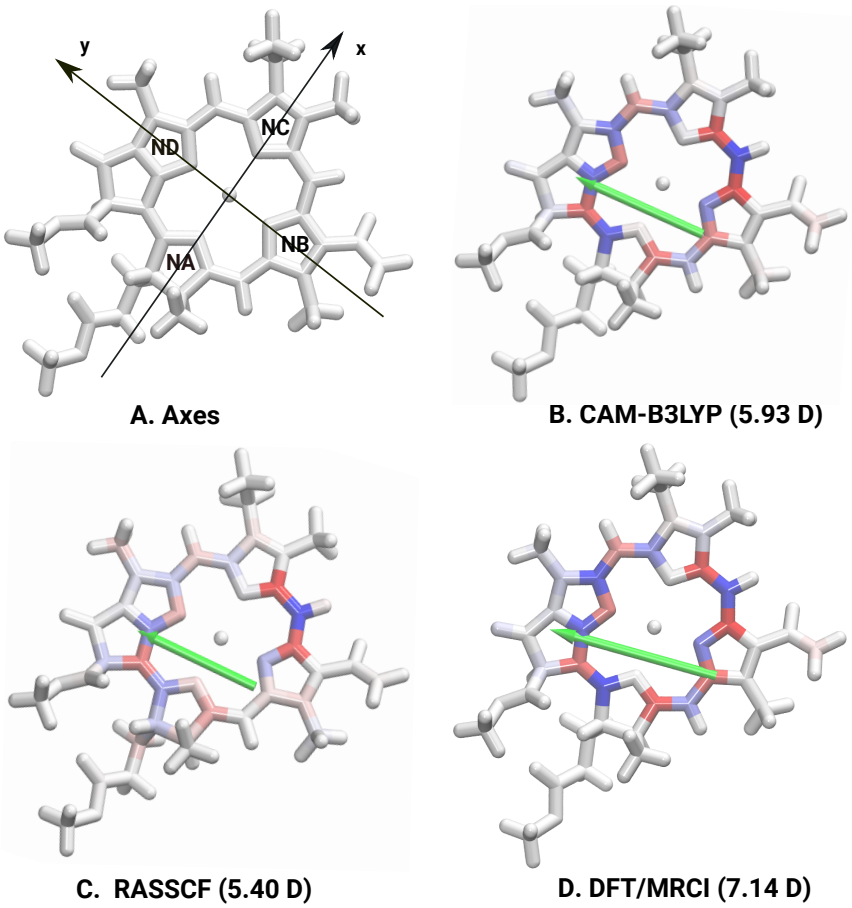

Figure 6.2: TrESP charge distributions of Chl-a for three different levels of theory. The positive and negative charges are represented by blue and red regions, respectively, while the intensity of the colors indicates the magnitude of the respective charges. A) Definition of the NB-ND direction, B) TD-DFT CAM-B3LYP, C) RASSCF and D) DFT/MRCI. The green arrows indicate the respective dipole moments.

Three different approaches are presented which output atomic transition charges for the chlorophyll molecule. These schemes yield rather similar results especially concerning the direction of the dipole moment. The CAM-B3LYP TD-DFT (5.93 D,

angle between NB-ND axis and transition dipole of 3.3°) and the RASSCF (5.48 D, angle of 3.5°) yield dipole moment strengths closest to the experimental value of 4.6 D [167]. The DFT/MRCI scheme with 7.14 D (angle of 5.1°) overestimate the dipole moment even more. It is interesting to note that in a previous study on a set of smaller molecules [339], it has been shown that the DFT/MRCI approach overestimates dipole moments by values between 0 and 1 D. The respective transition charge distributions are depicted in Fig. 6.2 and do show rather similar distributions.

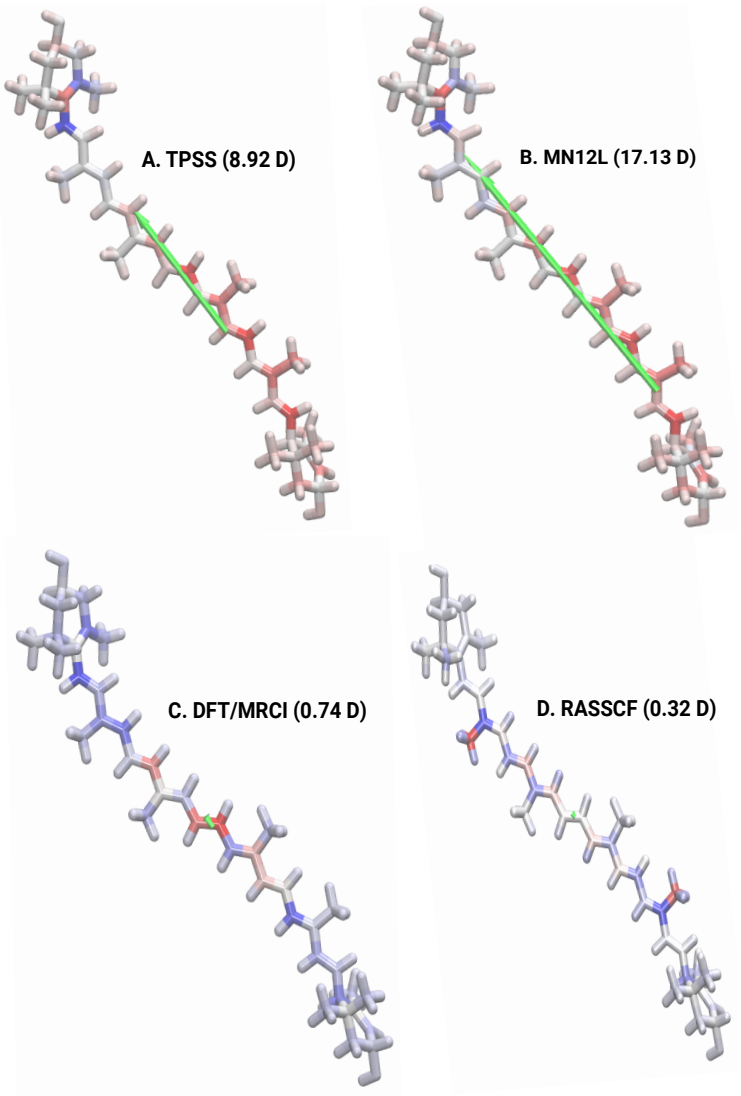

Figure 6.3: TrESP charge distributions of Lut for four different levels of theory. The positive and negative charges are represented by blue and red regions, respectively, while the intensity of the colors indicates the magnitude of the respective charges. A) TD-DFT TPSS, B) TD-DFT MN12L, C) DFT/MRCI, and D) RASSCF.

For the lutein molecule CAM-B3LYP fails to determine the correct ordering of excited states as previously reported in literature [262]. In this earlier study, it was found, however, that with the TPSS and the MN12L functionals employing the TDA the correct ordering of states is achieved with reasonable excitation ener-

gies. Thus, it was suggested that together with a scaling of the dipole moment, i.e., of the transition charges, the respective approaches can be employed for coupling calculations as well. The dipole moments for these functionals, are quite high, i.e., 8.92 D for TPSS and 17.13 D for MN12L, taking into account that the respective state has experimentally shown to be dark. Thus, we will not further consider theses two functionals. The DFT-MRCI calculations lead to transition charges resulting in a dipole moment of 0.74 D, i.e., at least a factor 10 smaller than those from the above TD-DFT calculations and very similar to earlier DFT/MRCI calculations of the same molecule performed with smaller configuration and active space [262]. In the DFT/MRCI calculation the predominant contributions to the S_1 state are in decreasing order double excitation HOMO/LUMO, single excitation HOMO-1/ LUMO, single excitation HOMO/LUMO+1, simultaneous single excitation HOMO-1/ LUMO and single excitation HOMO/LUMO+1 as well as the Hartree-Fock/DFT ground state. Even for the HOMO/LUMO double excitation the square of the corresponding coefficient in the wave function expansion is only 0.26. Obviously S_1 is badly described by a single configuration and has a strong multiconfiguration character. Each of the five configurations mentioned above is of $^1A_g{}^-$ type if perfect C_{2h} symmetry is assumed. In total, double excitations contribute 53 % to the sum of squared coefficients of the wave function expansion, triple excitations 10 % and quadruple excitations 3 %. The rather large percentage of triple and quadruple excitation shows the necessity of a multi-reference method for the S_1 state of lutein.

The RASSCF transition charges from Khokhlov and Belov [266] lead to a very small dipole moment of 0.32 D when putting the published transition charges onto the present B3LYP equilibrium structure. The last two approaches are likely consistent with finding a (nearly) dark state in experiment. Thus, subsequently these different transition charge distributions are employed to determine the Chl-Lut coupling along an MD trajectory. The corresponding charge distributions are shown in Fig. 6.3. As can be seen, the state-specific RASSCF calculation leads to a very symmetric transition charge distribution while the DFT/MRCI results do show some clear asymmetry, a difference which leads to specific variations in the coupling distributions as shown below.

We want to note in passing that the sign of the transition dipole moment (and the whole transition charge distribution) is actually a matter of convention since it is not an observable. The square of the transition dipole moment, however, is

an observable and proportional to the oscillator strength of the transition. For simplicity and to avoid additional confusion, we made sure that in all different approaches we use the same sign convention for the transition dipole moments which can be assumed to be real.

6.3.2 Distribution of the Excitonic Couplings of the Chl-a 612/Lut1 Pairs

In a next step we used the TrESP coupling approach with various combinations of the above transition charge distributions to determine the excitonic coupling between Chl-a 612 and Lut1. These calculations are being performed along the MD trajectories of the different LHCII monomer states.

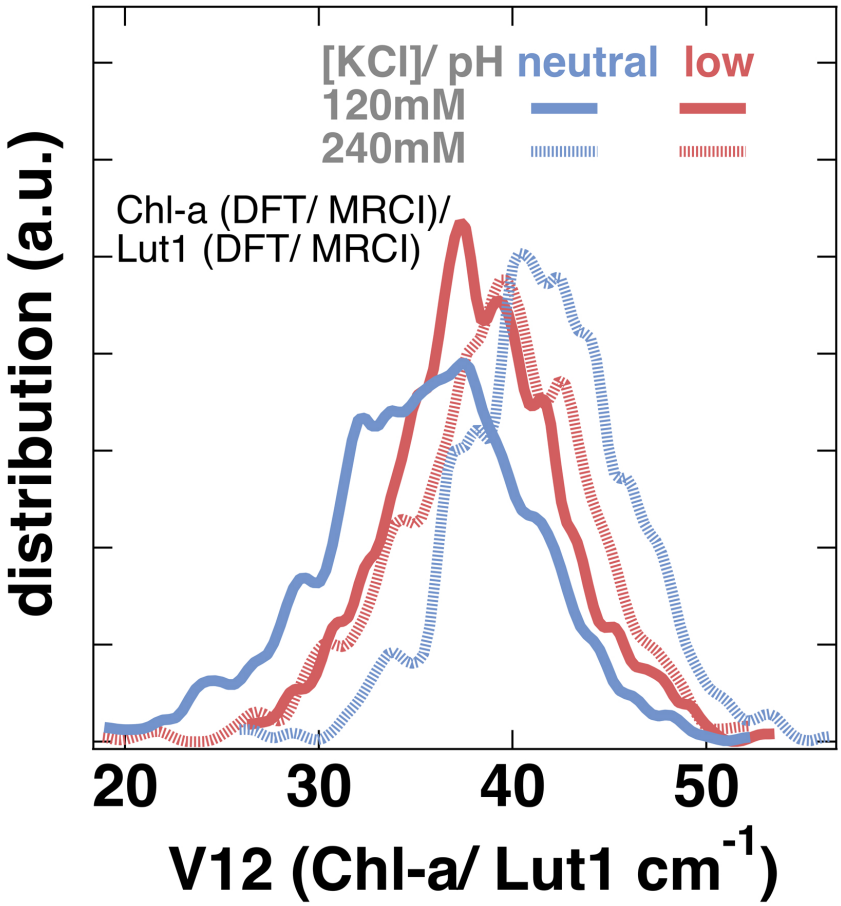

Figure 6.4: TrESP coupling between Chl-a and Lut1 based on the transition charges from DFT/MRCI for both chromophores.

The experimental literature agrees that at low pH there is the possibility of energy transfer within LHCII from the Chl-a Q_y state to the dark S_1 state of the caroteinoid which has a shorter lifetime [36, 270]. Actually, a change in coupling is expected when changing between pH conditions and ionic strengths. If one

would see such a variation in our different setups, this finding could significantly contribute to the insight into the molecular details of NPQ.

In a first step, we determine the Chl-a 612/Lut1 TrESP couplings along the MD trajectories for the four different LHCII states, i.e., with two different pH values and two different ionic strengths based on the DFT/MRCI transition charges for both pigments (see Fig. 6.4). The coupling values for all four cases are distributed at values around 40 cm^{-1}. For the low pH case, no dependence on the ionic strength can be observed. At neutral pH, i.e., the light-harvesting state, however, the low ionic strength data shows lower coupling values and the high ionic strength data higher coupling values (relative to the low pH case). The width of these distribution is around 15 to 20 cm^{-1} resulting from the conformational fluctuations along the MD trajectories. In the case of the DFT/MRCI based excitonic couplings, the trends for the ionic strength effects match those of the RASSCF based couplings (see below). However, there is a clear trend that at low ionic strength and pH, the couplings are slightly higher than those calculated at neutral pH. This finding is consistent with the general notion, that at low pH, one should expect an enhanced energy transfer from the Chl-a 612 Q_y to the Lut1 S_1 state (see above for quenching mechanisms) that should be associated with an increased coupling.

In a further step, the excitonic couplings have been calculated based on the RASSCF transition charges for the lutein molecule and the CAM-B3LYP transition charges for the chlorophyll molecule. Furthermore, RASSCF-derived transition charges have been considered for chlorophyll in order to compare with the CAM-B3LYP based TD-DFT calculations. The distribution of couplings, shown in Fig. 6.5, reveal that both CAM-B3LYP and RASSCF for chlorophyll exert the same kind of trend for the neutral and low pH states as well as the ionic strength as long as the lutein transition charges are described at the same level of theory. Since the transition charge distribution of the Lutein equilibrium state is almost symmetric for the state-specific RASSCF scheme and then projected onto the MD trajectory, the couplings fluctuate around zero. In case of the DFT/MRCI approach, the transition charges show fluctuations of the coupling values are around a finite value since already the equilibrium state has a finite albeit small transition dipole moment.

To further explore the factors that contribute to the reported Chl-a 612/ Lut1 couplings, we have calculated the separation distances and the orientation fac-

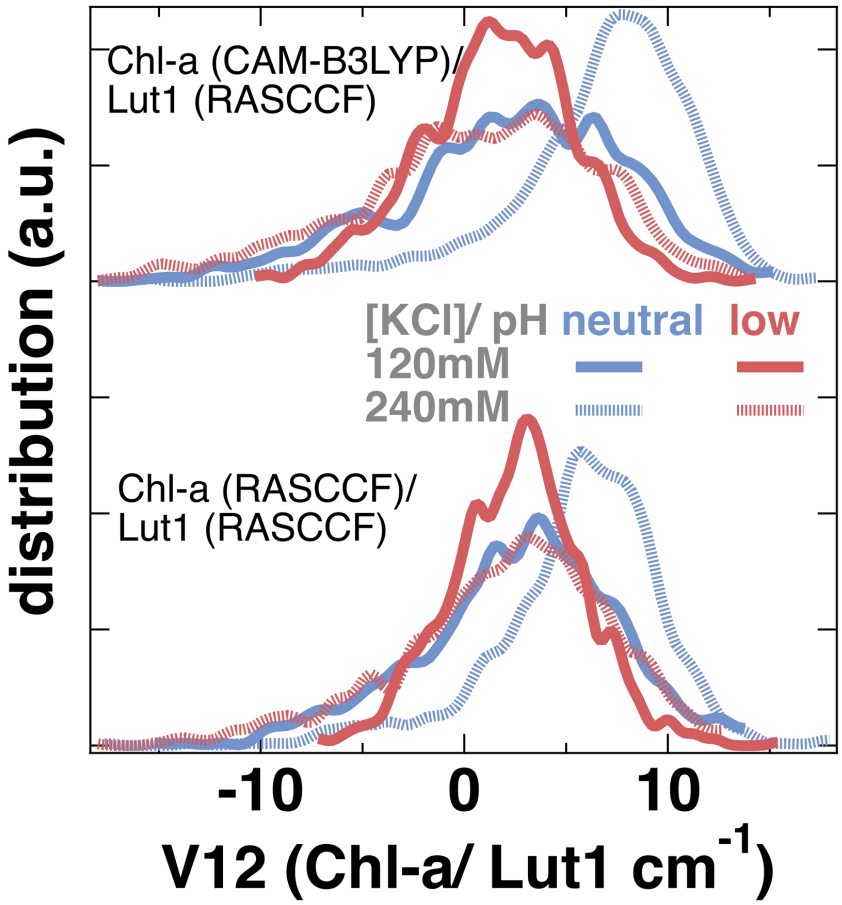

Figure 6.5: TrESP coupling between Chl-a/Lut1 based on the RASSCF charges for Lut1 and the CAM-B3LYP as well as RASSCF charges for Chl-a.

tor (k^2) of the Chl-a 612/ Lut1 pair in each LHCII monomer state probed herein [340]. The separation distances are calculated as the distances between the Center of Mass (CoM) of the NB-ND atoms in Chl-a 612 and the CoM of the C15-C35 central bond atoms of Lut1 (numbering from the crystal structure of the major LHCII from spinach, chain A) [46]. The k^2 factor depends on the relative orientations of the donor and acceptor transition dipole moments as $k^2 = (\sin\Theta_D \sin\Theta_A \cos\Phi - 2\cos\Theta_D \cos\Theta_A)^2$ where Φ denotes the angle between the planes containing the two transition dipoles while Θ_D or Θ_A are the angles between the donor or acceptor transition dipole and the vector joining the donor and acceptor [340]. The two transition dipole moments are defined in terms of rigid molecules, along the NB-ND atoms for Chl-a 612 (donor) and along the central C15-C35 atoms for Lut1 (acceptor) [245]. The separation distances, as reported in Fig. 6.6, show a general trend. The neutral pH LHCII states exert larger Chl-a 612/ Lut1 distances compared to the low pH states that should correlate with a smaller excitonic coupling in the pair as it is expected for the light harvesting states [245]. The ionic strength seems also to affect the separation distances for the neutral pH

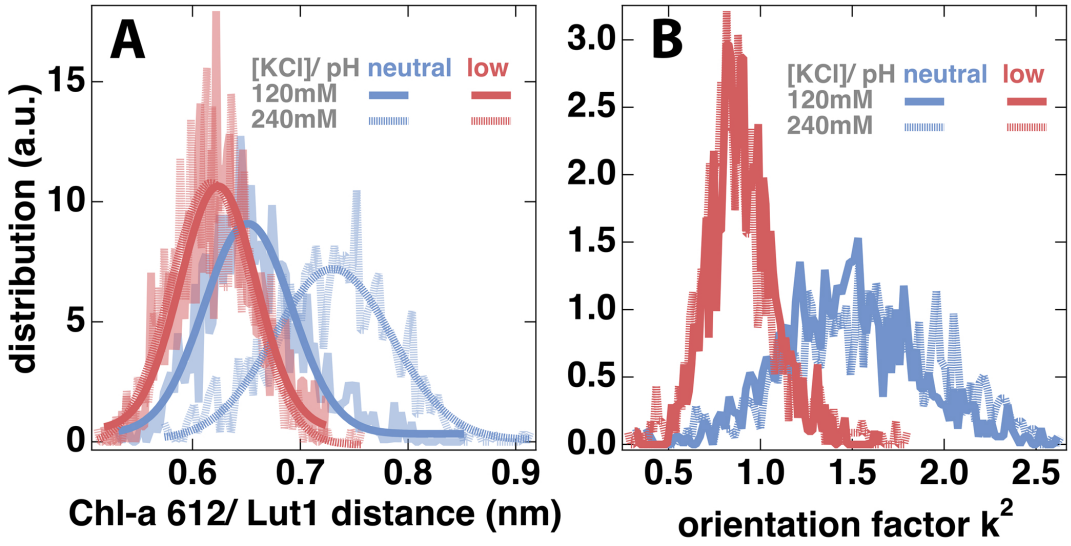

Figure 6.6: Distances and orientational factor k^2 between Chl-a 612 and Lut1 based on the molecular dynamics simulations. Gaussian functions are used to fit distance distributions in the left panel.

LHCII state. This latter effect on the Chl-a 612/ Lut1 separation is not explicitly captured in the excitonic couplings calculated with the TrESP method with the transition charges derived at either the MRCI or the RASSCF levels. Moreover, the orientation factors k^2 reported in Fig. 6.6 are independent of the ionic strength and grouped for the neutral and low pH LHCII states. The low pH monomer states exert k^2 values close to 1 which indicates parallel transition dipoles for the acceptor and donor along with an efficient excitonic energy transfer [340]. This latter is also in line with a proposed model for NPQ (low pH) based on the Chl-a 612/ Lut1 pair that should include efficient energy transfer between the Q_y/ S_1 states, respectively [259]. We propose, thus, that both the separation distances, as well as the orientations of the Chl-a 612/ Lut1 species are affected by the pH state of the major LHCII monomer. The sensitivity of the couplings to this diversity, however, seems to be based on the method of choice to derive the transition charges for the TrESP calculation. Further simulations and analysis are needed to also probe the associated conformational changes of the protein scaffold that induces the aforementioned degrees of freedom for the Chl-a 612/ Lut1 pair, at different LHCII pH states. The latter, however, falls outside the scope of this study and will be addressed in the future. For the moment, we note that the residue Q197 has been proposed earlier to be involved in the orientational changes induced to Lut1 under NPQ conditions (low pH) as it forms an hydrogen bonding interaction connecting helix D with Lut1 [319]. Helix D has also been reported [319, 324] to act as a chemiosmotic sensor in LHCII that can be associated with changes in the

Chl-a 612/ Lut1 pair as those reported herein.

The distributions in Figs. 6.4 and 6.5 reveal no significant shift for the neutral/low pH states in terms of the Chl-a 612/Lut1 excitonic couplings at low KCl concentrations. Based on the proposed details of the NPQ mechanism at the molecular level, one would, however, expected some clear change in the couplings upon pH transitions. This insensitivity to the pH value could be due to inadequate sampling of only 200 ns that might not be enough to sample a transition from the quenched to the-light harvesting mode at neutral pH. We have to note that the starting structure, i.e., the crystal structure of the major LHCII from spinach, represents a quenched state [245]. The insensitivity to pH could also be a result of a "monomer effect" on the inter-pigment couplings since it has earlier been proposed that the inter-pigment distances are increased in the transition from the trimeric to the monomeric LHCII [341]. Thus, the Chl-a 612/Lut1 excitonic couplings in the monomeric state could be rather insensitive to the environmental pH. Moreover, we note that the different pH states are simulated by protonating lumen-exposed key residues of the LHCII monomer [324]. At the same time, the KCl concentration seems to affect the excitonic couplings within the LHCII monomer as can be observed by the shift of the latter to larger values for the 240 mM KCl concentration at neutral pH (see Fig. 6.5, dashed blue line). This finding possibly can be associated with the experimental finding that ion fluxes affect the LHCII dynamics [305]. As can be observed in Fig. 6.6, the separation distance between the Chl-a 612 and the Lut1 pigments is affected by the ionic strength. However, their orientation factor k^2 seems insensitive to the ionic strength but sensitive to the LHCII pH state. Based on our model setup, Cl^- ions can be accumulated near helix D of LHCII in the low pH state while more K^+ ions are expected to accumulate in the same region in the neutral pH state. These enhanced ion densities can indeed be found in our simulations (data not shown). This shielding of the lumenal sites of LHCII can have diverse effects on their conformations at the different lumenal pH states. For the neutral pH case, the increase of the ionic strength can lead to an extensive shielding of lumenal sites with negative charges by the K^+ ions that can partially counteract the pH effect. The in vivo situation, however, can be more complicated [342]. For example, the recovery from NPQ is associated with an increased flux of K^+ ions in the lumenal space and a decrease of the H^+ ions that could lead to deprotonations at the lumenal sites. At the same time, a still obscure interplay between ion fluxes of K^+, Cl^-, Mg^{2+} and Ca^{2+} into the lumenal

and stromal spaces and the charges of either the LHCII or the thylakoid membrane tunes the photosynthetic mechanism and NPQ as discussed in the literature [342]. This latter effects cannot be captured in our models but the reported changes in the Chl-a 612/ Lut1 pair in terms of separation distance, orientation factor k^2, and excitonic couplings can be considered as indicative of the sensitivity of the LHCII to the ionic strength. More elaborate models and further analysis are needed to address the effect of the ionic strength that can be associated accurately with the in vivo case.

The absolute values of the couplings at the DFT/MRCI level are higher than those obtained from RASSCF because of the higher transition dipole moment obtained for both molecules at the DFT/MRCI level compared to the RASSCF and CAM-B3LYP values. As discussed above, we refrained here from any additional scaling and are more interested in relative effects rather than quantitative accuracy which is hard to obtain for the present Chl-Lut pair.

6.4 Conclusions

In this article, we have evaluated different levels of theory for the description of the Chl-a 612/Lut1 excitonic couplings within a major LHCII monomer of photosystem II. These results will help us in future studies to also give important insight into the non-photochemical quenching (NPQ) mechanism that is activated in higher plants under bright-light conditions and has been proposed to relate to the Chl-a 612/Lut1 excitonic pair. At the same time we want to point out that there are several Chl-Car pairs within LHCII. Two of these have the chlorin rings parallel to the carotenoid conjugation planes (Chl-612/ Lut1 and Chl-603/ Lut2) while also others exist (like the Neo/ Chl-604/ Chl-606, Vio/ Chl-613/ Chl-614). In the present study we, however, have focused on one particular Chl-Car pair, i.e., Chl-a 612/Lut1. To this end, we have modeled one monomeric unit of the LHCII and calculated the excitonic couplings using the TrESP method with transition charges derived by various quantum chemical methods. We have shown that DFT functionals like TPSS and MN12L, which can correctly predict the dark state of lutein, fail to determine the correct transition dipole moments of the carotenoids and subsequently strongly overestimate the excitonic couplings. On the other hand, multi-reference methods like DFT/MRCI and RASSCF can determine transition dipole moments consistent with the S_1 state being a dark state. One has to note

that during the state-specific RASSCF calculations the "assumed C_{2h}" symmetry of the Lut molecule was partially enforced by considering only symmetric active spaces [266]. A fully C_{2h}-symmetric molecule would actually have a vanishing dipole moment. In the present DFT/MRCI calculations, no special symmetry assumptions were included but still a quite low dipole moment was obtained. We found that a shift in the excitonic coupling for low pH values exists when we are calculating the couplings using the DFT/MRCI derived charges. This finding seems to correlate with the NPQ induction at low pH in the major LHCII complex. However, for RASSCF we did not observe any significant difference for the low and neutral pH states in the current setup. As discussed above, this finding might, however, be due to the fact that the MD simulations were too short or the fact that only a monomer was simulated.

The present study showed that the transition charges and thus also the couplings involving especially the lutein molecules are very sensitive to the level of theory (including size of configuration and active space in the DFT/MRCI approach). Thus, conclusions on the coupling should be made with some caution and keeping this sensitivity in mind. Moreover, the transition charges have only been determined for the (B3LYP) equilibrium conformations. Especially for the flexible lutein molecule there is a chance that these transition charges do change more significantly based on the actual conformation. Calculations of TrESP transition charges along a trajectory have been performed for a test system [162], but are currently out of range especially for the lutein molecule in which a multireference formalism has to be employed. In summary, we were able to give some more insights into the determination of transition charges and couplings of the Chl-a 612/Lut1 pair but due to the complexity of the problem, more research in this direction is needed.

Acknowledgments

Funding through the DFG-Research Training group "Quantum Mechanical Materials Modelling" is gratefully acknowledged. Moreover, we are very thankful to the group of Prof. Christel Marian and especially Dr. Martin Kleinschmidt for providing access to the DFT/MRCI code and additional insight into the approach. Computational time for this study was allocated within the HPC-Europa3 grant to V.D. (HPC17K4FRZ) at the Supercomputer Hazel Hen (Cray XC40) at the HPC Center

Stuttgart (HLRS) along with access to the Black Pearl compute cluster at Jacobs University Bremen.

Chapter 7

Outlook on the Modeling of Porphyrin/Clay-surface Artificial LH Complex

Motivated by the energy transfer network of the LH complexes of plants, bacteria and algae, people have tried to mimic them artificially. In experiment, it is found that porphyrin molecules attached on inorganic clay surfaces show remarkable energy transfer with an efficiency close to almost 100% [50]. Here, we have built an inorganic clay surface with the help of the CHARMM-GUI webserver [286] and attached four free-base porphyrin molecules on top of the surface. Two different types of porphyrins are considered, e.g., Tetrakis(1-methylpyridinium-3-yl) Porphyrin (m-TMPyP) and Tetrakis(1-methylpyridinium-4-yl)Porphyrin (p-TMPyP) which are found positively charged. A typical arrangement of a porphyrin/clay surface is shown in Fig. 7.1. After energy minimization, 2 ns NVT

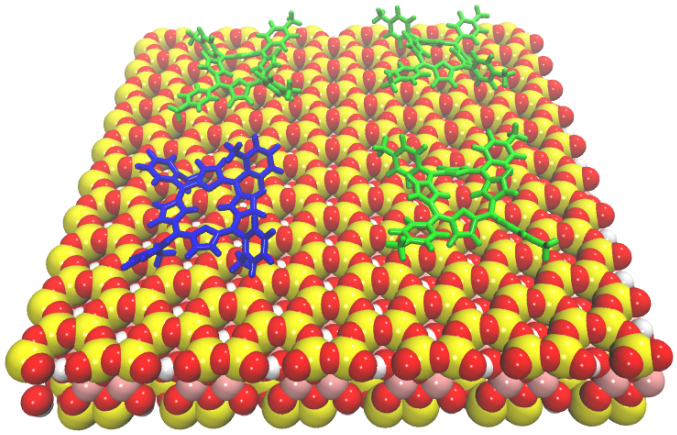

Figure 7.1: Three p-TMPyP (green) and one m-TMPyP (blue) molecules attached on a montmorillonite clay surface.

equilibration followed by a 5 ns NPT simulation is performed with the GROMACS MD engine [133]. Moreover, position restraint were applied on the porphyrin molecules during the simulation. Finally, a 50 ps production run was carried out and the trajectories were stored at a 1 fs stride. This generates 50,000 frames which were then utilized for site energy and excitonic coupling calculations. Site energies are calculated based on TD-LC-DFTB method in a QM/MM framework as implemented in the DFTB+ package [69]. The lowest excitation energy for each molecule is extracted along the trajectory and the associate histogram is shown in Fig. 7.2A. The distributions are Gaussian shape and well separated from each other. Moreover, the excitonic couplings between the porphyrins have also been

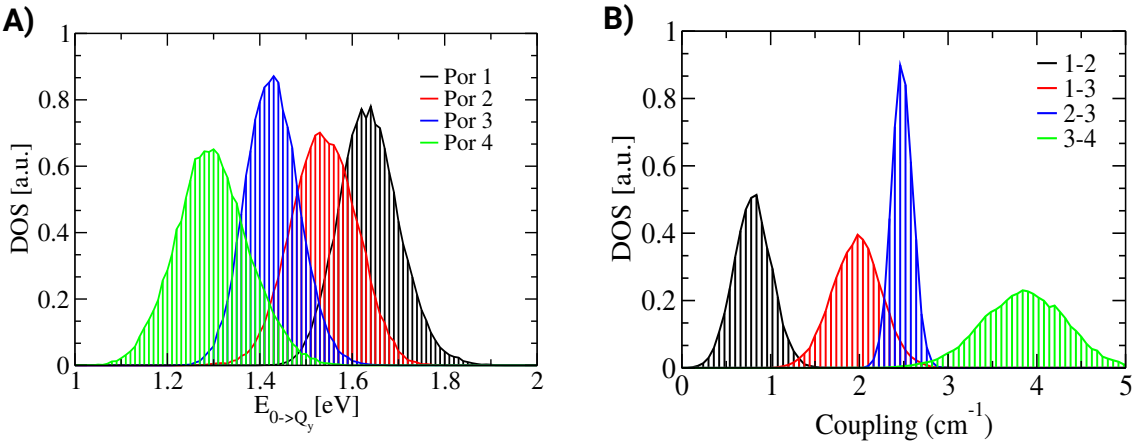

Figure 7.2: A) Excitation energy and B) excitonic coupling distribution of porphyrin pigment molecules along classical MD trajectory.

calculated based on TrESP approach [73] where the transition charges were extracted based on the Gaussian program of suits [333] followed by the Multiwfn package [161]. The coupling distribution is represented in Fig. 7.2B. The site energies and couplings can be coupled together to build a Hamiltonian of the system to be to calculate the time evolution of excitons between the porphyrin molecules. At the moment, the simulation was performed by employing the position restraint over the porphyrin pigments, however in future studies this can be removed by making a regular arrangement of anionic charge on the surface. Moreover, in future studies QM/MM MD simulation followed by the extraction of spectral densities will be performed and they would be compared with the biological LH complexes of plant and bacteria. Furthermore, an enlarged periodic system can also be constructed and the rate of exciton diffusion will be investigated in future studies.

Chapter 8

Summary

The aim of this thesis is to develop a robust and efficient methodology to investigate molecular photoinduced processes of the LH complexes. Previous schemes based on classical ground state MD simulations often suffer from the poor quality of geometries and vibrational dynamics during the excited state analysis. For this reason, a multiscale scheme is presented where the state-of-the-art QM/MM MD simulations are applied for the ground state to remove the geometry mismatch problem. The spectral densities calculated based on this improved scheme show a remarkable agreement with the experimental counterpart for model LH complexes. The numerical cost of QM/MM MD is reduced by employing DFTB method for the pigment molecules. Subsequently, the numerical cost for the excited state is reduced by employing the TD-LC-DFTB method also in a QM/MM setting.

In the first part of the results, an extensive benchmark study of the TD-LC-DFTB method has been performed for the excitation energies and excitonic couplings of BChl molecules in gas-phase and within protein complex. Various higher level QM methods like DFT/MRCI, ADC(2), LC-DFT and hybrid DFT functionals have been compared during the benchmark studies. The super-molecule approach as well as the couplings based on transition charges have been computed during the investigation of excitonic couplings. The TD-LC-DFTB methods appears as a promising alternative compared to higher level QM methods with minimal loss of accuracy but with a three orders of magnitude faster speed compared to the LC-DFT functionals with DZP basis set. After performing the benchmark calculations, the TD-LC-DFTB is then applied to compute the site energies and spectral densities along the DFTB-QM/MM MD trajectory for the FMO complex of bacteria. Moreover, exciton dynamics calculations have also been performed based on an ensemble-averaged wave packet based scheme for the same complex.

In the second part, the present multiscale scheme has been employed on LH complexes of plant systems. The major antenna LHCII and the minor antenna CP29 complexes of the PSII system which are controlling the nonphotochemical regulations of higher plants are considered during the study. The spectral density agreement with experiments is much better compared to the bacterial LH complex which probably because of non-resolved peaks at some frequency regions for the latter system. Moreover, the exciton couplings and transfer rates at different pH states have also been calculated for the LHCII complex to give an overview of the non-photochemical quenching phenomena. Two different variants of force fields AMBER and OPLS have been employed in a QM/MM MD setting with DFTB for the CP29 complex. Both force fields show similar spectral densities which suggest that both force fields can be applied to model the LH complexes. Furthermore, excitonic couplings based on TrESP approach have been determined and coupled with the TD-LC-DFTB based site energy to build the Hamiltonian of the system for the CP29 complex. Finally, the Hamiltonian is propagated in a wave-packet based scheme in order to reveal the exciton dynamics between pigment networks.

In the final part of the thesis, an artificial LH complex is modeled by attaching porphyrin molecules on top of a clay surface. The surface behaves as protein environment like the biological LH complexes to hold the porphyrin pigment molecules in place. Such kind of porphyrin-clay system has experimentally been found to reveal remarkable energy transfer efficiency. After the system preparation, classical MD simulations followed by excitation energy calculations based on the TD-LC-DFTB approach has been performed for each porphyrin molecules. Moreover, excitonic couplings have also been calculated based on TrESP approach. As an extension of this system, currently spectral densities based on QM/MM MD simulations and exciton dynamics calculations are in progress. Moreover, spectral densities which were computed for the LH complexes will be utilized to perform density matrix calculations in future studies.

Appendix A

Chapter 2: Supporting Information

A.1 Computational Details

A.1.1 Equilibration and classical MD simulation of the LH complexes

The LH2 complex was minimized using the steepest descent algorithm (max. 50000 steps with a tolerance of 1000 kJ mol^{-1} nm^{-1}). Subsequently, the system was equilibrated for 3 ns at a temperature of 300 K using the Nosé-Hoover thermostat [343, 344] with a time step of 1 fs. During this step, the heavy atoms of the protein and all chromophores have been restrained to their initial positions by harmonic potentials (force constant: 1000 kJ mol^{-1} nm^{-1}). In addition, an NPT equilibration was performed with a length of 8 ns and a pressure of 1 bar using the Parrinello-Rahman barostat [345] and a time step of 2 fs. Subsequently, the restraints were removed and an NPT equilibration of 1 ns was performed. After the equilibration, the LH2 complex has been simulated for 1 ns.

As for the LH2 complexes, also for the simulations of the FMO complex, periodic boundary conditions were applied and long-range interactions were determined using the Particle-Mesh Ewald method. The FMO complex has been equilibrated in the same way as the LH2 complex. The NVT equilibration was performed with a length of 1 ns and the NPT equilibration with a length of 5 ns. The production run performed at 300 K, had a length of 100 ns with a timestep of 1 fs. From the 100 ns MD trajectory, 1 ns was taken to generate the sampled structures for the computation of the excitation energies and Coulomb couplings.

A.1.2 Excitonic Coupling

In the supermolecular approach, both the Coulombic and exchange interaction are considered by default. The Frenkel Hamiltonian for a two level donor and acceptor system can be written as

$$H_{mn} = \begin{pmatrix} E_m & V_{mn} \\ V_{nm} & E_n \end{pmatrix} . \tag{A.1}$$

In this expression, $E_{m,n}$ denote the excitation energies for the individual monomer and V_{mn} the excitonic coupling. For identical donor and acceptor molecules, i.e., if $E_m = E_n$ are equal, the eigenvalues are given by $\lambda_{1,2} = \frac{1}{2}(E_1 - E_2)$, where E_1 and E_2 are the two lowest excitonic energies in a supermolecular framework [160, 346].

For chromophores which are well separated the excitonic coupling can be estimated accurately by calculating the Coulomb coupling only, since the exchange part decays exponentially with distance. One way to accurately calculate the Coulomb coupling is the TrESP approach (transition charges by electrostatic potential). In this approach, the molecular transition density of each individual molecule is fitted by so-called atomic transition charges q_i^T. The coupling can be subsequently determined using [27, 73]

$$V_{mn} = \frac{1}{4\pi\epsilon_0} \sum_{i,j=1}^{m,n} \frac{q_i^T q_j^T}{\mid r_i - r_j \mid} . \tag{A.2}$$

In LC-DFTB, the computation of Coulomb couplings in a spirit of Mulliken transition charges is based on DFTB2 with the time-dependent extension. The Coulomb couplings V_{mn} are obtained using

$$V_{mn} = \sum_{a,b=m,n} Q_a Q_b \gamma_{ab} \tag{A.3}$$

where Q_a and Q_b denote the Mulliken transition charges and where the γ-function describes the second-order Coulomb interaction. Following the scheme of Ref. [124], the approach was extended using LC-DFTB. The advantages of computing Coulomb couplings in the spirit of DFTB is given by the transition charges, which can be calculated “on the fly” along a MD trajectory but depends on the accuracy of the DFTB method.

A.2 Benchmark

A.2.1 Retinal

Table A.1: Excitation energies (eV) of all-*trans* retinal geometries optimized in vacuum using different methods. Bond length alternation (BLA) is given in Å.

	CASSCF	HF	BH-LYP	B3LYP	DFTB	BLYP
BLA[a]	0.100	0.069	0.035	0.028	0.025	0.023
SORCI[a]	2.10	2.07	2.04	1.95	1.91	1.89
ZINDO/S	2.36	2.38	2.33	2.28	2.25	2.24
CAM-B3LYP	2.68	2.77	2.80	2.76	2.69	2.68
LC-BLYP	2.75	2.76	2.70	2.62	2.57	2.56
ωB97X	2.82	2.82	2.76	2.67	2.62	2.61
LC-DFTB	2.63	2.69	2.69	2.60	2.57	2.55
ADC(2)	1.94	2.01	2.03	1.93	1.89	1.87
SOS-ADC(2)	2.32	2.28	2.20	2.08	2.05	2.01

[a] Taken from Ref. 99.

Twist of β-ionone ring

Table A.2: Excitation energies (eV) of a 6-s-cis-11-cis PSB in vacuum for different twist angles of the β-ionone ring.

	33°	60°	90°	171°
SORCI[a]	1.96	1.99	2.28	1.95
ZINDO/S	2.32	2.40	2.58	2.27
CAM-B3LYP	2.68	2.66	3.08	2.70
LC-BLYP	2.63	2.70	2.94	2.60
WB97X	2.69	2.77	3.00	2.66
LC-DFTB	2.59	2.57	2.94	2.59
ADC(2)	1.94	2.03	2.27	1.92
SOS-ADC(2)	2.15	2.26	2.40	2.08

[a] Taken from Ref. 99.

Potential energy surface (PES)

LC-DFTB is benchmarked for the description of the potential energy surface (PES) from the 6-s-*cis*-11-*cis* PSB to a 6-s-*trans*-11-*cis* PSB configuration. The ground state pathway is taken, optimized with PBE0 and the energy profiles of the first two excited states are calculated using LC-DFTB. Fig. A.1 compares LC-DFTB with CC2 results from Ref. [347], where the same optimized geometries were used. LC-DFTB describes the PES qualitatively correct when compared to the CC2 results. Similar results have been obtained for the CAM-B3LYP functional (data not

shown), which corrects the wrong behavior of B3LYP displaying a red shift of the potential energy surface of the first excited state [347]. This failure of standard TD-DFT functionals can be seen also for TD-DFTB in Fig. A.1.

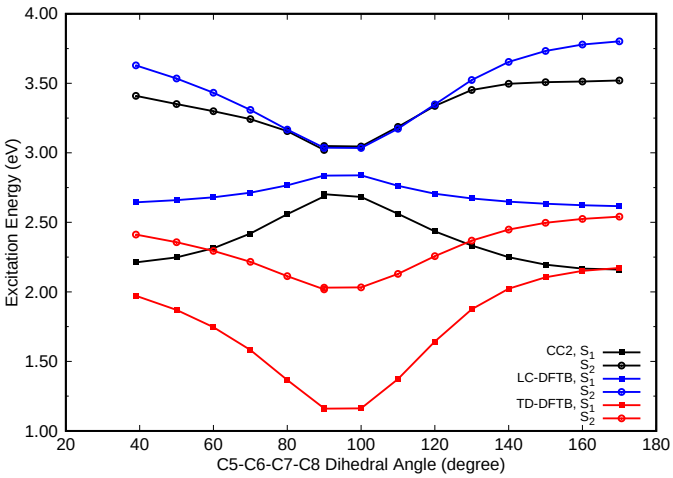

Figure A.1: Potential energy curves (S_1 and S_2) for the ground state isomerization coordinate from 6-s-cis- to 6-s-trans-PSB11. The CC2 values are taken from Ref. 347.

A.2.2 Bacteriochlorophyll a

Geometric and conformational impact on the absorption spectrum

Table A.3: Excitation energies (eV) of BChl a in vacuum. Structures optimized with HF, DFT and SCC-DFTB. D1 values are given in parenthesis.

	HF	CAM-B3LYP	BH-LYP	B3LYP	DFTB	BLYP
BLA (Å)	0.102	0.032	0.019	0.005	0.004	0.004
ZINDO/S	2.137	1.568	1.512	1.466	1.458	1.445
HF/CIS	3.326	2.358	2.120	1.865	1.840	1.814
TD-DFTB	1.822	1.801	1.859	1.811	1.796	1.765
TD-BP86	2.060	2.091	2.147	2.086	2.057	2.042
TD-B3LYP	2.181	2.121	2.173	2.137	2.122	2.100
LC-DFTB*	2.369	1.906	1.934	1.865	1.848	1.811
LC-DFTB	2.398	1.908	1.926	1.853	1.833	1.800
CAM-B3LYP	2.474	2.034	2.041	1.986	1.965	1.948
LC-BLYP	2.779	2.031	1.954	1.857	1.832	1.817
ωB97X	2.826	2.048	1.967	1.867	1.843	1.826
DFT/MRCI	1.861	1.652	1.694	1.644	1.621	1.596
SOS-CC2*	2.480	1.684	1.751	1.844	1.828	1.807
	(0.1204)	(0.1959)	(0.1854)	(0.0960)	(0.0968)	(0.1150)
SOS-ADC(2)*	2.404	1.438	1.538	1.749	1.732	1.672
	(0.0577)	(0.0834)	(0.0796)	(0.0562)	(0.056)	(0.0639)

* Modified side chains.

The BLA of the optimized BChl a structure has been calculated to study the structural differences using the diaza[18]-annulene substructure as described in the main text.

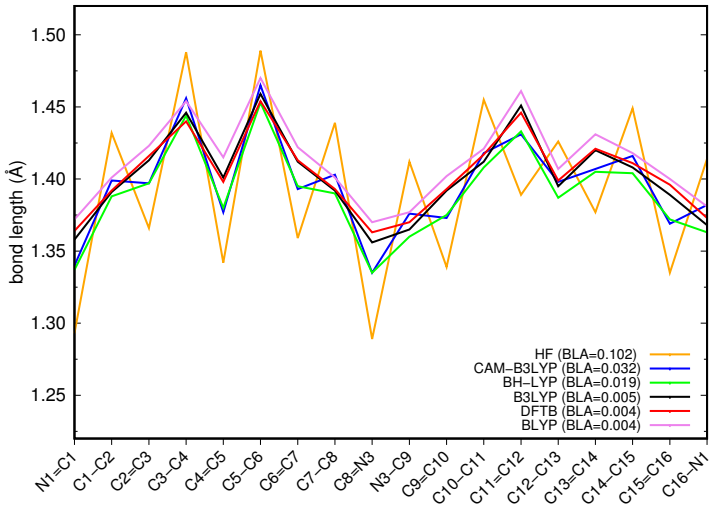

Figure A.2: Bond lengths of BChl a in vacuum obtained by different optimization methods and BLA values (Å).

In Fig. A.2, the bond lengths are plotted as well as the BLA values (in Å). In contrast to all other methods, HF shows a completely different trend of the bond lengths, i.e., an alternation of the single and double bonds over the whole ring. Standard DFT functionals (B3LYP and BLYP) as well as DFTB yield less alternations reflected also by the small BLA ($\sim$ 0.004) compared to HF (0.102). In a previous study [108] it was reported already that B3LYP leads to an improved description of BChl a geometries compared to HF, which is consistent with the results here, i.e., a significant overestimation of the BLA using HF. DFTB reveals a similar BLA as B3LYP and is therefore applicable for, e.g., QM/MM MD simulations of LH complexes. The larger the amount of HF in the functional, the stronger is the alternation of bond length as seen in the case of BH-LYP (0.019) or CAM-B3LYP (0.032) showing a higher BLA than B3LYP. The optimized structures of BChl a in vacuum show a planar structure, except the one obtained using CAM-B3LYP showing a bowl shape. This bowl shape can also be found in proteins. Hence, this structure is helpful to see whether a different shape has an influence on the excitation energies, as discussed below. SOS-CC2 and SOS-ADC(2) result in a slight red shift when computing the excitation energies on this geometry, which is not found by the other methods.

Effect of electrostatic environment

Table A.4: Vertical excitation energies (eV) in vacuum and with protein environment of BChl a chromophores in the FMO complex of *P. aestuarii*. Structures taken from Ref. 102.

	1	2	3	4	5	6	7
BLA (Å)	+0.006	+0.009	-0.004	+0.015	+0.017	+0.028	-0.008
vacuum							
ZINDO/S (10,10)	1.483	1.481	1.494	1.489	1.520	1.518	1.487
TD-DFTB	1.806	1.797	1.805	1.793	1.815	1.793	1.811
B3LYP	2.098	2.107	2.114	2.094	2.114	2.099	2.108
LC-DFTB	1.837	1.836	1.834	1.832	1.868	1.863	1.839
CAM-B3LYP	1.971	1.976	1.977	1.971	2.001	2.008	1.977
ωB97X	1.855	1.863	1.851	1.879	1.927	1.978	1.861
DFT/MRCI	1.647	1.636	1.642	1.633	1.645	1.633	1.634
SOS-ADC(2)	1.724	1.639	1.844	1.487	1.485	1.437	1.695
protein							
ZINDO/S (10,10)	1.482	1.474	1.504	1.511	1.587	1.829	1.491
TD-DFTB	1.756	1.755	1.784	1.764	1.806	1.796	1.778
B3LYP	2.076	2.080	2.102	2.084	2.113	2.119	2.091
LC-DFTB	1.805	1.821	1.835	1.822	1.892	1.975	1.844
CAM-B3LYP	1.960	1.972	1.978	1.977	2.034	2.138	1.983
ωB97X	1.849	1.883	1.868	1.920	2.023	2.263	1.902
DFT/MRCI	1.619	1.605	1.636	1.628	1.667	1.700	1.632
SOS-ADC(2)	1.611	1.456	1.670	1.449	1.512	1.705	1.538

Table A.5: Shifts (protein-vacuum) of the vertical excitation energies (eV) of BChl a chromophores in the FMO complex of *P. aestuarii*. Structures taken from Ref. 102.

	1	2	3	4	5	6	7
ZINDO/S	-0.001	-0.007	+0.010	+0.022	+0.067	+0.311	+0.004
TD-DFTB	-0.050	-0.042	-0.021	-0.029	-0.009	+0.003	-0.033
B3LYP	-0.022	-0.027	-0.012	-0.010	-0.001	+0.020	-0.017
LC-DFTB	-0.032	-0.015	+0.001	-0.010	+0.024	+0.112	+0.005
CAM-B3LYP	-0.011	-0.004	+0.001	+0.006	+0.033	+0.130	+0.006
ωB97X	-0.006	+0.020	+0.017	+0.041	+0.096	+0.285	+0.041
DFT/MRCI	-0.028	-0.031	-0.006	-0.005	0.022	+0.067	-0.002
SOS-ADC(2)	-0.113	-0.183	-0.174	-0.038	0.027	+0.268	-0.157

Exciton coupling I: Computational Cost

The computational cost for the supermolecular calculations has to be pointed out here: Using ORCA and the LC-DFT functional CAM-B3LYP taking 6 cores in parallel, the computation time takes about 2–3 days for one BChl a dimer, while for LC-DFTB it takes only about 15 minutes on a single core. Moreover, the Coulomb

couplings computed using LC-DFTB are obtained in just few seconds. This highlights the power of the LC-DFTB approach for fast computations and applications for the study of larger systems such as LH complexes.

Exciton coupling II: Light Harvesting Complex II (LH2) B850 ring

Table A.6: Exciton couplings and Coulomb couplings for the respective BChl a dimers $\alpha\beta$ (V_1) and $\beta\alpha$ (V_2) of the LH2 B850 ring. The distance is measured between the respective Mg ions. The excitonic couplings have been determined using the supermolecular approach as half of the energy splitting. The partial charges of the TrESP and Tr-Mulliken values are based on CAM-B3LYP. The mean absolute error (MAE) is given in the last row with respect to the supermolecular results using the ωB97X and CAM-B3LYP functionals.

Distance	Type	Supermolecular approach			Coulomb Coupling		
(Å)		ωB97X	CAM-B3LYP	LC-DFTB	TrESP	Tr-Mulliken	LC-DFTB
9.63	V^2	0.071	0.070	0.065	0.061	0.058	0.075
9.28	V^1	0.052	0.052	0.049	0.045	0.039	0.052
9.53	V^2	0.066	0.065	0.061	0.058	0.056	0.072
8.55	V^1	0.047	0.050	0.049	0.036	0.028	0.034
9.47	V^2	0.073	0.074	0.064	0.061	0.055	0.073
8.94	V^1	0.055	0.055	0.060	0.047	0.040	0.052
9.44	V^2	0.072	0.072	0.068	0.060	0.057	0.074
9.51	V^1	0.043	0.042	0.041	0.038	0.033	0.046
9.86	V^2	0.066	0.065	0.062	0.059	0.057	0.073
8.95	V^1	0.045	0.047	0.047	0.039	0.033	0.044
9.55	V^2	0.061	0.059	0.058	0.054	0.049	0.066
9.15	V^1	0.073	0.081	0.077	0.057	0.050	0.066
9.26	V^2	0.072	0.076	0.065	0.057	0.051	0.069
8.60	V^1	0.059	0.067	0.067	0.041	0.033	0.041
9.38	V^2	0.071	0.075	0.065	0.057	0.055	0.069
8.83	V^1	0.061	0.068	0.067	0.048	0.040	0.051
MAE wrt ωB97X	-	-	0.003	0.005	0.011	0.016	0.005

Table A.7: Previous studies on exciton couplings of LH2 complexes based on the X-ray structure. The Coulomb couplings of the most strongly coupled BChl a dimers are displayed.

		Methods		Coulomb Couplings	
Reference	X-ray Structure	Excitation Energy	Coulomb Couplings	cm^{-1}	eV
Krüger et *al.* [348] (1998)	LH2 *Rps. ac.*	CIS (3-21G*)	TDC	238 213	0.03 0.03
Cory et *al.* [120] (1998)	LH2 *Rs. ms.*	INDO-CIS	INDO-CIS effective Hamiltonian	790 369	0.10 0.05
Scholes et *al.* [349] (1999)[a]	LH2 *Rps. ac.*	CIS	CIS (6-31G*) (scaled exp.)	320 255	0.04 0.03
Madjet et *al.* [73] (2006)	LH2 *Rps. ac.*	CIS, TD-DFT/B3LYP (6-31G*)	TrESP, CIS TrESP,TD-DFT/B3LYP	245 211	0.03 0.03
Neugebauer [166] (2008)	LH2 *Rps. ac.*	TD-DFT +FDE (SOAP/TZP)	supermol. TD-DFT + FDE supermol. TD-DFT[b] FDEc	242 252 232 200	0.03 0.03 0.03 0.02
Cupellini et *al.* [117] (2016)	LH2 *Rps. ac.*	TD-DFT + MMPOL, CAM-B3LYP (6-31G(d))	TD-DFT + MMPOL by EXAT[c]	409 362	0.05 0.04
Segatta et *al.* [127] (2017)	LH2 *Rps. ac.*	RASSCF/RASPT2 TD-DFT + MMPol CAM-B3LYP	TDC[c] TD-DFT + MMPol	563 474 336 288	0.07 0.06 0.04 0.04

[a]also performed supermol. calc. CIS(6-31G*): 0.09 eV (730 cm^{-1}) and 0.07 eV (550 cm^{-1}); [b]DFT E_{xc} functional of GGA type: exchange by Becke, and correlation functional by PW91 [166]; [c]used program EXAT for computing the excitonic Hamiltonian [117, 350]; [d]no explicit screening factor used

Table A.8: Previous studies on Coulomb couplings of LH2 complexes computed on sampled structures along classical MD trajectories. Values of the most strongly coupled BChl a dimers are displayed.

		Methods		Coulomb Couplings	
Reference	X-Ray Structure, MD	Excitation Energy	Coulomb Coupling	cm^{-1}	eV
Olbrich et *al.* [27] (2011)	LH2 *Rs. ms.*, 12 ps	ZINDO/S-CIS	PDA[a]	274	0.03
			TrESP, TD-DFT/B3LYP	173	0.02
				140	0.02
Cupellini et *al.* [117] (2016)	LH2 *Rps. ac.*, 100ns	TD-DFT + MMPol,	TD-DFT + MMPol	339	0.04
		CAM-B3LYP (6-31G(d))	by EXAT[b]	317	0.04

[a] transition densities obtained by ZINDO/S-CIS

[b] EXAT is the program used for computing the excitonic Hamiltonian, cf. Ref. [117, 350]

A.3 Performance of LC-DFTB on biological model systems

A.3.1 Rhodopsins

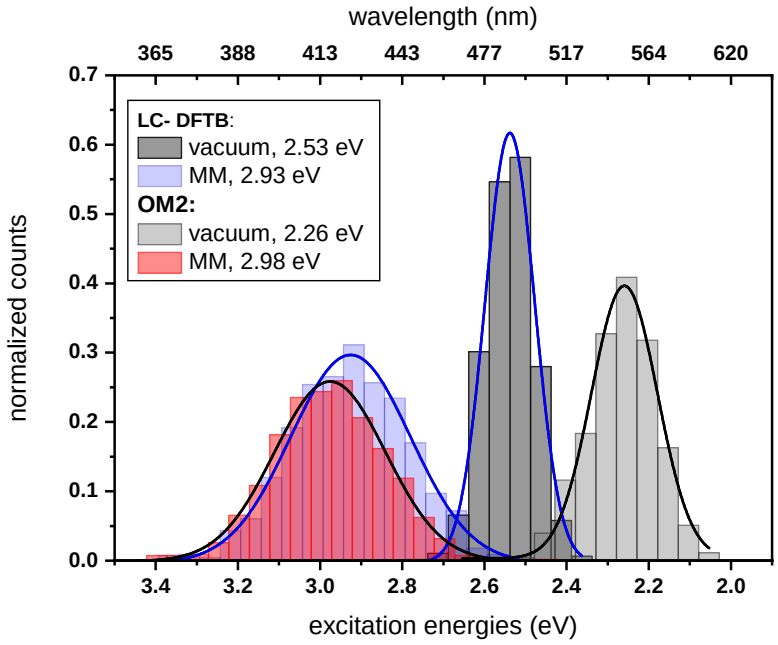

Figure A.3: Simulated absorption spectrum of ppR. LC-DFTB and OM2/MRCI have been used for the computation of the excitation energies. The histograms are based on snapshot geometries of the 1 ns-long QM/MM MD trajectories. Plotted are the excitation energies weighted by the oscillator strength for (i) only the retinal chromophore (vacuum) and (ii) with additional fixed MM point charges to account for the protein environment (MM). Gaussian functions are used to determine the corresponding maxima, in blue: LC-DFTB and in black: OM2/MRCI.

A.4 Light-harvesting complexes

A.4.1 LH2 complex of *Rs. molischianum*, QM/MM optimized model

Table A.9: BLA (Å), vacuum excitation energies (eV) and the resulting shifts (eV, protein-vacuum) have been determined of the B800 of LH2 from *Rhodospirillum (Rs.) molischianum*. The excitation energies have been calculated using LC-DFTB and ZINDO/S based on the DFTB QM/MM optimized model.

		LC-DFTB			ZINDO/S		
BChl	BLA	vacuum	protein	shift	vacuum	protein	shift
1	0.010	1.827	1.839	+0.012	1.458	1.522	+0.064
2	0.013	1.836	1.888	+0.052	1.463	1.604	+0.141
3	0.006	1.823	1.857	+0.034	1.456	1.571	+0.115
4	0.007	1.828	1.811	-0.017	1.461	1.442	-0.019
5	0.014	1.842	1.841	-0.001	1.471	1.465	-0.006
6	0.010	1.822	1.796	-0.026	1.453	1.428	-0.025
7	0.011	1.822	1.828	+0.006	1.456	1.485	+0.029
8	0.011	1.830	1.834	+0.004	1.465	1.481	+0.016

Table A.10: Same as in Tab. A.9, but for the B850 ring.

		LC-DFTB			ZINDO/S		
BChl	BLA	vacuum	protein	shift	vacuum	protein	shift
1	0.005	1.828	1.846	+0.018	1.457	1.498	+0.041
2	0.001	1.827	1.827	+0.000	1.454	1.454	+0.000
3	0.008	1.833	1.836	+0.003	1.463	1.474	+0.011
4	0.003	1.826	1.821	-0.005	1.452	1.460	+0.008
5	0.007	1.826	1.835	+0.009	1.456	1.473	+0.017
6	0.004	1.831	1.826	-0.005	1.456	1.464	+0.008
7	0.003	1.833	1.832	-0.001	1.458	1.461	+0.003
8	0.003	1.822	1.812	-0.010	1.448	1.444	-0.004
9	0.005	1.826	1.824	-0.002	1.457	1.466	+0.009
10	0.005	1.831	1.842	+0.011	1.453	1.461	+0.008
11	0.005	1.833	1.848	+0.015	1.460	1.517	+0.057
12	0.002	1.826	1.820	-0.006	1.449	1.447	-0.002
13	0.005	1.833	1.818	-0.015	1.461	1.455	-0.006
14	0.004	1.828	1.818	-0.010	1.449	1.440	-0.009
15	0.005	1.834	1.825	-0.009	1.459	1.461	+0.002
16	0.002	1.820	1.820	+0.000	1.446	1.470	+0.024

Table A.11: Average excitation energies and variances (eV) based on DFTB QM/MM optimized BChl a structures of the B800 and the B850 ring systems of LH2 from *Rs. molischianum*. Shown are the excitation energies for the individual BChl a chromophores with and without the influence of the protein environment. Moreover, the excitonic energies (eV), i.e., the lowest eigenvalues are shown for the ring systems. The excitation energies have been computed using ZINDO/S, Coulomb couplings with LC-DFTB and TrESP.

	B800	B850	B850 shift
vacuum[a]	1.460 ± 0.006	1.455 ± 0.005	–0.005
protein[a]	1.500 ± 0.062	1.465 ± 0.019	–0.035
ring system			
LC-DFTB	1.427	1.372	–0.055
TrESP	1.427	1.358	–0.069
Experimental [178]			–0.085

[a] BChl a monomer

LH2 complex, classical MD simulations

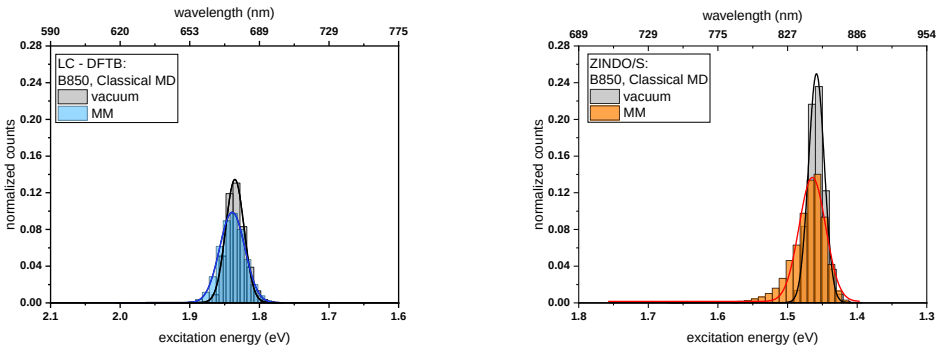

(a) (b)

Figure A.4: Simulated absorption spectrum of the B850 ring of LH2 from *Rs. molischianum*. (a) LC-DFTB has been used for the computation of the excitation energies; (b) ZINDO/S has been used for the computation of the excitation energies. All histograms are based on snapshot geometries along a classical MD trajectory of 1 ns length. Plotted are the excitation energies weighted by the oscillator strength for (i) only the BChl a chromophore (vacuum) and (ii) with additional fixed MM point charges to account for the protein environment (MM). Gaussian functions have been used to determine the corresponding maxima.

LH2 complex *Rs. molischianum* vs. *Rps. acidophila*

The LH2 complexes of *Rps. acidophila* and *Rs. molischianum* are different, e.g., in the number of chromophores or the distances between the chromophores. Although the main absorption maxima are in the same range, i.e., the rings are both called B800 and B850, they differ slightly in the absorption spectra as has been shown in previous studies [178, 352, 353].

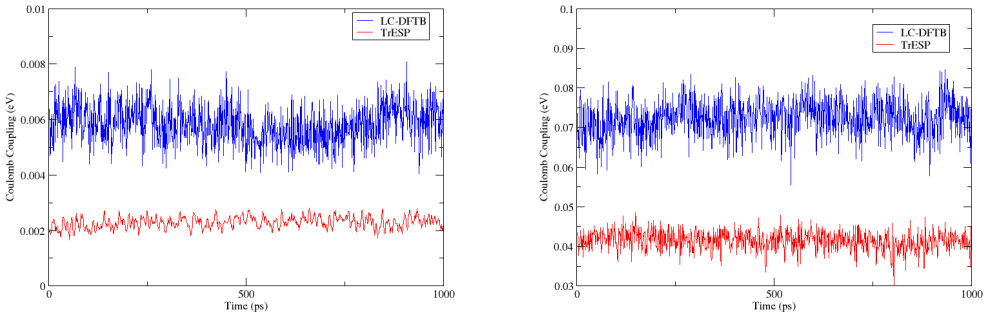

(a) (b)

Figure A.5: Coulomb couplings sampled along a classical MD trajectory of 1 ns length for (a) one BChl a dimer pair with the strongest Coulomb couplings chosen as example for the B800 ring and for (b) one BChl a dimer pair with the strongest Coulomb couplings chosen as example for the B850 ring.

Table A.12: Average excitation energies and standard deviations (eV) based on sampled structures along a classical MD trajectory of LH2 from *Rs. molischianum*. Shown are the excitation energies for the individual BChl a chromophores with and without the influence of the protein environment. The average excitation energies are obtained by averaging the maxima of Gaussian fits to the distributions of the respective chromophores. In addition, excitonic energies (eV), i.e., the lowest eigenvalues are shown for the complete ring systems. The excitonic energies have been obtained by the maxima of Gaussian fits to the distributions of the exciton energies, respectively. The excitation energies have been computed using ZINDO/S, Coulomb couplings using LC-DFTB and TrESP.

	B800	B850	B850 shift
vacuum[a]	1.462 ± 0.002	1.458 ± 0.004	–0.004
protein[a]	1.480 ± 0.008	1.466 ± 0.010	–0.014
ring system			
LC-DFTB	1.449	1.367	–0.082
TrESP	1.451	1.401	–0.050
Experimental [178]			–0.085

[a]BChl a monomer

The computation of both models using LC-DFTB shows differences in the excitation energy as well as excitonic energy ranges, especially for the B800 ring when using the DFTB QM/MM optimized models. The excitation energy range in vacuum is about twice as large for both ring systems of the LH2 complex *Rps. acidophila* compared to the LH2 complex *Rs. molischianum*. This indicates, that the BChl a geometries are differently modified through the respective protein environment. This is reflected also in the resulting energy shift between the rings, since the LH2 complex of *Rps. acidophila* shows an vacuum energy shift of 0.027 eV between both rings, while no shift is obtained for the LH2 complex of *Rs. molis-*

Table A.13: Excitonic energies (eV) of LH2 from *Rs. molischianum* on the LC-DFTB level of theory obtained for the DFTB QM/MM optimized model and sampled along an MD trajectory.

Excitonic energy	QM/MM optimized	classical MD
B800		
E_1	1.794	1.815
E_2	1.809	1.828
E_3	1.824	1.837
E_4	1.833	1.845
E_5	1.843	1.853
E_6	1.844	1.862
E_7	1.857	1.873
E_8	1.890	1.891
B850		
E_1	1.730	1.737
$E_{2,3}$	1.733, 1.738	1.746, 1.752
$E_{4,5}$	1.746, 1.748	1.759, 1.766
$E_{6,7}$	1.758, 1.765	1.774, 1.782
E_8	1.773	1,792
E_9	1.820	1,838
$E_{10,11}$	1.848, 1.849	1.861, 1.870
$E_{12,13}$	1.898, 1.908	1.914, 1.923
$E_{14,15}$	1.965, 1.968	1.975, 1.985
E_{16}	2.004	2.018

Table A.14: Excitonic energy range (eV) dependent how the averaged values are computed, of the QM/MM optimized model and the structures sampled along the MD trajectory of LH2 from *Rs. molischianum*. LC-DFTB and ZINDO/S have been used for the computations of the excitation energies. The Coulomb couplings have been calculated using LC-DFTB and TrESP. Values obtained by averaging firstly the Hamiltonians are given in parenthesis.

		QM/MM optimized	classical MD
B800			
Excitation energy	Coulomb coupling		
LC-DFTB	LC-DFTB	0.096	0.076 (0.030)
	TrESP	0.094	0.072 (0.024)
ZINDO/S	LC-DFTB	0.179	0.137 (0.034)
	TrESP	0.178	0.134 (0.029)
B850			
LC-DFTB	LC-DFTB	0.274	0.281 (0.265)
	TrESP	0.227	0.163 (0.147)
ZINDO/S	LC-DFTB	0.284	0.288 (0.265)
	TrESP	0.238	0.175 (0.147)

chianum. In both proteins the inclusion of the protein environment has minor effects, see Tab. A.15, i.e., the shifts increase only slightly. Differences are also found in the Coulomb coupling values of the B800 ring of *Rps. acidophila*, which are larger (0.007-0.010 eV) than in LH2 of *Rs. molischianum* (0.006 eV), since the

Table A.15: Average excitation energies and standard deviations (eV) based on DFTB QM/MM optimized BChl a structures of the B800 and the B850 ring systems sampled along a MD trajectory of LH2 from *Rps. acidophila*. Shown are the excitation energies for the individual BChl a chromophores with and without the influence of the protein environment. Moreover, excitonic energies (eV), i.e. the lowest eigenvalues are shown for the complete ring system. Excitation energies have been computed using LC-DFTB, Coulomb couplings using LC-DFTB and TrESP.

	B800	B850	B850 shift
QM/MM optimized			
vacuum[a]	1.845 ± 0.004	1.818 ± 0.002	–0.027
protein[a]	1.844 ± 0.012	1.813 ± 0.004	–0.031
ring system	1.802	1.707	–0.095
	1.811	1.714	–0.097[b]
classical MD			
vacuum[a]	1.838 ± 0.002	1.828 ± 0.002	–0.010
protein[a]	1.837 ± 0.004	1.827 ± 0.004	–0.010
ring system	1.799	1.718	–0.081
	1.814	1.726	–0.088[b]
Experimental [351], low temperature (1.2K, 5K)			–0.116
Experimental [351], room temperature			–0.102

[a]BChl a monomer; [b]second lowest excitonic energy value

BChl a chromophores are arranged slightly more close.

The structures from the MD trajectories, show a decrease of the differences between both LH2 complexes compared to the QM/MM optimized model, as shown in the figures in the main text (Sec. 4.2.1). This indicates, that the QM/MM optimized models obtain local minima, while sampling improves the description, as discussed in the main text. The resulting energy shifts of B800-B850 considering the sampled Hamiltonian is larger for LH2 of *Rps. acidophila* (0.081 eV) than for LH2 of *Rs. molischianum* (0.078 eV). This is qualitatively in agreement with experimental results, suggesting a slightly larger energy gap of LH2 of *Rps. acidophila* [178, 351–353]

Cupellini et al. [117] investigated the LH2 complex *Rps. acidophila*, whose work differs in several aspects from ours: (i) we use a DFTB QM/MM optimized model instead of the crystal structures, which could lead to deviations in the results, due to the missed lipid membrane and water environment; (ii) Cupellini et al. [117] made use of symmetry and considered only one BChl a chromophore of each type, i.e., one α, β, γ- BChl a chromophore. The geometry optimization of all chromophores breaks this symmetry which was there by construction of the system and leads to more static disorder, i.e., to a larger spread in the diagonal Hamiltonian matrix elements; (iii) to compute the Coulomb couplings, Cupellini

et al. [117] used CAM-B3LYP, which leads to similar values as LC-DFTB as shown in Sec. 3.2.4, main text. The LC-DFTB Coulomb approximation, however, tends to increase the values slightly. Further, Cupellini et al. [117] employed a polarizable embedding scheme decreasing the couplings slightly. In the case of the B800 ring Cupellini et al. [117] find a splitting of 0.03 eV considering the lowest and the highest excitonic energy, while we find a splitting of about 0.09 eV using LC-DFTB and TrESP. This mainly results from the diagonal disorder, since the couplings do not contribute much. For the B850 ring, they report a splitting of 0.205 eV, while LC-DFTB yields 0.274 eV and TrESP 0.227 eV. Here, the diagonal disorder is less important, and the main difference stems from the different couplings. However, the absolute value of the B850 splitting is overestimated independent of the used excitonic state as discussed in Ref. 117 by all computational approaches when compared to the experimental value of 0.179 eV at low temperatures [180].

Table A.16: Excitonic energies (eV) of LH2 *Rps. acidophila* using LC-DFTB for both, i.e. excitation energies and Coulomb couplings. Data are given for the QM/MM optimized model and for sampled structures along a MD trajectory.

Excitonic energy	QM/MM optimized	classical MD
B800		
E_1	1.802	1.799
E_2	1.811	1.814
E_3	1.826	1.823
E_4	1.832	1.832
E_5	1.838	1.841
E_6	1.849	1.850
E_7	1.852	1.859
E_8	1.867	1.869
E_9	1.923	1.882
E_9–E_1	0.121	0.083
B850		
E_1	1.707	1.718
$E_{2,3}$	1.714, 1.717	1.726, 1.731
$E_{4,5}$	1.725, 1.728	1.737, 1.742
$E_{6,7}$	1,735, 1.738	1.749, 1,755
$E_{8,9}$	1.744, 1.752	1.763, 1.771
$E_{10,11}$	1.813, 1.818	1.831, 1.839
$E_{12,13}$	1.850, 1.855	1.868, 1.876
$E_{14,15}$	1.903, 1.910	1.922, 1.930
$E_{16,17}$	1.962, 1.966	1.979, 1.987
E_{18}	1.998	2.017
E_{18}–E_1	0.291	0.299

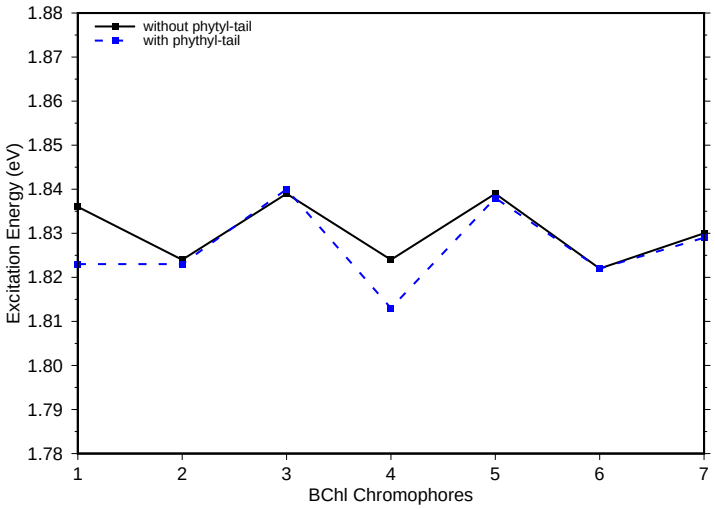

Figure A.6: Excitation energies (eV) in vacuum of the seven BChl a chromophores from FMO with and without the phythyl tail computed using LC-DFTB.

FMO complex, QM/MM optimized structure

Differences are found in the vacuum excitation energies for chromophore 1 and 4, when considering the complete BChl a chromophore, i.e. with the phythyl tail. These differences lead to a red shift for both chromophores and are in agreement with a previous study [185].

Table A.17: Coulomb couplings (eV) between all BChl a chromophores in the FMO complex using LC-DFTB. Monomer excitation energies using LC-DFTB are given on the diagonal and the strongest couplings in bold.

H_{mn}	1	2	3	4	5	6	7
1	1.829	**0.044**	0.003	0.002	0.002	0.002	0.000
2	**0.044**	1.802	**0.019**	0.004	0.002	0.005	0.004
3	0.003	**0.019**	1.835	**0.021**	0.001	0.005	0.000
4	0.002	0.004	**0.021**	1.808	**0.043**	0.010	**0.019**
5	0.002	0.002	0.001	**0.043**	1.831	**0.037**	0.001
6	0.002	0.005	0.005	0.010	**0.037**	1.798	**0.028**
7	0.000	0.004	0.000	**0.019**	0.001	**0.028**	1.854

FMO complex, classical MD simulation

The Coulomb couplings averaged along a classical MD trajectory are shown in Fig. A.8. LC-DFTB shows qualitatively the same trend as TrESP. As expected from the results presented in the benchmark study in the main text (Sec. 3.2.3 and 3.2.4), LC-DFTB overestimates the Coulomb couplings. Both LC-DFTB and TrESP

Table A.18: Maximum and minimum of excitation energy and excitonic energy of the DFTB QM/MM optimized BChl a chromophores of the FMO complex. ZINDO/S is used for the computation of excitation energies without (vacuum) and with the protein environment as fixed MM point charges. Coulomb couplings are computed using LC-DFTB and TrESP.

	Max	Min	shift
vacuum[a]	1.486	1.452	–0.034
protein[a]	1.544	1.451	–0.093
coupled chromophores			
LC-DFTB	1.567	1.408	–0.159
TrESP	1.553	1.428	–0.125
Experimental [183]	1.563	1.503	–0.060

[a]BChl a monomer

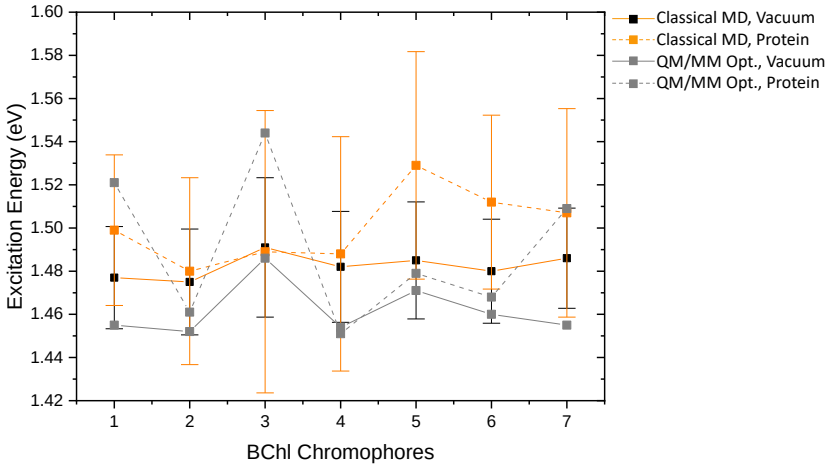

Figure A.7: Excitation energies (eV) of the FMO complex of the seven BChl a chromophores of the DFTB QM/MM optimized model and maxima of the Gaussian distributions of the classical MD sampled structures; calculated in vacuum and with fixed MM point charges using ZINDO/S.

display qualitatively the same trend as the Coulomb couplings obtained using TD-DFT/MMPol [185] and PDA [186] in previous studies. Differences are only found for the BChl a dimer 6-7, where the values increased from dimer 5-6 to dimer 6-7. One reason might be the different FMO complex in the case of Ref. [185] using the FMO complex of *P. aestuarii* while in the case of Ref. [186] the trimer of the FMO complex *C. tepidum* has been used.

Non-Gaussian energy distribution are obtained when using ZINDO/S. This behavior was already reported in a previous study concerning the trimer of the FMO complex using ZINDO/S for the excitation energies [27, 78].

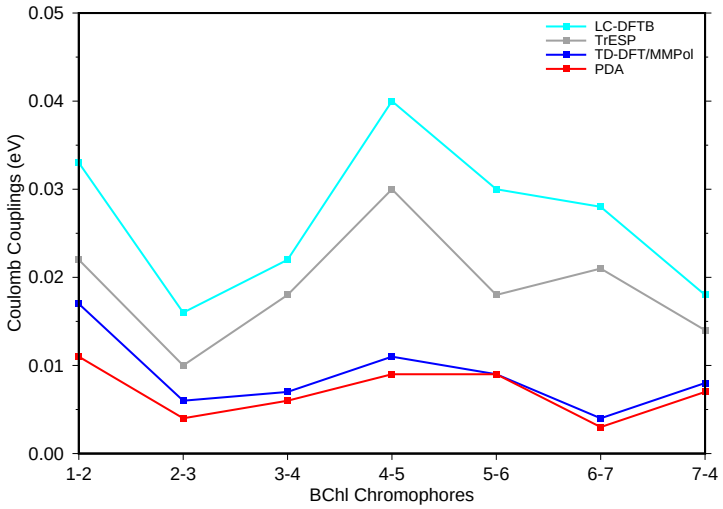

Figure A.8: Coulomb couplings (eV) averaged along a classical MD trajectory. The values for TD-DFT/MMPol have been taken from Ref. 185 and the values of PDA from Ref. 186.

Table A.19: Strongest Coulomb couplings (eV) computed using LC-DFTB for the DFTB QM/MM optimized model of BChl a dimers and average Coulomb couplings as maxima of Gaussian fits of the MD sampled structures.

BChl a dimer	QM/MM-optimized	Classical MD
1-2	0.044	0.033 ± 0.006
2-3	0.019	0.016 ± 0.001
3-4	0.021	0.022 ± 0.006
4-5	0.043	0.040 ± 0.005
5-6	0.037	0.029 ± 0.007
6-7	0.028	0.028 ± 0.005
7-4	0.019	0.018 ± 0.006

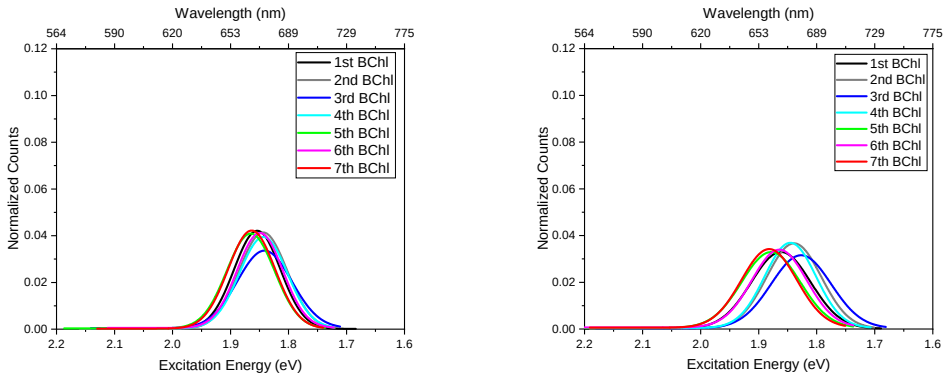

(a) (b)

Figure A.9: Excitation energies (eV) of the sampled BChl a chromophores of the FMO complex using LC-DFTB. (a) vacuum; (b) with fixed MM point charges.

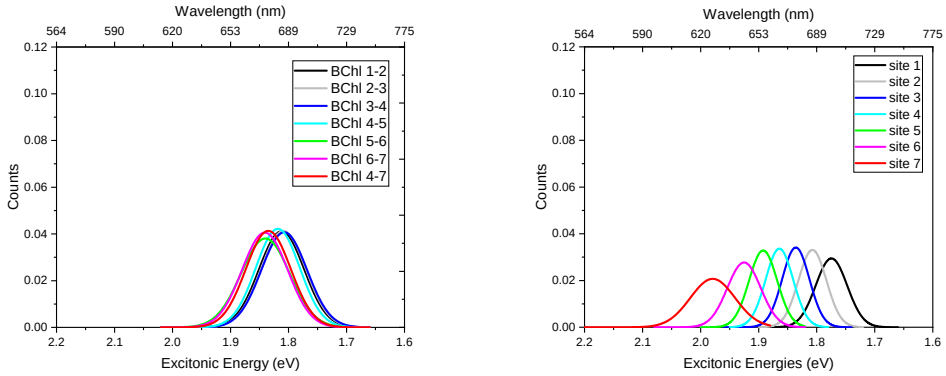

(a) (b)

Figure A.10: Excitonic energies (eV) of the sampled BChl a chromophores of the FMO complex using LC-DFTB. (a) BChl a dimers; (b) fully coupled system.

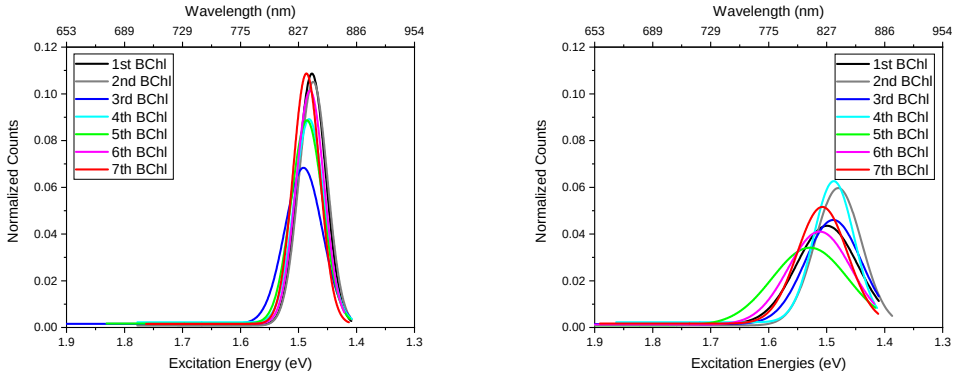

(a) (b)

Figure A.11: Excitation energies (eV) of the sampled BChl a chromophores of the FMO complex using ZINDO/S. (a) vacuum; (b) with fixed MM point charges.

Table A.20: Maximum and minimum excitation and excitonic energies of the structures along a MD simulation of the FMO complex. ZINDO/S is used for the computation of the excitation energies without (vacuum) and with the protein environment as fixed point charges. The Coulomb couplings have been computed using LC-DFTB and TrESP.

	Max	Min	shift
vacuum^a	1.491	1.475	–0.016
protein^a	1.529	1.480	–0.049
coupled chromophores			
LC-DFTB	1.657	1.436	–0.221
TrESP	1.648	1.446	–0.202
Experimental [183]	1.563	1.503	–0.060

Table A.21: Excitonic energies (eV) of the FMO complex from *C. tepidum* based on the QM/MM optimized structures and averaged along a MD trajectory. The excitation energies and the Coulomb couplings have been computed using LC-DFTB.

QM/MM-optimized	MD simulation
1.756	1.775
1.767	1.807
1.790	1.836
1.833	1.864
1.848	1.892
1.864	1.925
1.899	1.979

Appendix B

Chapter 3: Supporting Information

B.1 Computational Details

Starting point of the simulations was the crystal structure for the FMO complex of the green sulfur bacterium *Chlorobaculum tepidum* (pdb code: 3eni). The first seven missing residues were modeled using the MODELLER tool [354]. The protein was solvated using TIP3P water molecules in a cubic box with a side length of 121 Å. Moreover, the CHARMM36m force field has been employed in connection with the GROMACS MD engine in version 5.1.4. For the BChl pigments, the force field has been described in an earlier study [76]. After energy minimization, a 2 ns NVT run was performed at 300 K with a 1 fs integration time step keeping position restrains for protein and pigment molecules. Subsequently, a 5 ns NPT equilibration was carried out with a 2 fs time step, restraining protein backbone and pigment molecules. After that, another 5 ns NPT equilibration was performed using a 2 fs time step keeping restraints on the Cα atoms of the protein and the magnesium atoms of the pigment molecules. Finally, a 160 ns long NPT simulation was performed again using a 2 fs integration time step without any restraints. The LINCS algorithm has been applied constraining on all hydrogen bonds when the time step was 1 fs and on all bonds for the time step of 2 fs. During the first 1 ns and the final 100 ns, the coordinates were stored every 1 ps and 10 ps generating 1,000 and 10,000 frames, respectively, to be used in a proper sampling of the site energy calculations. Furthermore, we also collected the coordinates after 1 ns, 60 ns and 160 ns which were used as starting structures for the DFTB-QM/MM dynamics (see Table B.1).

For the QM/MM dynamics, we have chosen the DFTB3 level of theory together with the 3OB-f parameter set derived with a special emphasis on reproducing vi-

brational frequencies (DFTB3/3OB-f). The individual BChl pigments were treated using DFTB combined with the CHARMM36m force field as implemented in GROMACS and the DFTB+ interface [134, 197]. The phytyl tail was included in the MM region with a cut at the so-called C1-C2 bond and hydrogen atom capping. The same truncated structure of the pigment molecules has also been considered in the excitation energy and excitonic coupling calculations described below. From the three different staring conformations from the classical MD trajectory, 60 ps NPT production runs were performed with a time step of 0.5 fs without any bond constraints. Furthermore, the coordinates for the last 40 ps were stored using a stride of 1 fs. Thus, 3×40,000 frames were generated in total for the three different starting conformations which were subsequently used in the excitation energy calculations. Having three different starting conformations helps us to get an idea about the reproducibility of the spectral densities from the QM/MM MD trajectories. Furthermore, a 1.1 ns long QM/MM MD simulation was also carried out with 1 fs integration time step from the first set of initial geometries and the coordinates were saved for the last 1 ns with a 1 ps stride. This scheme produces a total of 1,000 frames which are used to calculate the average site energy for each pigment in the monomeric unit as shown in the Table B.1.

Table B.1: Table of combinations concerning the ground state dynamics and excited state calculations to determine spectral densities and/or couplings.

Ground State Dynamics	Length of Simulation	Excited State Calculation (QM/MM)		Spectral Density	Coupling
		TD-LC-DFTB	ZINDO/S-CIS		
QM/MM MD	40 ps	✓	✓	✓	✗
	40 ps	✓	✗	✓	✗
	40 ps	✓	✗	✓	✗
	1 ns	✓	✓	✗	✗
Classical MD	40 ps	✓	✗	✓	✓
	40 ps	✓	✗	✓	✗
	1 ns	✓	✗	✗	✗
	100 ns	✓	✓	✗	✗

To calculate the excitation energies and subsequently the wave packet dynamics for a classical MD trajectory, we used the starting conformation which was stored after 1 ns from the 160 ns long trajectory and performed a classical MD simulation of 40 ps length. The coordinates were stored every 1 fs while we used a time step of 0.5 fs for the integration not constraining any bonds in order to increase the similarity to the QM/MM dynamics. An additional 40 ps trajectory lead to further 40,000 frames. A second set of coordinates was produced with starting

conformations at 60 ns of the above described unbiased simulations. These two sets were then employed to determine the spectral densities based on classical MD simulations (see Table B.1). The computational cost for the QM/MM MD was roughly a factor of five higher than that for the classical MD.

Additionally, we performed *ab-initio* MD (AIMD) simulations in vacuum for a BChl molecule truncated at the C1-C2 bond. For the AIMDs, three DFT functionals were chosen: B3LYP, CAM-B3LYP and ωB97X using the def2-TZVP basis set as implemented in the ORCA program package [131]. The simulations were performed at 300 K using the Berendsen thermostat, which is the only thermostat implemented at the moment in the ORCA package. Due to the high computational costs, only a short production run of 100 fs using a 0.5 fs time step was performed. A simulation of the BChl in vacuum was also executed on the DFTB level of theory, using the 3OB and 3OB-f parameter sets. For consistency, thermostat and time step as well as time length are the same as for the AIMD simulations. The LC extension of DFTB could not be used here, since only the electronic part of Mg parameters exists so far, but not the repulsive part, which is needed to compute the ground state dynamics. These AIMD and DFTB MD simulations of BChl in vacuum were performed to investigate the bond length alternation (BLA) of the BChl chromophore. The BLA was computed on the vacuum sampled structures as well as on the sampled QM/MM and classical MD simulation of the FMO complex including the protein environment. For the latter ones, the first BChl chromophore is presented here as an example.

After collecting the snapshots from the ground state dynamics, we have used two approaches, i.e., TD-LC-DFTB and ZINDO/S-CIS, to determine the excitation energies of the individual BChl molecule in a QM/MM fashion. To this end, we moved the QM region into the center of the simulation box using the periodic boundary conditions and considered the rest of the box as point charge environment. In this way, one can significantly reduce spurious boundary effects in the non-periodic QM/MM excited state calculations. Here, we would like to point out that ZINDO/S is a short hand notation for ZINDO/S-CIS (10,10) which represents a configuration interaction singles calculations on a ZINDO/S Hamiltonian including the 10 highest occupied molecular orbitals (HOMOs) and the 10 lowest unoccupied molecular orbitals (LUMOs) as active space. Such a small active space has been used during the ZINDO/S parametrization and has successfully being used for BChl and Chl molecules [59, 254]. The TD-LC-DFTB calcula-

tions were performed using the OB2 parameter set as implemented in the DFTB+ code [69, 247, 248] whereas for the ZINDO/S calculations, we have employed the ORCA package [131]. For these two approaches the computational efforts differ, i.e., while a TD-LC-DFTB calculation takes around 2 min per snapshot, a ZINDO/S calculations needs about 15 seconds on a standard CPU. Furthermore, for the TD-LC-DFTB calculations, the range-separating parameter ω was chosen to be 0.3 which is close to the default of long-range corrected DFT functionals [197]. Subsequently, the Q_y state of the BChl pigments which is responsible for the absorption in the visible range was extracted from the 10 calculated excited states. In a next step, the energy autocorrelation functions of this state were determined and subsequently its cosine transformations was performed to obtain the spectral densities (details see below). The combinations of ground state simulations and excited state calculations which have been used for spectral density calculations can be found in Table B.1.

In addition, the excitonic couplings between the chromophores were calculated using the TrESP method [73, 75] (see below) for the first set of the classical MD simulations (see Table B.1) and used in three different calculations to determine the exciton dynamics. In the first calculation, the time-dependent couplings have been combined with the fluctuating TD-LC-DFTB site energies whereas in the second set, the coupling values have been averaged along the trajectory and then combined with the time-dependent site energies. In these first two calculations, the site energies were taken from the TD-LC-DFTB calculations along the classical MD-based trajectory. Finally, in the third calculation, the averaged classical MD-based coupling values have been combined with the TD-LC-DFTB site energies determined along the QM/MM MD trajectory. The 40 ps QM/MM and classical MD trajectories generated from the first set of starting coordinates were employed for the coupling and site energy calculations to perform the three variants of excitation energy transfer dynamics.

Among several approaches to calculate the excitonic coupling between pigment molecules, an efficient and accurate method is the TrESP (Transition charge from Electrostatic Potential) procedure [27, 73, 323, 332] in which the coupling is given by

$$V_{mn} = \frac{1}{4\pi\epsilon_0} \sum_{I,J}^{m,n} \frac{q_I^T \cdot q_J^T}{\mid r_m^I - r_n^J \mid} \,. \tag{B.1}$$

In this expression, q_I^T and q_J^T denote the transition charges of atom I and J from the

respective donor (m) and acceptor (n) pigments. In the present study, we have used the TrESP approach to determine the excitonic coupling along a classical MD trajectory. To this end, the transition charges based on TDDFT-B3LYP/6-31G* excited state calculations as reported by Madjet et al. [73] have been used. Moreover, a scaling factor of 0.724 has been employed to reproduced the experimental transition dipole moment of 6.3 D for a BChl molecule [167]. Furthermore, we have multiplied the coupling values with a distance-dependent screening factor as derived by Scholes et al. [59, 74] to take the environmental effects on excitonic coupling into account. This screening factor is given by

$$f(R_{mn}) = A\exp(-BR_{mn} + f_0) \tag{B.2}$$

where A, B and f_0 have values of 2.68, 0.27 and 0.54, respectively. The screening factor becomes 0.54 when the distance between two pigments is larger than 20 Å.

B.2 Bond Length Alternation

The bond length alternation (BLA) is defined as the difference between the single and double bond lengths along a conjugated chain or ring. Depending on the molecule, it can have a sizable impact on the excitation energies. For example, retinal shows a high correlation between the BLA values and the corresponding excitation energies as discussed in Ref. 197 and references therein. For retinal, an increase of the BLA values leads to blue shifted excitation energies. The measurement of the BLA is thus a geometrical criteria of the quality of the computational method to describe the geometry of the molecule, which in turn correlates with the excitation energies.

In Ref. 197, we computed the BLA for BChl structures, optimized in vacuum using different quantum methods. In case of the B3LYP level of theory, the BLA was found to be around 0.004 Å. A high BLA value (0.102 Å obtained for HF method) gives excitation energies blue shifted compared to the excitation energies obtained with a low BLA value of 0.004 Å. The influence of the protein environment was also discussed for the FMO complex, but showing only minor effects on the BLA values. The computed absorption spectra are also dependent on the BLA values, as these can influence the broadness of the spectrum. Hence, in the following the BLA values are investigated for sampled BChl structures. Fig. B.1 displays the BLA

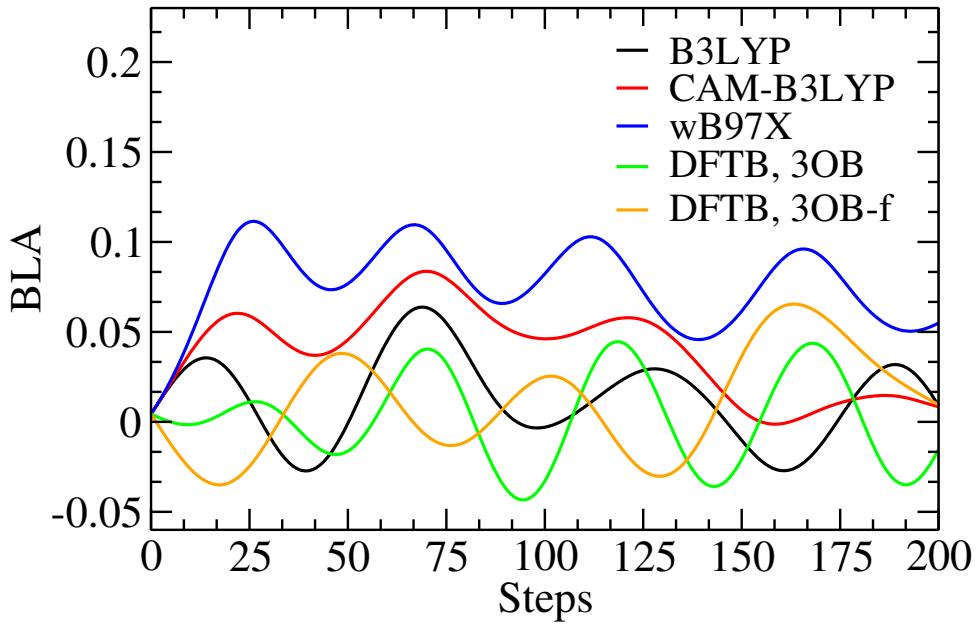

Figure B.1: BLA based on AIMD simulations in vacuum for a BChl molecule using three DFT functionals (B3LYP, CAM-B3LYP, ωB97X) and DFTB (parameter sets: 3OB, 3OB-f).

values of the 100 fs-long AIMD simulation and the MD simulations using DFTB. DFTB is based on GGA and it shows the same trend as B3LYP for the different parameter sets. The values are also in the same range as obtained for the optimized structure, see Ref. 197. As expected, the LC functionals lead to a higher range of BLA values, i.e, roughly double the range than obtained for B3LYP, and thus might lead to a bad description of delocalized bonds. This observation correlates with the amount of HF in the exchange part of the LC functionals, which is higher in ωB97X than in CAM-B3LYP. Furthermore, a high BLA value results in a blue shift in excitation energies as shown in Ref. 197 for the optimized structure of BChl molecule. Hence, LC functionals might lead to a wrong energy description of the chromophores in LH complexes, which has to be figured out in more detail in future studies. Thus, LC functionals might not lead to an improved geometry description of the BChl molecules, while B3LYP as well as DFTB do yield proper geometries.

Furthermore, the BLA has also been computed along a classical and a QM/MM MD trajectories of the FMO complex, see Fig. B.2. Both, classical and QM/MM simulation yield BLA values almost in the same range which signifies that the geometrical phase-space of the BChl is similar for DFTB as well as for classical force field. However, DFTB results in a more accurate description of the BChl geometries and, most importantly, of the vibrational frequencies which are key features in the accurate description of spectral density.

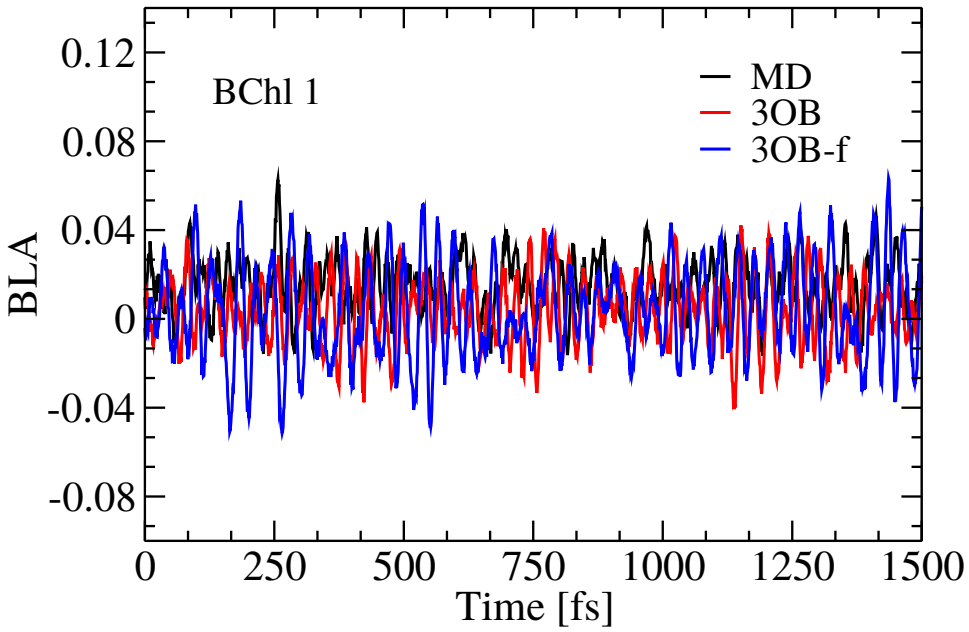

Figure B.2: BLA based on classical and QM/MM MD simulations of the FMO complex. For the QM/MM MD two DFTB parameter sets (3OB and 3OB-f) have been employed. As an example, the results for BChl 1 are shown.

B.3 Excitation Energy Distributions

In Fig. B.3A, a piece of a trajectory of these site energies is shown based on the QM/MM dynamics. Shown are the results from excitation energy calculations using TD-LC-DFTB and ZINDO/S. The absolute value of the ZINDO/S results is closer to the experiment than that of the DFTB findings since the former scheme is parameterized for this kind of molecules. At the same time, the TDDFT formalism based on LC or hybrid functionals is known to overestimate the absolute values of excitation energy gaps. For the present analysis such an overall overestimation is of no concern since we are only interested in relative excitation energies and fluctuations of these energies.

Shown in Fig. B.3B are the energy distributions along the 40 ps trajectories, termed as density of states (DOS) in the following, for the individual pigments based on the calculations in one monomer of the FMO trimer. As can be seen, shifts between the individual site energy exist with the average of BChl 2 being the lowest. Moreover, the distributions have a clear Gaussian form. As discussed in the main text, averaging over 1 ns using a much larger stride leads to site energies which are closer and with BChl 3 having the lowest energy. The results from the ZINDO/S calculations obviously show more skewed distributions as can be seen in Fig. B.3C. This asymmetry has been observed earlier [27, 77, 78] and is likely an artifact of the ZINDO/S parameterization which was done for geometries close to

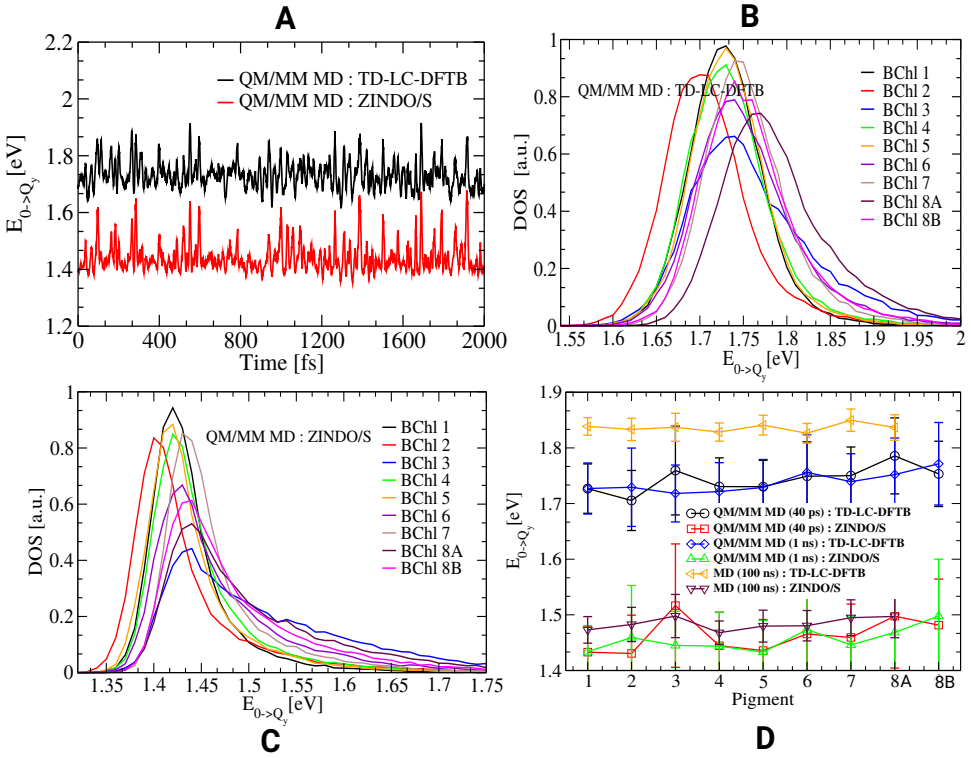

Figure B.3: A) Excited state energies along a piece of the QM/MM MD trajectory. B) Density states for the BChl pigments based on the TD-LC-DFTB level of theory. C) Same as A) but using ZINDO/S calculations for the excited state energies. D) Average site energies and the associate error bars for the different pigments in the FMO complex based on different trajectories and TD-LC-DFTB for the excited state calculations.

the equilibrium and not for geometries occurring during dynamical simulations. Again the distribution for BChl 2 shows a peak at the lowest energy for ZINDO/S as well.

One has to note that because of the skewed distributions of the ZINDO/S results, the average energy and the peak position are not identical while they do almost perfectly agree for the TD-LC-DFTB results. Moreover, as shown in our recent benchmark study, TD-LC-DFTB yields results more accurate than ZINDO/S which is actually overestimating the site energy fluctuations [197]. In that benchmark study, a monomeric unit of the FMO complex with seven BChl pigments has been taken into account yielding similar but slightly different results. For the case of classical MD as ground state dynamics, site energy as well as coupling distributions have been reported previously [27, 197].

B.4 Autocorrelation Function and Spectral Density

In context of open quantum system, the spectral density is the key input factor in order to study the exciton transfer dynamics in LH complexes. One way to obtain

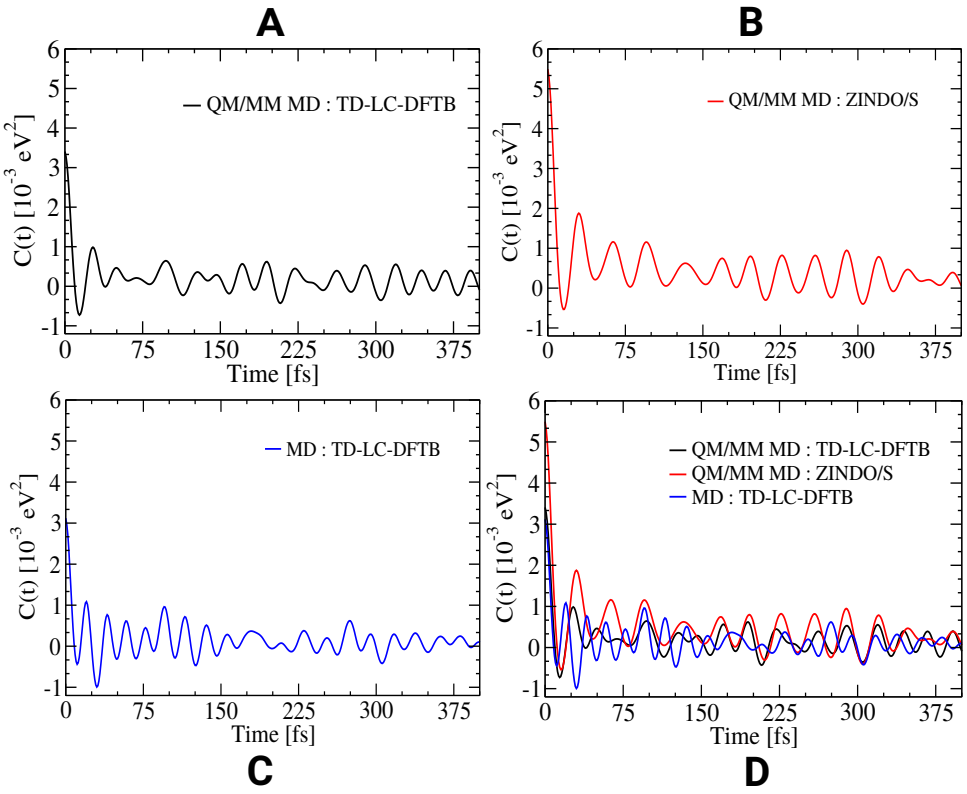

Figure B.4: A) Autocorrelation function averaged over the pigments in one monomer along the QM/MM dynamics based on TD-LC-DFTB calculations. B) Same as A) but based on the ZINDO/S level of theory. C) Autocorrelation function averaged over the trimer based on TD-LC-DFTB along the classical MD trajectory. D) All three curves shown in one panel.

this quantity is via the autocorrelation function of excitation energy gap fluctuations. The spectral density is then given as a cosine transform combined with some thermal factor (see main text for details). Average autocorrelation functions based on different computational approaches and their comparisons are shown in Fig. B.4. Figs. B.4 A and B represent the average autocorrelation function for a monomeric unit based on TD-LC-DFTB and ZINDO/S calculations along QM/MM trajectories. From these two figures it is clear that the fastest oscillation periods are around 22-32 fs which is equivalent to 1030-1550 cm^{-1} in the corresponding spectral density. However, for the classical MD trajectory (see Fig. B.4C), the fastest oscillation periods in the correlation function obtained from the classical MD trajectory is about 19-23 fs corresponding to 1450-1800 cm^{-1} which again is reflected in the respective spectral density. As examples, the individual spectral densities for the individual pigments and their averages are shown in Figs. B.5 and B.6 based on TD-LC-DFTB and ZINDO/S calculations along the QM/MM trajectories using the first set of initial coordinates.

As discussed in the main text, the QM/MM MD leads to major peak positions in the range of 1030-1550 cm^{-1} irrespective of the method for the excited state

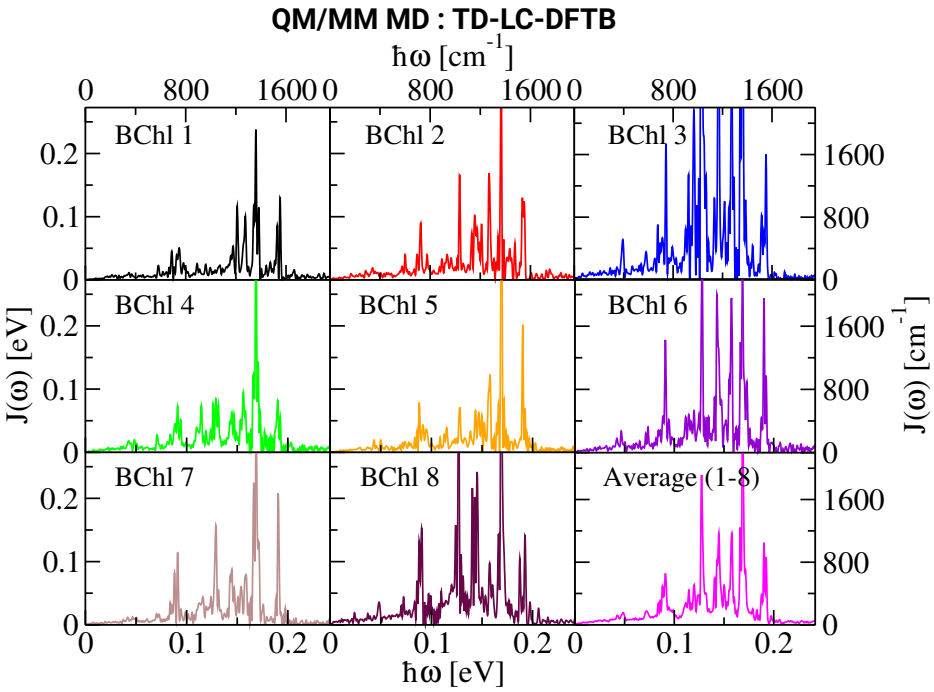

Figure B.5: Spectral densities for the individual pigments in a monomer and their average based on TD-LC-DFTB calculations along a QM/MM MD trajectory.

calculations, i.e., the TD-LC-DFTB or the ZINDO/S approach. Moreover, we have also mentioned earlier that the ZINDO/S results overestimate the environmental influence especially in the lower frequency region compared to the TD-LC-DFTB calculations. The obtained individual spectral densities can be employed as input for density matrix calculations of the exciton transfer dynamics in forthcoming work.

The spectral densities of the individual pigments determined from the TD-LC-DFTB and ZINDO/S calculations along the QM/MM dynamics of 40 ps length are represented in the SI while the average over a monomeric unit is shown in the main text. The major peak positions are in the range of 1030 to 1550 cm^{-1} for each BChl pigment irrespective of the theory of the excited state calculations. This signifies that the shortest oscillation periods in the auto correlation functions are around 22-32 fs (see S2). The major peaks originate mainly from intra-molecular vibrational modes involving C=C, C=N and C=O bond stretching [217]. The intensity of the average spectral density is higher in the case of ZINDO/S calculations than for the TD-LC-DFTB method especially in the low-frequency region as shown in Fig. B.7. A similar difference between the ZINDO/S and TDDFT along a classical MD for the FMO complex has already been reported earlier [78]. Moreover, in our recent benchmark study, we already concluded that ZINDO/S does overestimate the environmental effects to some degree [197]. We note in passing

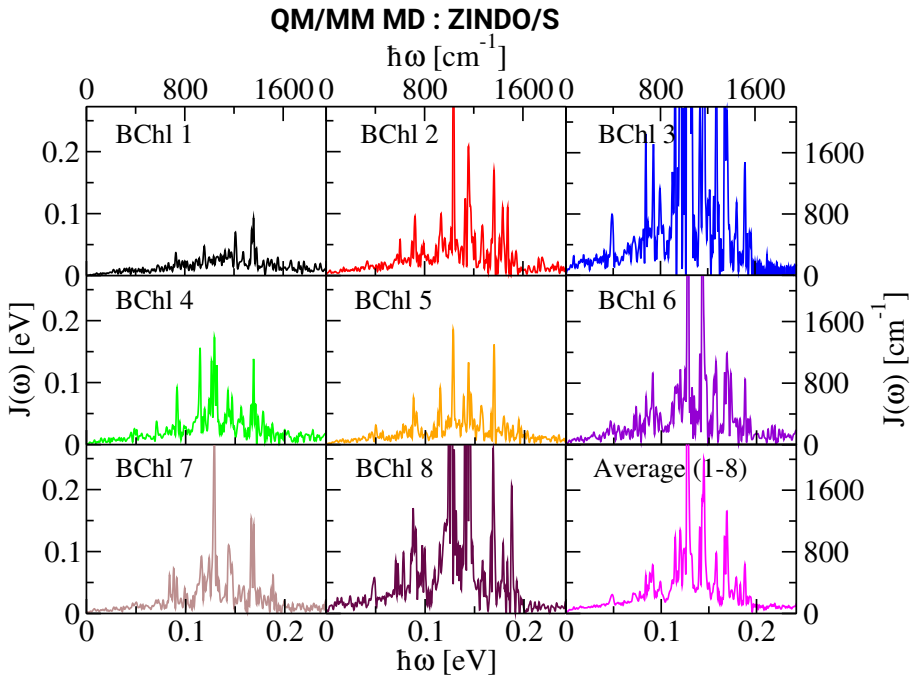

Figure B.6: Same as Fig. B.5 but based on the ZINDO/S method for the excited state energies.

that the low-frequency regions of spectral densities are mainly due to electrostatic interactions with the environment of the individual pigment molecules [66].

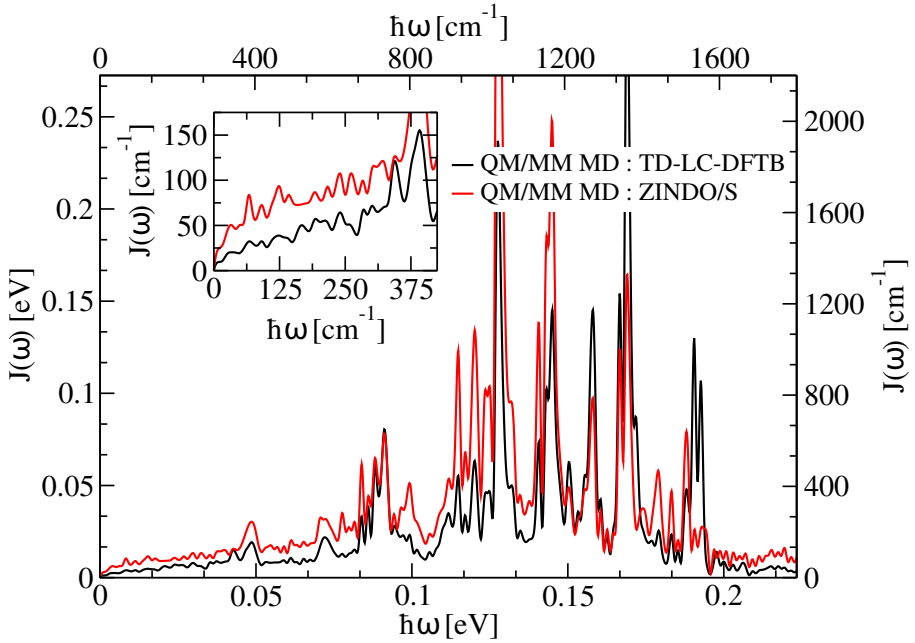

Figure B.7: Average spectral densities of the FMO complex based on TD-LC-DFTB and ZINDO/S excited state calculations along the QM/MM MD trajectory.

B.5 Sampling Issues for the Spectral Density

The QM/MM MD-based spectral densities show quite some differences in the amplitudes at specific frequencies between the individual pigments as can be seen in

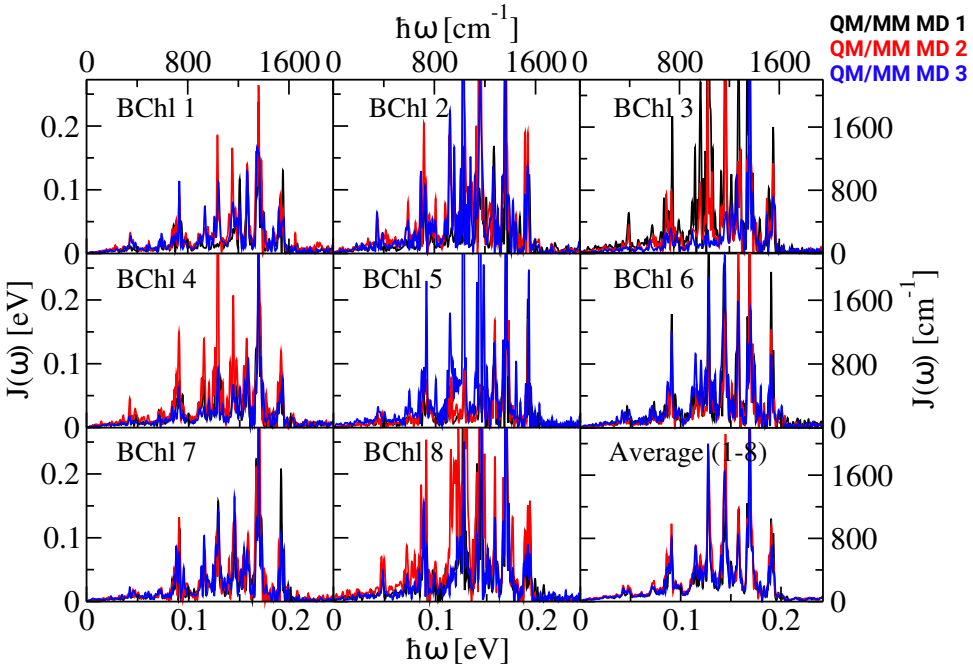

Figure B.8: Spectral densities for the individual BChl pigments along the QM/MM MD trajectories for the three different starting conformations based on the TD-LC-DFTB level of theory.

the SI. To investigate this finding further, we performed QM/MM MD and classical force field-based ground-state simulations with different starting conditions as shown in Figs. B.8 and B.9, respectively. To this end, conformations after 1 ns, 60 ns and 160 ns equilibration have been taken as starting structures and QM/MM dynamics simulations were performed followed by TD-LC-DFTB excitation energy calculations as described earlier. For the classical MD results, the first two conformations, i.e., after 1 ns and after 60 ns, have been used as starting conformations for the respective excitation energy calculations. Moreover, for the classical MD-based trajectory, the average spectral density for individual pigment has been determined using an average over the trimer structure. In case of the QM/MM dynamics shown in Fig. B.8, the peak heights across the full frequency range differ significantly among the three sets. Some peaks only appear in certain sets and not in others. These variations strongly indicate that the sampling is not perfect yet.

However, for the two different sets of spectral densities based on classical MD trajectories with different starting structures, the variations are much smaller as can be seen in Fig. B.9. This finding is surprising since the length of the trajectories and the autocorrelation functions are the same in the case of the QM/MM MD and the classical MD simulations. It is important to note that in the Fourier transform of the energy autocorrelation function only those internal modes appear which are

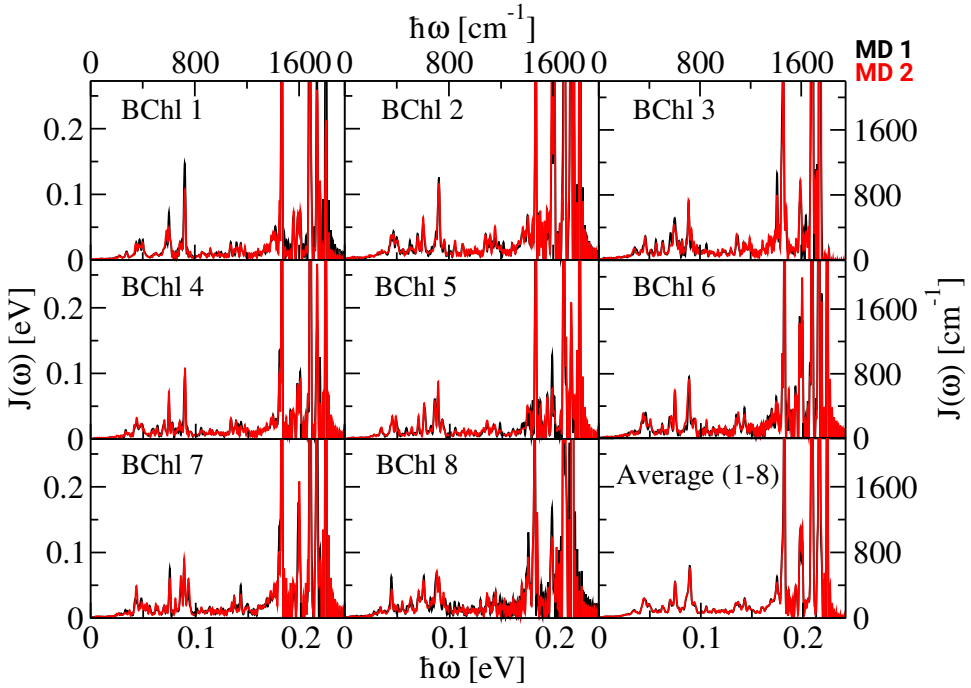

Figure B.9: Same as Fig. B.8 but based on two different classical MD trajectories.

initially excited or to which energy is re-distributed. It looks as if this energy re-distribution within the BChl molecules is faster in the case of the classical dynamics than in the case of the QM/MM dynamics in which the BChl molecules are treated quantum mechanically. Apparently, more sampling is needed in the case of the QM/MM dynamics with varying initial excitations of the internal modes. The amplitude of certain modes in the spectral densities might be underestimated if they are hard to excite although they strongly couple to the environment. In this context "hard to excite" refers to collective modes of the BChl molecule which need rather specific concerted motions of several atoms [217].

B.6 Experimental Spectral Density

The experimental spectral density can be represented as the contribution of two parts

$$J^{exp}(\omega) = J_0^{exp}(\omega) + J_{vib}^{exp}(\omega) \tag{B.3}$$

where $J_0^{exp}(\omega)$ represents the continuous component of the spectral density which is due to the environment of the pigments. This part is represented by an over-damped Brownian oscillator describing the low-frequency part of the bath [255]. Moreover, $J_{vib}^{exp}(\omega)$ denotes the discrete components as under-damped Brownian oscillators and mainly result from high-frequency intramolecular vibrational modes of the pigment molecules [255]. This discrete component is responsible for the

peaks in the total spectral density. In delta fluorescence line narrowing (ΔFLN) experiments only the Huang-Rhys (HR) factor and its corresponding frequencies are measured for LH complexes based on which several broadening expressions have been reported for the line-shape of the spectral density. Here, we have modeled the first part of spectral density by a log-normal distribution introduced by Kell and coworkers [216]

$$J_0^{exp}(\omega) = \frac{\hbar\omega S}{\sigma\sqrt{2\pi}} \exp^{-[\ln(\omega/\omega_c)]^2/2\sigma^2} \tag{B.4}$$

The HR factor S, cut-off frequency ω_c and standard deviation σ have been extracted from Fig. 1 in Ref. 216. The second component of the spectral density has been fitted by a Lorentzian function given by [203]

$$J_{vib}^{exp}(\omega) = \frac{2\hbar}{\pi} \sum_k s_k \omega_k^3 \frac{\omega\gamma_k}{(\omega_k^2 - \omega^2)^2 + \omega^2\gamma_k^2} \tag{B.5}$$

For this part, the HR factors s_k and its corresponding frequencies ω_k have been taken from Table 1 in Ref. 215. The broadening factor γ_k is an (to some extend) arbitrary factor in this expression which controls the broadening of the individual peaks and can lead to a varying number of peaks in case of peak overlaps. In this study, we used a value as $\hbar\gamma_k = 5$ cm^{-1} to obtain intensities comparable to our theoretical findings.

B.7 Comparison to Other Computed Spectral Densities

As in the present study, the spectral density calculated by Kim et al. [184] has been determined using an energy gap autocorrelation function followed by a cosine transform multiplied by a thermal factor. However, as described in the main text, the authors first constructed PESs for the ground and first excited state and subsequently performed dynamical simulations using these pre-determined surfaces for the force determination [184, 207, 355]. Such kind of consistent potential construction for a large molecule like BChl is, however, numerically expensive within the DFT framework. Subsequently an efficient approach based on the so-called Shepard interpolation correction was established to reduce the computational cost [356]. In contrast, in the present study “on-the-fly” forces us-

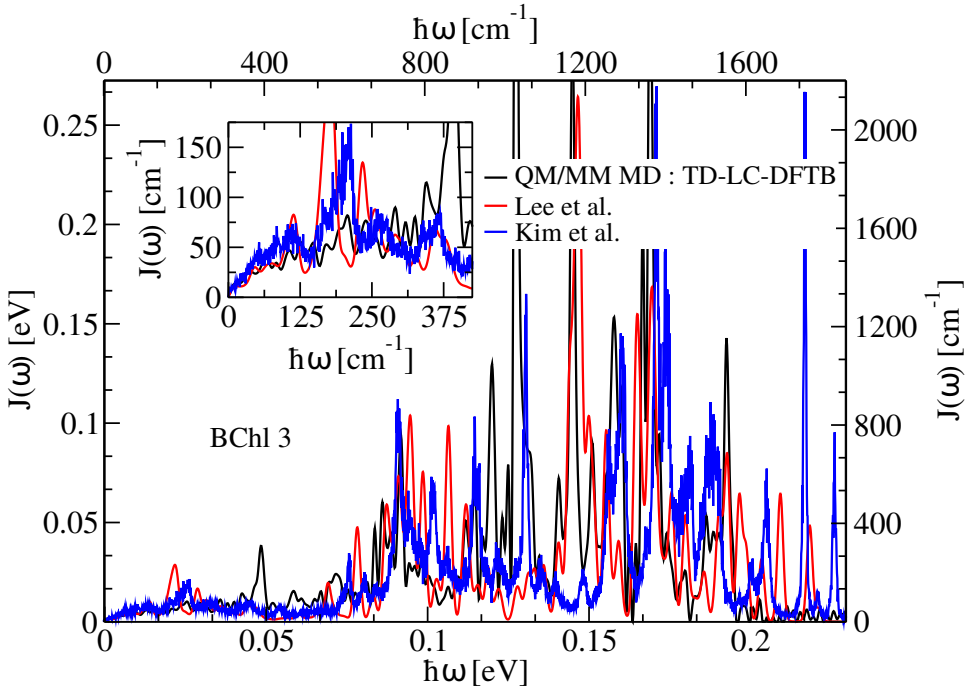

Figure B.10: Comparison of the present QM/MM MD-based spectral density of BChl 3 determined using the TD-LC-DFTB approach averaged over the three different initial conformations and the results by Lee and Coker [67] as well as by Kim et al. [184].

ing the DFTB formalism were employed for the QM/MM dynamics. In contrast, in the case of Lee and Coker [67], the intra-molecular and the intermolecular counterpart of the spectral density were determined separately. While the former is based on a normal mode analysis of randomly selected geometry-optimized structures from a MD trajectory, the latter was determined using a partial charge coupling scheme similar to that used by Renger and co-workers along a classical MD trajectory [73, 191, 205]. Although this combination scheme yields quite good agreement with experiment, the determination of system-bath coupling constants for the individual modes involves numerous TDDFT calculations rendering this approach computationally expensive. Later on, a so-called vertical gradient approximation was implemented by Padula et al. [200] assuming harmonic PESs for the ground and excited state. This additional approximation significantly reduces the number of necessary TDDFT calculations and retains an accuracy similar to that obtained by Lee and Coker [67]. In all these theoretical simulations including the present one, special procedures were introduced to remove the geometry mismatch problem. The comparison between the present results using all three sets of QM/MM MD trajectories discussed above and the results by Kim et al. [184] as well as Lee and Coker [67] is shown in Fig. B.10. This comparison has been done for one BChl, number 3 in this case, since in the calculations individual pigments

are accessible. All three spectral densities roughly cover the same frequency range which much better agrees with experiment than the classical MD-based findings. Concerning the amplitudes of the spectral densities from Kim et al. [184] as well as Lee and Coker [67] there is, however, a caveat, since there seems to be a slight confusion concerning the prefactor $1/\pi$ in Refs. 67 and 184 as well as the data presented in Ref. 195. From Fig. 4 in the main text it should be clear, however, that the present spectral density compares nicely to experiment and certainly not worse but maybe even slightly better than the two other computed spectral densities especially in the high frequency region. This finding might be due to the usage of the B3LYP functional for the ground state of the BChl molecule in these two other studies which is known to overestimate the frequencies of the C=C, C=N and C=O bond stretching [71].

B.8 Wave Packet Dynamics

In the main text, we have presented results of the wave packet dynamics based on two "mixed" trajectories where the site energies have been calculated based on the TD-LC-DFTB method along QM/MM MD trajectories while the couplings have been determined as averages of coupling values along a classical trajectory. This mixture has been proposed since it would be numerically quite expensive to perform QM/MM dynamics include all pigments in a QM description. Here, we show that this kind of "mixed" approach is valid as long the coupling fluctuations do not influence the exciton dynamics. For this purpose, we have performed two sets of calculations. In one set we have taken the time-dependent coupling fluctuations whereas in the second set the time-independent average coupling values have been taken as input. In both calculations, the site energies were used in the time-dependent form which is important since resonances between site energies can strongly influence the transfer rates. For these two sets, the site energies were calculated based on the TD-LC-DFTB method and the coupling were determined based on the TrESP approach as described earlier. Moreover, in these two types of calculations, the first set of the classical MD trajectory was taken into account.

The comparison of the dynamics based on the time-dependent and average coupling values using the same site energy trajectory is shown in Fig. B.11. Initially only BChl 1 was excited and subsequently one can observe how the excitation is moving on to neighboring pigments in an FMO monomer. The dynamics based

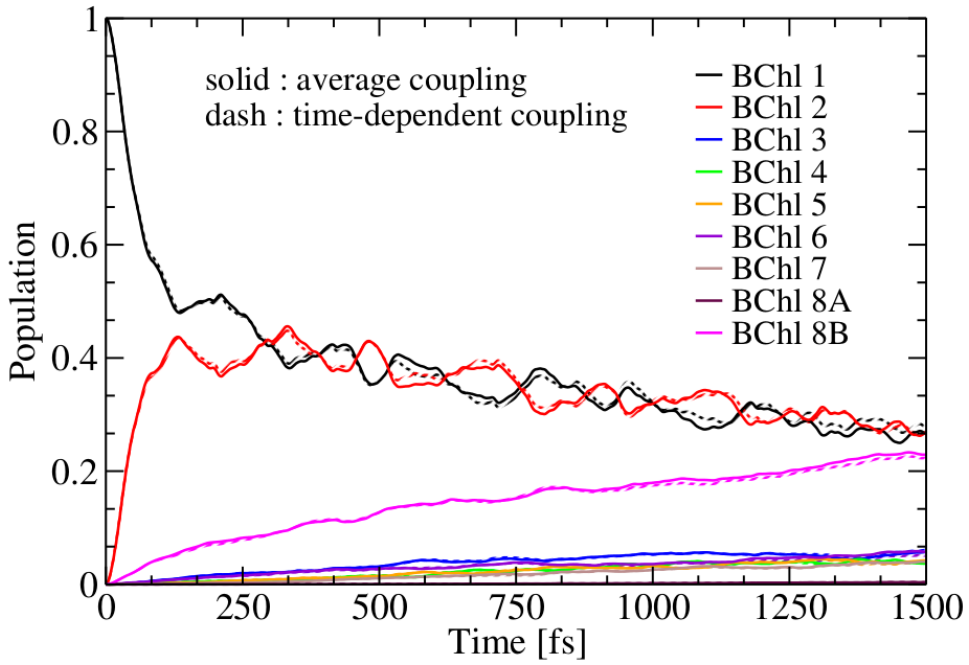

Figure B.11: Exciton transfer dynamics in a FMO monomer based on TD-LC-DFTB site energies and TrESP couplings along a classical MD trajectory. The dash line represents the results for the time-dependent coupling values whereas the solid lines depicts the findings using time-averaged average coupling values.

on the two variants of coupling values does not differ significantly between the two results. This finding clearly suggests that the influence of the coupling fluctuations on the exciton dynamics can be neglected. Averaging also the site energies in time, however, would lead to significant changes in the dynamics. In conclusion, the “mixed” wave packet dynamics based on site energies from QM/MM MD trajectories and average coupling values from a classical MD trajectory should lead to reasonable results.

Appendix C

Chapter 4: Supporting Information

C.1 Site Energy Distributions for the Individual Chl-a Pigments

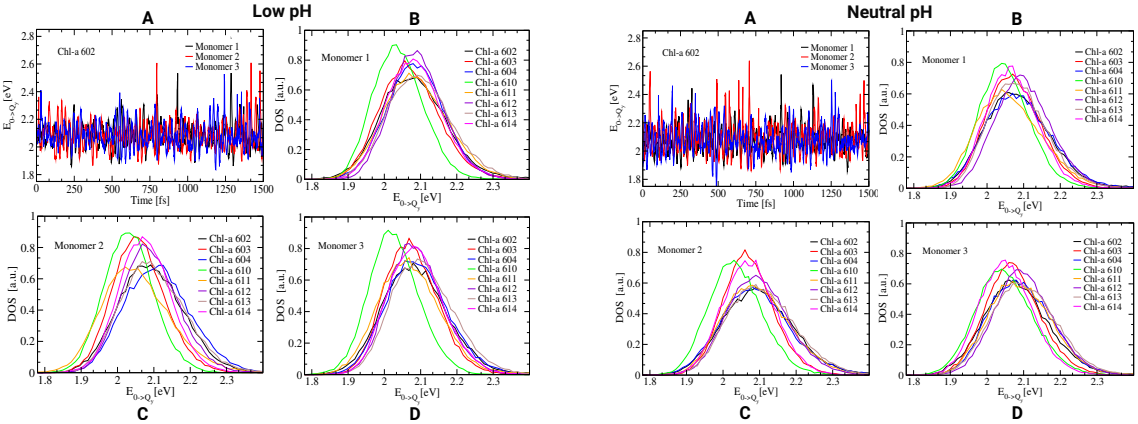

Figure C.1: Calculations at low and neutral lumenal pH values are shown in the left and right panels, respectively. A) Excited state calculation based on the TD-LC-DFTB approach along a piece of a QM/MM MD trajectory. B-D) Density of states for the individual Chl-a molecules in different monomers. Here the first set of the 40 ps QM/MM MD trajectories is shown.

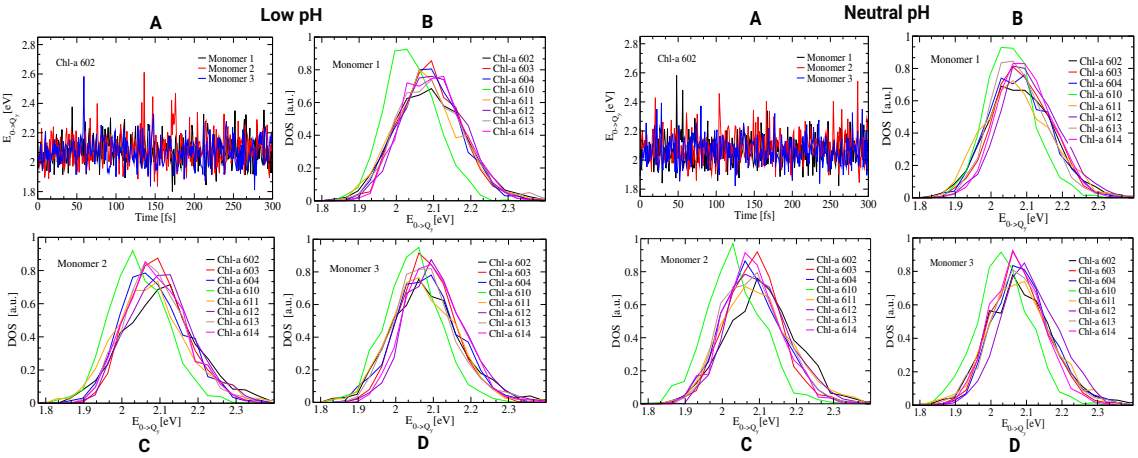

Figure C.2: Same as Fig. C.1 but based on 1 ns QM/MM MD trajectories.

C.2 Autocorrelation Functions and Spectral Densities for the Individual Chl-a Pigments

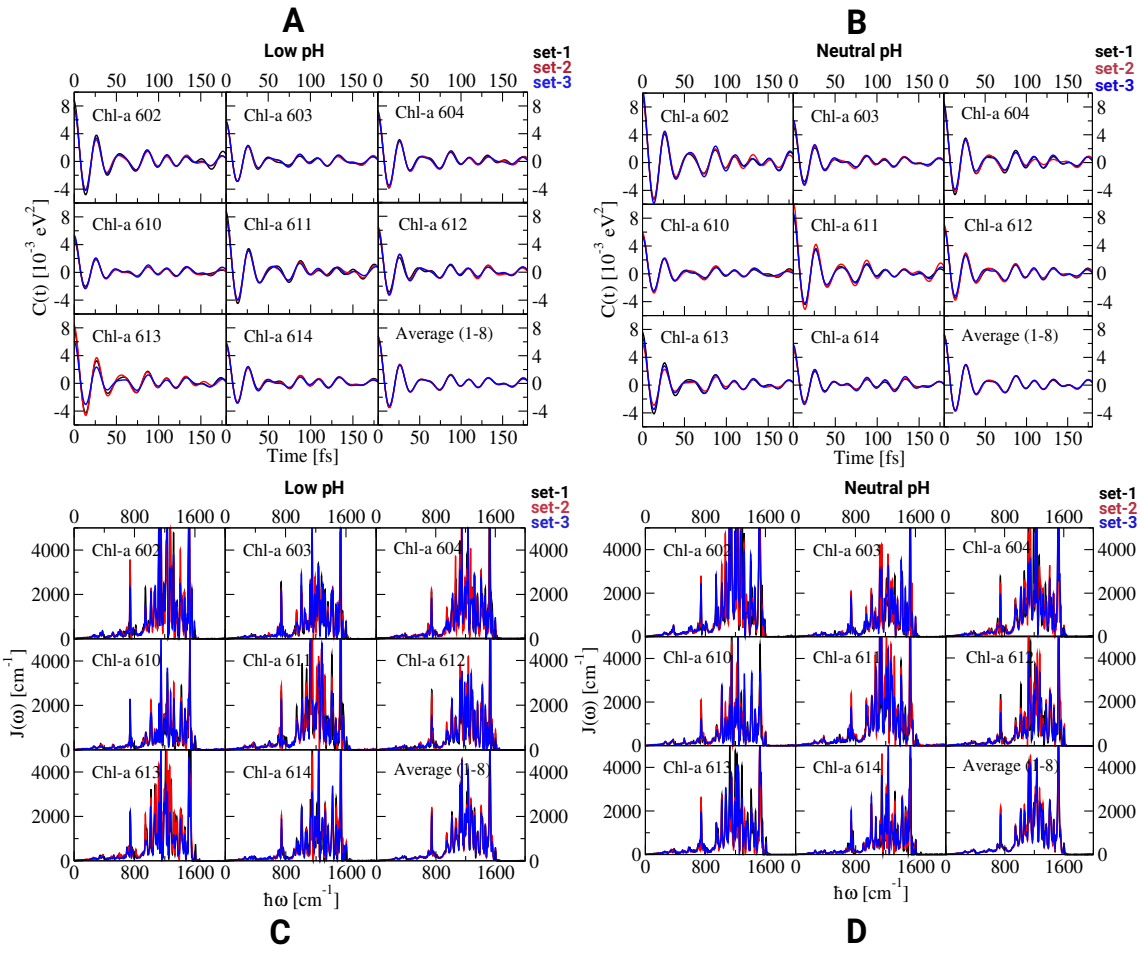

Figure C.3: A, B) Average autocorrelation functions for the individual Chl-a pigments from different starting geometries at low and neutral lumenal pH. C,D) The respective spectral densities based on the autocorrelation functions.

Table C.1: Reorganization energies corresponding to the individual Chl-a pigments averaged over all three sets of QM/MM MD trajectories at both pH states.

Pigment	Low pH (cm^{-1})	Neutral pH (cm^{-1})
Chl-a 602	1266	1568
Chl-a 603	910	927
Chl-a 604	1110	1271
Chl-a 610	787	879
Chl-a 611	1264	1427
Chl-a 612	972	1046
Chl-a 613	1167	1079
Chl-a 614	895	856

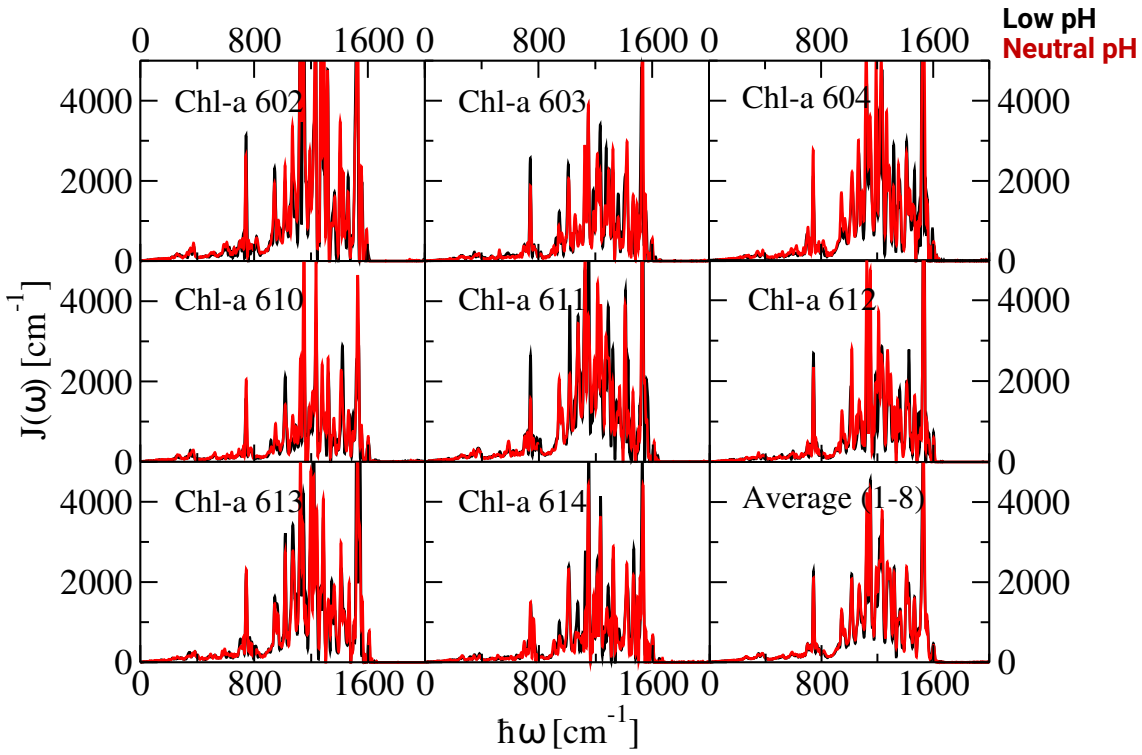

Figure C.4: Spectral density comparison for each Chl-a at low and neutral pH state based on the first set of 40 ps QM/MM MD trajectory.

C.3 Comparison of Experimental Spectral Density with Different Broadening Parameter

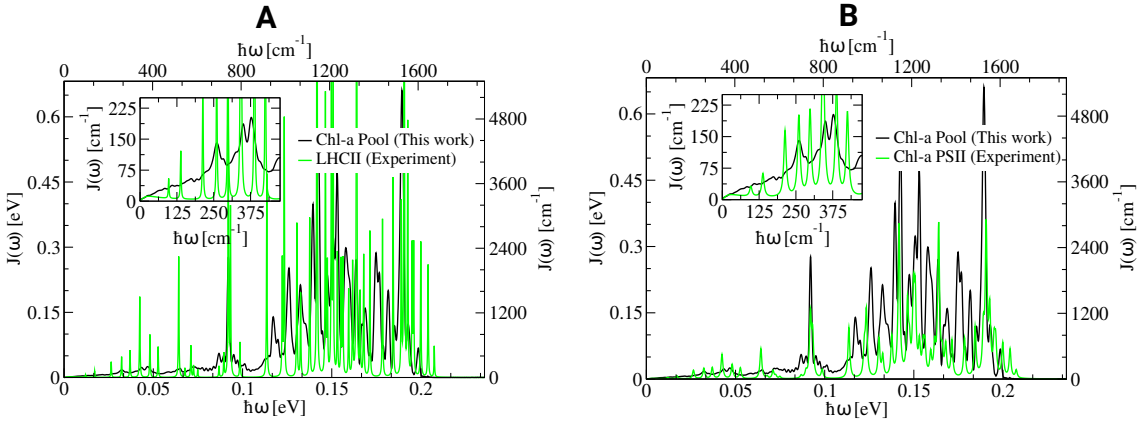

Figure C.5: A) Comparison between the computed and the experimental spectral density as shown in the main text with the broadening parameter set to 3 cm^{-1} as given in the Ref. 218. B) Same as panel A but now the experimental spectral density is measured for the PSII complex [255] with a broadening parameter of 10 cm^{-1} as given in Refs. 82, 256.

C.4 Excitonic Coupling between Chl-a 612/Lut-1 Pair

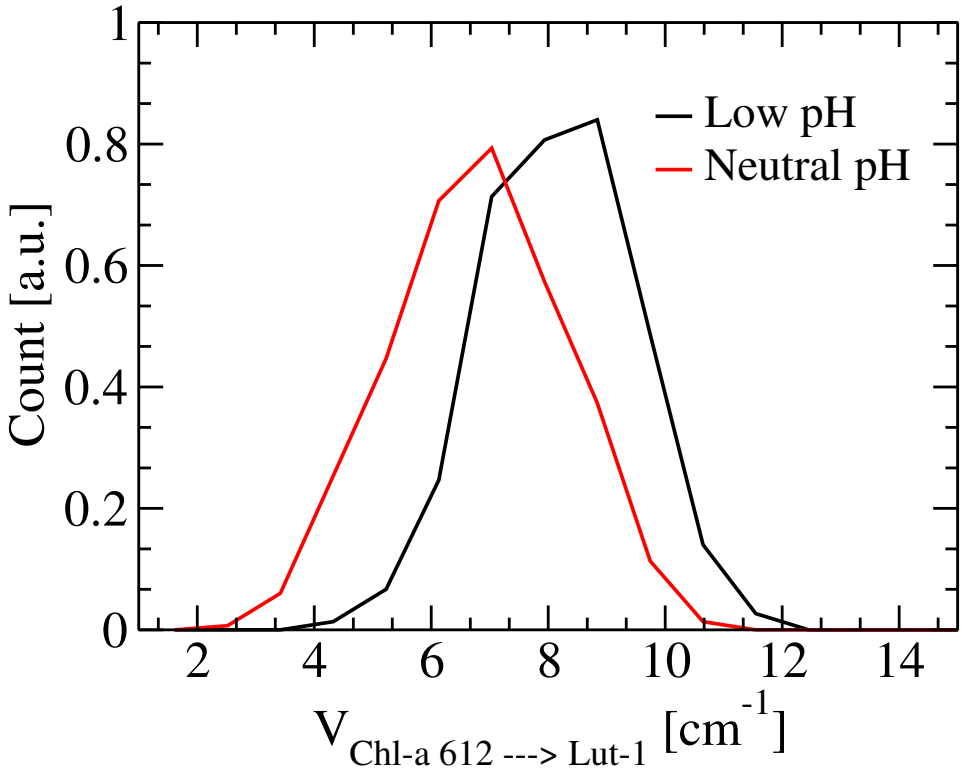

Figure C.6: Excitonic coupling distribution between Chl-a 612/Lut-1 pair at low and neutral pH states. These data are extracted from our previous study based on a 500 ns classical MD trajectory [225] but here they are scaled with a screening factor as explained in the main text.

Appendix D

Chapter 5: Supporting Information

D.1 Structural Comparison of Chl and BChl Molecules

As shown in Fig. D.1, Chl-a and Chl-b molecules differ only at the outside of the porphyrin ring where the methyl group (CH3) is exchanged by an aldehyde (CHO) being the only reason for the blue shift in the site energies of the Chl-b molecules. This shift has, however, almost no effect on the correlation functions or spectral densities as discussed in the main text. Moreover, in case of bacterial systems, although an acetyl (COCH3) group is present instead of the ethylene group (CH=CH2), the change of a double to a single bond inside the porphyrin ring is likely the main reason for the change in the vibrational dynamics leading to a different number of peaks and unlike intensities in the spectral densities as shown in the main part.

D.2 Density of States

Distributions of the excitation energy fluctuations are sometimes also termed densities of states (DOS). The DOS for the individual Chl pigments of the CP29 complex are displayed in Figs. D.2 and D.3 based on the TD-LC-DFTB calculations along the two 60 ps-long and the 1 ns-long QM/MM MD trajectories. The distributions are clearly of Gaussian form in line with our previous studies of other LH complexes [197, 241]. Moreover, the results based on the different trajectories result in very similar distributions and average values for the individual Chl molecules. However, the different pigments have slightly shifted distributions among each other leading to an energy ladder within the CP29 complex. In case of the Chl-a molecules, this shift is small whereas for the Chl-b pigments considerable

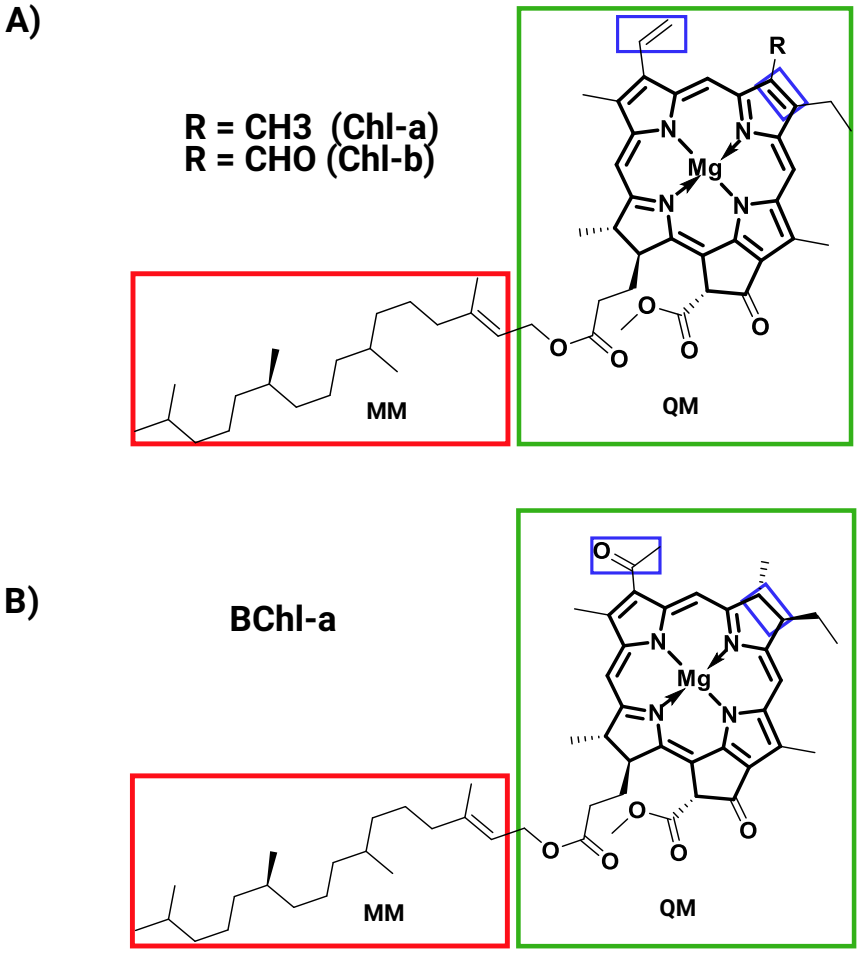

Figure D.1: A) Structure of Chl molecules present in plants highlighting the separation between the regions treated quantum mechanically and based on force fields in the ground and excited state calculations. The methyl group (R = CH3) of the Chl-a molecule is oxidized to an aldehyde (R = CHO) in a Chl-b molecule. B) Structure of a BChl-a pigment of bacteria as utilized in previous studies within a QM/MM framework [197, 241]. The regions highlighted in blue in both panels indicate the structural differences between the pigments of plants and bacteria.

shifts are clearly noticeable in Figs. D.2 and D.3.

D.3 Shifted Site Energies

Our computed excitation energies, i.e., site energies are overestimated compared to the experimental results due to the known shortcoming of DFT approaches as already detailed before [197, 241, 282]. For this reason, we introduced a common shift for the present results towards the experimental findings by Jassas et al. [289] as well as Mascoli et al. [290]. The present site energies have been shifted such that the site energies averaged over all Chl-a and Chl-b pigments coincide with those from the experiments as shown in Fig. D.4. The present shifted site energies are in the same range as found in the experimental measurements. The

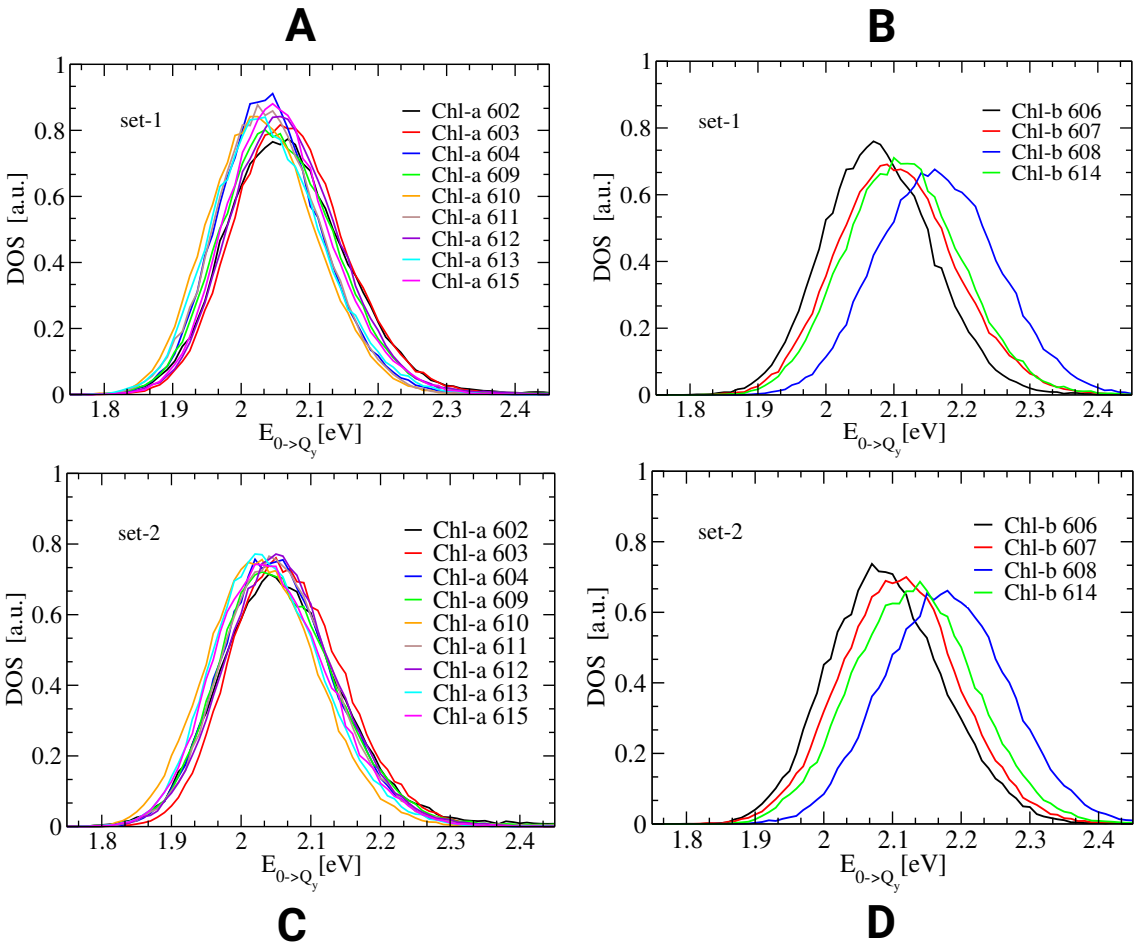

Figure D.2: A) Densities of state for the Chl-a molecules extracted from the first 60 ps-long QM/MM MD trajectory. B) Density of states for the Chl-b molecules extracted from the first 60 ps-long QM/MM MD trajectory. C) Same as A) but based on the second 60 ps-long QM/MM MD trajectory. D) Same as B) but based on the second 60 ps-long QM/MM MD trajectory.

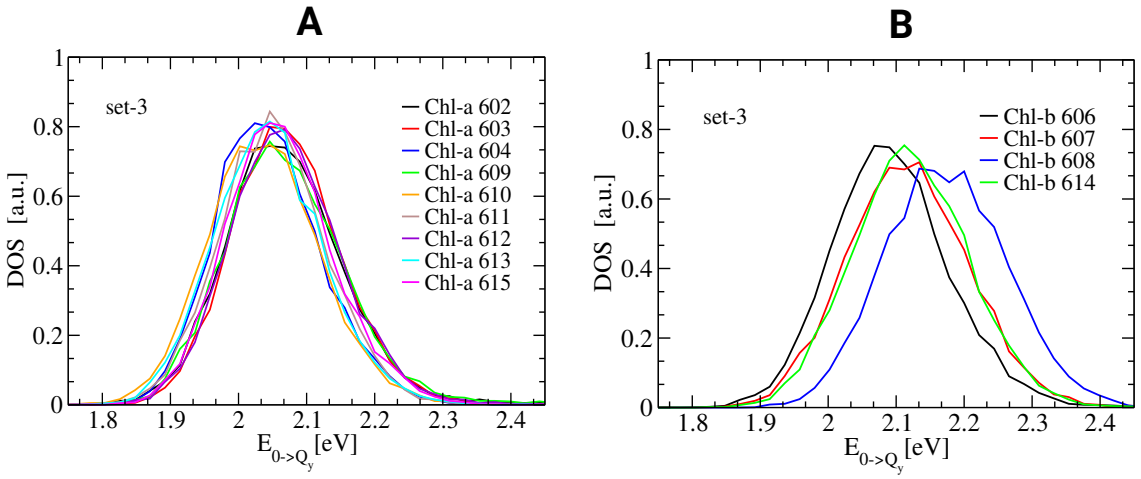

Figure D.3: Same as Fig. D.2 but based on the 1 ns-long QM/MM MD trajectory.

properly shifted energies are, for example, required for a reasonable modeling of absorption spectra while for the exciton transfer dynamics the fluctuations are of key importance.

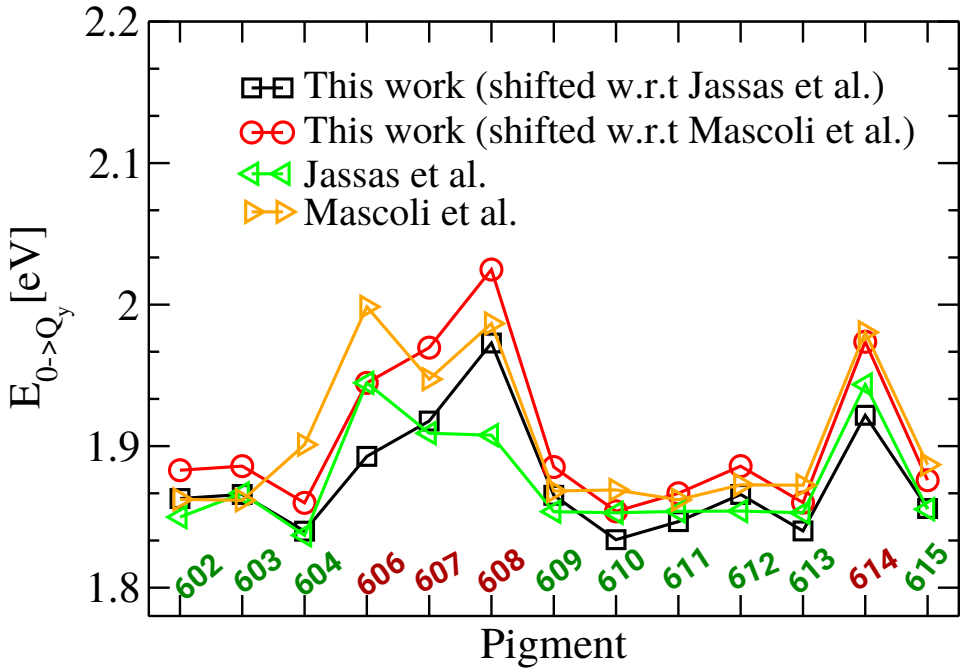

Figure D.4: The present site energies are shifted with respect to the experimental measurements by Jassas et al. [289] as well as Mascoli et al. [290]

D.4 Spectral Densities for Two Different Sets of QM/MM MD Simulations

The spectral density for the nine Chl-a and the four Chl-b chromophores have been calculated individually using the procedure described in the main text. The two sets of 60 ps QM/MM MD trajectories generated from different starting structures have been taken into account since sampling problems in the spectral densities were found in a previous study [241, 282]. Figures D.5 and D.6 show the spectral densities for the individual Chl molecules of the CP29 complex based on two sets of QM/MM MD trajectories as calculated in the present study.

Figures D.5 and D.6 indicate sampling issues as the peak heights are moderately different between the two sets for some Chl pigments. The frequencies of the major peaks are in the range of 1030 to 1550 cm^{-1} which can be attributed to collective modes of C=C, C=O and C=N intramolecular vibrations as described in the main part. The internal modes which are initially excited or receive their energy by re-distribution appear in the Fourier transformations of the energy autocorrelation functions. In case of QM/MM trajectories, however, the energy re-distribution seems to be slower than in purely force field-based simulations leading to slightly different amplitudes of the peaks in the spectral densities. For this reason, an en-

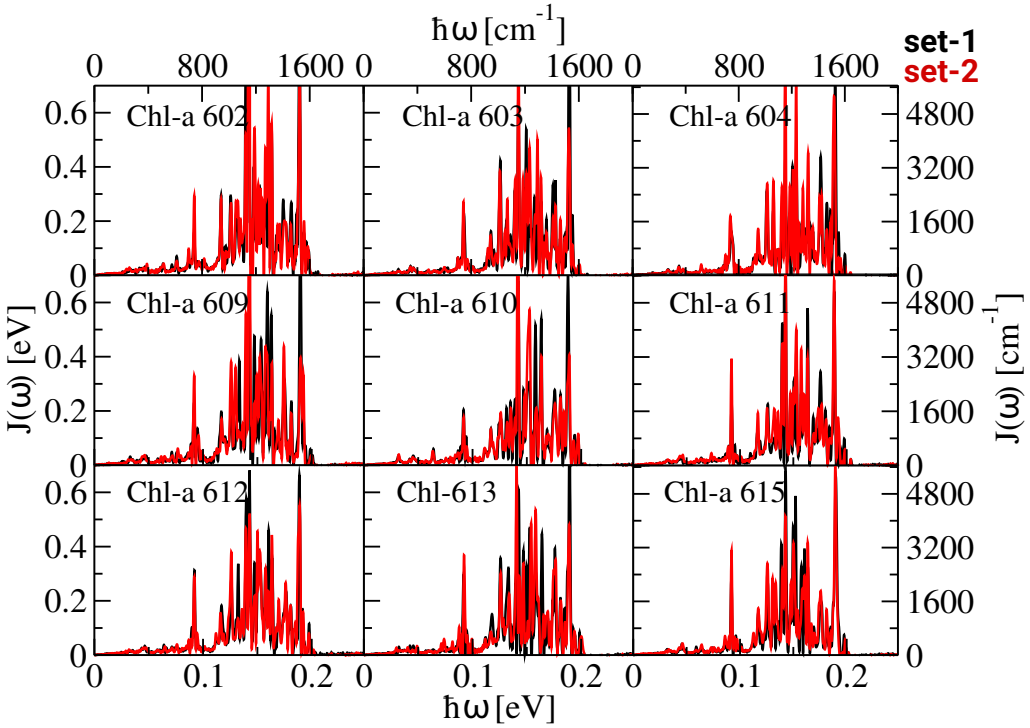

Figure D.5: Spectral densities for the nine Chl-a pigments based on the two 60 ps-long QM/MM MD trajectories.

hanced sampling is required with different starting geometries for the QM/MM dynamics.

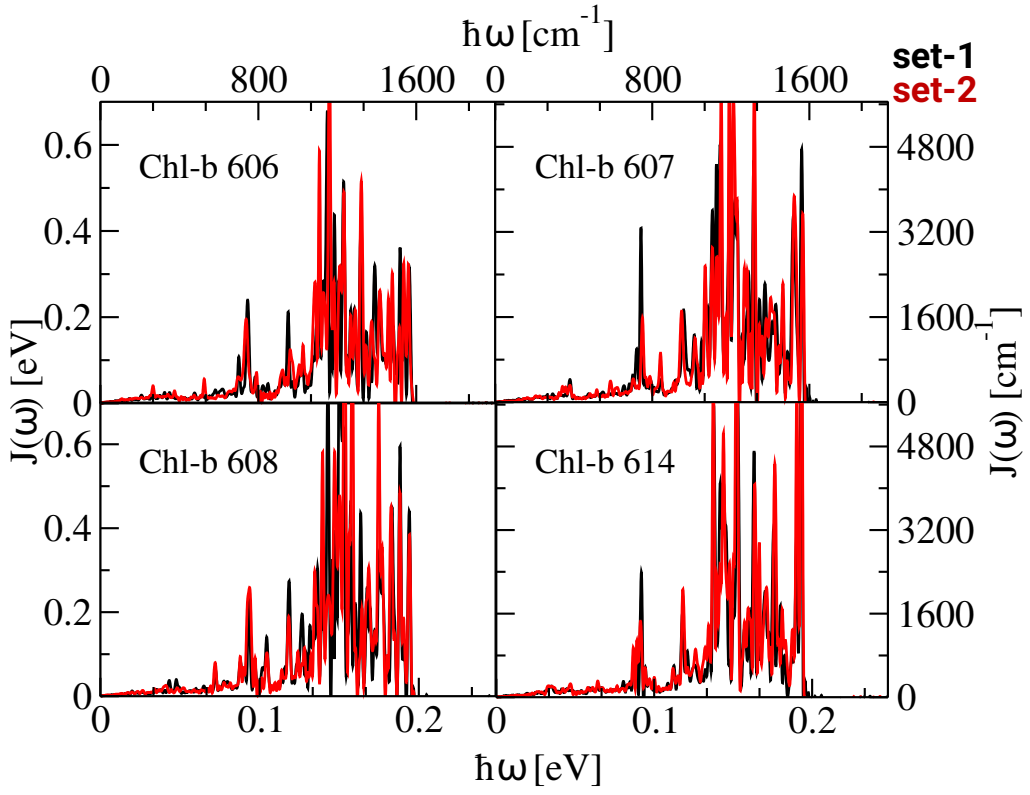

Figure D.6: Same as Fig. D.5 but for the four Chl-b pigments.

D.5 Comparison of Experimental Spectral Density between Plant and Bacterial LH Complexes

In plants, Chl are the major pigments and BChl molecules in bacteria. The structural differences between these two types of pigments are shown in Fig. D.1. Because of having one C=C double bond less, BChl molecules are more flexible compared to Chl pigments. For this reason, BChl molecules seem to show a larger number of vibrational peaks in the experimental spectral densities compared to the Chl molecules as shown in Fig. D.7. In spite of having similar peak positions,

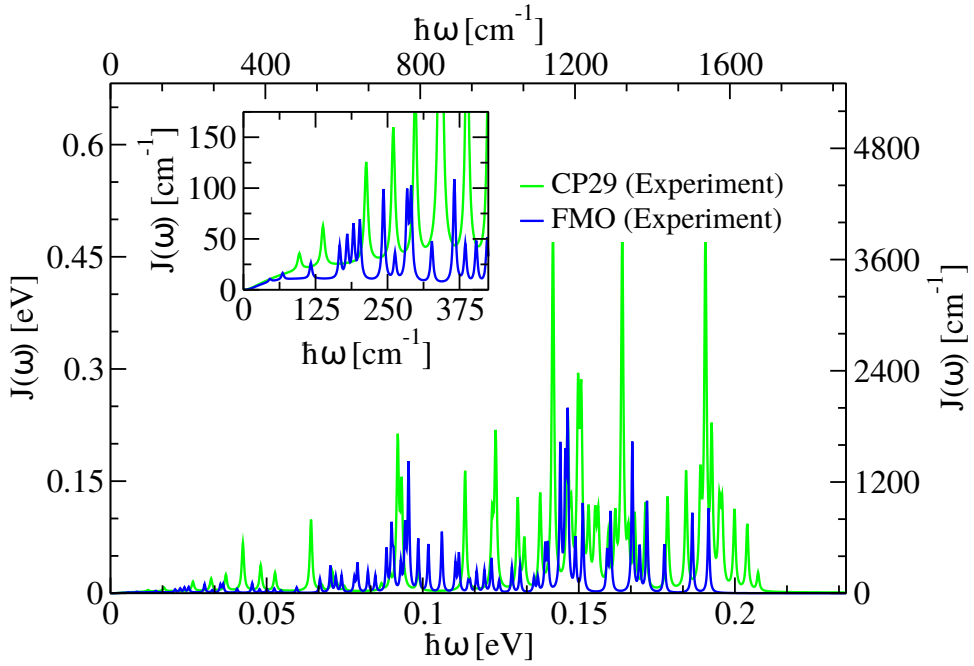

Figure D.7: Experimental spectral density comparison between the CP29 complex [216, 290] from plants and the FMO complex [215, 216] from bacteria.

the amplitudes of the peaks are higher in the plant LH system which is due to the larger site energy fluctuations in Chl molecules compared to the BChl pigments. The origin of the larger fluctuations is probably related to the higher value of Q_y excitation energies in Chl molecules. Further investigations are, however, required as explained in the main text.

D.6 Absorption Spectrum at Low Temperature

The absorption spectrum of the CP29 complex has been calculated within the Redfield approximations as described in the main text. The calculated spectrum at 300 K is shown is also shown there whereas the spectrum at A low temperature

of 77 K is depicted in Fig. D.8. The width of the main peak is a comparable to that of the experimental spectrum measured one at 77 K [357]. Moreover, the vibrational sideband towards higher energy also shows a nice agreement with experiment. However, the shoulder in the low-energy energy region is not present in experiment and is probably due to too low site energies of some pigments.

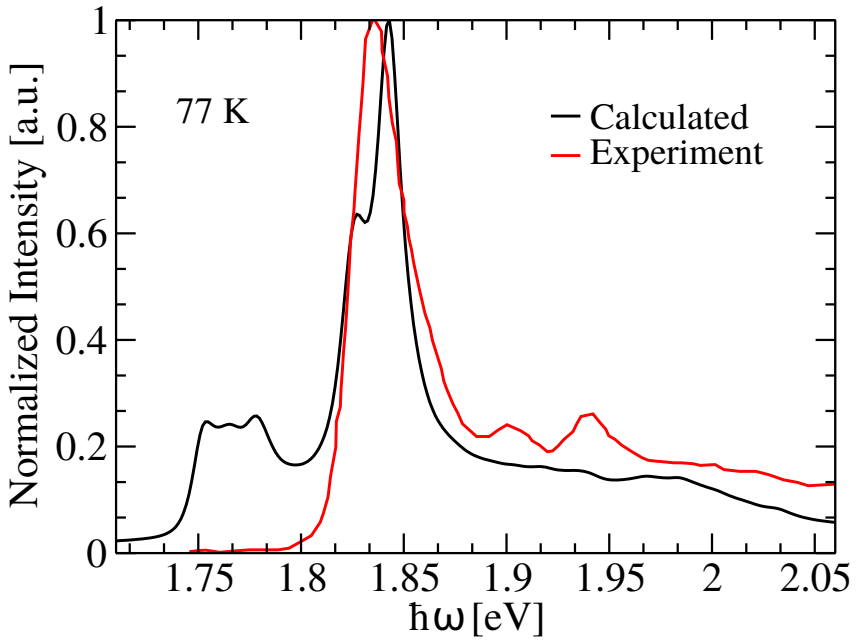

Figure D.8: Absorption spectra modeled at 77 K compared to the experimental counterpart [357].

D.7 TrESP Charges for Chl-a and Chl-b Pigments

The TrESP charges for the Chl-a and Chl-b pigments have been calculated with the help of the ORCA [131] and Multiwfn [161] programs. The phytyl tail was truncated at the C1-C2 bond since it plays almost no role in the transition energies in gas phase. The details of the procedure are described in the method section of the main text. Table D.1 lists the partial transition charges for the heavier atoms of the Chl-a and Chl-b molecules. The charges for the hydrogen atoms were set to zero during the fitting procedure of the transition densities.

Table D.1: Transition charges (in elementary charges) of the heavy atoms belonging to the Chl-a and Chl-b pigment molecules. The atom names are the same as in the crystal structure used here [47]. The charges for the hydrogen atoms were set to zero in the fitting procedure. The listed charges are usually scaled before the TrESP coupling calculations to reproduce experimental dipole moments as explained in the main text. The Q_y transition dipole moment is assigned approximately along NB-ND axis of the Chl molecules.

Chl-a	**Charge** $\times$ $\mathbf{10^3}$	**Chl-b**	**Charge** $\times$ $\mathbf{10^3}$
MG	5.906	MG	4.038
CHA	-112.870	CHA	-96.339
CHB	42.984	CHB	38.518
CHC	133.029	CHC	162.163
CHD	-61.417	CHD	-69.612
NA	-17.786	NA	-26.087
C1A	119.324	C1A	117.212
C2A	-0.944	C2A	7.000
C3A	-2.051	C3A	8.548
C4A	-98.329	C4A	-92.469
CMA	-6.256	CMA	-10.610
CAA	0.598	CAA	-8.272
CBA	2.377	CBA	-1.417
CGA	-0.820	CGA	-0.244
O1A	-2.916	O1A	1.287
O2A	5.314	O2A	4.502
NB	81.451	NB	85.542
C1B	-77.909	C1B	-60.316
C2B	-1.300	C2B	-3.200
C3B	-1.977	C3B	7.658
C4B	-131.939	C4B	-150.283
CMB	-20.197	CMB	-17.025
CAB	-0.882	CAB	-3.194
CBB	-26.859	CBB	-18.858
NC	21.980	NC	40.763
C1C	-128.399	C1C	-131.555
C2C	14.758	C2C	-6.930
C3C	-14.975	C3C	-18.621
C4C	63.002	C4C	49.001

CMC	1.853	CMC	19.832
CAC	-4.869	CAC	-8.196
CBC	-2.990	CBC	-3.368
ND	-84.710	ND	-77.530
C1D	89.460	C1D	85.016
C2D	15.705	C2D	9.888
C3D	14.556	C3D	22.569
C4D	109.052	C4D	91.643
CMD	27.878	CMD	25.728
CAD	1.074	CAD	-3.076
OBD	21.169	OBD	20.160
CBD	28.287	CBD	11.927
CGD	-5.231	CGD	4.967
O1D	6.431	O1D	-1.261
O2D	-7.232	O2D	-0.617
CED	7.038	CED	3.415
C1	-0.370	C1	-1.506
		OMC	-10.789

References

[1] R. E. Blankenship, *Molecular Mechanisms of Photosynthesis* (Wiley, 2014), 2nd edition.

[2] D. O. Hall and K. K. Rao, *Photosynthesis* (Cambridge University Press, 1999).

[3] R. E. Blankenship, D. M. Tiede, J. Barber, G. W. Brudvig, G. Fleming, M. Ghirardi, M. R. Gunner, W. Junge, D. M. Kramer, A. Melis, T. A. Moore, C. C. Moser, D. G. Nocera, A. J. Nozik, D. R. Ort, W. W. Parson, R. C. Prince and R. T. Sayre, *Comparing Photosynthetic and Photovoltaic Efficiencies and Recognizing the Potential for Improvement*, Science **332**, 805 (2011).

[4] F. Hyder, K. Sudhakar and R. Mamat, *Solar PV Tree Design: A Review*, Renew. Sust. Energ. Rev. **82**, 1079 (2018).

[5] B. O'regan and M. Grätzel, *A Low-cost, High-efficiency Solar Cell based on Dye-sensitized Colloidal TiO 2 Films*, Nature **353**, 737 (1991).

[6] A. Kojima, K. Teshima, Y. Shirai and T. Miyasaka, *Organometal Halide Perovskites as Visible-light Sensitizers for Photovoltaic Cells*, J. Am. Chem. Soc. **131**, 6050 (2009).

[7] J. Burschka, N. Pellet, S.-J. Moon, R. Humphry-Baker, P. Gao, M. K. Nazeeruddin and M. Grätzel, *Sequential Deposition As a Route to High-performance Perovskite-sensitized Solar Cells*, Nature **499**, 316 (2013).

[8] M. Liu, M. B. Johnston and H. J. Snaith, *Efficient Planar Heterojunction Perovskite Solar Cells by Vapour Deposition*, Nature **501**, 395 (2013).

[9] G. McDermott, S. M. Prince, A. A. Freer, A. M. Hawthornthwaite Lawless, M. Z. Papiz, R. J. Cogdell and N. W. Isaacs, *Crystal Structure of an Integral Membrane Light-Harvesting Complex from Photosynthetic Bacteria*, Nature **374**, 517 (1995).

[10] R. J. Cogdell, A. Gall and J. Köhler, *The Architecture and Function of the Light-Harvesting Apparatus of Purple Bacteria: From Single Molecules to in Vivo Membranes*, Q. Rev. Biophys. **39**, 227 (2006).

[11] A. V. Ruban, *Light Harvesting Control in Plants*, FEBS Lett. **592**, 3030 (2018).

[12] A. V. Ruban, *Evolution under the Sun: Optimizing Light Harvesting in Photosynthesis*, J. Exp. Bot. **66**, 7 (2014).

[13] D. A. Bryant and N.-U. Frigaard, *Prokaryotic Photosynthesis and Phototrophy*

Illuminated, Trends Microbiol. **14**, 488 (2006).

[14] R. Buick, *When did Oxygenic Photosynthesis Evolve?* .

[15] G. S. Engel, T. R. Calhoun, E. L. Read, T. K. Ahn, T. Mancal, Y. C. Cheng, R. E. Blankenship and G. R. Fleming, *Evidence for Wavelike Energy Transfer Through Quantum Coherence in Photosynthetic Systems*, Nature **446**, 782 (2007).

[16] T. Brixner, J. Stenger, H. M. Vaswani, M. Cho, R. E. Blankenship and G. R. Fleming, *Two-Dimensional Spectroscopy of Electronic Couplings in Photosynthesis*, Nature **434**, 625 (2005).

[17] P. G. Wolynes, *Some Quantum Weirdness in Physiology*, Proc. Natl. Acad. Sci. USA **106**, 17247 (2009).

[18] G. Panitchayangkoon, D. Hayes, K. A. Fransted, J. R. Caram, E. Harel, J. Wen, R. E. Blankenship and G. S. Engel, *Long-Lived Quantum Coherence in Photosynthetic Complexes at Physiological Temperature*, Proc. Natl. Acad. Sci. USA **107**, 12766 (2010).

[19] J. Cao, R. J. Cogdell, D. F. Coker, H.-G. Duan, J. Hauer, U. Kleinekathöfer, T. L. C. Jansen, T. Mančal, R. J. D. Miller, J. P. Ogilvie, V. I. Prokhorenko, T. Renger, H.-S. Tan, R. Tempelaar, M. Thorwart, E. Thyrhaug, S. Westenhoff and D. Zigmantas, *Quantum Biology Revisited*, Sci. Adv. **6**, eaaz4888 (2020).

[20] N. Christensson, H. F. Kauffmann, T. Pullerits and T. Mančal, *Origin of Long-Lived Coherences in Light-Harvesting Complexes*, J. Phys. Chem. B **116**, 7449 (2012).

[21] A. Ishizaki and G. R. Fleming, *Quantum Coherence in Photosynthetic Light Harvesting*, Annu. Rev. Condens. Matter Phys. **3**, 333 (2012).

[22] G. D. Scholes, *Green Quantum Computers*, Nat. Phys. **6**, 402 (2010).

[23] A. Singharoy, C. Maffeo, K. H. Delgado-Magnero, D. J. K. Swainsbury, M. Şener, U. Kleinekathöfer, J. W. Vant, J. Nguyen, A. Hitchcock, B. Isralewitz, I. Teo, D. E. Chandler, J. E. Stone, J. C. Phillips, T. V. Pogorelov, M. I. Mallus, C. Chipot, Z. Luthey-Schulten, D. P. Tieleman, C. N. Hunter, E. Tajkhorshid, A. Aksimentiev and K. Schulten, *Atoms to Phenotypes: Molecular Design Principles of Cellular Energy Metabolism*, Cell **179**, 1098 (2019).

[24] R. E. Fenna and B. W. Matthews, *Chlorophyll Arrangement in a Bacteriochlorophyll Protein from* Chlorobium Limicola, Nature **258**, 573 (1975).

[25] D. E. Tronrud, J. Wen, L. Gay and R. E. Blankenship, *The Structural Basis*

for the Difference in Absorbance Spectra for the FMO Antenna Protein from Various Green Sulfur Bacteria, Photosynth. Res. **100**, 79 (2009).

[26] S. Shim, P. Rebentrost, S. Valleau and A. Aspuru Guzik, *Atomistic Study of the Long-Lived Quantum Coherences in the Fenna-Matthew-Olson Complex*, Biophys. J. **102**, 649 (2012).

[27] C. Olbrich, T. L. C. Jansen, J. Liebers, M. Aghtar, J. Strümpfer, K. Schulten, J. Knoester and U. Kleinekathöfer, *From Atomistic Modeling to Excitation Dynamics and Two-Dimensional Spectra of the FMO Light-Harvesting Complex*, J. Phys. Chem. B **115**, 8609 (2011).

[28] C. Olbrich, J. Strümpfer, K. Schulten and U. Kleinekathöfer, *Quest for Spatially Correlated Fluctuations in the FMO Light-Harvesting Complex*, J. Phys. Chem. B **115**, 758 (2011).

[29] H.-G. Duan, V. I. Prokhorenko, R. J. Cogdell, K. Ashraf, A. L. Stevens, M. Thorwart and R. J. D. Miller, *Nature Does Not Rely on Long-Lived Electronic Quantum Coherence for Photosynthetic Energy Transfer*, Proc Natl Acad Sci USA **114**, 8493 (2017).

[30] E. Thyrhaug, R. Tempelaar, M. J. P. Alcocer, K. Žídek, D. Bína, J. Knoester, T. L. C. Jansen and D. Zigmantas, *Identification And Characterization Of Diverse Coherences In The Fenna-Matthews-Olson Complex*, Nat. Chem. **10**, 780 (2018).

[31] E. Harel and G. S. Engel, *Quantum Coherence Spectroscopy Reveals Complex Dynamics in Bacterial Light-Harvesting Complex 2 (LH2)*, Proc. Natl. Acad. Sci. USA **109**, 706 (2012).

[32] J. Koepke, X. Hu, C. Muenke, K. Schulten and H. Michel, *The Crystal Structure of the Light Harvesting Complex II (B800-850) from* Rhodospirillum molischianum, Structure **4**, 581 (1996).

[33] T. Mirkovic, E. E. Ostroumov, J. M. Anna, R. van Grondelle, Govindjee and G. D. Scholes, *Light Absorption and Energy Transfer in the Antenna Complexes of Photosynthetic Organisms*, Chem. Rev. **117**, 249 (2017).

[34] R. G. Alden, E. Johnson, V. Nagarajan and W. W. Parson, *Calculations of Spectroscopic Properties of the LH2 Bacteriochlorophyll-Protein Antenna Complex from Rhodopseudomonas Acidophila*, J. Phys. Chem. B **101**, 4667 (1997).

[35] X. Hu, T. Ritz, A. Damjanović and K. Schulten, *Pigment Organization and Transfer of Electronic Excitation in the Photosynthetic Unit of Purple Bacteria*,

J. Phys. Chem. B **101**, 3854 (1997).

[36] A. V. Ruban, R. Berera, C. Ilioaia, I. H. Van Stokkum, J. T. Kennis, A. A. Pascal, H. Van Amerongen, B. Robert, P. Horton and R. Van Grondelle, *Identification of a Mechanism of Photoprotective Energy Dissipation in Higher Plants*, Nature **450**, 575 (2007).

[37] A. V. Ruban, M. P. Johnson and C. D. P. Duffy, *The Photoprotective Molecular Switch in the Photosystem II Antenna*, Biochim. Biophys. Acta (BBA) - Bioenergetics **1817**, 167 (2012).

[38] J. Chmeliov, A. Gelzinis, E. Songaila, R. Augulis, C. D. P. Duffy, A. V. Ruban and L. Valkunas, *The Nature of Self-Regulation in Photosynthetic Light-Harvesting Antenna*, Nat. Plants **2**, 16045 (2016).

[39] E. Bergantino, A. Segalla, A. Brunetta, E. Teardo, F. Rigoni, G. M. Giacometti and I. Szabo, *Light- and pH-dependent Structural Changes in the PsbS Subunit of Photosystem II*, Proc. Natl. Acad. Sci. USA **100**, 15265 (2003).

[40] V. Daskalakis, *Protein-Protein Interactions Within Photosystem II under Photoprotection: The Synergy Between CP29 Minor Antenna, Subunit S (PsbS) and Zeaxanthin at All-atom Resolution*, Phys. Chem. Chem. Phys. **20**, 11843 (2018).

[41] N. Liguori, S. R. R. Campos, A. Baptista and R. Croce, *Molecular Anatomy of Plant Photoprotective Switches: The Sensitivity of Psbs to the Environment, Residue by Residue*, J. Phys. Chem. Lett. **10**, 1737 (2019).

[42] D. Shevela, L. O. Björn & *al.*, *Evolution of the Z-scheme of Photosynthesis: a Perspective*, Photosynth. Res. **133**, 5 (2017).

[43] L. Tian, P. Xu, V. U. Chukhutsina, A. R. Holzwarth and R. Croce, *Zeaxanthin-dependent Nonphotochemical Quenching Does Not Occur in Photosystem I in the Higher Plant Arabidopsis Thalianaa*, Proc. Natl. Acad. Sci. **114**, 4828 (2017).

[44] H. Ryu, A. Fuwad, S. Yoon, H. Jang, J. C. Lee, S. M. Kim and T.-J. Jeon, *Biomimetic Membranes with Transmembrane Proteins: State-of-the-art in Transmembrane Protein Applications*, Int. J. Mol. Sci. **20**, 1437 (2019).

[45] G. R. Fleming, G. S. Schlau-Cohen, K. Amarnath and J. Zaks, *Design Principles of Photosynthetic Light-harvesting*, Faraday Discuss. **155**, 27 (2012).

[46] Z. Liu, H. Yan, K. Wang, T. Kuang, J. Zhang, L. Gui, X. An and W. Chang, *Crystal Structure of Spinach Major Light-Harvesting Complex at 2.72 Å Resolution*, Nature **428**, 287 (2004).

[47] X. Pan, M. Li, T. Wan, L. Wang, C. Jia, Z. Hou, X. Zhao, J. Zhang and W. Chang, *Structural Insights into Energy Regulation of Light-Harvesting Complex CP29 from Spinach*, Nat. Struct. Mol. Bio. **18**, 309 (2011).

[48] S. Mathew, A. Yella, P. Gao, R. Humphry Baker, B. F. E. Curchod, N. Ashari Astani, I. Tavernelli, U. Rothlisberger, N. Khaja and M. Grätzel, *Dye-sensitized Solar Cells with 13% Efficiency Achieved through the Molecular Engineering of Porphyrin Sensitizers*, Nat. Chem. **6**, 242 (2014).

[49] J. Zhang, J.-Z. Zhang, H.-B. Li, Y. Wu, Y. Geng and Z.-M. Su, *Rational Modifications on Champion Porphyrin Dye SM315 Using Different Electron-withdrawing Moieties Toward High Performance Dye-sensitized Solar Cells*, Phys. Chem. Chem. Phys. **16**, 24994 (2014).

[50] Y. Ishida, T. Shimada, D. Masui, H. Tachibana, H. Inoue and S. Takagi, *Efficient Excited Energy Transfer Reaction in Clay/Porphyrin Complex toward an Artificial Light-Harvesting System*, J. Am. Chem. Soc. **133**, 14280 (2011).

[51] S. Takagi, T. Shimada, Y. Ishida, T. Fujimura, D. Masui, H. Tachibana, M. Eguchi and H. Inoue, *Size-matching Effect on Inorganic Nanosheets: Control of Distance, Alignment, and Orientation of Molecular Adsorption as a Bottom-up Methodology for Nanomaterials*, Langmuir **29**, 2108 (2013).

[52] Y. Ohtani, T. Shimada and S. Takagi, *Artificial Light-harvesting System with Energy Migration Functionality in a Cationic Dye/Inorganic Nanosheet Complex*, J. Phys. Chem. C **119**, 18896 (2015).

[53] T. Förster, *Zwischenmolekulare Energiewanderung und Fluoreszenz*, Annalen der physik **437**, 55 (1948).

[54] D. L. Dexter, *A Theory of Sensitized Luminescence in solids*, J. Chem. Phys. **21**, 836 (1953).

[55] E. Collini, C. Y. Wong, K. E. Wilk, P. M. G. Curmi, P. Brumer and G. D. Scholes, *Coherently Wired Light-harvesting in Photosynthetic Marine Algae at Ambient Temperature*, Nature **463**, 644 (2010).

[56] E. Collini and G. D. Scholes, *Coherent Intrachain Energy Migration in a Conjugated Polymer at Room Temperature*, Science **323**, 369 (2009).

[57] H.-G. Duan, V. I. Prokhorenko, E. Wientjes, R. Croce, M. Thorwart and R. J. D. Miller, *Primary Charge Separation in the Photosystem II Reaction Center Revealed by a Global Analysis of the Two-dimensional Electronic Spectra*, Sci. Rep. **7**, 12347 (2017).

[58] V. May and O. Kühn, *Charge and Energy Transfer in Molecular Systems*

(Wiley–VCH, 2011), 3rd edition.

[59] C. Olbrich and U. Kleinekathöfer, *Time-Dependent Atomistic View on the Electronic Relaxation in Light-Harvesting System II*, J. Phys. Chem. B **114**, 12427 (2010).

[60] C. Olbrich, J. Strümpfer, K. Schulten and U. Kleinekathöfer, *Theory and Simulation of the Environmental Effects on FMO Electronic Transitions*, J. Phys. Chem. Lett. **2**, 1771 (2011).

[61] L. Viani, C. Curutchet and B. Mennucci, *Spatial and Electronic Correlations in the PE545 Light-Harvesting Complex*, J. Phys. Chem. Lett. **4**, 372 (2013).

[62] C. Curutchet and B. Mennucci, *Quantum Chemical Studies of Light Harvesting*, Chem. Rev. **117**, 294 (2017).

[63] F. Segatta, L. Cupellini, M. Garavelli and B. Mennucci, *Quantum Chemical Modeling of the Photoinduced Activity of Multichromophoric Biosystems*, Chem. Rev. **119**, 9361 (2019).

[64] C. Olbrich, J. Liebers and U. Kleinekathöfer, *Modeling of Light-Harvesting in Purple Bacteria Using a Time-Dependent Hamiltonian Approach*, phys. stat. sol. (b) **248**, 393 (2011).

[65] M. Aghtar, J. Liebers, J. Strümpfer, K. Schulten and U. Kleinekathöfer, *Juxtaposing Density Matrix and Classical Path-Based Wave Packet Dynamics*, J. Chem. Phys. **136**, 214101 (2012).

[66] M. Aghtar, J. Strümpfer, C. Olbrich, K. Schulten and U. Kleinekathöfer, *Different Types of Vibrations Interacting with Electronic Excitations in Phycoerythrin 545 and Fenna-Matthews-Olson Antenna Systems*, J. Phys. Chem. Lett. **5**, 3131 (2014).

[67] M. K. Lee and D. F. Coker, *Modeling Electronic-Nuclear Interactions for Excitation Energy Transfer Processes in Light-Harvesting Complexes*, J. Phys. Chem. Lett. **7**, 3171 (2016).

[68] M. Elstner, D. Porezag, G. Jungnickel, J. Elsner, M. Haugk, T. Frauenheim, S. Suhai and G. Seifert, *Self-consistent-charge Density-functional Tight-binding Method for Simulations of Complex Materials Properties*, Phys. Rev. B **58**, 7260 (1998).

[69] J. J. Kranz, M. Elstner, B. Aradi, T. Frauenheim, V. Lutsker, A. D. Garcia and T. A. Niehaus, *Time-Dependent Extension of the Long-Range Corrected Density Functional Based Tight-Binding Method*, J. Chem. Theory Comput. **13**, 1737 (2017).

[70] M. Gaus, Q. Cui and M. Elstner, *DFTB3: Extension of the Self-Consistent-Charge Density-Functional Tight-Binding Method (SCC-DFTB)*, J. Chem. Theory Comput. **7**, 931 (2011).

[71] M. Gaus, A. Goez and M. Elstner, *Parametrization and Benchmark of DFTB3 for Organic Molecules*, J. Chem. Theory Comput. **9**, 338 (2013).

[72] V. Lutsker, B. Aradi and T. A. Niehaus, *Implementation and Benchmark of a Long-Range Corrected Functional in the Density Functional Based Tight-Binding Method*, J. Chem. Phys. **143**, 184107 (2015).

[73] M. E. Madjet, A. Abdurahman and T. Renger, *Intermolecular Coulomb Couplings from Ab Initio Electrostatic Potentials: Application to Optical Transitions of Strongly Coupled Pigments in Photosynthetic Antennae and Reaction Centers*, J. Phys. Chem. B **110**, 17268 (2006).

[74] G. D. Scholes, C. Curutchet, B. Mennucci, R. Cammi and J.Tomasi, *How Solvent Controls Electronic Energy Transfer and Light Harvesting*, J. Phys. Chem. B **111**, 13253 (2007).

[75] T. Renger and F. Müh, *Theory of Excitonic Couplings in Dielectric Media: Foundation of Poisson-TrEsp Method and Application to Photosystem I Trimers*, Photosynth. Res. **111**, 47 (2012).

[76] A. Damjanović, I. Kosztin, U. Kleinekathöfer and K. Schulten, *Excitons in a Photosynthetic Light-Harvesting System: A Combined Molecular Dynamics, Quantum Chemistry and Polaron Model Study*, Phys. Rev. E **65**, 031919 (2002).

[77] M. Aghtar, J. Strümpfer, C. Olbrich, K. Schulten and U. Kleinekathöfer, *The FMO Complex in a Glycerol-Water Mixture*, J. Phys. Chem. B **117**, 7157 (2013).

[78] S. Chandrasekaran, M. Aghtar, S. Valleau, A. Aspuru-Guzik and U. Kleinekathöfer, *Influence of Force Fields and Quantum Chemistry Approach on Spectral Densities of BChl a in Solution and in FMO Proteins*, J. Phys. Chem. B **119**, 9995 (2015).

[79] S. Valleau, A. Eisfeld and A. Aspuru Guzik, *On the Alternatives for Bath Correlators and Spectral Densities from Mixed Quantum-Classical Simulations*, J. Chem. Phys. **137**, 224103 (2012).

[80] A. Ishizaki and G. R. Fleming, *Theoretical Examination of Quantum Coherence in a Photosynthetic System at Physiological Temperature*, Proc. Natl. Acad. Sci. USA **106**, 17255 (2009).

[81] C. Kreisbeck, T. Kramer, M. Rodriguez and B. Hein, *High-Performance Solution of Hierarchical Equations of Motion for Studying Energy Transfer in Light-Harvesting Complexes*, J. Chem. Theory Comput. **7**, 2166 (2011).

[82] C. Kreisbeck, T. Kramer and A. Aspuru-Guzik, *Scalable High-Performance Algorithm for the Simulation of Exciton Dynamics. Application to the Light-Harvesting Complex II in the Presence of Resonant Vibrational Modes*, J. Chem. Theory Comput. **10**, 4045 (2014).

[83] T. L. C. Jansen, *Simple Quantum Dynamics with Thermalization*, J. Phys. Chem. A **122**, 172 (2018).

[84] S. L. Logunov, L. Song and M. A. El-Sayed, *Excited-state Dynamics of a Protonated Retinal Schiff base in Solution*, J. Phys. Chem. **100**, 18586 (1996).

[85] G. G. Kochendoerfer, S. W. Lin, T. P. Sakmar and R. A. Mathies, *How Color Visual Pigments are Tuned*, Trends Biochem. Sci. **24**, 300 (1999).

[86] I. Chizhov, G. Schmies, R. Seidel, J. R. Sydor, B. Lüttenberg and M. Engelhard, *The Photophobic Receptor from Natronobacterium Pharaonis: Temperature and Ph Dependencies of the Photocycle of Sensory Rhodopsin II*, Biophys. J. **75**, 999 (1998).

[87] R. R. Birge and C. F. Zhang, *Two-photon Double Resonance Spectroscopy of Bacteriorhodopsin. Assignment of the Electronic and Dipolar Properties of the Low-lying 1 Ag*–g-like and 1 B*+ u-like π, π* states*, J. Chem. Phys. **92**, 7178 (1990).

[88] M. Hoffmann, M. Wanko, P. Strodel, P. H. König, T. Frauenheim, K. Schulten, W. Thiel, E. Tajkhorshid and M. Elstner, *Color Tuning in Rhodopsins: The Mechanism for the Spectral Shift between Bacteriorhodopsin and Sensory Rhodopsin II*, J. Am. Chem. Soc. **128**, 10808 (2006).

[89] M. Wanko, M. Hoffmann, T. Frauenheim and M. Elstner, *Computational Photochemistry of Retinal Proteins*, J. Comput. Aided Mol. Des. **20**, 511 (2006).

[90] M. Gouterman, *Spectra of Porphyrins*, J. Mol. Spectrosc. **6**, 138 (1961).

[91] M. Gouterman and G. H. Wagnière, *Spectra of Porphyrins*, J. Mol. Spectrosc. **127**, 108 (1963).

[92] M. Umetsu, Z. Wang, K. Yoza, M. Kobayashi and T. Nozawa, *Interaction of Photosynthetic Pigments with Various Organic Solvents 2. Application of Magnetic Circular Dichroism to Bacteriochlorophyll a and Light-harvesting Complex 1.*, Biochim. Biophys. Acta **1457**, 106 (2000).

[93] E. Thyrhaug, K. Zidek, J. Dostál, D. Bina and D. Zigmantas, *Exciton Structure and Energy Transfer in the Fenna-Matthews-Olson Complex*, J. Phys. Chem. Lett. **0**, null (2016).

[94] J. Neugebauer, *Subsystem-based Theoretical Spectroscopy of Biomolecules and Biomolecular Assemblies*, ChemPhysChem **10**, 3148 (2009).

[95] M. T. Milder, B. Brüggemann, R. van Grondelle and J. L. Herek, *Revisiting the Optical Properties of the FMO Protein*, Photosynth. Res. **104**, 257 (2010).

[96] M. Schreiber and V. Buss, *Origin of the Bathochromic Shift in the Early Photointermediates of the Rhodopsin Visual Cycle: A CASSCF/CASPT2 Study*, Int. J. Quantum Chem. **95**, 882 (2003).

[97] N. Ferré and M. Olivucci, *Probing the Rhodopsin Cavity with Reduced Retinal Models at the CASPT2/CASSCF/AMBER Level of Theory*, J. Am. Chem. Soc. **125**, 6868 (2003).

[98] A. J. A. Aquino, M. Barbatti and H. Lischka, *Excited-State Properties and Environmental Effects for Protonated Schiff Bases: A Theoretical Study*, ChemPhysChem **7**, 2089 (2006).

[99] M. Wanko, M. Hoffmann, P. Strodel, A. Koslowski, W. Thiel, F. Neese, T. Frauenheim and M. Elstner, *Calculating Absorption Shifts for Retinal Proteins: Computational Challenges*, J. Phys. Chem. B **109**, 3606 (2005).

[100] A. Anda, T. Hansen and L. D. Vico, *Multireference Excitation Energies for Bacteriochlorophylls a within Light Harvesting System 2*, J. Chem. Theory Comput. **12**, 1305 (2016).

[101] A. Anda, L. De Vico and T. Hansen, *Intermolecular Modes between LH2 Bacteriochlorophylls and Protein Residues: The Effect on the Excitation Energies*, J. Phys. Chem. B **121**, 5499 (2017).

[102] N. H. List, C. Curutchet, S. Knecht, B. Mennucci and J. Kongsted, *Toward Reliable Prediction of the Energy Ladder in Multichromophoric Systems: A Benchmark Study on the FMO Light-Harvesting Complex*, J. Chem. Theory Comput. **9**, 4928 (2013).

[103] R. Send and D. Sundholm, *Coupled-cluster Studies of the Lowest Excited States of the 11-Cis-Retinal Chromophore*, Phys. Chem. Chem. Phys. **9**, 2862 (2007).

[104] R. Send and D. Sundholm, *The Role of the β-Ionone Ring in the Photochemical Reaction of Rhodopsin*, J. Phys. Chem. A **111**, 27 (2007).

[105] R. Send, D. Sundholm, M. P. Johansson and F. Pawlowski, *Excited State*

Potential Energy Surfaces of Polyenes and Protonated Schiff Bases, J. Chem. Theory Comput. **5**, 2401 (2009).

[106] O. Valsson and C. Filippi, *Photoisomerization of Model Retinal Chromophores: Insight from Quantum Monte Carlo and Multiconfigurational Perturbation Theory*, J. Chem. Theory Comput. **6**, 1275 (2010).

[107] C. M. Suomivuori, N. O. Winter, C. Hättig, D. Sundholm and V. R. Kaila, *Exploring the Light-Capturing Properties of Photosynthetic Chlorophyll Clusters Using Large-Scale Correlated Calculations*, J. Chem. Theory Comput. **12**, 2644 (2016).

[108] J. Linnanto and J. Korppi-Tommola, *Quantum Chemical Simulation of Excited States of Chlorophylls, Bacteriochlorophylls and their Complexes*, Phys. Chem. Chem. Phys. **8**, 663 (2006).

[109] D. Jacquemin, E. A. Perpète, G. Scalmani, M. J. Frisch, R. Kobayashi and C. Adamo, *Assessment of the Efficiency of Long-range Corrected Functionals for Some Properties of Large Compounds*, J. Chem. Phys. **126**, 0 (2007).

[110] D. Jacquemin, E. A. Perpète, G. E. Scuseria, I. Ciofini and C. Adamo, *TD-DFT Performance for the Visible Absorption Spectra of Organic Dyes: Conventional Versus Long-range Hybrids*, J. Chem. Theory Comput. **4**, 123 (2008).

[111] I. V. Rostov, R. D. Amos, R. Kobayashi, G. Scalmani and M. J. Frisch, *Studies of the Ground and Excited-state Surfaces of the Retinal Chromophore using CAM-B3LYP*, J. Phys. Chem. B **114**, 5547 (2010).

[112] Y. Tawada, T. Tsuneda, S. Yanagisawa, T. Yanai and K. Hirao, *A Long-range-corrected Time-dependent Density Functional Theory*, J. Chem. Phys. **120**, 8425 (2004).

[113] O. Valsson, C. Filippi and M. E. Casida, *Regarding the Use and Misuse of Retinal Protonated Schiff Base Photochemistry as a Test Case for Time-dependent Density-functional Theory*, J. Chem. Phys. **142**, 144104 (2015).

[114] T. Yanai, D. P. Tew and N. C. Handy, *A New Hybrid Exchange–Correlation Functional Using the Coulomb-attenuating Method (CAM-B3LYP)*, Chem. Phys. Lett. **393**, 51 (2004).

[115] M. Higashi, T. Kosugi, S. Hayashi and S. Saito, *Theoretical Study on Excited States of Bacteriochlorophyll a in Solutions with Density Functional Assessment*, J. Phys. Chem. B **118**, 10906 (2014).

[116] T. Wolter, M. Elstner, S. Fischer, J. C. Smith and A.-N. Bondar, *Mechanism by which Untwisting of Retinal Leads to Productive*, J. Phys. Chem. B **119**,

2229 (2015).

[117] L. Cupellini, S. Jurinovich, M. Campetella, S. Caprasecca, C. A. Guido, S. M. Kelly, A. T. Gardiner, R. J. Cogdell and B. Mennucci, *An Ab Initio Description of the Excitonic Properties of LH2 and Their Temperature Dependence*, J. Phys. Chem. B **120**, 11348 (2016).

[118] A. D. Bacon and M. C. Zerner, *An Intermediate Neglect of Differential Overlap Theory for Transition Metal Complexes: Fe, Co and Cu Chlorides*, Theor. Chim. Acta **53**, 21 (1979).

[119] M. C. Zerner, G. H. Loew, R. F. Kirchner and U. T. Mueller Westerhoff, *An Intermediate Neglect of Differential Overlap Technique for Spectroscopy of Transition-Metal Complexes. Ferrocene*, J. Am. Chem. Soc. **102**, 589 (1980).

[120] M. G. Cory, M. C. Zerner, X. Hu and K. Schulten, *Electronic Excitations in Aggregates of Bacteriochlorophylls*, J. Phys. Chem. B **102**, 7640 (1998).

[121] K. Welke, J. S. Frahmcke, H. C. Watanabe, P. Hegemann and M. Elstner, *Color Tuning in Binding Pocket Models of the Chlamydomonas-type Channelrhodopsins*, J. Phys. Chem. B **115**, 15119 (2011).

[122] T. A. Niehaus, *Approximate Time-Dependent Density Functional Theory*, J. Mol. Struct.: THEOCHEM **914**, 38 (2009).

[123] T. A. Niehaus and F. Della Sala, *Range Separated Functionals in the Density Functional based Tight-binding Method: Formalism*, Phys. Status Solidi B **249**, 237 (2012).

[124] J. J. Kranz and M. Elstner, *Simulation of Singlet Exciton Diffusion in Bulk Organic Materials*, J. Chem. Theory Comput. **12**, 4209 (2016).

[125] L. Stojanovic, S. G. Aziz, R. H. Hilal, F. Plasser, T. A. Niehaus and M. Barbatti, *Nonadiabatic Dynamics of Cycloparaphenylenes with TD-DFTB Surface Hopping*, J. Chem. Theory Comput. (2017).

[126] C. Steinmann and J. Kongsted, *Electronic Energy Transfer in Polarizable Heterogeneous Environments: A Systematic Investigation of Different Quantum Chemical Approaches*, J. Chem. Theory Comput. **11**, 4283 (2015).

[127] F. Segatta, L. Cupellini, S. Jurinovich, S. Mukamel, M. Dapor, S. Taioli, M. Garavelli and B. Mennucci, *A Quantum Chemical Interpretation of Two-Dimensional Electronic Spectroscopy of Light-Harvesting Complexes*, J. Am. Chem. Soc. **139**, 7558 (2017).

[128] R. Ahlrichs, M. Bär, M. Häser, H. Horn and C. Kölmel, *Electronic Structure Calculations on Workstation Computers: The Program System Turbomole*,

Chem. Phys. Lett. **162**, 165 (1989).

[129] A. Schäfer, H. Horn and R. Ahlrichs, *Fully Optimized Contracted Gaussian Basis Sets for Atoms Li to Kr*, J. Chem. Phys. **97**, 2571 (1992).

[130] A. Schäfer, C. Huber and R. Ahlrichs, *Fully Optimized Contracted Gaussian Basis Sets of Triple Zeta Valence Quality for Atoms Li to Kr*, J. Chem. Phys. **100**, 5829 (1994).

[131] F. Neese, *Software Update: The ORCA Program System, Version 4.0*, WIREs Comput. Mol. Sci. **8**, e1327 (2018).

[132] J. Almlöf, T. H. Fischer, P. G. Gassman, A. Ghosh and M. Häser, *Electron Correlation in Tetrapyrroles. Ab initio Calculations on Porphyrin and the Tautomers of Chlorin*, J. Phys. Chem. **97**, 10964 (1993).

[133] M. J. Abraham, T. Murtola, R. Schulz, S. Páll, J. C. Smith, B. Hess and E. Lindahl, *GROMACS: High Performance Molecular Simulations through Multi-Level Parallelism from Laptops to Supercomputers*, SoftwareX **1**, 19 (2015).

[134] T. Kubař, K. Welke and G. Groenhof, *New QM/MM Implementation of the DFTB3 Method in the Gromacs Package*, J. Comput. Chem. **36**, 1978 (2015).

[135] M. Eichinger, P. Tavan, J. Hutter and M. Parrinello, *A Hybrid Method for Solutes in Complex Solvents: Density Functional Theory Combined with Empirical Force Fields*, J. Chem. Phys. **110**, 10452 (1999).

[136] H. C. Watanabe, K. Welke, D. J. Sindhikara, P. Hegemann and M. Elstner, *Towards an Understanding of Channelrhodopsin Function: Simulations Lead to Novel Insights of the Channel Mechanism.*, J. Mol. Biol. **425**, 1795 (2013).

[137] J. Huang and A. D. MacKerell, *CHARMM36 All-atom Additive Protein Force Field: Validation Based on Comparison to NMR Data*, J. Comput. Chem. **34**, 2135 (2013).

[138] M. Gaus, X. Lu, M. Elstner and Q. Cui, *Parameterization of DFTB3/3OB for sulfur and phosphorus for chemical and biological applications*, J. Chem. Theory Comput. **10**, 1518 (2014).

[139] B. Hess, C. Kutzner, D. V. D. Spoel and E. Lindahl, *GROMACS 4: Algorithms for Highly Efficient, Load-balanced, and Scalable Molecular Simulation*, J. Chem. Theory Comput. **4**, 435 (2008).

[140] A. MacKerell, D. Bashford, M. Bellott, R. Dunbrack, J. Evanseck, M. Field, S. Fischer, J. Gao, H. Guo, S. Ha, D. Joseph McCarthy, L. Kuchnir, K. Kuczera, F. Lau, C. Mattos, S. Michnick, T. Ngo, D. Nguyen, B. Prodhom, W. Rei-

her, B. Roux, M. Schlenkrich, J. Smith, R. Stote, J. Straub, M. Watanabe, J. Wiorkiewicz Kuczera, D. Yin and M. Karplus, *All-Atom Empirical Potential for Molecular Modeling and Dynamics Studies of Proteins*, J. Phys. Chem. B **102**, 3586 (1998).

[141] C. S. López, O. N. Faza, S. L. Estévez and A. R. De Lera, *Computation of Vertical Excitation Energies of Retinal and Analogs: Scope and Limitations*, J. Comput. Chem. **27**, 116 (2006).

[142] S. Hirata and M. Head-Gordon, *Time-dependent Density Functional Theory Within the Tamm–dancoff Approximation*, Chem. Phys. Lett. **314**, 291 (1999).

[143] K. Eichkorn, O. Treutler, H. Öhm, M. Häser and R. Ahlrichs, *Auxiliary Basis Sets to Approximate Coulomb Potentials*, Chem. Phys. Lett. **242**, 652 (1995).

[144] F. Neese, F. Wennmohs, A. Hansen and U. Becker, *Efficient, Approximate and Parallel Hartree-fock and Hybrid DFT Calculations. A 'chain-of-spheres' Algorithm for the Hartree-fock Exchange*, Chem. Phys. **356**, 98 (2009).

[145] F. Weigend, *Accurate Coulomb-fitting Basis Sets for H to Rn*, Phys. Chem. Chem. Phys. **8**, 1057 (2006).

[146] J. D. Chai and M. Head-Gordon, *Systematic Optimization of Long-range Corrected Hybrid Density Functionals*, J. Chem. Phys. **128**, 084106 (2008).

[147] T. A. Niehaus, S. Suhai, F. Della Sala, P. Lugli, M. Elstner, G. Seifert and T. Frauenheim, *Tight-Binding Approach to Time-Dependent Density-Functional Response Theory*, Phys. Rev. B **63**, 085108 (2001).

[148] R. Baer and D. Neuhauser, *Density Functional Theory with Correct Long-Range Asymptotic Behavior*, Phys. Rev. Lett. **94**, 2 (2005).

[149] E. Livshits and R. Baer, *A Well-Tempered Density Functional Theory of Electrons in Molecules*, Phys. Chem. Chem. Phys. **9**, 2932 (2007).

[150] C. M. Marian, A. Heil and M. Kleinschmidt, *The DFT/MRCI Method*, WIREs Comput. Mol. Sci. **0**, e1394 (2018).

[151] S. Maity, A. Gelessus, V. Daskalakis and U. Kleinekathöfer, *On a Chlorophyll-Caroteinoid Coupling in LHCII*, Chem. Phys. **526**, 110439 (2019).

[152] C. Hättig and F. Weigend, *CC2 Excitation Energy Calculations on Large Molecules Using the Resolution of the Identity Approximation*, J. Chem. Phys. **113**, 5154 (2000).

[153] C. Hättig, *Structure Optimizations for Excited States with Correlated Second-Order Methods: CC2 and ADC(2)*, Adv. Quantum Chem. **50**, 37 (2005).

[154] N. O. C. Winter and C. Hättig, *Scaled opposite-spin CC2 for ground and excited states with fourth order scaling computational costs*, J. Chem. Phys. **134**, 184101 (2011).

[155] N. O. C. Winter, N. K. Graf, S. Leutwyler and C. Hättig, *Benchmarks for 0–0 transitions of aromatic organic molecules: DFT/B3LYP, ADC(2), CC2, SOS-CC2 and SCS-CC2 compared to high-resolution gas-phase data*, Phys. Chem. Chem. Phys. **15**, 6623 (2013).

[156] A. Koslowski, M. E. Beck and W. Thiel, *Implementation of a General Multireference Configuration Interaction Procedure With Analytic Gradients in a Semiempirical Context Using the Graphical Unitary Group Approach*, J. Comput. Chem. **6**, 714 (2003).

[157] W. Weber and W. Thiel, *Orthogonalization Corrections for Semiempirical Methods*, Theo. Chem. Acc. **103**, 495 (2000).

[158] Y. Guo, F. E. Beyle, B. M. Bold, H. C. Watanabe, A. Koslowski, W. Thiel, P. Hegemann, M. Marazzi and M. Elstner, *Active site structure and absorption spectrum of channelrhodopsin-2 wild-type and C128T mutant*, Chem. Sci. **7**, 3879 (2016).

[159] A. Kubas, F. Hoffmann, A. Heck, H. Oberhofer, M. Elstner and J. Blumberger, *Electronic Couplings for Molecular Charge Transfer: Benchmarking CDDFT, FODFT, and FODFTB against High-Level* ab initio *Calculations*, J. Chem. Phys. **140**, 104105 (2014).

[160] E. P. Kenny and I. Kassal, *Benchmarking Calculations of Excitonic Couplings Between Bacteriochlorophylls*, J. Phys. Chem. B **120**, 25 (2016).

[161] T. Lu and F. Chen, *Multiwfn: A Multifunctional Wavefunction Analyzer*, J. Comput. Chem. **33**, 580 (2012).

[162] H. Kitoh-Nishioka, D. Yokogawa and S. Irle, *Förster Resonance Energy Transfer between Fluorescent Proteins: Efficient Transition Charge-based Study*, J. Phys. Chem. C **121**, 4220 (2017).

[163] S. Ahuja, M. Eilers, A. Hirshfeld, E. C. Y. Yan, M. Ziliox, T. P. Sakmar, M. Sheves and S. O. Smith, *6-s-cis Conformation and Polar Binding Pocket of the Retinal Chromophore in the Photoactivated State of Rhodopsin* , J. Am. Chem. Soc. **131**, 15160 (2009).

[164] L. H. Andersen, I. B. Nielsen, M. B. Kristensen, M. O. El Ghazaly, S. Haacke, M. B. Nielsen and M. Å. Petersen, *Absorption of Schiff-Base Retinal Chromophores in Vacuo*, J. Am. Chem. Soc. **127**, 12347 (2005).

[165] C. L. Janssen and I. M. Nielsen, *New diagnostics for coupled-cluster and Møller–Plesset perturbation theory*, Chem. Phys. Lett. **290**, 423 (1998).

[166] J. Neugebauer, *Photophysical Properties of Natural Light-harvesting Complexes Studied by Subsystem Density Functional Theory*, J. Phys. Chem. B **112**, 2207 (2008).

[167] R. S. Knox and B. Q. Spring, *Dipole Strengths in the Chlorophylls*, Photochem. Photobiol. **77**, 497 (2003).

[168] R. Mathies and L. Stryer, *Retinal has a Highly Dipolar Vertically Excited Singlet State: Implications of Vision*, Proc. Natl. Acad. Sci. USA **73**, 2169 (1976).

[169] P. A. Plötz, T. Niehaus and O. Kühn, *A New Efficient Method for Calculation of Frenkel Exciton Parameters in Molecular Aggregates*, J. Chem. Phys. **140**, 174101 (2014).

[170] T. Kubař, P. Benjamin Woiczikowski, G. Cuniberti and M. Elstner, *Efficient Calculation of Charge-transfer Matrix Elements for Hole Transfer in DNA*, J. of Phys. Chem. B **112**, 7937 (2008).

[171] B. Moore and J. Autschbach, *Density Functional Study of Tetraphenylporphyrin Long-range Exciton Coupling*, ChemistryOpen **1**, 184 (2012).

[172] N. Schieschke, B. M. Bold, D. Holub, M. Hoffman, A. Dreuw, M. Elstner and S. Höfener, *to be published*.

[173] J. S. Frähmcke, M. Wanko, P. Phatak, M. A. Mroginski and M. Elstner, *The Protonation State of Glu181 in Rhodopsin Revisited: Interpretation of Experimental Data on the Basis of QM/MM Calculations*, J. Phys. Chem. B **114**, 11338 (2010).

[174] I. B. Nielsen, L. Lammich and L. H. Andersen, *S1 and S2 excited states of gas-phase schiff-base retinal chromophores*, Phys. Rev. Lett. **96**, 13 (2006).

[175] M. Wanko, M. Hoffmann, T. Frauenheim and M. Elstner, *Effect of Polarization on the Opsin Shift in Rhodopsins. 1. A Combined QM/QM/MM Model for Bacteriorhodopsin and Pharaonis Sensory Rhodopsin II*, J. Phys. Chem. B **112**, 11462 (2008).

[176] M. Wanko, M. Hoffmann, J. Frähmcke, T. Frauenheim and M. Elstner, *Effect of Polarization on the Opsin Shift in Rhodopsins. 2. Empirical Polarization Models for Proteins*, J. Phys. Chem. B **112**, 11468 (2008).

[177] L. Janosi, I. Kosztin and A. Damjanović, *Theoretical Prediction of Spectral and Optical Properties of Bacteriochlorophylls in Thermally Disordered*

LH2 Antenna Complexes, J. Chem. Phys. **125**, 014903 (2006).

[178] J.-P. Zhang, R. Fujii, P. Qian, T. Inaba, T. Mizoguchi and Y. Koyama, *Mechanism of the Carotenoid-to-bacteriochlorophyll Energy Transfer Via the S_1 State in the LH2 Complexes from Purple Bacteria*, J. Phys. Chem. B **104**, 3683 (2000).

[179] A. Damjanović, T. Ritz and K. Schulten, *Energy Transfer between Carotenoids and Bacteriochlorophylls in Light-Harvesting Complex II of Purple Bacteria*, Phys. Rev. E **59**, 3293 (1999).

[180] M. Pajusalu, M. Rätsep, G. Trinkunas and A. Freiberg, *Davydov Splitting of Excitons in Cyclic Bacteriochlorophyll a Nanoaggregates of Bacterial Light-harvesting Complexes Between 4.5 and 263 K*, ChemPhysChem **12**, 634 (2011).

[181] S. S. Skourtis, D. H. Waldeck and D. N. Beratan, *Fluctuations in Biological and Bioinspired Electron-Transfer Reactions*, Annu. Rev. Phys. Chem. **61**, 461 (2010).

[182] P. B. Woiczikowski, T. Kubař, R. Gutiérrez, R. A. Caetano, G. Cuniberti and M. Elstner, *Combined Density Functional Theory and Landauer Approach for Hole Transfer in DNA along Classical Molecular Dynamics Trajectories*, J. Chem. Phys. **130**, 215104 (2009).

[183] D. Hayes and G. S. Engel, *Extracting the Excitonic Hamiltonian of the Fenna-Matthews-Olson Complex Using Three-dimensional Third-Order Electronic Spectroscopy*, Biophys. J. **100**, 2043 (2011).

[184] C. W. Kim, B. Choi and Y. M. Rhee, *Excited State Energy Fluctuations in the Fenna-Matthews-Olson Complex from Molecular Dynamics Simulations with Interpolated Chromophore Potentials*, Phys. Chem. Chem. Phys. **20**, 3310 (2018).

[185] S. Jurinovich, C. Curutchet and B. Mennucci, *The Fenna-Matthews-Olson Protein Revisited: A Fully Polarizable (TD)DFT/MM Description*, ChemPhysChem **15**, 3194 (2014).

[186] X. Jia, Y. Mei, J. Z. H. Zhang and Y. Mo, *Hybrid QM/MM Study of FMO Complex with Polarized Protein-Specific Charge*, Sci. Rep. **5**, 17096 (2015).

[187] J. Wen, H. Zhang, M. L. Gross and R. E. Blankenship, *Membrane Orientation of the FMO Antenna Protein from* Chlorobaculum Tepidum *As Determined by Mass Spectrometry-based Footprinting*, Proc. Natl. Acad. Sci. USA **106**, 6134 (2009).

[188] B. W. Matthews, R. E. Fenna, M. C. Bolognesi, M. F. Schmid and J. M. Olson, *Structure of a Bacteriochlorophyll A-protein from the Green Photosynthetic Bacterium Prosthecochloris aestuarii*, J. Mol. Biol. **131**, 259 (1979).

[189] H. Lee, Y.-C. Cheng and G. R. Fleming, *Coherence Dynamics in Photosynthesis: Protein Protection of Excitonic Coherence*, Science **316**, 1462 (2007).

[190] S. Irgen-Gioro, K. Gururangan, R. G. Saer, R. E. Blankenship and E. Harel, *Electronic Coherence Lifetimes of the Fenna-Matthews-Olson Complex and Light Harvesting Complex II*, Chem. Sci. **10**, 10503 (2019).

[191] J. Adolphs and T. Renger, *How Proteins Trigger Excitation Energy Transfer in the FMO Complex of Green Sulfur Bacteria.*, Biophys. J. **91**, 2778 (2006).

[192] M. Schmidt am Busch, F. Müh, M. E.-A. Madjet and T. Renger, *The Eighth Bacteriochlorophyll Completes the Excitation Energy Funnel in the FMO Protein*, J. Phys. Chem. Lett. **2**, 93 (2011).

[193] J. Gao, W.-J. Shi, J. Ye, X. Wang, H. Hirao and Y. Zhao, *QM/MM Modeling of Environmental Effects on Electronic Transitions of the FMO Complex*, J. Phys. Chem. B **117**, 3488 (2013).

[194] A. Sisto, C. Stross, M. W. van der Kamp, M. O'Connor, S. McIntosh-Smith, G. T. Johnson, E. G. Hohenstein, F. R. Manby, D. R. Glowacki and T. J. Martinez, *Atomistic Non-Adiabatic Dynamics of the LH2 Complex with a GPU-Accelerated Ab Initio Exciton Model*, Phys. Chem. Chem. Phys. **19**, 14924 (2017).

[195] S. J. Jang and B. Mennucci, *Delocalized Excitons in Natural Light-Harvesting Complexes*, Rev. Mod. Phys. **90**, 035003 (2018).

[196] K. Claridge, D. Padula and A. Troisi, *How Fine-Tuned for Energy Transfer Is the Environmental Noise Produced by Proteins around Biological Chromophores?*, Phys. Chem. Chem. Phys. **20**, 17279 (2018).

[197] B. M. Bold, M. Sokolov, S. Maity, M. Wanko, P. M. Dohmen, J. J. Kranz, U. Kleinekathöfer, S. Höfener and M. Elstner, *Benchmark and Performance of Long-Range Corrected Time-Dependent Density Functional Tight Binding (LC-TD-DFTB) on Rhodopsins and Light-Harvesting Complexes*, Phys. Chem. Chem. Phys. **22**, 10500 (2020).

[198] T. Renger and F. Müh, *Understanding Photosynthetic Light-Harvesting: A Bottom Up Theoretical Approach*, Phys. Chem. Chem. Phys. **15**, 3348 (2013).

[199] S. Jurinovich, L. Viani, C. Curutchet and B. Mennucci, *Limits and Potentials of Quantum Chemical Methods in Modelling Photosynthetic Antennae*, Phys.

Chem. Chem. Phys. **17**, 30783 (2015).

[200] D. Padula, M. H. Lee, K. Claridge and A. Troisi, *Chromophore-Dependent Intramolecular Exciton-Vibrational Coupling in the FMO Complex: Quantification and Importance for Exciton Dynamics*, J. Phys. Chem. B **121**, 10026 (2017).

[201] H. Do and A. Troisi, *Developing Accurate Molecular Mechanics Force Fields for Conjugated Molecular Systems*, Phys. Chem. Chem. Phys. **17**, 25123 (2015).

[202] K. Claridge and A. Troisi, *Developing Consistent Molecular Dynamics Force Fields for Biological Chromophores Via Force Matching*, J. Phys. Chem. B (2018).

[203] A. M. Rosnik and C. Curutchet, *Theoretical Characterization of the Spectral Density of the Water-Soluble Chlorophyll-Binding Protein from Combined Quantum Mechanics/Molecular Mechanics Molecular Dynamics Simulations*, J. Chem. Theory Comput. **11**, 5826 (2015).

[204] S. M. Blau, D. I. G. Bennett, C. Kreisbeck, G. D. Scholes and A. Aspuru-Guzik, *Local Protein Solvation Drives Direct Down-Conversion in Phycobiliprotein PC645 Via Incoherent Vibronic Transport*, Proc. Natl. Acad. Sci. USA **115**, E3342 (2018).

[205] Y. Jing, R. Zheng, H.-X. Li and Q. Shi, *Theoretical Study of the Electronic-Vibrational Coupling in the Q_y States of the Photosynthetic Reaction Center in Purple Bacteria*, J. Phys. Chem. B **116**, 1164 (2012).

[206] M. K. Lee, P. Huo and D. F. Coker, *Semiclassical Path Integral Dynamics: Photosynthetic Energy Transfer with Realistic Environment Interactions*, Annu. Rev. Phys. Chem. **67**, 639 (2016).

[207] C. W. Kim and Y. M. Rhee, *Constructing an Interpolated Potential Energy Surface of a Large Molecule: A Case Study with Bacteriochlorophyll a Model in the Fenna-Matthews-Olson Complex*, J. Chem. Theory Comput. **12**, 5235 (2016).

[208] C. W. Kim, J. W. Park and Y. M. Rhee, *Effect of Chromophore Potential Model on the Description of Exciton-Phonon Interactions*, J. Phys. Chem. Lett. **6**, 2875 (2015).

[209] A. Dreuw and M. Head-Gordon, *Failure of Time-Dependent Density Functional Theory for Long-Range Charge-Transfer Excited States: The Zincbacteriochlorin-Bacteriochlorin and Bacteriochlorophyll-Spheroidene Complexes*, J. Am. Chem. Soc. **126**, 4007 (2004).

[210] R. J. Magyar and S. Tretiak, *Dependence of Spurious Charge-Transfer Excited States on Orbital Exchange in TDDFT: Large Molecules and Clusters*, J. Chem. Theory Comput. **3**, 976 (2007).

[211] M. Nottoli, S. Jurinovich, L. Cupellini, A. T. Gardiner, R. Cogdell and B. Mennucci, *The Role of Charge-Transfer States in the Spectral Tuning of Antenna Complexes of Purple Bacteria*, Photosynth. Res. **137**, 215 (2018).

[212] A. Domínguez, B. Aradi, T. Frauenheim, V. Lutsker and T. A. Niehaus, *Extensions of the Time-Dependent Density Functional Based Tight-Binding Approach*, J. Chem. Theory Comput. **9**, 4901 (2013).

[213] F. Häse, S. Valleau, E. Pyzer-Knapp and A. Aspuru-Guzik, *Machine Learning Exciton Dynamics*, Chem. Sci. **7**, 5139 (2016).

[214] L. Viani, M. Corbella, C. Curutchet, E. J. O'Reilly, A. Olaya Castro and B. Mennucci, *Molecular Basis of the Exciton-Phonon Interactions in the PE545 Light-Harvesting Complex*, Phys. Chem. Chem. Phys. **16**, 16302 (2014).

[215] M. Rätsep and A. Freiberg, *Electron-Phonon and Vibronic Couplings in the FMO Bacteriochlorophyll a Antenna Complex Studied by Difference Fluorescence Line Narrowing*, J. Lumin. **127**, 251 (2007).

[216] A. Kell, X. Feng, M. Reppert and R. Jankowiak, *On the Shape of the Phonon Spectral Density in Photosynthetic Complexes*, J. Phys. Chem. B **117**, 7317 (2013).

[217] M. Ceccarelli, P. Procacci and M. Marchi, *An Ab Initio Force Field for the Cofactors of Bacterial Photosynthesis*, J. Comput. Chem. **24**, 129 (2003).

[218] V. Novoderezhkin, M. A. Palacios, H. van Amerongen and R. van Grondelle, *Energy-Transfer Dynamics in the LHCII Complex of Higher Plants: Modified Redfield Approach*, J. Phys. Chem. B **108**, 10363 (2004).

[219] V. I. Novoderezhkin and R. van Grondelle, *Physical Origins and Models of Energy Transfer in Photosynthetic Light-Harvesting*, Phys. Chem. Chem. Phys. **12**, 7352 (2010).

[220] M. Aghtar, U. Kleinekathöfer, C. Curutchet and B. Mennucci, *Impact Of Electronic Fluctuations And Their Description On The Exciton Dynamics In The Light-Harvesting Complex PE545*, J. Phys. Chem. B **121**, 1330 (2017).

[221] L. Tian, W. J. Nawrocki, X. Liu, I. Polukhina, I. H. Van Stokkum and R. Croce, *Ph Dependence, Kinetics and Light-Harvesting Regulation of Nonphotochemical Quenching in Chlamydomonas*, Proc. Nat. Acad. Sci. **116**, 8320 (2019).

[222] A. Melis, *Photosystem-II Damage and Repair Cycle in Chloroplasts: What Modulates the Rate of Photodamage in Vivo?*, Trends Plant Sci. **4**, 130 (1999).

[223] D. Wagner, D. Przybyla, R. op den Camp, C. Kim, F. Landgraf, K. P. Lee, M. Würsch, C. Laloi, M. Nater, E. Hideg & *al.*, *The Genetic Basis of Singlet Oxygen-Induced Stress Responses of Arabidopsis Thaliana*, Science **306**, 1183 (2004).

[224] V. Daskalakis, S. Papadatos and U. Kleinekathöfer, *Fine Tuning of the Photosystem II Major Antenna Mobility within the Thylakoid Membrane of Higher Plants*, Biochim. Biophys. Acta - Biomembranes **1861**, 183059 (2019).

[225] V. Daskalakis, S. Maity, C. L. Hart, T. Stergiannakos, C. D. P. Duffy and U. Kleinekathöfer, *Structural Basis for Allosteric Regulation in the Major Antenna Trimer of Photosystem II*, J. Phys. Chem. B **123**, 9609 (2019).

[226] H. van Amerongen and R. van Grondelle, *Understanding the Energy Transfer Function of LHCII, the Major Light-Harvesting Complex of Green Plants*, J. Phys. Chem. B **105(3)**, 604 (2001).

[227] A. Kume, T. Akitsu and K. N. Nasahara, *Why is Chlorophyll B Only Used in Light-Harvesting Systems?*, J. Plant Res. **131**, 961 (2018).

[228] R. Croce and H. van Amerongen, *Natural Strategies for Photosynthetic Light Harvesting*, Nat. Chem. Biol. **10**, 492 (2014).

[229] V. I. Novoderezhkin, M. A. Palacios, H. van Amerongen and R. van Grondelle, *Excitation Dynamics in the LHCII Complex of Higher Plants: Modeling Based on the 2.72 Å Crystal Structure*, J. Phys. Chem. B **109**, 10493 (2005).

[230] G. S. Schlau-Cohen, T. R. Calhoun, N. S. Ginsberg, E. L. Read, M. Ballottari, R. Bassi, R. van Grondelle and G. R. Fleming, *Pathways of Energy Flow in LHCII from Two-dimensional Electronic Spectroscopy*, J. Phys. Chem. B **113**, 15352 (2009).

[231] F. Müh, M. E.-A. Madjet and T. Renger, *Structure-Based Identification of Energy Sinks in Plant Light-Harvesting Complex II*, J. Phys. Chem. B **114**, 13517 (2010).

[232] F. Müh and T. Renger, *Refined Structure-based Simulation of Plant Light-harvesting Complex II: Linear Optical Spectra of Trimers and Aggregates*, Biochim. Biophys. Acta.-Bioenergetics **1817**, 1446 (2012).

[233] X. Su, J. Ma, X. Wei, P. Cao, D. Zhu, W. Chang, Z. Liu, X. Zhang and M. Li, *Structure and Assembly Mechanism of Plant C2S2M2-type PSII-LHCII Super-*

complex, Science **357**, 815 (2017).

[234] P. Huo and D. F. Coker, *Iterative Linearized Density Matrix Propagation for Modeling Coherent Excitation Energy Transfer in Photosynthetic Light Harvesting*, J. Chem. Phys. **133**, 184108 (2010).

[235] C. Kreisbeck and A. Aspuru-Guzik, *Efficiency of Energy Funneling in the Photosystem II Supercomplex of Higher Plants*, Chem. Sci. **7**, 4174 (2016).

[236] I. Conti, G. Cerullo, A. Nenov and M. Garavelli, *Ultrafast Spectroscopy of Photoactive Molecular Systems from First Principles: Where We Stand Today and Where We Are Going*, J. Am. Chem. Soc. **142**, 16117 (2020).

[237] B. Mennucci and S. Corni, *Multiscale Modelling of Photoinduced Processes in Composite Systems*, Nat. Rev. Chem. **3**, 315 (2019).

[238] K. F. Fox, V. Balevičius, J. Chmeliov, L. Valkunas, A. V. Ruban and C. D. Duffy, *The Carotenoid Pathway: What Is Important for Excitation Quenching in Plant Antenna Complexes?*, Phys. Chem. Chem. Phys. **19**, 22957 (2017).

[239] T. Renger, A. Klinger, F. Steinecker, M. Schmidt am Busch, J. Numata and F. Müh, *Normal Mode Analysis of the Spectral Density of the Fenna-Matthews-Olson Light-Harvesting Protein: How the Protein Dissipates the Excess Energy of Excitons*, J. Phys. Chem. B **116**, 14565 (2012).

[240] K. Claridge, D. Padula and A. Troisi, *On the Arrangement of Chromophores in Light Harvesting Complexes: Chance Versus Design*, Faraday Discuss. **221**, 133 (2019).

[241] S. Maity, B. M. Bold, J. D. Prajapati, M. Sokolov, T. Kubař, M. Elstner and U. Kleinekathöfer, *DFTB/MM Molecular Dynamics Simulations of the FMO Light-Harvesting Complex*, J. Phys. Chem. Lett. **11**, 8660 (2020).

[242] C. Liu, Y. Rao, L. Zhang and C. Yang, *Identification of the Roles of Individual Amino Acid Residues of the Helix E of the Major Antenna of Photosystem II (LHCII) by Alanine Scanning Mutagenesis*, J. Biochem. **156**, 203 (2014).

[243] X.-P. Li, A. M. Gilmore, S. Caffarri, R. Bassi, T. Golan, D. Kramer and K. K. Niyogi, *Regulation of Photosynthetic Light Harvesting Involves Intrathylakoid Lumen Ph Sensing by the PsbS Protein*, J. Biol. Chem. **279**, 22866 (2004).

[244] T. J. Dolinsky, J. E. Nielsen, J. A. McCammon and N. A. Baker, *PDB2PQR: An Automated Pipeline for the Setup of Poisson-Boltzmann Electrostatics Calculations*, Nucleic Acids Res. **32**, W665 (2004).

[245] N. Liguori, X. Periole, S. J. Marrink and R. Croce, *From Light-Harvesting to Photoprotection: Structural Basis of the Dynamic Switch of the Major Antenna*

Complex of Plants (LHCII), Sci. Rep. **5**, 15661 (2015).

[246] A. A. Pascal, Z. Liu, K. Broess, B. van Oort, H. van Amerongen, C. Wang, P. Horton, B. Robert, W. Chang and A. Ruban, *Molecular Basis of Photoprotection and Control of Photosynthetic Light-Harvesting*, Nature **436**, 134 (2005).

[247] B. Hourahine, B. Aradi, V. Blum, F. Bonafé, A. Buccheri, C. Camacho, C. Cevallos, M. Y. Deshaye, T. Dumitrică, A. Dominguez, S. Ehlert, M. Elstner, T. Van Der Heide, J. Hermann, S. Irle, J. J. Kranz, C. Köhler, T. Kowalczyk, T. Kubař, I. S. Lee, V. Lutsker, R. J. Maurer, S. K. Min, I. Mitchell, C. Negre, T. A. Niehaus, A. M. N. Niklasson, A. J. Page, A. Pecchia, G. Penazzi, M. P. Persson, J. Řezáč, C. G. Sánchez, M. Sternberg, M. Stöhr, F. Stuckenberg, A. Tkatchenko, V. W.-Z. Yu and T. Frauenheim, *DFTB+, a Software Package for Efficient Approximate Density Functional Theory Based Atomistic Simulations*, J. Chem. Phys. **152**, 124101 (2020).

[248] B. Aradi, B. Hourahine and T. Frauenheim, *DFTB+, a Sparse Matrix-based Implementation of the DFTB Method*, J. Phys. Chem. A **111**, 5678 (2007).

[249] T. Renger, V. May and O. Kühn, *Ultrafast Excitation Energy Transfer Dynamics in Photosynthetic Pigment-Protein Complexes*, Phys. Rep. **343**, 137 (2001).

[250] S. Jurinovich, L. Viani, I. G. Prandi, T. Renger and B. Mennucci, *Towards an Ab Initio Description of the Optical Spectra of Light-Harvesting Antennae: Application to the CP29 Complex of Photosystem II*, Phys. Chem. Chem. Phys. **17**, 14405 (2015).

[251] V. Sláma, L. Cupellini and B. Mennucci, *Exciton Properties and Optical Spectra of Light Harvesting Complex II from a Fully Atomistic Description*, Phys. Chem. Chem. Phys. **22**, 16783 (2020).

[252] L. Zhang, D.-A. Silva, H. Zhang, A. Yue, Y. Yan and X. Huang, *Dynamic Protein Conformations Preferentially Drive Energy Transfer Along the Active Chain of the Photosystem II Reaction Centre*, Nat. Commun. **5**, 4170 (2014).

[253] J. Ridley and M. C. Zerner, *An Intermediate Neglect of Differential Overlap Technique for Spectroscopy: Pyrrole and the Azines*, Theor. Chim. Acta **32**, 111 (1973).

[254] M. A. Thompson and M. C. Zerner, *A Theoretical Examination of the Electronic Structure and Spectroscopy of the Photosynthetic Reaction Center from Rhodopseudomonas Viridis*, J. Am. Chem. Soc. **113**, 8210 (1991).

[255] D. I. Bennett, K. Amarnath and G. R. Fleming, *A Structure-Based Model of Energy Transfer Reveals the Principles of Light Harvesting in Photosystem II Supercomplexes*, J. Am. Chem. Soc. **135**, 9164 (2013).

[256] P. Bhattacharyya and G. R. Fleming, *The Role of Resonant Nuclear Modes in Vibrationally Assisted Energy Transport: The LHCII Complex*, J. Chem. Phys. **153**, 044119 (2020).

[257] J. J. Roden, D. I. Bennett and K. B. Whaley, *Long-Range Energy Transport in Photosystem II*, J. Chem. Phys. **144**, 245101 (2016).

[258] R. Stones, H. Hossein-Nejad, R. van Grondelle and A. Olaya-Castro, *On the Performance of a Photosystem II Reaction Centre-Based Photocell*, Chem. Sci. **8**, 6871 (2017).

[259] V. Balevičius, K. F. Fox, W. P. Bricker, S. Jurinovich, I. G. Prandi, B. Mennucci and C. D. Duffy, *Fine Control of Chlorophyll-Carotenoid Interactions Defines the Functionality of Light-harvesting Proteins in Plants*, Sci. Rep. **7**, 13956 (2017).

[260] L. Cupellini, D. Calvani, D. Jacquemin and B. Mennucci, *Charge Transfer from the Carotenoid Can Quench Chlorophyll Excitation in Antenna Complexes of Plants*, Nat. Commun. **11**, 662 (2020).

[261] J. Chmeliov, W. P. Bricker, C. Lo, E. Jouin, L. Valkunas, A. V. Ruban and C. D. P. Duffy, *An 'All Pigment' Model of Excitation Quenching in LHCII*, Phys. Chem. Chem. Phys. **17**, 15857 (2015).

[262] O. Andreussi, S. Knecht, C. M. Marian, J. Kongsted and B. Mennucci, *Carotenoids and Light-Harvesting: From DFT/MRCI to the Tamm-Dancoff Approximation*, J. Chem. Theory Comput. **11**, 655 (2015).

[263] D. Loco, F. Buda, J. Lugtenburg and B. Mennucci, *The Dynamic Origin of Color Tuning in Proteins Revealed by a Carotenoid Pigment*, J. Phys. Chem. Lett. **9**, 2404 (2018).

[264] M. Bondanza, L. Cupellini, F. Lipparini and B. Mennucci, *The Multiple Roles of the Protein in the Photoactivation of Orange Carotenoid Protein*, Chem **6**, 187 (2019).

[265] P. J. Walla, P. A. Linden, K. Ohta and G. R. Fleming, *Excited-State Kinetics of the Carotenoid S1 State in LHC II and Two-Photon Excitation Spectra of Lutein and β-carotene in Solution: Efficient Car S1$\rightarrow$ Chl Electronic Energy Transfer Via Hot S1 States?*, J. Phys. Chem. A **106**, 1909 (2002).

[266] D. Khokhlov and A. Belov, *Ab Initio Model for the Chlorophyll-Lutein Exciton*

Coupling in the LHCII Complex, Biophys Chem. **246**, 16 (2019).

[267] C. MacGregor-Chatwin, P. J. Jackson, M. Şener, J. W. Chidgey, A. Hitchcock, P. Qian, G. E. Mayneord, M. P. Johnson, Z. Luthey-Schulten, M. J. Dickman, D. J. Scanlan and C. N. Hunter, *Membrane Organization of Photosystem I Complexes in the Most Abundant Phototroph on Earth*, Nat. Plants **5**, 879 (2019).

[268] L. Nicol, W. J. Nawrocki and R. Croce, *Disentangling the Sites of Non-Photochemical Quenching in Vascular Plants*, Nat. Plants **5**, 1177 (2019).

[269] J. M. Buck, J. Sherman, C. R. Bártulos, M. Serif, M. Halder, J. Henkel, A. Falciatore, J. Lavaud, M. Y. Gorbunov, P. G. Kroth *& al.*, *Lhcx Proteins Provide Photoprotection via Thermal Dissipation of Absorbed Light in the Diatom Phaeodactylum Tricornutum*, Nat. Comm. **10**, 1 (2019).

[270] G. de la Cruz Valbuena, F. VA Camargo, R. Borrego-Varillas, F. Perozeni, C. D'Andrea, M. Ballottari and G. Cerullo, *Molecular Mechanisms of Nonphotochemical Quenching in the LHCSR3 Protein of Chlamydomonas reinhardtii*, J. Phys. Chem. Lett. **10**, 2500 (2019).

[271] X.-P. Li, O. Björkman, C. Shih, A. R. Grossman, M. Rosenquist, S. Jansson and K. K. Niyogi, *A Pigment-binding Protein Essential for Regulation of Photosynthetic Light Harvesting*, Nature **403**, 391 (2000).

[272] V. Correa-Galvis, G. Poschmann, M. Melzer, K. Stühler and P. Jahns, *PsbS Interactions Involved in the Activation of Energy Dissipation in Arabidopsis*, Nat. Plants **2**, 1 (2016).

[273] Z. Guardini, M. Bressan, R. Caferri, R. Bassi and L. Dall'Osto, *Identification of a Pigment Cluster Catalysing Fast Photoprotective Quenching Response in CP29*, Nat. Plants **6**, 303 (2020).

[274] L. Dall'Osto, S. Cazzaniga, M. Bressan, D. Paleček, K. Židek, K. K. Niyogi, G. R. Fleming, D. Zigmantas and R. Bassi, *Two Mechanisms for Dissipation of Excess Light in Monomeric and Trimeric Light-Harvesting Complexes*, Nat. Plants **3**, 17033 (2017).

[275] M. Son and G. S. Schlau-Cohen, *Flipping a Protein Switch: Carotenoid-Mediated Quenching in Plants*, Chem **5**, 2749 (2019).

[276] C. Duffy, J. Chmeliov, M. Macernis, J. Sulskus, L. Valkunas and A. Ruban, *Modeling of Fluorescence Quenching by Lutein in the Plant Light-Harvesting Complex LHCII*, J. Phys. Chem. B **117**, 10974 (2013).

[277] X. Wei, X. Su, P. Cao, X. Liu, W. Chang, M. Li, X. Zhang and Z. Liu, *Structure*

of Spinach Photosystem II-LHCII Supercomplex at 3.2 Å Resolution, Nature **534**, 69 (2016).

[278] F. Müh, D. Lindorfer, M. S. am Busch and T. Renger, *Towards a Structure-Based Exciton Hamiltonian for the CP29 Antenna of Photosystem II*, Phys. Chem. Chem. Phys. **16**, 11848 (2014).

[279] K. F. Fox, C. Ünlü, V. Balevičius Jr, B. N. Ramdour, C. Kern, X. Pan, M. Li, H. van Amerongen and C. D. Duffy, *A Possible Molecular Basis for Photoprotection in the Minor Antenna Proteins of Plants*, Biochim. Biophys. Acta. -Bioenergetics **1859**, 471 (2018).

[280] M. Lapillo, E. Cignoni, L. Cupellini and B. Mennucci, *The Energy Transfer Model of Nonphotochemical Quenching: Lessons from the Minor CP29 Antenna Complex of Plants*, Biochimica et Biophysica Acta -Bioenergetics **1861**, 148282 (2020).

[281] V. Daskalakis, S. Papadatos and T. Stergiannakos, *The Conformational Phase Space of the Photoprotective Switch in the Major Light Harvesting Complex II*, Chem. Comm. **56**, 11215 (2020).

[282] S. Maity, V. Daskalakis, M. Elstner and U. Kleinekathöfer, *Multiscale QM/MM Molecular Dynamics Simulations of the Trimeric Major Light-Harvesting Complex II*, Phys. Chem. Chem. Phys. **23**, 7407 (2021).

[283] Y. Duan, C. Wu, S. Chowdhury, M. C. Lee, G. Xiong, W. Zhang, R. Yang, P. Cieplak, R. Luo, T. Lee & *al.*, *A Point-Charge Force Field for Molecular Mechanics Simulations of Proteins Based on Condensed-Phase Quantum Mechanical Calculations*, J. Comput. Chem. **24**, 1999 (2003).

[284] L. Zhang, D.-A. Silva, Y. Yan and X. Huang, *Force Field Development for Cofactors in the Photosystem II*, J. Comput. Chem. **33**, 1969 (2012).

[285] I. G. Prandi, L. Viani, O. Andreussi and B. Mennucci, *Combining Classical Molecular Dynamics and Quantum Mechanical Methods for the Description of Electronic Excitations: The Case of Carotenoids*, J. Comput. Chem. **37**, 981 (2016).

[286] S. Jo, T. Kim, V. G. Iyer and W. Im, *CHARMM-GUI: A Web-Based Graphical User Interface for CHARMM*, J. Comput. Chem. **29**, 1859 (2008).

[287] A. W. S. Da Silva and W. F. Vranken, *ACPYPE-Antechamber Python Parser Interface*, BMC Res. Notes **5**, 367 (2012).

[288] C. Curutchet, G. D. Scholes, B. Mennucci and R. Cammi, *How Solvent Controls Electronic Energy Transfer and Light Harvesting: Toward a Quantum-*

mechanical Description of Reaction Field and Screening Effects, J. Phys. Chem. B **111**, 13253 (2007).

[289] M. Jassas, J. Chen, A. Khmelnitskiy, A. P. Casazza, S. Santabarbara and R. Jankowiak, *Structure-Based Exciton Hamiltonian and Dynamics for the Reconstituted Wild-Type CP29 Protein Antenna Complex of the Photosystem II*, J. Phys. Chem. B **122**, 4611 (2018).

[290] V. Mascoli, V. Novoderezhkin, N. Liguori, P. Xu and R. Croce, *Design Principles of Solar Light Harvesting in Plants: Functional Architecture of the Monomeric Antenna CP29*, Biochim. Biophys. Acta - Bioenergetics **1861**, 148156 (2020).

[291] W. L. Jorgensen and J. Tirado-Rives, *The OPLS [Optimized Potentials for Liquid Simulations] Potential Functions for Proteins, Energy Minimizations for Crystals of Cyclic Peptides and Crambin*, J. Am. Chem. Soc. **110**, 1657 (1988).

[292] H. Rahman and U. Kleinekathöfer, *Chebyshev Hierarchical Equations of Motion for Systems with Arbitrary Spectral Densities and Temperatures*, J. Chem. Phys. **150**, 244104 (2019).

[293] M. Schröder, U. Kleinekathöfer and M. Schreiber, *Calculation of Absorption Spectra for Light-harvesting Systems Using Non-Markovian Approaches As Well As Modified Redfield Theory*, J. Chem. Phys. **124**, 084903 (2006).

[294] T.-C. Dinh and T. Renger, *Towards an Exact Theory of Linear Absorbance and Circular Dichroism of Pigment-protein Complexes: Importance of Non-secular Contributions*, J. Chem. Phys. **142**, 034104 (2015).

[295] T. J. Zuehlsdorff, A. Montoya-castillo, J. A. Napoli, T. E. Markland and C. M. Isborn, *Optical Spectra in the Condensed Phase: Capturing Anharmonic and Vibronic Features Using Dynamic and Static Approaches*, J. Chem. Phys. **151**, 074111 (2019).

[296] E. Belgio, G. Tumino, S. Santabarbara, G. Zucchelli and R. Jennings, *Reconstituted CP29: Multicomponent Fluorescence Decay from an Optically Homogeneous Sample*, Photosynth. Res. **111**, 53 (2012).

[297] A. J. Burgess, R. Retkute, S. P. Preston, O. E. Jensen, M. P. Pound, T. P. Pridmore and E. H. Murchie, *The 4-Dimensional Plant: Effects of Wind-Induced Canopy Movement on Light Fluctuations and Photosynthesis*, Front. Plant Sci. **7**, 1392 (2016).

[298] R. Retkute, S. E. Smith-Unna, R. W. Smith, A. J. Burgess, O. E. Jensen, G. N.

Johnson, S. P. Preston and E. H. Murchie, *Exploiting Heterogeneous Environments: Does Photosynthetic Acclimation Optimize Carbon Gain in Fluctuating Light?*, J. Exp. Bot. **66**, 2437 (2015).

[299] I. McConnell, G. Li and G. W. Brudvig, *Energy Conversion in Natural and Artificial Photosynthesis*, Chem. & Bio. **17**, 434 (2010).

[300] S. Takahashi and N. Murata, *How Do Environmental Stresses Accelerate Photoinhibition?*, Trends Plant Sci. **13**, 178 (2008).

[301] S. Shabala, *Plant Stress Physiology* (Cabi, 2017).

[302] A. V. Ruban, *Nonphotochemical Chlorophyll Fluorescence Quenching: Mechanism and Effectiveness in Protecting Plants from Photodamage*, Plant Physiol. **170**, 1903 (2016).

[303] J. Kromdijk, K. Głowacka, L. Leonelli, S. T. Gabilly, M. Iwai, K. K. Niyogi and S. P. Long, *Improving Photosynthesis and Crop Productivity by Accelerating Recovery from Photoprotection*, Science **354**, 857 (2016).

[304] K. Głowacka, J. Kromdijk, K. Kucera, J. Xie, A. P. Cavanagh, L. Leonelli, A. D. B. Leakey, D. R. Ort, K. K. Niyogi and S. P. Long, *Photosystem Ii Subunit S Overexpression Increases the Efficiency of Water Use in a Field-grown Crop*, Nat. Commun. **9**, 868 (2018).

[305] R. Kaňa and Govindjee, *Role of Ions in the Regulation of Light-Harvesting*, Front. Plant Sci. **7**, 1849 (2016).

[306] H. Kirchhoff, *Structural Changes of the Thylakoid Membrane Network Induced by High Light Stress in Plant Chloroplasts*, Philos. Trans. Royal Soc. B **369**, 20130225 (2014).

[307] L. Tian, E. Dinc and R. Croce, *LHCII Populations in Different Quenching States Are Present in the Thylakoid Membranes in a Ratio That Depends on the Light Conditions*, J. Phys. Chem. Lett. **6**, 2339 (2015).

[308] A. V. Ruban, D. Phillip, A. J. Young and P. Horton, *Carotenoid-Dependent Oligomerization of the Major Chlorophyll A/B Light Harvesting Complex of Photosystem II of Plants*, Biochemistry **36**, 7855 (1997).

[309] P. Horton, A. V. Ruban and M. Wentworth, *Allosteric Regulation of the Light-harvesting System of Photosystem II*, Philos. Trans. Royal Soc. B **355**, 1361 (2000).

[310] A. J. Townsend, F. Saccon, V. Giovagnetti, S. Wilson, P. Ungerer and A. V. Ruban, *The Causes of Altered Chlorophyll Fluorescence Quenching Induction in the Arabidopsis Mutant Lacking All Minor Antenna Complexes*, Biochim.

Biophys. Acta (BBA) - Bioenergetics **1859**, 666 (2018).

[311] M. G. Müller, P. Lambrev, M. Reus, E. Wientjes, R. Croce and A. R. Holzwarth, *Singlet Energy Dissipation in the Photosystem II Light-Harvesting Complex Does Not Involve Energy Transfer to Carotenoids*, ChemPhysChem **11**, 1289 (2010).

[312] M. Wahadoszamen, I. Margalit, A. M. Ara, R. Van Grondelle and D. Noy, *The Role of Charge-transfer States in Energy Transfer and Dissipation Within Natural and Artificial Bacteriochlorophyll Proteins*, Nat. Commun. **5**, 5287 (2014).

[313] S. Bode, C. C. Quentmeier, P.-N. Liao, N. Hafi, T. Barros, L. Wilk, F. Bittner and P. J. Walla, *On the Regulation of Photosynthesis by Excitonic Interactions Between Carotenoids and Chlorophylls*, Proc. Natl. Acad. Sci. U.S.A. **106**, 12311 (2009).

[314] T. K. Ahn, T. J. Avenson, M. Ballottari, Y.-C. Cheng, K. K. Niyogi, R. Bassi and G. R. Fleming, *Architecture of a Charge-Transfer State Regulating Light Harvesting in a Plant Antenna Protein*, Science **320**, 794 (2008).

[315] S. Park, A. L. Fischer, C. J. Steen, M. Iwai, J. M. Morris, P. J. Walla, K. K. Niyogi and G. R. Fleming, *Chlorophyll-Carotenoid Excitation Energy Transfer in High-Light-Exposed Thylakoid Membranes Investigated by Snapshot Transient Absorption Spectroscopy*, J. Am. Chem. Soc. **140**, 11965 (2018).

[316] N. E. Holt, D. Zigmantas, L. Valkunas, X.-P. Li, K. K. Niyogi and G. R. Fleming, *Carotenoid Cation Formation and the Regulation of Photosynthetic Light Harvesting*, Science **307**, 433 (2005).

[317] T. J. Avenson, T. K. Ahn, D. Zigmantas, K. K. Niyogi, Z. Li, M. Ballottari, R. Bassi and G. R. Fleming, *Zeaxanthin Radical Cation Formation in Minor Light-harvesting Complexes of Higher Plant Antenna*, J. Biol. Chem. **283**, 3550 (2008).

[318] Z. Li, T. K. Ahn, T. J. Avenson, M. Ballottari, J. A. Cruz, D. M. Kramer, R. Bassi, G. R. Fleming, J. D. Keasling and K. K. Niyogi, *Lutein Accumulation in the Absence of Zeaxanthin Restores Nonphotochemical Quenching in the Arabidopsis Thaliana NPQ1 Mutant*, Plant Cell **21**, 1798 (2009).

[319] H. Yan, P. Zhang, C. Wang, Z. Liu and W. Chang, *Two Lutein Molecules in LHCII Have Different Conformations and Functions: Insights into the Molecular Mechanism of Thermal Dissipation in Plants*, Biochem. Biophys. Res. Commun. **355**, 457 (2007).

[320] C. Ilioaia, M. P. Johnson, P.-N. Liao, A. A. Pascal, R. Van Grondelle, P. J. Walla, A. V. Ruban and B. Robert, *Photoprotection in Plants Involves a Change in Lutein 1 Binding Domain in the Major Light-Harvesting Complex of Photosystem II*, J. Biol. Chem. **286**, 27247 (2011).

[321] R. Remelli, C. Varotto, D. Sandona, R. Croce and R. Bassi, *Chlorophyll Binding to Monomeric Light-harvesting Complex a Mutation Analysis of Chromophore-Binding Residues*, J. Biol. Chem. **274**, 33510 (1999).

[322] S. Caffarri, K. Broess, R. Croce and H. van Amerongen, *Excitation Energy Transfer and Trapping in Higher Plant Photosystem II Complexes with Different Antenna Sizes*, Biophys. J. **100**, 2094 (2011).

[323] K. J. Fujimoto, *Electronic Coupling Calculations with Transition Charges, Dipoles, and Quadrupoles Derived from Electrostatic Potential Fitting*, J. Chem. Phys. **141**, 214105 (2014).

[324] S. Papadatos, A. C. Charalambous and V. Daskalakis, *A Pathway for Protective Quenching in Antenna Proteins of Photosystem II*, Sci. Rep. **7**, 2523 (2017).

[325] J. H. Starcke, M. Wormit, J. Schirmer and A. Dreuw, *How Much Double Excitation Character Do the Lowest Excited States of Linear Polyenes Have?*, Chem. Phys. **329**, 39 (2006).

[326] S. Knecht, C. M. Marian, J. Kongsted and B. Mennucci, *On the Photophysics of Carotenoids: A Multireference DFT Study of Peridinin*, J. Phys. Chem. B **117**, 13808 (2013).

[327] R. Spezia, S. Knecht and B. Mennucci, *Excited State Characterization of Carbonyl Containing Carotenoids: A Comparison Between Single and Multireference Descriptions*, Phys. Chem. Chem. Phys. **19**, 17156 (2017).

[328] P. López-Tarifa, N. Liguori, N. van den Heuvel, R. Croce and L. Visscher, *Coulomb Couplings in Solubilised Light Harvesting Complex II (LHCII): Challenging the Ideal Dipole Approximation from TDDFT Calculations*, Phys. Chem. Chem. Phys. **19**, 18311 (2017).

[329] R. G. Walters, A. V. Ruban and P. Horton, *Identification of Proton-Active Residues in a Higher Plant Light-Harvesting Complex*, Proc. Natl. Acad. Sci. USA **93**, 14204 (1996).

[330] G. Noctor, D. Rees, A. Young and P. Horton, *The Relationship between Zeaxanthin, Energy-dependent Quenching of Chlorophyll Fluorescence, and Transthylakoid Ph Gradient in Isolated Chloroplasts*, Biochim. Biophys. Acta -

Bioenergetics **1057**, 320 (1991).

[331] V. Daskalakis and S. Papadatos, *The Photosystem II Subunit S under Stress*, Biophys. J. **113**, 2364 (2017).

[332] T. Renger, *Theory of Excitation Energy Transfer: From Structure to Function*, Photosynth. Res. **102**, 471 (2009).

[333] M. J. Frisch, G. W. Trucks, H. B. Schlegel, G. E. Scuseria, M. A. Robb, J. R. Cheeseman, G. Scalmani, V. Barone, B. Mennucci, G. A. Petersson, H. Nakatsuji, M. Caricato, X. Li, H. P. Hratchian, A. F. Izmaylov, J. Bloino, G. Zheng, J. L. Sonnenberg, M. Hada, M. Ehara, K. Toyota, R. Fukuda, J. Hasegawa, M. Ishida, T. Nakajima, Y. Honda, O. Kitao, H. Nakai, T. Vreven, J. A. Montgomery, Jr., J. E. Peralta, F. Ogliaro, M. Bearpark, J. J. Heyd, E. Brothers, K. N. Kudin, V. N. Staroverov, R. Kobayashi, J. Normand, K. Raghavachari, A. Rendell, J. C. Burant, S. S. Iyengar, J. Tomasi, M. Cossi, N. Rega, J. M. Millam, M. Klene, J. E. Knox, J. B. Cross, V. Bakken, C. Adamo, J. Jaramillo, R. Gomperts, R. E. Stratmann, O. Yazyev, A. J. Austin, R. Cammi, C. Pomelli, J. W. Ochterski, R. L. Martin, K. Morokuma, V. G. Zakrzewski, G. A. Voth, P. Salvador, J. J. Dannenberg, S. Dapprich, A. D. Daniels, Ö. Farkas, J. B. Foresman, J. V. Ortiz, J. Cioslowski and D. J. Fox, *Gaussian 09 Revision A.02* (2009), Gaussian Inc. Wallingford CT 2009.

[334] A. B. Parusel and S. Grimme, *A Theoretical Study of the Excited States of Chlorophyll a and Pheophytin a*, J. Phys. Chem. B **104**, 5395 (2000).

[335] A. Heil, M. Kleinschmidt and C. M. Marian, *On the Performance of DFT/MRCI Hamiltonians for Electronic Excitations in Transition Metal Complexes: The Role of the Damping Function*, J. Chem. Phys. **149**, 164106 (2018).

[336] S. Grimme and M. Waletzke, *A Combination of Kohn-Sham Density Functional Theory and Multi-Reference Configuration Interaction Methods*, J. Chem. Phys. **111**, 5645 (1999).

[337] I. Lyskov, M. Kleinschmidt and C. M. Marian, *Redesign of the DFT/MRCI Hamiltonian*, J. Chem. Phys. **144**, 034104 (2016).

[338] A. Heil and C. M. Marian, *DFT/MRCI Hamiltonian for Odd and Even Numbers of Electrons*, J. Chem. Phys. **147**, 194104 (2017).

[339] M. R. Silva-Junior, M. Schreiber, S. P. A. Sauer and W. Thiel, *Benchmarks for Electronically Excited States: Time-Dependent Density Functional Theory and Density Functional Theory Based Multireference Configuration Interaction*, J.

Chem. Phys. **129**, 104103 (2008).

[340] A. Kyrychenko, M. V. Rodnin, C. Ghatak and A. S. Ladokhin, *Joint Refinement of FRET Measurements Using Spectroscopic and Computational Tools*, Anal. Biochem. **522**, 1 (2017).

[341] S. Thallmair, P. A. Vainikka and S. J. Marrink, *Lipid Fingerprints and Cofactor Dynamics of Light-harvesting Complex II in Different Membranes*, Biophys. J. **116**, 1446 (2019).

[342] R. Kaňa and Govindjee, *Role of Ions in the Regulation of Light-Harvesting*, Front. Plant Sci. **7**, 1849 (2016).

[343] W. G. Hoover, *Canonical Dynamics: Equilibrium Phase-space Distributions*, Phys. Rev. A **31**, 1695 (1985).

[344] S. Nosé, *A Molecular Dynamics Method for Simulations in the Canonical Ensemble*, Mol. Phys. **52**, 255 (1984).

[345] M. Parrinello and A. Rahman, *Polymorphic Transitions in Single Crystals: A New Molecular Dynamics Method*, J. Appl. Phys. **52**, 7182 (1981).

[346] V. Stehr, R. F. Fink, B. Engels, J. Pflaum and C. Deibel, *Singlet Exciton Diffusion in Organic Crystals Based on Marcus Transfer Rates*, J. Chem. Theory Comput. **10**, 1242 (2014).

[347] A. Dwyer, *Weak Interactions and Excited States from Coulomb-attenuated DFT*, PhD thesis, Durham University (2011).

[348] B. Krueger, G. Scholes and G. Fleming, *Calculation of Couplings and Energy Transfer Pathways Between the Pigments of LH2 by the Ab Initio Transition Density Cube Method*, J. Phys. Chem. B **102**, 5378 (1998).

[349] G. D. Scholes, I. R. Gould, R. J. Cogdell and G. R. Fleming, *Ab Initio Molecular Orbital Calculations of Electronic Couplings in the LH2 Bacterial Light-Harvesting Complex of Rps. Acidophila*, J. Phys. Chem. B **103**, 2543 (1999).

[350] S. Jurinovich, L. Cupellini, C. A. Guido and B. Mennucci, *Exat: Excitonic Analysis Tool*, J. Comput. Chem. **39**, 279 (2018).

[351] R. Kunz, K. Timpmann, J. Southall, R. J. Cogdell, J. Köhler and A. Freiberg, *Fluorescence-excitation and Emission Spectra from LH2 Antenna Complexes of Rhodopseudomonas Acidophila as a Function of the Sample Preparation Conditions*, J. Phys. Chem. B **117**, 12020 (2013).

[352] S. Georgakopoulou, R. N. Frese, E. Jonson, C. Koolhaas, R. J. Cogdell, R. van Grondelle and G. van der Zwan, *Absorption and CD Spectroscopy and Modeling of Various LH2 Complexes from Purple Bacteria*, Biophys. J.

82, 2184 (2002).

[353] M. I. Mallus, Y. Shakya, J. D. Prajapati and U. Kleinekathöfer, *Environmental Effects on the Dynamics in the Light-Harvesting Complexes LH2 and LH3 Based on Molecular Simulations*, Chem. Phys. **515**, 141 (2018).

[354] N. Eswar, B. Webb, M. A. Marti Renom, M. S. Madhusudhan, D. Eramian, M.-Y. Shen, U. Pieper and A. Sali, *Comparative Protein Structure Modeling Using Modeller*, Curr. Protoc. Bioinformatics **15**, 561 (2006).

[355] J. W. Park and Y. M. Rhee, *Constructing Polyatomic Potential Energy Surfaces by Interpolating Diabatic Hamiltonian Matrices with Demonstration on Green Fluorescent Protein Chromophore*, J. Chem. Phys. **140**, 164112 (2014).

[356] M. Higashi and S. Saito, *Quantitative Evaluation of Site Energies and Their Fluctuations of Pigments in the Fenna-Matthews-Olson Complex with an Efficient Method for Generating a Potential Energy Surface*, J. Chem. Theory Comput. **12**, 4128 (2016).

[357] E. Belgio, A. P. Casazza, G. Zucchelli, F. M. Garlaschi and R. C. Jennings, *Band Shape Heterogeneity of the Low-energy Chlorophylls of CP29: Absence of Mixed Binding Sites and Excitonic Interactions*, Biochemistry **49**, 882 (2010).